

Exsolution depth and migration pathways of mineralising fluids in porphyry deposit-forming magmatic systems

Submitted by Lawrence Christopher Carter to the University of Exeter as a thesis for the degree of Doctor of Philosophy in Geology, March 2022.

This thesis is available for Library use on the understanding that it is copyright material and that no quotation from the thesis may be published without proper acknowledgement.

I certify that all material in this thesis which is not my own work has been identified and that no material has previously been submitted and approved for the award of a degree by this or any other University.

Signed:  _____



British
Geological
Survey

UNIVERSITY OF
EXETER



Abstract

Porphyry-type deposits provide most of the world's Cu and Mo, and a large proportion of Au and other metals, vital in the transition towards a green economy. They form from hydrothermal fluids exsolving in the upper parts of large, long-lived, trans-crustal magmatic systems. Whilst they are the most intensively studied of all ore-deposit types, our understanding of how they develop is fragmented as their 3D architecture is rarely well exposed. As such, it remains unclear why and which magmatic systems become capable of forming ore deposits, how mineralising fluids are transported from their source magmas in sufficient quantities, and over what time scales such magmatic-hydrothermal systems evolve. Understanding these aspects is vital for the development of exploration models to identify magmatic centres which may host porphyry-type deposits and where within them most mineralisation may lie.

To address this, the archetypal Yerington batholith, Nevada, USA, was studied as it is exceptionally well exposed in 3D and has provided constraints for most modern porphyry exploration models. From detailed field investigations and micro-textural, geochemical and high precision geochronological studies, the magmatic system underwent a major and abrupt change in chemical composition over a period of <200 kyrs that was coincident with the initiation of ore formation. This switch, which is documented across the plutonic to volcanic record, is attributed to a change in the source of magmas from the mid- to lower crust, to form the older McLeod quartz monzodiorite and Bear quartz monzonite plutons, to the lower crust (~30 km depth) to produce the Luhr Hill granite. The latter, which was emplaced within the older plutons at a depth of ~3-8 km, contains pegmatitic pods and massive silica bodies indicating high degrees of undercooling and volatile-undersaturation. Deeper and more evolved portions of the Luhr Hill granite magma were episodically intruded upwards as aplite dykes. These underwent progressive depressurisation and associated volatile exsolution to form a crystal mush of feldspar and quartz which contained a network of inter-crystal pathways for the upward migration of mineralising fluids from large volumes of the evolving, water-rich, deep regions of the underlying Luhr Hill granite pluton. As a result of these processes, the dykes contain unidirectional solidification textures (USTs), quartz segregations, mineralised miarolitic cavities, and finally A-type veins, with a continuum to B-type veins driven by cyclic hydrofracturing, just below and within the region of porphyry-style mineralisation.

These findings: i) Suggest that the increase in a magma's ore-forming potential is not solely driven by a progressive multi-million year ramp-up in ore-forming constituents, but also through a rapid (<200 kyrs) switch in magma source and the nature of the plumbing system; ii) Narrow the temporal-geochemical footprint of magmas associated with porphyry mineralisation; iii) Provide evidence for the transport and focussing of magmatic-hydrothermal fluids through crystal mush dykes, from extensive regions of underlying magmas; and iv) Provide a spatial-temporal framework for exploration geologists to assess the 4D architecture of porphyry magmatic systems. These findings should be incorporated into future models of the nature and formation of porphyry- and similar-type deposits and will help provide an early filter in exploration before more invasive and expensive techniques are employed.

Acknowledgements

This project was supported by a NERC GW4+ Doctoral Training Partnership studentship from the Natural Environment Research Council (NERC) [NE/L002434/1], with additional support from the British Geological Survey and the Natural History Museum, London, and was allied to the NERC Highlight Topic project 'From Arc Magmas to Ores (FAMOS): A Mineral Systems Approach' [NE/P017452/1]. I am grateful for additional funding from the SEGF's Hugh McKinstry Fund to support fieldwork, a NERC NIGL isotope facilities grant for CA-ID-TIMS analyses, a UK National Ion Beam Centre pump-primer grant to support Total-IBA, an SEG travel grant to support conference attendance, funding from the SEGF to attend the SEG student fieldtrip, and additional support from SelfFrag AG.

I am grateful for the field support and drill core access provided by George Eliopoulos and Todd Bonsall of Quaterra Resources and Matt Cunningham of Hudbay Resources (previously Mason Resources), made possible by initial introductions from David First. I am grateful for early supervisory support and input from Robin Shail, Robin Armstrong and Kathy Cashman. Sam Broom-Fendley is thanked for feedback and advice throughout the project. I thank Steve Pendray, Dan Parvaz and Adrian Wood for sample preparation support. Joe Pickles and Jens Anderson are thanked for SEM and EPMA support along with Gavyn Rollinson for QEMSCAN[®] analysis and offering analytical advice throughout the project. Malcolm Spence and Sharon Uren are thanked for their assistance throughout, Tiff Barry, Lin Marvin-Dorland and Adam Cox for whole-rock XRF and ICP-MS analysis, Catia Costa and Geoff Grime for Total-IBA, Yannick Buret for LA-ICP-MS analysis and his thought-provoking input, Ian Millar for zircon Lu-Hf isotopic analysis and David Selby for molybdenite Re-Os geochronology. I am grateful to Axel Müller for his feedback on a 'crystal mush dykes' draft manuscript, and Jamie Wilkinson and other FAMOS collaborators for fruitful discussions throughout the project.

I am very appreciative to Doug Kirwin for his informal mentorship and support, providing feedback on draft 'textual indicators' manuscripts, invigorating discussions, and for sharing huge catalogues of photographs and observations.

I am extremely grateful to Simon Tapster for his supervisory support, expertise in geochemistry and geochronology, and for always pushing me to reach my potential.

Ben Williamson never ceased to go above and beyond, providing invaluable advice, influential support, and meticulous editing – morning, noon or night! I will be forever grateful for his exceptional supervision.

Finally, thank you to the support from my family and thank you to Laura for putting up with all of this.

I only wish that my mother, Hilary, were still here to celebrate this achievement in style.

'Laboris Gloria Ludi'.

Contents

Abstract.....	i
Acknowledgements	ii
List of figures.....	ix
List of tables	xi
List of supplementary figures.....	xi
List of supplementary data	xii
Author's declaration.....	xiii
1 Introduction	1
1.1 Project rationale	1
1.2 Research objectives and approaches	2
1.3 Publication and presentation of this work.....	3
1.4 Thesis structure.....	5
2 Literature Review	8
2.1 Porphyry-type copper deposits.....	8
2.1.1 Overview.....	8
2.1.2 Spatial-temporal distribution	9
2.1.3 Modern concepts of magmatic plumbing	10
2.1.4 Deposit formation and architecture.....	12
2.1.5 Porphyry-style mineralisation.....	14
2.1.6 Hydrothermal alteration in porphyry systems.....	15
2.1.7 Porphyry fertility indicators.....	23
2.1.8 Outstanding questions	24
2.2 Textures associated with mineralised granites.....	27
2.3 The Yerington batholith, Nevada – Geological setting.....	34
2.3.1 Introduction.....	34
2.3.2 Geography.....	36
2.3.3 Tectonic setting.....	36

2.3.4	Early Mesozoic rocks	38
2.3.5	The Yerington batholith.....	39
2.3.6	Younger Jurassic Igneous Rocks	44
2.3.7	Cenozoic Rocks and Structural Geology	45
2.4	The Yerington batholith, Nevada – Economic geology	45
2.4.1	Overview.....	45
2.4.2	Production history	46
2.4.3	Yerington deposit.....	47
2.4.4	Bear deposit	49
2.4.5	MacArthur deposit.....	49
2.4.6	Ann Mason deposit.....	49
3	Textural indicators of mineralisation potential in porphyry magmatic systems – a framework from the archetypal Yerington District, Nevada	51
3.1	Abstract.....	51
3.2	Introduction	52
3.3	Geological setting – the Yerington porphyry system, Nevada	53
3.4	Methods	54
3.4.1	SEM-EDX-CL.....	54
3.4.2	QEMSCAN®.....	55
3.4.3	EPMA	56
3.4.4	Ti-in-quartz geothermometry	56
3.5	Results and discussion.....	57
3.5.1	Massive silica bodies and pegmatitic pods	57
3.5.2	Macro textures of the magmatic-hydrothermal transition	59
3.5.3	Magmatic-hydrothermal textures elsewhere	67
3.5.4	Exploration vectors	68
3.6	Conclusions.....	70
3.7	Declaration of co-authorship	71
3.8	Supplementary Data.....	71

4	Crystal mush dykes as conduits for mineralising fluids in the Yerington porphyry copper district, Nevada.....	72
4.1	Abstract.....	72
4.2	Introduction	73
4.3	Results and Discussion.....	75
4.4	Conclusions.....	87
4.5	Methods	88
4.5.1	Polished thin sections.....	88
4.5.2	SEM-EDX-CL.....	89
4.5.3	QEMSCAN®.....	89
4.5.4	EPMA	90
4.5.5	Total-IBA.....	91
4.5.6	Ti-in-quartz geothermometry	93
4.6	Declaration of co-authorship	94
4.7	Supplementary figures	96
4.8	Supplementary data.....	106
5	A rapid change in magma plumbing taps porphyry copper deposit-forming magmas.....	107
5.1	Abstract.....	107
5.2	Introduction	108
5.3	The construction of a porphyry-forming magmatic system.....	109
5.4	Temporal constraints from field relationships.....	111
5.5	Absolute age constraints on magmatic system evolution.....	115
5.6	Geochemical change within the magmatic system.....	119
5.7	Isotopic constraints on magma pathways.....	124
5.8	Depth of melt evolution.....	126
5.9	A rapid change in magmatic plumbing to tap porphyry ore-forming magmas.....	127

5.10	Genetic implications for porphyry deposit-forming magmatic systems	132
5.11	Conclusions	134
5.12	Methods	134
5.12.1	QEMSCAN®	135
5.12.2	Electric Pulse Fragmentation (EPF)	135
5.12.3	Whole-rock XRF and ICP-MS analysis, and CIPW normative mineralogy.....	136
5.12.4	Zircon separation.....	137
5.12.5	Zircon LA-ICP-MS	138
5.12.6	Zircon U-Pb CA-ID-TIMS geochronology	138
5.12.7	Zircon Lu-Hf isotopes	140
5.12.8	Rhenium-Osmium molybdenite geochronology.....	141
5.13	Declaration of co-authorship	142
5.14	Supplementary figures	143
5.15	Supplementary data.....	161
6	Synthesis and outlook	162
6.1	The Yerington batholith - Construction and magmatic-hydrothermal mineralisation.....	162
6.2	Plumbing of porphyry deposit-forming magmatic systems	164
6.3	Crystal mush fluid conduits in porphyry systems.....	166
6.4	Exploration tools.....	169
6.4.1	Geochemical signatures	169
6.4.2	Textural vectors	170
6.5	Scope for future research.....	172
6.5.1	Study areas for future research	172
6.5.2	Develop a self-consistent thermal and temporal framework for the magmatic components of the porphyry deposit-forming system.	173

6.5.3	Develop a self-consistent thermal and temporal framework for the hydrothermal components of porphyry systems.....	173
6.5.4	Define 'crystal mush' fluid flow parameters.....	175
6.5.5	Develop new integrated numerical simulations for the crustal-scale extraction and transport of mineralising fluids within porphyry systems. .	175
6.5.6	Develop new mineralogical toolkits for exploring magmatic-hydrothermal systems.	176
6.6	Key conclusions	176
7	References.....	178

List of figures

Fig. 2.1 Map of porphyry Cu systems worldwide.....	10
Fig. 2.2 Schematic section through an upper crustal magmatic system	12
Fig. 2.3 Schematic cross section through an active porphyry Cu system	14
Fig. 2.4 Lowell and Guilbert's (1970) classic schematic model for the distribution of alteration and ore minerals within a porphyry system.....	20
Fig. 2.5 Generalised alteration-mineralisation zonation for a non-telescoped porphyry Cu system	22
Fig. 2.6 Formation of UST's	32
Fig. 2.7 Quartz and alkali feldspar crenulated layers in a porphyritic aplite	33
Fig. 2.8 Plumose alkali feldspar layers in aplite	34
Fig. 2.9 Map and reconstructed section through the Yerington District, Nevada	35
Fig. 2.10 Early Jurassic (195 Ma) plate reconstruction	37
Fig. 2.11 Tectonic setting of the Yerington batholith	38
Fig. 2.12 Generalised composite column of the Yerington District.....	40
Fig. 2.13 Paragenetic diagram for the Yerington batholith	44
Fig. 2.14 Map of the Yerington Batholith.....	46
Fig. 2.15 Simplified composite-level map of the Yerington mine.....	48
Fig. 3.1 Pre-tilt cross section through the Yerington District, Nevada	54
Fig. 3.2 Field photograph of a quartz-feldspar pegmatitic pod and a massive silica body in the exposed cupola of the Luhr Hill granite.....	59
Fig. 3.3 Photographs of interfingering quartz segregations within aplite dykes.....	61
Fig. 3.4 Field photographs of quartz USTs in aplitic dykes	62
Fig. 3.5 Photograph, QEMSCAN® and EPMA Ti-in-quartz analysis of chalcopyrite-molybdenite-mineralised quartz USTs in an aplite dyke from the Ann Mason porphyry deposit.	64
Fig. 3.6 Tukey box plot of Ti-in-quartz crystallisation temperature for Luhr Hill granite, a pegmatitic pod within the Luhr Hill granite, and quartz USTs	66
Fig. 3.7 Photographs of mineralised miarolitic cavities within aplite dykes which cross-cut the Luhr Hill granite.....	66
Fig. 3.8 Summary schematic section showing the spatial and temporal distribution of magmatic-hydrothermal textures within an undercooled granitic cupola associated with porphyry-style mineralisation.....	70

Fig. 4.1 Pre-tilt cross section through the Yerington porphyry copper district, Nevada.....	74
Fig. 4.2 Quartz-feldspar pegmatitic orbs in the Luhr Hill granite cupola.....	78
Fig. 4.3 Magmatic-hydrothermal textures in aplite dykes	79
Fig. 4.4 Fluid exsolution and mineralisation in aplite dykes	80
Fig. 4.5 Mineralising aplitic mush at the magmatic-hydrothermal transition	82
Fig. 4.6 Timing and temperature of crystallisation in aplite crystal mush dykes	85
Fig. 4.7 Crystal mush dykes acting as fluid conduits: Schematic cross-section	87
Fig. 5.1 Pre-tilt cross section through the Yerington District, Nevada	110
Fig. 5.2 Simplified geological map of the Yerington District, Nevada	111
Fig. 5.3 Temporal relations in the Yerington magmatic system.....	114
Fig. 5.4 Geochronological framework for the Yerington porphyry system.....	118
Fig. 5.5 Chondrite-normalised (McDonough and Sun, 1995) mean whole-rock REE plots	119
Fig. 5.6 Whole-rock geochemical compositions of plutonic units in the Yerington magmatic system	120
Fig. 5.7 Zircon trace element signatures through the Yerington magmatic system	123
Fig. 5.8 Zircon ϵ_{Hf_t} through the Yerington magmatic system	125
Fig. 5.9 Depth of different magma sources	127
Fig. 5.10 A rapid switch in magmatic plumbing to tap porphyry-mineralising magmas.....	131
Fig. 6.1 Schematic models for the plumbing of porphyry deposit-forming magmatic systems.....	166
Fig. 6.2 Schematic models for the source of magmatic aqueous fluids in porphyry systems	169
Fig. 6.3 Summary integration of magmatic-hydrothermal textural exploration vectors.....	171

List of tables

Table 2.1 Nomenclature and general paragenesis of veins from a typical porphyry deposit.....	15
Table 2.2 Summary of the principal alteration-mineralisation types in porphyry systems	18
Table 5.1 Treatment conditions for electric pulse fragmentation.....	136

List of supplementary figures

Sup. fig. 4.1 Massive silica body in the Luhr Hill granite cupola	96
Sup. fig. 4.2 Dykes in granite cupola	97
Sup. fig. 4.3 Spatial distribution of aplite dykes	98
Sup. fig. 4.4 Aplite dyke temporal relations	99
Sup. fig. 4.5 B-type veins in aplite dyke.....	100
Sup. fig. 4.6 Aplite dyke groundmass	101
Sup. fig. 4.7 Wormy groundmass quartz in an aplite dyke	102
Sup. fig. 4.8 Wormy groundmass quartz in an aplite dyke adjacent to a mineralised miarolitic cavity.....	103
Sup. fig. 4.9 Wormy groundmass quartz in an aplite dyke alongside an early quartz vein.....	104
Sup. fig. 4.10 Multiple quartz generations in the aplite dyke and mineralised miarolitic cavity	105
Sup. fig. 5.1 Plutonic contacts	143
Sup. fig. 5.2 Igneous banding in Luhr Hill granite	144
Sup. fig. 5.3 Textural evidence for undercooling, magmatic-hydrothermal fluid exsolution and mineralisation in aplite dykes.....	145
Sup. fig. 5.4 Zircons in aplite dyke which hosts mineralised miarolitic cavities	146
Sup. fig. 5.5 Zircons in aplite dyke which hosts miarolitic cavities	147
Sup. fig. 5.6 Zircons in aplite dyke which host miarolitic cavities.....	148
Sup. fig. 5.7 Propylitic alteration in Fulstone Spring Volcanics	149
Sup. fig. 5.8 Samples for molybdenite Re-Os age determinations	150
Sup. fig. 5.9 Chondrite-normalized (McDonough and Sun, 1995) mean whole-rock REE plots.....	151

Sup. fig. 5.10 Plutonic TAS diagram (Middlemost, 1994) and whole-rock geochemistry through the Yerington magmatic system.....	152
Sup. fig. 5.11 Dy/Yb versus SiO ₂ for plutonic units.....	153
Sup. fig. 5.12 Zircon REE patterns	154
Sup. fig. 5.13 Zircon trace element signatures through the Yerington magmatic system.....	155
Sup. fig. 5.14 Zircon trace element signatures through the Yerington magmatic system.....	156
Sup. fig. 5.15 Zircon trace element signatures through the Yerington magmatic system.....	157
Sup. fig. 5.16 Zircon trace element signatures for plutonic units of the Yerington porphyry system	158
Sup. fig. 5.17 Zircon εHf through the Yerington magmatic system.....	159
Sup. fig. 5.18 Depth of different magma sources	160

List of supplementary data

Supplementary Data 3.1: QEMSCAN® automated mineralogical assessment data.....	71
Supplementary Data 3.2: EPMA data	71
Supplementary Data 4.1: EPMA and Total-IBA analyses.....	106
Supplementary Data 4.2: QEMSCAN® data.....	106
Supplementary Data 5.1: Full sample list.....	161
Supplementary Data 5.2: Zircon U-Pb CA-ID-TIMS and molybdenite Re-Os geochronology data.....	161
Supplementary Data 5.3: QEMSCAN® automated mineralogical assessment data	161
Supplementary Data 5.4: Whole-rock XRF & ICP-MS geochemistry data ...	161
Supplementary Data 5.5: Zircon LA-ICP-MS data.....	161
Supplementary Data 5.6: Zircon Lu-Hf isotope data	161

Author's declaration

Illogan, Cornwall, March 2022

I hereby certify that all material in this thesis which is not my own work has been identified and that no material has previously been submitted and approved for the award of a degree by this or any other university.

Chapters 3, 4 & 5 contain work that is the result of collaboration with others. Each of these chapters has its own declaration of co-authorship, which lists the names and contributions of all collaborators.

Signed:

A handwritten signature in black ink, appearing to be 'L. Carter', written in a cursive style.

Lawrence Christopher Carter

1 Introduction

1.1 Project rationale

Porphyry-type deposits are a vital source of copper, molybdenum, gold and other metals which are in increasing demand for green technologies such as electric vehicles, wind turbines and photovoltaic cells (Sillitoe, 2010; Herrington, 2021; Watari et al., 2021). They typically form from magmatic-hydrothermal fluids that exsolve from large and long-lived calc-alkaline to slightly alkaline, water-rich and relatively oxidising trans-crustal magmatic systems, mostly in subduction related tectonic settings (Richards, 2005; Sillitoe, 2010; Wilkinson, 2013; Richards, 2015). With copper demand forecast to increase by 140-350% from 2010 to 2050 (Elshkaki et al., 2016; Watari et al., 2021), the discovery of new porphyry deposits remains a key target for most major mining companies. However, not only are porphyry-type deposits extremely rare, their formation requiring a series of specific conditions and events during the evolution of magmatic-hydrothermal systems (Wilkinson, 2013), but most large near-surface examples have already been found (Richards, 2003) and exploration campaigns are having to focus on increasingly deeper and/or complex targets (e.g. Cooke et al., 2017). Exploration success is therefore heavily reliant on our fundamental understanding of where and why porphyry deposits form, along with how we can use textural and geochemical information to vector towards centres of mineralisation.

Due largely to their economic significance, porphyry deposits are amongst the most intensively studied of all mineralisation types (Richards, 2018). Our fundamental understanding of how porphyry-forming magmatic-systems operate is however limited by the paucity of exposure of these systems, particularly of their deeper 'root-zones' (Seedorff et al., 2008). As a consequence, key questions remain: Are the magmatic-hydrothermal processes that lead to ore-formation preserved as chemical and textural features in the rock record, and, if so, how can these be used to vector towards mineralisation? How are sufficient quantities of mineralising fluids extracted from source magmas and transported upwards into the ore-forming environment? Over what timescales do these mechanisms occur?

This research aimed to readdress these knowledge gaps through field, geochemical and geochronological studies on the archetypal Yerington District, Nevada. The District contains a uniquely exposed ~8 km deep section through a magmatic system, from volcanic to plutonic environments, including four porphyry deposits (Proffett and Dilles, 1984; Dilles, 1987; Dilles et al., 2000). Yerington has previously provided fundamental constraints for our understanding of the formation of porphyry systems (e.g. Dilles, 1987; Seedorff et al., 2005; Sillitoe, 2010; Wilkinson, 2013) and numerical models of batholith construction and porphyry mineralisation (Weis et al., 2012; Schöpa et al., 2017).

1.2 Research objectives and approaches

Objective i): Assess how magmatic disequilibrium textures (e.g. miarolitic cavities and pegmatitic pods) can be used to navigate the spatial and temporal architecture of mineralised magmatic-hydrothermal systems, and as exploration tools. This was achieved by identifying and describing key textures in outcrop and drill core, including their spatial and temporal association with mineralisation, detailed characterisation using scanning electron microscopy with cathodoluminescence imaging (SEM-CL), QEMSCAN[®] automated mineralogical analysis and Ti-in-quartz thermometry (method of Wark and Watson, 2006), using Ti concentrations from electron probe microanalysis (EPMA), and comparison with textural observations from elsewhere. The compilation of these data generated a self-consistent framework of magmatic and magmatic-hydrothermal textures along with a genetic model.

Objective ii): Determine the environments and causes of fluid exsolution and migration in porphyry magmatic systems. This was addressed by studying textures indicative of fluid exsolution, flow, and mineralisation in outcrop and drill core using naked eye and hand-lens observations, optical microscopy, SEM and CL imaging, energy-dispersive X-ray spectroscopy (EDX), QEMSCAN[®], EPMA, total ion beam analysis (Total-IBA) and Ti-in-quartz geothermometry. Integration of this data provided evidence on the nature of magmatic-hydrothermal fluid transport which was incorporated into a new model for how porphyry deposit-forming fluids are extracted and migrate from their source magmas.

Objective iii): Evaluate the relative timing of batholith construction, including dyke emplacement, and geochemical signatures, timescales and drivers of mineralisation. This was achieved by integrating first-order field observations with a broad suite of micro-textural, geochemical and geochronological data, specifically whole-rock major and trace element compositions, zircon geochemical and Lu-Hf isotopic signatures, and high precision zircon U-Pb and molybdenite Re-Os geochronology. When combined, this data underpinned a new 4D model for how the ore-forming potential of the magmatic system evolved.

1.3 Publication and presentation of this work

Most of the work presented in this thesis has either been published (or is in review at the time of writing) as journal articles or presented at national and international scientific conferences, as listed below.

Journal Articles

Carter, L. C., Tapster, S. R., Williamson, B. J., Buret, Y., Selby, D., Rollinson, G. K., Millar, I. & Parvaz, D. B. A rapid change in magma plumbing taps porphyry copper deposit-forming magmas. *Scientific Reports* **12**, 17272. <https://doi.org/10.1038/s41598-022-20158-y>

Carter, L. C. & Williamson, B. J., 2022. Textural indicators of mineralisation potential in porphyry magmatic systems – a framework from the archetypal Yerington District, Nevada. *Ore Geology Reviews* **143**, 104783. <https://doi.org/10.1016/j.oregeorev.2022.104783>

Carter, L. C., Williamson, B. J., Tapster, S. R., Costa, C., Grime, G. W. & Rollinson, G. K., 2021. Crystal mush dykes as conduits for mineralising fluids in the Yerington porphyry copper district, Nevada. *Communications Earth & Environment* **2**, 59. <https://doi.org/10.1038/s43247-021-00128-4>

Conference Presentations

Carter, L. C., Tapster, S., Williamson, B. J., Buret, Y., Selby, D., Millar, I., Rollinson, G. K. & Parvaz, D. 2022. An abrupt switch in magmatic plumbing taps porphyry copper deposit-forming magmas. SEG 2022 Denver, Minerals for our future.

Carter, L. C., Williamson, B. J., Tapster, S. R., Costa, C., Grime, G. W. & Rollinson, G. K., 2021. Crystal mush dykes as conduits for porphyry copper deposit-forming fluids. SEG 100: Celebrating a Century of Discover, Whistler (Online).

Carter, L. C., Tapster, S. R., Williamson, B. J., Buret, Y., Millar, I., Selby, D., & Parvaz, D. B., 2021. Abrupt switch in magmatic plumbing to tap porphyry copper-‘fertile’ magmas. SEG 100: Celebrating a Century of Discover, Whistler (Online).

Carter, L. C., Tapster, S. R., Williamson, B. J., Buret, Y., Selby, D. & Parvaz, D. B., 2021. The 4D Trans-Crustal Architecture of a Porphyry Copper-Forming Magmatic System. Goldschmidt, Lyon (Online). <https://doi.org/10.7185/gold2021.6175>

Carter, L. C., Tapster, S. R., Williamson, B. J. & Buret, Y., 2020. The porphyry fertility switch – detail from the Yerington District, Nevada. MDSG annual meeting (Online).

Carter, L. C., Williamson, B. J, Tapster, S. R., Costa, C. & Grime, G. W., 2020. Crystal mush dykes as the source and conduit for porphyry deposit forming fluids. SEG Student Showcase (Online).

Carter, L. C., Williamson, B. J, Tapster, S. R., Costa, C. & Grime, G. W., 2020. Total-IBA Detailing Mineralising Fluid Migration & Exsolution to form Porphyry Copper Deposits. 17th International Conference on Nuclear Microprobe Technology and Applications (ICNMTA) (Online).

Carter, L. C., Williamson, B. J., Armstrong, R. N., Tapster, S. & Buret, Y., 2020. Yerington District, Nevada: New porphyry system petrogeochronology. MDSG annual meeting, NHM, London.

Carter, L. C., Williamson, B. J., Armstrong, R. N. & Tapster, S., 2020. Exsolution and migration of mineralising fluids in porphyry magmatic systems - Evidence from the Yerington District, Nevada. MDSG annual meeting, NHM, London.

Carter, L. C., Williamson, B. J., Armstrong, R. N. & Tapster, S., 2019. Mineralising fluid exsolution and migration in porphyry systems - New perspectives from the Yerington District, Nevada. SEG 2019 Santiago, South American Metallogeny: Sierra to Craton. [SEG award for best student presentation]

Carter, L. C., Williamson, B. J., Armstrong, R. N. & Tapster, S., 2019. The nature of fluid exsolution and migration in porphyry systems - evidence from the Yerington District, Nevada. Proceedings of the 15th SGA Biennial Meeting, Glasgow, Scotland, pp. 973-976.

Carter, L. C., Williamson, B. J., Armstrong, R. N. & Tapster, S., 2019. New perspectives into the timing and nature of fluid exsolution and migration in Cu porphyry-forming magmatic systems – evidence from the Yerington District, Nevada. EGU general assembly - Geophysical Research Abstracts, Vol. 21, EGU2019-13169.

Carter, L. C., Williamson, B. J., Armstrong, R. N. & Tapster, S., 2019. Exsolution depth and migration pathways of mineralising fluids in porphyry systems – examples from the Yerington District, Nevada. Applied Earth Science, 128(2), p. 42. <https://doi.org/10.1080/25726838.2019.1601354> [RioTinto award for best PhD student presentation]

1.4 Thesis structure

This thesis is comprised of six chapters. Chapter 1 provides a general introduction and Chapter 2 a review of existing work in the field. These are followed by the main body of the thesis which is made up of three manuscripts (Chapters 3-5) which contain the results of the four year PhD study. Each of these chapters are structured as standalone papers, with their own brief introduction and literature review. Some repetition therefore occurs, particularly between the thesis introduction chapters (Chapter 1 and 2) and the introduction sections of each manuscript. To reduce repetition, some specific concepts and literature are only introduced where specifically needed in Chapters 3-5, and were not summarised in Chapters 1 or 2.

The manuscripts that form the basis of Chapters 3-5 were in a journal-specific style which needed editing to match the format of the thesis. All relevant data for each of these chapters are included as self-contained Supplements at the end of each Chapter (with URL links to online Databases). The plural is used for first-person pronouns in each of these manuscripts to conform with the author lists. Contributions from co-authors and other collaborators are stated in the author contributions and acknowledgements sections for each manuscript. The intellectual development of the hypotheses and interpretations presented in all of

these manuscripts are my own. The outcomes of Chapters 3-5 and their implications are summarised in Chapter 6 along with recommendations for future work. References cited in the text are listed at the end of the thesis. Brief summaries of the contents of each chapter are listed below.

Chapter 1 – Introduction that provides the rationale and scope of the study, a basic introduction to the Yerington District, research aims and structure of the thesis.

Chapter 2 – Literature review covering porphyry-type copper deposits, textures associated with mineralised granites, and the Yerington District.

Chapter 3 – ‘Textural indicators of mineralisation potential in porphyry magmatic systems – a framework from the archetypal Yerington District, Nevada’. This manuscript provides a framework of magmatic-hydrothermal textures and discusses their formation and metallogenic associations along with how they can aid exploration geologists navigate the spatial and temporal architecture of porphyry and related systems. This manuscript has been published in *Ore Geology Reviews* and is referred to as Carter and Williamson (2022) in the remainder of the thesis.

Chapter 4 – ‘Crystal mush dykes as conduits for mineralising fluids in the Yerington porphyry copper district, Nevada’. This manuscript addresses the missing link in models for the formation of porphyry-type copper deposits – how vast quantities of mineralising fluids are extracted and transported from their source magmas and focussed into the ore-forming environment. In doing so this provides the first field, petrographic and microscale evidence for magmatic-hydrothermal fluid transport through what is termed ‘crystal mush dykes’. This manuscript was published in *Communications Earth & Environment* and is referred to as Carter et al. (2021) in the remainder of the thesis.

Chapter 5 – ‘A rapid change in magma plumbing taps porphyry copper deposit-forming magmas’. This manuscript provides a new geochemical and high-resolution geochronological framework for the Yerington porphyry system. In doing so, it identifies an abrupt change in magma chemistry coincident with the

onset of ore formation, which is documented across the entire plutonic to volcanic record. This manuscript was published in *Scientific Reports* and is referred to as Carter et al. (2022) in the remainder of the thesis.

Chapter 6 – ‘Synthesis and outlook’. A synthesis of outcomes from Chapters 3-5 and their implications, along with conclusions and recommendations for further studies.

References – References cited in the thesis.

2 Literature Review

2.1 Porphyry-type copper deposits

2.1.1 Overview

Porphyry copper systems provide about 75%, 50% and 20% of the world's copper, molybdenum and gold, respectively, along with most rhenium and lesser amounts of other metals (Ag, Pd, Te, Se, Bi, Zn and Pb) (Sillitoe, 2010). Porphyry systems contain the world's largest known exploitable concentrations of contained copper (203 Mt; Los Bronces-Río Blanco, central Chile) and molybdenum (2.5 Mt; El Teniente, central Chile) and the second largest of gold (129 Moz; Grasberg, Indonesia) (Sillitoe, 2010, and references therein). In the 21st century, this, along with the mining industry's preference for low grade, high tonnage deposits, makes them high priority exploration targets (Cooke et al., 2017). As a result, the magmatic-hydrothermal processes leading to mineralisation in porphyry systems has been a focal point of research over the last few decades (key overviews include Lowell and Guilbert, 1970; Sillitoe, 1973; Dilles, 1987; Richards et al., 2005; Seedorff et al., 2005; Sillitoe, 2010; Wilkinson, 2013).

Porphyry copper systems have been defined as large volumes (10 - >100 km³) of hydrothermally-altered rock centred on porphyry stocks, which may also contain associated skarn, carbonate replacement, sediment-hosted and high and intermediate sulphidation epithermal mineralisation (Sillitoe, 2010). These large systems, often comprising multiple plutons, have magmatic-hydrothermal histories spanning millions of years, but ore formation typically occurred during multiple short-lived events with durations of a few hundred thousand years (Seedorff et al., 2005; Sillitoe, 2010). They are typically associated with calc-alkaline magmatic systems above active subduction zones, although some can be found in post-collisional settings (Richards, 2003). In subduction zone environments, as the oceanic plate and overlying sediments subduct, increasing pressures and temperatures causes them to dehydrate. This releases fluids into the overlying mantle wedge causing it to melt and produce water-rich arc-type magmas that rise to high levels in the crust (Wilkinson, 2013).

Porphyry Cu ± Mo ± Au deposits (hereby referred to as porphyry Cu deposits), of sizes ranging from <10 Mt to >10 Gt, are mostly found at depths of several km within porphyry systems (Sillitoe, 2010; Wilkinson, 2013). These may be associated with Cu, Au and/or Zn skarns at their margins and high and intermediate sulphidation epithermal Au ± Ag ± Cu mineralisation at higher levels (Sillitoe, 2010). In porphyry Cu deposits, ore minerals typically occur in veins and as disseminations with relatively low grades; commonly less than 1% Cu in a copper porphyry, about 0.1% Mo in a molybdenum porphyry and about 1 g/t Au where this is economically important. Ore and surrounding rock is characterised by numerous generations of closely spaced veins and veinlets (stockwork), which mark the pathways of hydrothermal fluids, between which the rock is pervasively altered. Key hypogene ore minerals are chalcopyrite, bornite, chalcocite, molybdenite and native Au (Sillitoe, 2010). Supergene oxidation and enrichment, occurring in the weathering environment to depths of several hundred metres, has a major impact on the economic viability of porphyry Cu deposits, transforming Cu grade locally to two to three times the hypogene tenor (Sillitoe, 2005).

Porphyry Cu deposits have a strong association with relatively oxidised and water- and sulphur-rich magmas (Ballard, et al., 2002; Sillitoe, 2010). Their causative igneous intrusions are typically of I-type and magnetite-series affiliation (Ishihara, 1981), and are metaluminous and medium-K calc-alkaline, although they may also fall into the high-K calc-alkaline (shoshonitic) or alkaline fields (Sillitoe, 2010). They also typically have a distinctive trace element chemistry, for example with high Sr/Y and La/Yb ratios (Richards, 2011; Chiaradia et al., 2012).

2.1.2 Spatial-temporal distribution

Porphyry Cu deposits (**Fig. 2.1**) are most commonly spatially and temporally related to magmatic arcs, and often form beneath dormant volcanic centres (Richards and Tosdal, 2001; Seedorff et al., 2005; Sillitoe, 2010). Some have been identified as forming in post-subduction environments, such as collisional or extensional regimes (Richards, 2009). For the most part, porphyry Cu deposits form in spatially restricted segments, or belts, of volcanic arcs (<1000 km in length). At the district scale, porphyry Cu deposits are typically found to occur in clusters, in equidimensional groupings or in alignments up to 30 km in length,

orientated either parallel or transverse to magmatic arcs (Sillitoe, 2010). They are spatially and temporally associated with larger granitic intrusions, specifically with high-level cupolas and dyke complexes (Dilles, 1987; Sillitoe, 2010; Richards, 2016) with cross-cutting relationships between veins and intrusive rocks indicating temporal overlap of hydrothermal alteration, ore mineralisation and porphyry dyke emplacement (Proffett, 2003; Seedorff and Einaudi, 2004; Redmond and Einaudi, 2010). Within the long-lived magmatic arcs, porphyry deposits form over relatively brief periods of time (<20 Myrs), with preceding and subsequent magmatism not generating mineralisation (e.g. Dilles and Wright, 1988). This has been suggested to be due to the convergence of a number of typical arc processes, including the onset of compressive tectonics (Sillitoe, 1998), which traps magmas at the base of the crust where they become enriched in volatiles (e.g. Richards, 2003; Rohrlach and Loucks, 2005; Loucks, 2014).

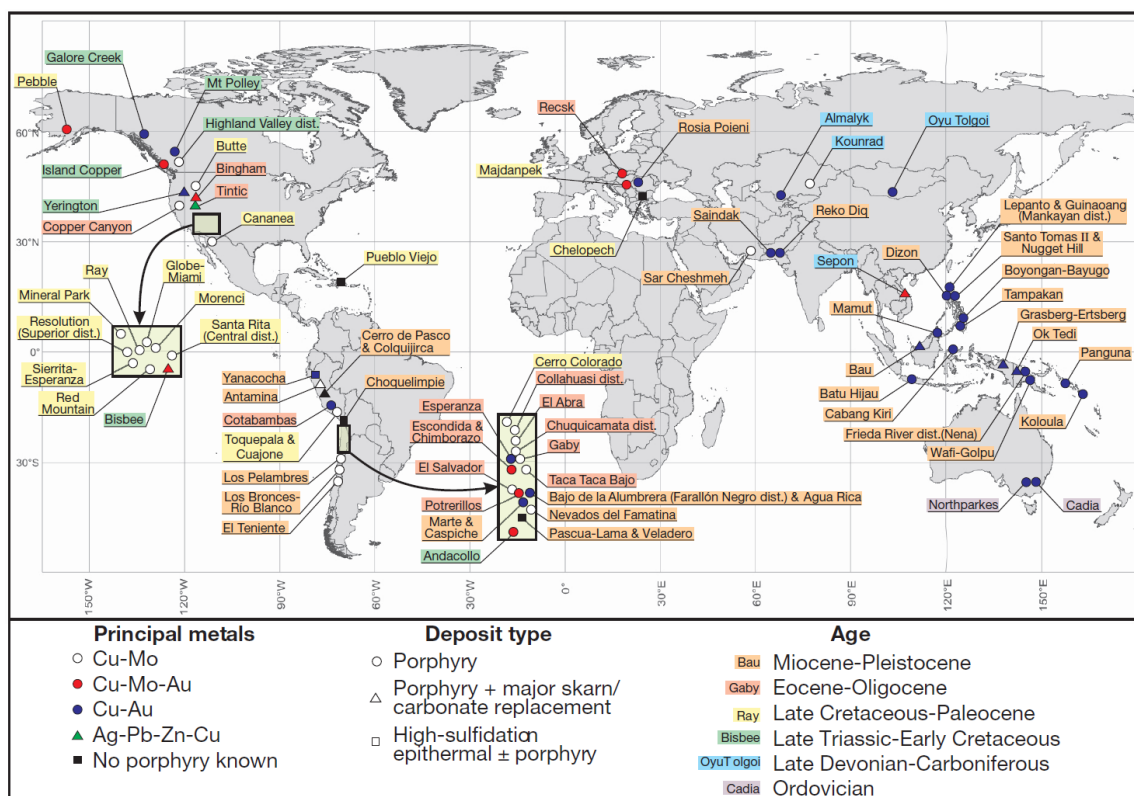


Fig. 2.1 Map of porphyry Cu systems worldwide, colour coded by age and style of mineralisation. From Sillitoe (2010).

2.1.3 Modern concepts of magmatic plumbing

For over 100 years, felsic magmatic systems were thought to consist of large, long-lived, closed, melt-dominated, convecting silicic magma reservoirs ('magma

chambers') in the upper crust (Daly, 1911) (**Fig. 2.2A**). These were thought to produce porphyry deposits due to the release and focusing of magmatic-hydrothermal fluids, and associated mineralisation at higher levels (e.g. Dilles, 1987; Cloos, 2001), and to supply magmas for volcanic eruptions. Over the past few decades, however, from geological, geophysical, geochemical, petrological and volcanological observations, this paradigm has been questioned. This has been partly driven by thermodynamic and mechanical modelling which suggests that magma chambers are very difficult to form and maintain (Cashman et al., 2017; Jackson et al., 2018). Additionally, there is a paucity of geophysical evidence for crystal-poor bodies of large volume in the shallow crust (e.g. Miller and Smith, 1999). As a result, our understanding of igneous processes and the plumbing of magmatic systems is evolving towards a trans-crustal scale model (**Fig. 2.2B**) where the magma chamber is just a shallow expression of a much larger magmatic system (e.g. Cashman et al., 2017; Sparks and Cashman, 2017; Jackson et al., 2018; Glazner, 2021). Magmas accumulate in an open-, rather than closed-system, and can be affected by crustal assimilation (DePaolo, 1981) and replenishment by successive dyke or sill injections from greater depths (Anderson, 1976; Schöpa et al., 2017). From thermal modelling, the initial stages of melt segregation and fractionation occur in dynamic regions of the lower crust (e.g. Hildreth and Moorbath, 1988; Annen et al., 2006), giving a continuum from mafic cumulates at depth and granitic intrusives at higher levels in the crust (Jagoutz and Schmidt, 2012).

In recent years, there has been a growing consensus that trans-crustal magmatic systems are dominated by 'crystal mush', where 'mush' refers to 'any system of crystals and melt in which the crystals form a continuous framework through which melt is distributed' (Cashman et al., 2017). Mush exists at or above the solidus, and is synonymous with partially molten rock (Cashman et al., 2017). The rheological transition from magma (or 'eruptible melt'; Sparks and Cashman, 2017) to mush occurs over a narrow range of crystal contents, typically between 55 - 65%, which is associated with a many orders of magnitude increase in viscosity and a marked increase in strength (Rosenberg and Handy, 2005; Costa et al., 2009; Sparks and Cashman, 2017). However extensive porosity can exist within mechanically coherent frameworks of tabular silicate minerals with crystal fractions as high as ~0.75 (Holness, 2018). In addition, it has been demonstrated

experimentally that melt extraction from cooling mushes increases close to their solidus and operates efficiently at crystal fractions of 0.6–0.93 (Pistone et al., 2020). Significantly, mushes can exist at temperatures a few hundred degrees lower than for ‘eruptible magmas’, particularly when they have high water contents (Gelman et al., 2013). Significantly, when considering the extraction of magmatic-hydrothermal fluids and the formation of porphyry deposits, the existence of crystal mush dramatically widens the temporal-spatial window of physical conditions necessary for fluid flow and extraction within a system.

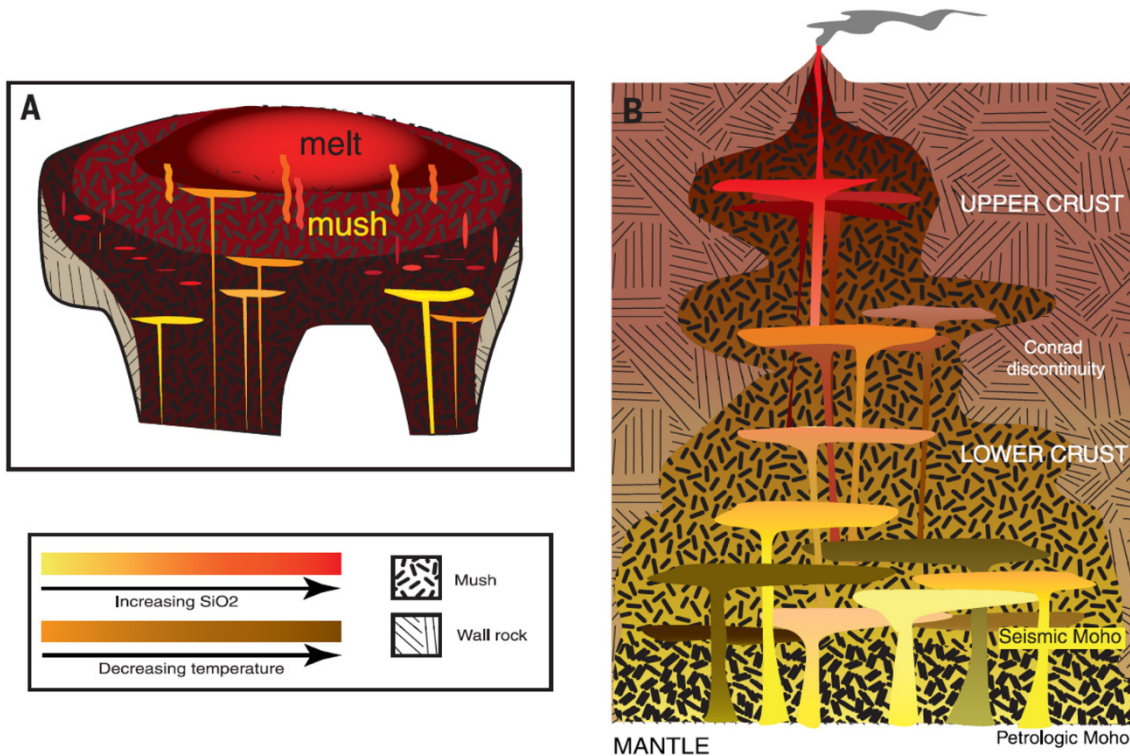


Fig. 2.2 A) Schematic section through an upper crustal magmatic system where silicic melts segregate from underplated mafic magma that is intermittently resupplied from deeper levels. B) Schematic section through a trans-crustal magmatic system, where melt evolution in the deep crust produces melts that are transferred to mid- and finally upper crustal levels. Modified from Cashman et al. (2017).

2.1.4 Deposit formation and architecture

Mineralisation in porphyry systems is centred on the apexes of large, long-lived magmatic systems (**Fig. 2.2** & **Fig. 2.3**) (e.g. Cline and Bodnar, 1991; Buret et al., 2016), which extend to high crustal levels but have their routes in the lower crust (e.g. Annen et al., 2006). It is caused by the exsolution of magmatic-hydrothermal fluids from calc-alkaline magmas in upper crustal plutons and dykes, focusing of these fluids through narrow zones and the deposition of ore minerals due to depressurisation, cooling, wall-rock reaction and possibly mixing

with external fluids (Richards, 2003; Sillitoe, 2010; Wilkinson, 2013). Whilst it is generally understood that the mineralising fluids are purely derived from underlying magmas (e.g. Cline and Bodnar, 1991), some studies suggest that externally-derived fluids may also be involved, largely in associated alteration, for example formation waters convecting around magmatic centres (e.g. Dilles & Einaudi, 1992; Dilles et al., 2000). However, recent isotopic work on the Northparkes Cu-Au district, New South Wales, suggests that magmatic fluids dominate the formation of all mineralisation and alteration assemblages, including the distal the propylitic halo (Pacey et al., 2020).

The exsolution of magmatic volatiles and other mechanisms discussed above are not rare phenomena during the cooling of plutonic rocks (Richards, 2009), indeed it has been concluded by several authors that any typical calc-alkaline magma has the potential to form porphyry Cu deposits (e.g. Dilles, 1987; Cline and Bodnar, 1991; Richards, 2003). What is surprising is that economic porphyry deposits are extremely rare (Wilkinson, 2013). This suggests that ore formation is reliant on a number of other factors, for example the efficiency by which metals are stripped from the magma (e.g. Cloos, 2001; Shinohara et al., 1995) and the focusing of sufficient volumes of fluids through narrow zones of mineralisation (Wilkinson, 2013). The mechanism by which mineralising fluids are extracted from their source magmas and transported upwards into the ore-forming environment is, however, not clearly understood (e.g. Dilles, 1987; Sillitoe, 2010). Since porphyry systems extend over a wide range of depths (2 to 15 km; Sillitoe, 2010), specific tectonic conditions (such as large scale extensional faulting) are required to expose their deep (~5-15 km) roots (Sillitoe, 1973; Richards, 2005; Seedorff et al., 2008; Sillitoe, 2010). There are only a very small number of examples where this is known to have occurred, with the Yerington batholith, Nevada, being the best known and studied (e.g. Dilles, 1987; Dilles et al., 2000). In most deposits, only the porphyry intrusions themselves are observed. These are typically in the form of small (<1 km) bodies with a range of dimensions, from plug-like stocks to elongate dykes which have similar assemblages to their underlying coarse-grained felsic plutons (Seedorff et al., 2008).

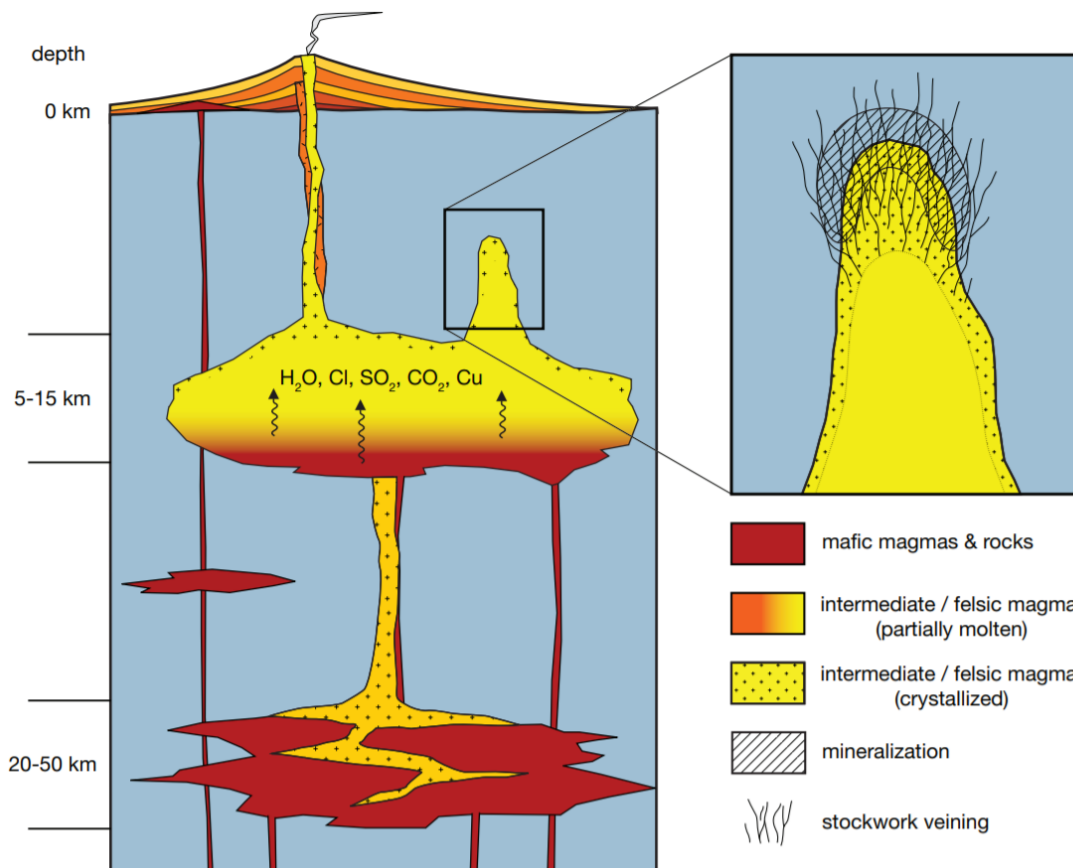


Fig. 2.3 Schematic cross section through an active porphyry Cu system featuring a lower crustal source region (20- to 50-km depth), an upper crustal magma reservoir (5–15 km), that feeds a volcanic edifice, and an apophysis with incipient stockwork mineralisation (2–5 km). From Audétat and Simon (2012).

2.1.5 Porphyry-style mineralisation

Porphyry-style mineralisation typically occurs within large-scale low-grade (<1% Cu) stockworks of quartz veinlets and veins, and within disseminations, closely-spaced fractures and breccias throughout the ore-system (Sillitoe, 2000, 2010). Since most ore is typically hosted in veinlets and veins, there is a strong correlation between quartz vein density and ore-grade (Seedorff et al., 2005). In most porphyry deposits, veins characteristically formed in a highly distinctive sequence. The most-widely cited scheme for this is based on detailed work at El Salvador (Gustafson and Hunt, 1975). This classified veins based on descriptive mineralogy, texture and nature of alteration envelopes (**Table 2.1**).

Sillitoe (2010) simplified this scheme by subdividing veinlet sequences into three groups: 1) early, quartz- and sulphide-free veinlets containing either actinolite,

magnetite (M-type after Clark, 1993), (early) biotite (EB-type after Gustafson and Quiroga, 1995), and K-feldspar, and typically lacking alteration selvages; 2) sulphide-bearing, granular quartz-dominated veinlets with either narrow or no recognizable alteration selvages (A- and B-types after Gustafson and Hunt, 1975); and 3) late, crystalline quartz-sulphide veins with prominent, feldspar-destructive alteration selvages (D-type after Gustafson and Hunt, 1975). M-, EB-, A- and B- type veinlets are mainly formed during potassic alteration, whereas D-type veins accompany chlorite-sericite, sericitic and advanced-argillic alteration (**Table 2.2**). Whilst many deposits exhibit single veinlet sequences, repetitions may occur where there are multiple episodes of porphyry intrusion and/or fluid pulses; repeated veinlet reopening during subsequent veining events may further complicate classification. Typically, A- and B-type veinlets host the majority of Cu, and B-type veinlets most Mo. Whether the ore minerals are co-precipitated with veinlet quartz, or introduced later remains debatable (Sillitoe, 2010).

Table 2.1 Nomenclature and general paragenesis of veins from a typical porphyry deposit, compiled by Vry (2010). The EB- and C-type classification is from Gustafson and Quiroga (1995), and the A-, B- and D-type from Gustafson and Hunt (1975). Associated alteration styles are after Seedorff et al. (2005).

Vein Type	Vein Mineralogy	Vein Texture	Alteration	Morphology
EB	Biotite±sulphides-quartz-albite-anhydrite-actinolite	Perthitic K-feldspar; fine grained, equigranular; no symmetry.	Albite-K-feldspar-biotite-sericite-anhydrite.	Randomly orientated; discontinuous; segmented; thin alteration halos.
A	Quartz-K-feldspar-anhydrite-bornite-chalcopryrite±biotite	Perthitic K-feldspar; fine grained; equigranular; no symmetry.	K-feldspar.	Randomly orientated; discontinuous; segmented; thin alteration halos.
B	Quartz-anhydrite-sulphide	Coarse grained, approaching cockscomb texture; symmetrical with sulphides±quartz in the centre.	None.	Regular; continuous; internal banding present
C	Sulphide-sericite-biotite-anhydrite±quartz	Coarse grained.	Sericite-alkali feldspar-biotite-chlorite.	Regular; continuous.
D	Pyrite-anhydrite±quartz-carbonate	Quartz shows good crystal form; anhydrite-sulphides show banding.	Feldspar destructive; sericite-chlorite.	Continuous; locally irregular; systematically orientated.

2.1.6 Hydrothermal alteration in porphyry systems

Hydrothermal alteration is a chemical replacement of the original minerals in a rock by new minerals where an aqueous high temperature fluid solution delivers the chemical reactants and removes the aqueous reaction products (Reed, 1997). It is widely known that the nature of alteration provides insights into the

post-formation history of a rock. Alteration is ubiquitous around hydrothermal mineral deposits and the distribution and type of alteration relates, at least in part, to the nature of the ore deposit. Spatially, alteration haloes are much larger than their related ore deposits and so provide a wider exploration target (Seedorff et al., 2005; Sillitoe, 2010; Halley et al., 2015). A fundamental understanding of the alteration is however required for it to provide a vector towards mineralisation.

It is no surprise that hydrothermally altered rock is a characteristic component of porphyry-style deposits. Pervasive in the ore zone and surrounding rock, it also commonly extends for several kilometres beyond the limits of the ore body. A number of characteristic alteration assemblages, that form at different temperatures and as a result of interactions with varying types of fluids, can be found in both typical porphyry intrusions and their host rocks (e.g. Lowell and Guilbert, 1970; Gustafson and Hunt, 1975; Seedorff et al., 2005; Sillitoe, 2010). Although details of their patterns and distribution differ between deposits, porphyry Cu systems display a consistent, broad scale alteration pattern that typically affects several cubic kilometres of rock (Sillitoe, 2010). Classification of alteration types (or facies) can be based on the presence of one, or combinations of, minerals, texture, parent rock and/or dominant chemical change. Up to six classes can be distinguished and mapped in porphyry systems: sodic-calcic, potassic, propylitic, chlorite-sericite, sericitic/phyllic and advanced argillic – although each have several aliases (Seedorff et al., 2005; Sillitoe, 2010). These zones are described below and summarised in **Table 2.2**.

Sodic-calcic alteration occurs in some deposits, or is preserved at depth, and is hypothesised to form due to infiltration of saline waters at circa 450°C (Carten, 1986). If present, it is found central to the axis of the system, but below the lower depth limits of the ore zone (Seedorff et al., 2008; Sillitoe, 2010). The distribution of sodic-calcic alteration is reported to be controlled by actinolite-(quartz-plagioclase-tourmaline) veinlets (~400-450°C) and epidote-(pyrite-quartz) veinlets (~400°C or less). Magnetite-amphibole-plagioclase veins ('M veins', M emphasizing the abundance of magnetite; Clark, 1993) are also associated with sodic-calcic alteration in certain tonalitic-granodioritic porphyry Cu-(Au-Mo) systems (Seedorff et al., 2005). Generally, sodic-calcic alteration is sulphide and metal poor (except for magnetite; Fe) but can host mineralisation in Au-rich

porphyry deposits (Sillitoe, 2010). Carten (1986) stated that the absence of sodic-calcic, or sodic, alteration from some porphyry deposits may result from the inadequate development of deep-level convection cells or inadequate exposure of the entire hydrothermal system. He concluded that the alteration facies could go undetected unless mining operations were extended to greater depths or late, post-ore, faulting exposes the deep-level portions of intrusions.

Potassic alteration is ubiquitous and characteristic of the ore zone and deeper levels of most deposits, in particular the barren core beneath and within an ore shell. It overprints the inner zone of magmatic intrusions, is the result of metasomatic addition of potassium at high temperatures (450-600°C), and often grades outwards into propylitic alteration. Quartz, K-feldspar and/or biotite are key minerals (Sillitoe, 2010). Biotite predominates where there are relatively mafic porphyry intrusions (Seedorff et al., 2005) whilst K-feldspar increases in abundance where they are more felsic (granodioritic to quartz monzonitic); more rarely, sodic plagioclase may occur in both settings (Sillitoe, 2010). These minerals are of course most often part of the rock's primary assemblage, but potassic alteration is defined where a significant proportion of the K-feldspar and/or biotite has replaced earlier plagioclase and mafic minerals. Chlorite, actinolite, albite, sericite, andalusite, anhydrite, tourmaline, pyrite and magnetite, amongst others, can also form part of the alteration assemblage, with a high concentration of magnetite being a common feature within the core or ore shells. Potassic alteration is reported to become generally less intense from older to younger porphyry intrusions (Sillitoe, 2010).

Propylitic alteration is extensively developed around most porphyry deposits and can extend several kilometres from the deposit, with decreasing intensity, forming peripheral halos to potassic zones. It results from an addition of H₂O, CO₂ and often S²⁻ to the host rocks at ~250-400°C. Closely resembling greenschist-facies metamorphic assemblages, key minerals are epidote, chlorite and calcite, with pyrite commonly present. Iron oxides, apatite and sericite may also be present (Seedorff et al., 2005; Sillitoe, 2010).

Table 2.2 Summary of the principal alteration-mineralisation types in porphyry systems. Collated from Seedorff et al. (2005), Sillitoe (2010) and Thompson and Thompson (1996).

Alteration type ¹	Environments	Key minerals	Ancillary minerals	Sulphide assemblages	Contemporaneous veinlets ²	Veinlet selvages	Economics
Sodic-calcic	Deep, beneath deposits, and inner zones of magmatic intrusions, generated by hot Na-rich acid fluids	Albite/oligoclase, actinolite, magnetite	Diopside, epidote, garnet	Typically absent	Magnetite ± actinolite (M-type)	Albite/oligoclase	Usually barren, ore bearing locally
Potassic (K-silicate)	Inner zone of magmatic intrusions, generated by hot (>500°C), K-rich acid fluids	Biotite, K-feldspar	Actinolite, epidote, sericite, andalusite, albite, carbonate, tourmaline, magnetite	Pyrite-chalcocopyrite, chalcocopyrite ± bornite, bornite ± digenite ± chalcocopyrite	Biotite (EB-type), K-feldspar, quartz-biotite-sericite-K-feldspar-andalusite-sulphides (EDM/T4-type), quartz-sulphides ± magnetite (A-type), quartz-molybdenite ± pyrite ± chalcocopyrite (B-type)	EDM-type with sericite ± biotite ± K-feldspar ± andalusite ± disseminated, locally K-feldspar around A- and B-types	Main ore contributor
Propylitic (~greenschist facies)	Outer zone of magmatic intrusions, intermediate to deep levels	Chlorite, epidote, albite, carbonate	Actinolite, hematite, magnetite	Pyrite (± sphalerite, galena)	Pyrite, epidote		Barren, other than subepithermal veins
Chlorite-sericite (Intermediate argillic)	Upper parts of porphyry core zone. Usually a widespread overprint on previous alteration. Can lie between advanced argillic and propylitic (100-300°C)	Chlorite, sericite/illite, hematite (martite, specularite)	Carbonate, epidote, smectite	Pyrite-chalcocopyrite	Chlorite ± sericite ± sulphides	Chlorite, sericite/illite	Common ore contributor
Sericitic (phyllic)	Upper parts of porphyry systems. Forms a (often late) peripheral halo around previous zones, moderate temperature (200-450°C)	Quartz, sericite	Pyrophyllite, carbonate, tourmaline, specularite	Pyrite ± chalcocopyrite (pyrite-enargite ± tennantite, pyrite-bornite ± chalcocite, pyrite-sphalerite)	Quartz-pyrite ± other sulphides (D-type)	Quartz-sericite	Commonly barren, but may constitute ore
Advanced argillic (acid sulphate, secondary quartzite)	Intense alteration, often the roof of intrusions/porphyry deposits, and constitute lithocaps	Quartz (partly residual, vuggy), alunite, pyrophyllite, dickite, kaolinite	Diaspore, andalusite, zunyite, corundum, dumortierite, topaz, specularite	Pyrite-enargite, pyrite-chalcocite, pyrite-covellite	Pyrite-enargite ± Cu sulphides	Quartz-alunite, quartz-pyrophyllite/dickite, quartz-kaolinite	Can constitute ore in lithocaps and their roots

¹ Arranged from believed oldest (top) to youngest (bottom), other than propylitic which is the lateral equivalent of potassic. Advanced argillic can also form above potassic early in system genesis

² Many veinlets in potassic, chlorite-sericite, and sericitic alteration contain anhydrite, which also occurs as late monomineralic veinlets

Giving rise to distinctive pale green rocks, chlorite-sericite ('css', also termed intermediate argillic) alteration forms at similar temperatures to the phyllic zone (see below), but from fluids with lower acidity, and is widespread in the shallow parts of porphyry systems, overprinting pre-existing potassic assemblages. It generally caps the ore zone although it can be mineralised. The alteration results in partial to complete transformation of mafic minerals to chlorite, plagioclase to sericite (fine-grained muscovite) and/or illite, and magnetite to hematite, with pyrite and chalcopyrite (Sillitoe, 2010).

Sericitic (also termed phyllic) alteration normally overprints and partially or wholly destroys potassic and chlorite-sericite assemblages, forming an (often-late) peripheral halo around previous zones in the upper parts of porphyry systems. It forms at moderate temperatures (200-450°C) and from strongly acid fluids adding H⁺ ions and removing K, Na, Ca, Mg, Ti and Fe during metasomatic reactions. Key minerals are quartz, sericite and pyrite, with pyrite commonly dominating due to effective removal of Cu from previously formed sulphides (Sillitoe, 2010). This assemblage tends to overprint/destroy the parent texture so that it appears bleached and relatively homogeneous in hand sample. K-feldspar, kaolinite, calcite, biotite, rutile, anhydrite, topaz and tourmaline may also be present (Seedorff et al., 2005; Sillitoe, 2010).

Argillic alteration develops at shallow levels in the hydrothermal system, above and around the phyllic zone. It forms due to intense acid, low-temperature (100-300°C) metasomatism which results in the leaching of feldspars and mafic silicates producing clays. Key minerals are kaolinite, (vuggy) quartz, alunite, pyrophyllite and dickite. Biotite, illite, chlorite, diaspora, zunyite, corundum, andalusite may also be present, amongst others (Sillitoe, 2010). Sillitoe (2010) suggested that advanced argillic alteration beneath lithocaps commonly displays a characteristic patchy texture, often seen as pyrophyllite patches embedded in silicified rock, although the patches may also comprise alunite or kaolinite.

Based on the San Manuel-Kalamazoo deposit, Arizona, Lowell and Guilbert (1970) proposed the model in **Fig. 2.4** for the distribution of alteration and mineralisation in porphyry systems. The deposit is centred on a Laramide (65 Ma)

quartz monzonite stock emplaced in Cretaceous aluminous sediments and contains 140 million tons of ore (hypogene Cu at 0.45%, hypogene Mo at 0.15% and supergene Cu at 0.35%) of which 70% occurs in the igneous host rocks and the rest in the surrounding country rock (Misra, 2000). The Lowell and Guilbert model shows a sequence of alteration zones from the core outwards: potassic (quartz – orthoclase – biotite); phyllic (quartz – sericite – pyrite); argillic (quartz – kaolinite – montmorillonite); propylitic (epidote – calcite – chlorite). The ore zone is best developed near the interface between the potassic and phyllic zones (**Fig. 2.4b**) (Lowell and Guilbert, 1970; Misra, 2000).

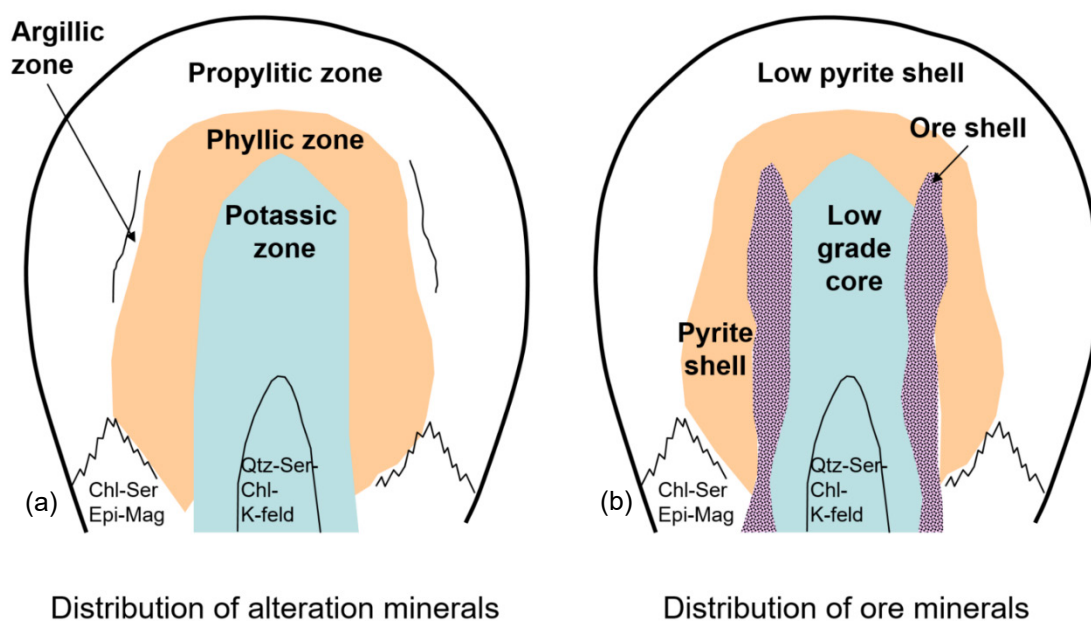


Fig. 2.4 Lowell and Guilbert's (1970) classic schematic model for the distribution of (a) alteration and (b) ore minerals within a porphyry system, based on the San Manuel-Kalamazoo deposit, Arizona.

The generalised pattern of vertical and lateral zoning depicted in the Lowell and Guilbert model has proved extremely useful in exploration and as a framework for the architecture of porphyry systems, especially for silica-saturated, high Mo, low Au deposits at continental margins, but it does not, and never was, intended to apply to every porphyry deposit. Of note, in many deposits (for example, El Salvador, Chile) phyllic alteration overprints earlier alteration types rather than forming an intermediate zone between the potassic and propylitic zones. Apparent deviations from the model may be due to level of exposure issues,

inhomogeneity, post-ore faulting and metamorphism, whereas real deviations may be caused by differences in the size and composition of the central intrusion, wall rock mineralogy, flow pathways and composition of hydrothermal fluids, rock permeability and the extent of supergene alteration (Lowell and Guilbert, 1970; Misra, 2000).

Quartz-diorite or diorite-syenite (rather than granodiorite-quartz monzonite) intrusions show the clearest divergence from the Lowell and Guilbert model. Hollister (1975) proposed a 'diorite model' for some British Columbia low-silica alkaline porphyries, where alteration-mineralisation patterns were significantly influenced by low $\text{SiO}_2:(\text{Na}_2\text{O}+\text{K}_2\text{O})$ ratios in their associated diorite intrusions. Alteration zoning in these systems may be indistinct, and phyllic alteration poorly developed or absent. Of note however is that chalcopyrite:pyrite ratios are commonly such that hypogene copper contents are high enough ($>0.4\%$) to make ore grade without the benefit of supergene enrichment (Misra, 2000; Liu et al., 2016).

Sillitoe (2010) presented a revised model for the zonation of alteration and mineralisation in porphyry systems (**Fig. 2.5**); this was partly based on suggestions in Seedorff et al. (2005). The mineral assemblages of each alteration zone are shown in **Table 2.2**. Sillitoe's scheme, which is not tied to a particular type deposit, but built from a wider database of observations from a number of economically important systems worldwide, is now the generally accepted model. The highest-grade ore is commonly situated in the potassic alteration zone but can also be hosted in the chlorite-sericite zone. Where the phyllic (sericitic) zone hosts mineralisation, this has probably overprinted earlier ore-bearing potassic / chlorite-sericite zones.

Lithocaps represent the upper parts of porphyry systems. These are mainly lithologically controlled zones of pervasive advanced argillic alteration with sub-vertical, structurally-controlled roots. Most lithocaps observed today are just erosional remnants, which may overlie or conceal porphyry deposits, but intact examples are believed to cover areas of up to 100 km^2 , with thickness of over 1 km. The advanced argillic zones may extend upwards to palaeowater tables if suitable aquifers were present. This can be observed in the field as sub-horizontal

tabular bodies of massive opaline or chalcedonic silicification up to 10 m or so thick, with an overlying vadose zone marked by obvious steam-heated alteration characterised by powdery cristobalite, alunite and kaolinite (Sillitoe, 2010). Their areal extent is much larger than the underlying porphyry deposits hence exploration activities must be able to locate their roots if an ore deposit is to be found through drilling (Cooke et al., 2017).

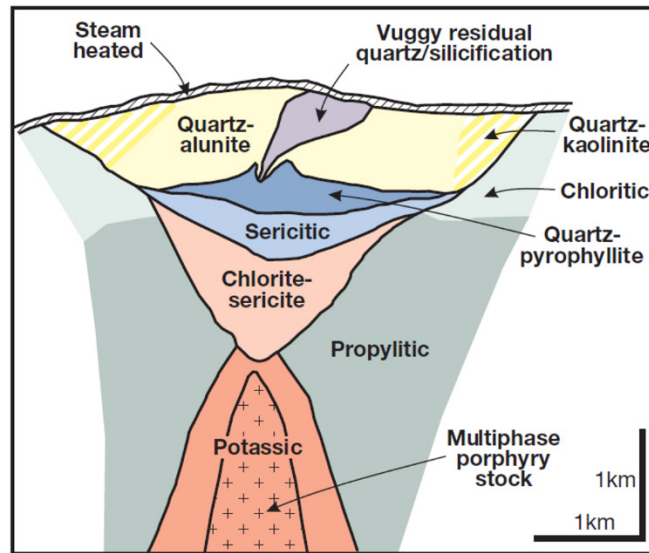


Fig. 2.5 (a) Generalised alteration-mineralisation zonation for a non-telescoped porphyry Cu system. This emphasises the commonly barren gap between the lithocap and porphyry stock. The sodic-calcic zone is not labelled as is often poorly preserved. From Sillitoe (2010).

It has been shown from stable isotope and fluid inclusion data that a minimum of two fluids are involved in the hydrothermal systems forming porphyry deposits. This includes one or more magmatic-hydrothermal fluids in the core of the system – which could have transported ore metals – and convecting external fluids in the outer alteration zones. The hydrothermal fluids that caused the peripheral propylitic and sodic-calcic alteration zones around porphyry deposits have been interpreted to be due to convecting connate fluids (e.g. Dilles and Einaudi, 1991; Dilles et al., 2000). Seedorff et al. (2008) stated that magmatic centres can be regarded as sources of perturbations to the regional ground-water flow regime in aquifers that comprise the source of external fluids in magmatic-hydrothermal systems. However, more recent work suggests all alteration assemblages can be explained by magmatic fluids (e.g. Runyon et al., 2019; Pacey et al., 2020). At Yerington mine, Nevada, numerous cycles of alteration-mineralisation are

documented at the level of the orebody along with multiple magmatic centres, where there are two vertically stacked cupolas. Alteration patterns at Ray (Mineral Creek, Arizona), and reversals in crosscutting relationships at Miami Inspiration (Globe-Miami district, Arizona), also suggest multiple magmatic centres triggering alteration-mineralisation. The relative rarity of known porphyries with root zones suitably exposed for such observations makes study of such relationships difficult (Seedorff et al., 2008).

Hydrothermal alteration/mineralisation is no doubt ubiquitous and characteristic of porphyry deposits and has been well studied to allow for description of discrete alteration zones and patterns. This understanding provides fundamental insights into the processes which form porphyry systems. Ultimately however, these models must always be used in the knowledge that porphyry systems have diverse mineralogical and geochemical compositions which are controlled by the initial magmatic fluid composition (dictated by magmatic compositions and processes), hydrologic factors (related to the degree of fracturing, depth of emplacement, host rock permeability, concurrent structural events, temperature and pressure gradients), wall rock compositions and the extent and timing of interaction of magmatic-hydrothermal and external fluids (Seedorff et al., 2005). Care must always be taken, therefore, when trying to draw analogues between different individual systems, especially if they lie within different porphyry belts.

2.1.7 Porphyry fertility indicators

During the early years of porphyry exploration, most deposits were found due their location at, or near, the surface. They could be identified during field studies or remote sensing from their characteristic alteration halos or supergene mineralisation blankets. However, most systems that are exposed at the surface have been discovered (Richards, 2003). Porphyry exploration in the 21st century is therefore having to increasingly focus on deeper targets and moves inexorably into areas of post-mineral cover. To overcome this, research efforts in recent years have focused on developing whole-rock and mineral geochemical indicators to assess whether certain magmatic systems may be mineralised, or 'fertile'. This new generation of exploration tools has largely been enabled by advances in geochemical analytical techniques (e.g. ICP-MS), particularly for measuring the concentrations of trace elements (e.g. see reviews in Cooke et al.,

2017; Cooke et al., 2020; Wilkinson et al., 2020). Their main advantage is in providing relatively cheap and low environmental impact methods for assessing the prospectivity of areas, at varying scales, prior to using more elaborate, expensive and/or invasive exploration techniques.

Examples of whole-rock geochemical fertility indicators are elevated Sr/Y, La/Yb, V/Sc and Eu/Eu*, when compared to poorly- or non-mineralised magmatic suites (e.g. Rohrlach and Loucks, 2005; Richards, 2011; Chiaradia et al., 2012; Loucks, 2014; Ahmed et al., 2020). From the range of mineral indicators being actively researched (e.g. apatite, plagioclase, tourmaline, titanite, epidote, magnetite; Cooke et al., 2017), zircon is arguably the most reliable since it is ubiquitous in granitoid systems, highly refractory and largely unaffected by hydrothermal alteration (e.g. Cherniak et al., 1997), and is also favourable for U-Pb geochronology (e.g. Schoene, 2014; Chelle-Michou and Schaltegger, 2018). Examples of zircon fertile geochemical signatures include Eu/Eu*, (Ce/Nd)/Y and Dy/Yb ratios (or steep MREE/HREE patterns) (e.g. Lu et al., 2016; Cooke et al., 2017; Loader et al., 2017). Crucially, these geochemical fertility signatures are mostly understood to reflect the hydrous nature of the magmas from which porphyry-type deposits form (e.g. Rohrlach and Loucks, 2005; Richards, 2011; Chiaradia et al., 2012; -2015; Richards et al., 2012; Wilkinson, 2013; Loucks, 2014; Chiaradia, 2015; Lu et al., 2016; Williamson et al., 2016; Nathwani et al., 2020; Lee et al., 2021). Significantly, the timescales over which these geochemical signatures develop is not well constrained, nor how these signatures are expressed through different parts the magmatic system, or in the overlying volcanic terrane.

2.1.8 Outstanding questions

Porphyry copper deposits are arguably the most studied and understood of all ore deposit types (e.g. Seedorff et al, 2005; Sillitoe, 2010; Richards, 2018). However, our fundamental understanding of how porphyry-forming magmatic-systems operate is limited by the paucity of exposure of these systems, particularly of their deeper 'root-zones' (Seedorff et al., 2008). As a consequence, there remain a number of outstanding fundamental questions in the genesis of porphyry-type deposits.

It is well understood that porphyry deposit-forming fluids are derived from large, long-lived magmatic systems (Cline and Bodnar, 1991; Buret et al., 2016; Tapster et al., 2016) where melt or mush reservoirs are at depths of between around 5 to 15 km (Richards, 2005; Sillitoe, 2010) or in more extensive transcrustal magmatic systems (e.g. Cashman et al., 2017; Sparks and Cashman, 2017; Jackson et al., 2018).

The current paradigm is that the hydrous magmas that form porphyry-deposits result from a long (multimillion year), arc-scale, subduction-driven 'ramp-up' in volatiles and ore-forming constituents in mid- to lower crustal magmatic reservoirs (Ballard et al., 2002; Rohrlach and Loucks, 2005; Chiaradia et al., 2009; Loucks, 2014; Rezeau et al., 2016; Chiaradia and Caricchi, 2017; Nathwani et al., 2021). Before emplacement into the upper crust, the magmatic system develops its ore-forming geochemical signatures over protracted time scales, in excess of ~ 5 Myrs, due to cyclical fractionation and re-charge of deep reservoirs by mafic magmas. The subduction-related tectonic regime has been suggested to progressively deepen the melt evolution zone and/or slow the upwards migration of magmas through the crust (Richards, 2003; Chiaradia et al., 2009; Chiaradia and Caricchi, 2017; Lee and Tang, 2020). Alternatively, the ore-forming potential of magmas, and associated geochemical signatures, may increase during evolution within an upper crustal staging ground (e.g. Dilles, 1987; Seedorff et al., 2005; Sillitoe, 2010; Dilles et al., 2015). Distinguishing the nature of magmatic evolution in the lead up to porphyry copper ore formation is problematic because of the paucity of vertically extensive exposure over the crustal windows of porphyry ore-forming systems (Seedorff et al., 2008); this has resulted in a fragmented understanding of the magmatic timescales associated with porphyry-deposit formation.

In addition, how ore-forming fluids are transported from parental reservoirs and focused into narrow, relatively shallow (ca. 2-5 km deep, Sillitoe, 2010; Richards, 2018), zones of economic mineralisation (Seedorff et al., 2008; Sillitoe, 2010; Weis, 2012; Wilkinson, 2013; Richards, 2016) is an important yet 'missing link' in our understanding of porphyry deposit formation (Dilles, 1987; Sillitoe, 2010).

Existing models commonly invoke: convection and injection of bubble-rich magma in upper crustal magma chambers and upwards emplacement to form porphyritic stocks and dykes (e.g. Candela, 1991; Shinohara et al., 1995; Cloos, 2001; Richards, 2005); accumulation of volatile-saturated melts in cupolas which act as exhaust valves episodically ejecting fluids and magma by repeated dyke injections (e.g. Dilles, 1987; Proffett, 2003; Sillitoe, 2010); or through sustaining brittle fracture networks (Weis, 2012). These generic concepts are still debated as there is a paucity of observational evidence for a critical link to porphyry ore genesis (Seedorff et al., 2008), and several issues remain.

For example, the injection of bubble-rich magma into stocks and dykes, and the accumulation of volatile-saturated melts within a cupola may occur, but these intrusions are too small to be capable of directly liberating sufficient volumes of mineralising fluids (Sillitoe, 2010). The fluids must therefore be extracted from a much larger parental magma chamber, with at least 50 km³ of magma required to provide sufficient volumes of fluids (Dilles, 1987; Cline and Bodnar, 1991). From a lack of compositional zoning in porphyry dykes and parental upper-crustal plutons and stocks, these bodies remain thermally unzoned during fluid extraction (Dilles, 1987), in contrast to the model of Burnham (1979) which illustrates thermal zonation. However, there is a paucity of geophysical evidence for crystal-poor bodies of large volumes in the shallow crust (e.g. Miller and Smith, 1999).

Consequently, there remain several fundamental gaps in our understanding of the genesis of porphyry-type deposits: the timescales and drivers for the evolution of a magmatic system's ore-forming potential and associated geochemical signatures; how sufficient volumes of mineralising fluids are transferred from parental magmas into the porphyry-forming environment (Dilles, 1987; Sillitoe, 2010); the nature and role of crystal mush in porphyry systems (e.g. Cashman et al., 2017); how textural and geochemical evidence for these processes is preserved; the timescales over which this occurs (Sillitoe, 2010); and if understanding of these textures, signatures and timescales can be used to vector towards mineralisation.

2.2 Textures associated with mineralised granites

Granitic rocks associated with mineralisation can be texturally complex and show variations within a given pluton, or amongst plutons in a suite. Textural types may include porphyritic, aplitic and pegmatitic domains, miarolitic cavities, unidirectional solidification textures (USTs), graphic and micrographic textures and dendritic, acicular and/or skeletal crystals in addition to normal (hypidiomorphic granular) granitic texture (e.g. Fenn, 1986; Kirkham and Sinclair, 1988; London, 1992; Candela, 1997; Kirwin, 2005; London and Morgan, 2012).

Candela (1997) stated that within igneous systems, variations in texture and morphology are functions of phase and melt composition, the melt's physical history, any pre-existing boundaries (nuclei), ripening, post crystallisation deformation and the magnitude of undercooling. Candela (1997) defines undercooling as 'the difference between the temperature at which the melt saturates with respect to a mineral, and the temperature at which the mineral actually nucleates and grows' and stated it to be the driving force for crystal nucleation and growth. The magnitude of undercooling has been observed to exert a major influence on crystal morphology (Swanson, 1977). Granitic rocks that are emplaced at shallow levels, where undercooling varies significantly, show the greatest textural variation, which can be used to assess the environments of crystallisation. In contrast, magmas at deeper crustal levels cool more slowly and therefore acquire an equilibrium texture, which depicts very little about magmatic conditions (Candela, 1997).

Porphyritic texture is commonly reported in shallow, ore-associated granites. This can be concluded to represent two-stage cooling when the same minerals are found among the phenocrysts and groundmass, with the groundmass produced by a sudden increase in undercooling (Candela, 1997).

Undercooling followed by volatile saturation, the latter which may occur due to 'first-' or 'second-type boiling' (Candela, 1991), can also induce disequilibrium textures such as skeletal quartz growth. Further undercooling as the magma rises could result in skeletal quartz being overgrown by more dendritic forms either in the groundmass or around pre-existing phenocrysts (Candela, 1997). In the crystallisation of felsic melts, this same process can produce quartz eyes

(rounded quartz phenocrysts, due to the ease of quartz nucleation relative to feldspar), pegmatites, graphic / micrographic intergrowths, aplites and miarolitic cavities (Fenn, 1986; Candela, 1997, and references therein; London, and Morgan, 2012).

Graphic / micrographic texture is defined as a cellular quartz-feldspar intergrowth. It is the sole texture that is unique to the crystallisation of a silicate (magmatic) melt, and is not found in veins (which form by the deposition of minerals from predominately aqueous fluid) (London & Morgan, 2012). Granophyric describes less regular quartz-feldspar intergrowths found in aplites and fine grained groundmass, and is often used interchangeably with micrographic texture. The textures collectively comprise, in part, skeletal quartz, dendritic quartz and feathery feldspar which, as above, are indicative of high degrees of undercooling (Candela, 1997).

Miarolitic cavities comprise of super-solidus crystals that project into, and terminate in, a void (or mass of hydrothermally precipitated minerals) which was once occupied by the magmatic volatile phase. They share the characteristic texture of external nucleation within pegmatites (Candela, 1997). London (1992) defined external nucleation as that on a bounding surface of a system (as seen in crustiform hydrothermal veins), rather than at a point that is internal to the system (such as crystallisation of an aplite or a typical granite). Through experimental studies, it has been demonstrated that pegmatitic textures, along with aplitic and graphic textures (and similar discussed above) require undercooling but not water saturation for their formation (e.g. Fenn, 1986; London, 1992). London and Morgan (2012) also discussed how pegmatite forming melts appear to have low enough H₂O so that the vapour phase exsolves only in the waning stages on consolidation. Experimental work (e.g. Swanson, 1977) has also shown that feldspar growth rates are lower in water-saturated than in water-undersaturated conditions. Candela (1997) concluded that pegmatitic, aplitic and graphic (and similar) textures are likely to form as result of varying degrees of undercooling, which may be related to the exsolution of a volatile phase upon ascent. They are therefore likely to be related, indirectly, to volatile exsolution as they have been shown to form in the absence of volatile saturation. Miarolitic cavities on the other hand were concluded not to share a common

genesis however and are taken as the best evidence for volatile phase saturation in magmas.

Despite the majority of granites having experienced volatile saturation at some point in their history, miarolitic cavities are not found (or at least reported) in most systems (Candella, 1997). This suggests that their formation requires bubble growth during magma ascent and decompression, followed closely by quenching of the melt. In an ascending, water-saturated melt, bubbles increase in size due to decompression. This can result in the simultaneous development of miarolitic cavities, micropegmatites (crystals <1 cm long) and micrographic/granophyric aplites, if it coincides with an increase in solidus temperature and crystallisation driven by undercooling. It is thought that the combination of larger bubbles and smaller crystals allows for a small portion of the magmatic volatile phase (MVP) to be preserved as miarolitic cavities, although this textural preservation is not uniform so the volume of miarolitic cavities in a given rock is likely unrelated to the actual ratio of MVP to melt. This suggests that for most granites (which lack miarolitic cavities), decompression was not strong enough to trigger significant crystallisation and bubble growth. The deeper the interval of crystallisation in the crust, the lower likelihood of forming miarolitic cavities, which should become uncommon at crystallisation pressures of >300 MPa. The formation of miarolitic cavities is therefore likely to be limited to the uppermost crust, but theoretically there is no maximum pressure for their formation (Candela and Blevin, 1995; Candela, 1997).

In a study of the Ruby Creek monzogranite, Eastern Australia, Candela and Blevin (1995) suggested that interconnected miarolitic cavities, generally found near roof zones of plutons, represent a snapshot of one type of magmatic volatile-phase permeability. They noted extensive connectivity in two-dimensions, which must be even greater in three dimensions, to form a self-supporting percolation network. This developed above the solidus along with pegmatites, aplites, and crenulated and unidirectional solidification texture (UST)-layered zones. They observed the intensity of interconnected miarolitic texture faded laterally and downwards. Marginal zones were described as often containing stockscheider (K-feldspar dominated pegmatite at upper and internal granitic contacts; Breiter et al., 2005) or pegmatite pods with strongly developed graphic margins, or being

biotite-rich. It was proposed that these textures are best developed at low crystallisation pressures, <~2.5 kbars.

This interconnected miarolitic texture is comparable to similar phenomena at Bajo de la Alumbrera, Argentina (Harris et al., 2004). It could explain how large quantities of MVP (and contained metals) were channelled into the apical region of the parental pluton through the dynamic zone of crystallisation before significant cooling (and dilution of the aqueous phase) took place. This could have occurred concurrently with the rise of buoyant plumes of bubbles + liquid + crystals (Candela, 1991). Regardless of whether this happened, for the generation of a magmatic-hydrothermal mineral deposit, such a mechanism for focusing large quantities of MVP into the apical region is essential for the economic concentration of metals. Evidence to support this is that relatively small apical regions/cupolas/stocks/dykes are very often the locus of mineralisation. Without the focussing of the MVP, metals will remain dispersed, and at low concentrations, across the igneous system.

Unidirectional solidification textures (UST's) are primary magmatic features which comprise parallel to sub-parallel banks of quartz crystals with orientated c-axis terminations (Shannon et al., 1982; Kirkham and Sinclair, 1988; Kirwin, 2005). They have previously been termed 'comb quartz layers' (e.g. Kirkham and Sinclair, 1988) and described as 'vein dykes' when observed within aplite dykes, e.g. in the Henderson Mo porphyry system, Colorado (e.g. White et al., 1981; Shannon et al., 1982). The upper contacts of some porphyry Cu intrusions are characterised by USTs (Sillitoe, 2010). They are characterised by morphological features indicative of mineral growth in one direction from a solid substrate (Shannon et al., 1982). Their formation is thought to be the result of pulsating pressure changes across cotectic boundaries within the quartz-feldspar stability field (Kirkham and Sinclair, 1988). The quartz stability field expands with increasing pressure (Tuttle and Bowen, 1958), so in cupolas where pressure varies, the cotectic boundary moves and alternate bands of quartz and feldspar develop (**Fig. 2.6**) (Kirwin, 2005). This is particularly so where an overpressured cupola is hydraulically fracturing, releasing pressure, and the fractures then heal so that the pressure builds up again.

USTs are generally found in multilayer sequences that range in thickness from centimetres to tens of metres at or near the apex of a cupola and are usually sub-parallel to wall rock contacts. They have been observed to be interlayered with aphanites, aplites, or their porphyritic equivalents. Individual layers are laterally continuous over at least 10 m, and the nature and thickness of UST zones can change over a few metres (Shannon et al., 1982; Kirkham and Sinclair, 1988; Kirwin, 2005). Kirwin (2005) speculated that the relatively small size of UST bands is why they are frequently not reported or not recognised. Alternatively, their preservation may be poor due to subsequent events such as brecciation, sheeted quartz vein emplacement etc.

UST formation at Oyu Tolgoi and in the porphyry Cu-Au systems of the Lachlan Fold Belt, Australia (Wilson, 2003; Kirwin, 2005) was associated with gold and chalcopyrite mineralisation. In most cases however, UST zones are not mineralised. They are however considered to be useful indicators of volatile-rich magmas at the district exploration scale. They may also represent the first stage of a series of dynamic processes which can evolve to form sheeted and stockwork veins and breccia pipes. In this context, porphyry-style mineralisation would be expected to be adjacent to the UST zone (Kirwin, 2005). The inconsistent development of USTs however does not make them a reliable means of subdividing porphyry systems (Sillitoe, 2010).

At the Henderson Mo porphyry system, Colorado, Shannon et al. (1982) used USTs to determine the relative ages of individual stocks, as well the as the positions and orientations of stock contacts. They concluded that, when used in conjunction with other geological data, they can be a powerful tool in unravelling an igneous suite's intrusive history. At Henderson, they defined three main types of USTs on the basis of crystal morphology: crenulated layers, dendritic layers and intergrowth layers. Kirwin (2005) also describes a diverse variety of UST morphologies associated with mineralised intrusions.

Crenulate layers are characterised by individual minerals showing euhedral morphologies (**Fig. 2.7**). These layers are principally composed of quartz and/or alkali feldspar. The layers are planar on one side, with euhedral terminations on the other which point away from the stock contact in the direction of growth. Aplite

fills the gaps between protruding crystals. Layers have been observed to range from 0.2 to 500 mm in thickness and the crystals from 0.2 to 300 mm (Shannon et al., 1982).

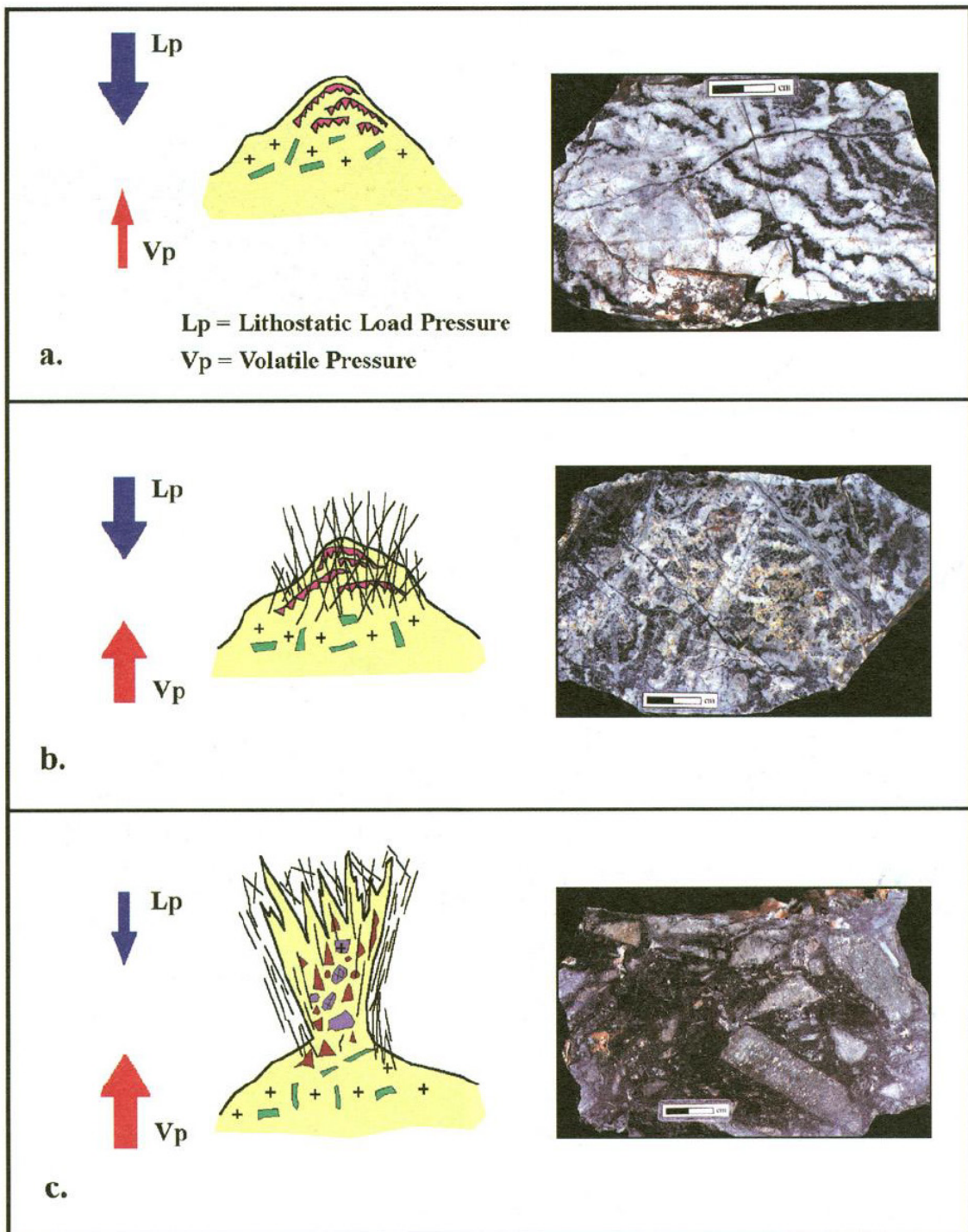


Fig. 2.6 (a) Formation of UST's as over pressured volatiles concentrate in a cupola. (b) Subsequent release of overpressure due to hydraulic fracturing of wall rocks and the formation of sheeted veins. (c) Catastrophic failure of wall rock and formation of a breccia pipe; pressure subsequently/suddenly drops to equilibrium. From Kirwin (2005). Scale bars 2 cm in total.

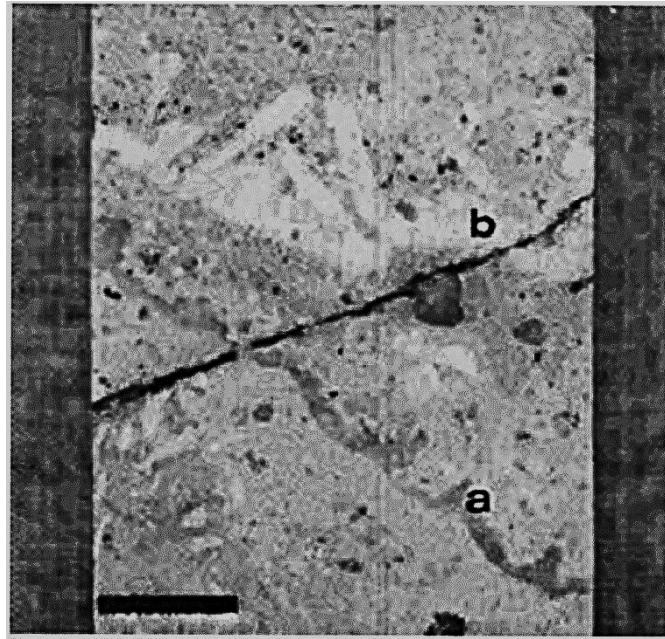


Fig. 2.7 Quartz (a) and alkali feldspar (b) crenulated layers in a porphyritic aplite. Scale bar is 1 cm. From Shannon et al. (1982).

Dendritic layers (**Fig. 2.8**) are characterised by dendritic crystals of quartz or plumose feldspar (most commonly alkali feldspar) in continuous layers, in an aplitic matrix, which are subparallel to intrusive contacts and are typically associated with crenulate layering. Layers bearing the texture have been observed to range from a few mm to 1 m with individual branching crystals seen up to 10 cm long. Steep chemical gradients in the granitic melt ahead of the dendritic layers have been inferred (Shannon et al., 1982).

Quartz and alkali-feldspar intergrowth layers are usually set in an aphanitic to aplitic matrix and have been observed from mm to cm thick and can be locally interlayered with crenulate and dendritic layers. Shannon et al. (1982) defined two end members: dendritic and micrographic. Dendritic intergrowths represent the simultaneous crystallisation of alkali feldspar and quartz, both with dendritic morphologies, and are characteristically macroscopic. Micrographic textures are characterised by the simultaneous crystallisation of alkali feldspar and quartz as complex intergrowths. The host feldspar generally forms large (0.5 to 5 cm) fan-shaped crystals which splay in the direction of growth. The included quartz crystals are rod- or lamellar-shaped and are very fine grained to microscopic. Micrographic textures have been observed as overgrowths on alkali feldspar crystal faces in crenulate layers (Shannon et al., 1982).

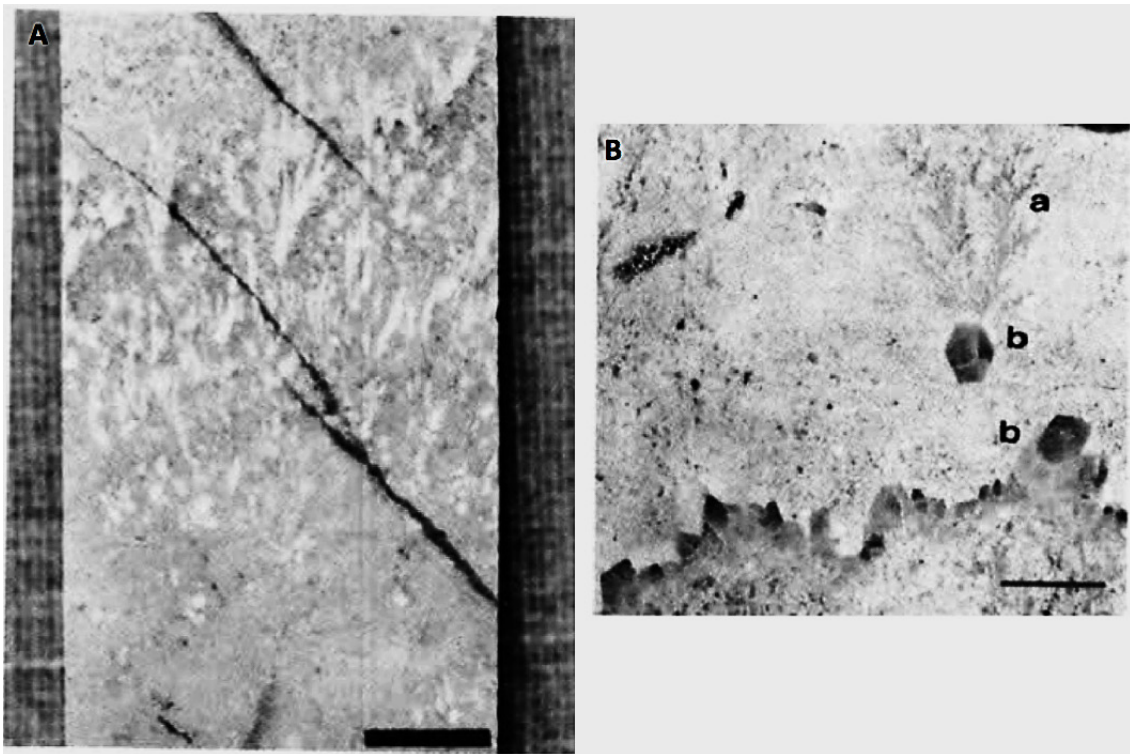


Fig. 2.8 A) Plumose alkali feldspar layers in aplite. Direction of crystallisation is upwards. There is a distinct difference in aplite grain size above and below the layers. Scale bar = 1 cm. B) Dendritic quartz layers associated with a quartz crenulate layer in aplite. The dendrites have a moss-like habit (a) and locally nucleate on crenulate quartz crystals (b). Direction of crystallisation is upwards. Scale bar = 0.5 cm. From Shannon et al. (1982).

2.3 The Yerington batholith, Nevada – Geological setting

2.3.1 Introduction

The Yerington District, Nevada, USA, contains four known porphyry Cu(-Mo-Au) deposits: Ann Mason, Yerington, Bear and MacArthur (**Fig. 2.9**). These are all directly associated with the Jurassic age Yerington batholith (Proffett and Dilles, 1984; Dilles et al., 2000; Proffett, 2007). Combined, these deposits host measured and indicated resources in excess of 9 Mt contained Cu (Dilles and Proffett, 1995; Bryan, 2014; Henderson et al., 2014; Hudbay Minerals Inc., 2021). Late Cenozoic Basin and Range extensional faulting, associated fault block rotation and westward tilting (Proffett, 1977; Dilles et al., 2000) have exposed a <1 to ~8 km palaeodepth cross-section through Jurassic rocks of the district (Dilles, 1987). This, along with mapped relative timing relations (Proffett and Dilles, 1984) and radiometric ages (Dilles and Wright, 1988; Banik et al., 2017), has provided a unique opportunity to detail the four-dimensional geometry of a large upper-crustal magmatic system, related magmatic-hydrothermal products

and associated porphyry copper mineralisation (Dilles et al., 2000; Proffett, 2007).

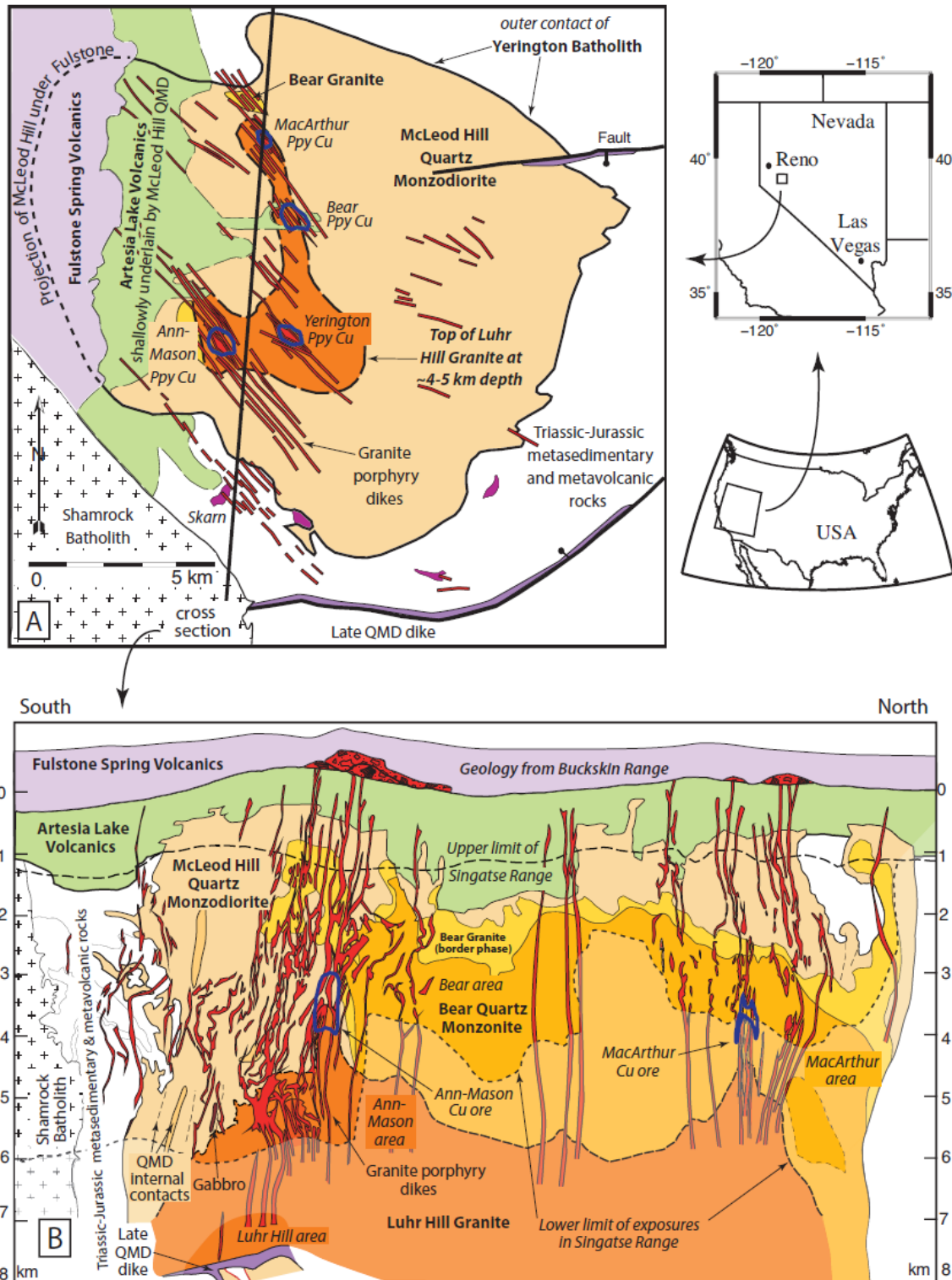


Fig. 2.9 A) Location and schematic map of the Yerington District, Nevada. B) Reconstructed cross section through the Yerington District up to a paleo-depth of 8 km. From Schöpa et al. (2017), modified after Dilles (1987).

2.3.2 Geography

The Yerington District is located in Lyon County, west-central Nevada. It is approximately 75 km southeast of Reno and 45 km southeast of Carson City (the capital of Nevada), adjacent to the city of Yerington. The topography of Lyon County is characterised by mountain ranges surrounded by wide-open valleys. Yerington lies within the Mason Valley, through which the Walker River runs from south to north. The Mason Valley is bound by the Singatse Range to the west and by the Wassuk Range to the east. To the west of the Singatse Range lies the Smith Valley, which in turn is bound by the Buckskin Range to the west.

The city of Yerington, with a population of approximately 3,100 inhabitants, is the main seat for Lyon County and through its history has primarily served as a regional ranching and farming centre. Mason, an unincorporated community, and Weed Heights, a company town built to support the Yerington mining operation in the 1950s, also lie within the district (Kulla et al., 2017).

The highways and roads to Yerington and Weed Heights are well developed and paved, with Highway 95 in Yerington acting as the main artery that connects the town to the interstate highway system. Field access to the district beyond Weed Heights is primarily by an all-weather dirt road (Mason Pass), a lesser quality dirt road (Mickey Pass) and a network of unmarked dirt roads of varying quality.

West-central Nevada is characterised by a high altitude temperate climate, with warm to hot summers and cool winters. The high altitude and Sierra Nevada Mountain range place the district in a rain shadow where precipitation is minimal, mainly as snow in winter. Mean temperatures in the summer vary between 19 and 23°C and in winter between 0 and 4°C. Maximum temperatures reach 33°C in summer and minimum temperatures -7°C in winter. Vegetation throughout the district consists of interspersed sagebrush and low profile desert shrubs. Trees are rare.

2.3.3 Tectonic setting

The middle Jurassic composite Yerington batholith (Proffett and Dilles, 1984; Dilles, 1987; Dilles and Wright, 1988; Banik et al., 2017) lies within a volcanic-arc terrane, in the early Mesozoic marine province, which formed due to subduction

to the west (Speed, 1978; Dilles and Wright, 1988) (**Fig. 2.10**). The batholith is believed to be underlain by late Precambrian or Palaeozoic oceanic crust, which is overlain by Palaeozoic continental margin-arc volcanic and volcanoclastic rocks, as well as continent-derived terrigenous sedimentary units (Stewart, 1972; Speed, 1979). These rocks lie to the west of the inferred Precambrian craton, which is marked by the 0.7060 initial strontium isopleth for Mesozoic igneous rocks (Dilles, 1987) (**Fig. 2.11**).

Late Cenozoic Basin and Range extensional faulting and associated fault block rotation has exposed a < 1 to ~ 8 km palaeodepth cross-section through the Yerington batholith (Proffett, 1977; Proffett and Dilles, 1984; Dilles, 1987), discussed further in section 2.3.7.

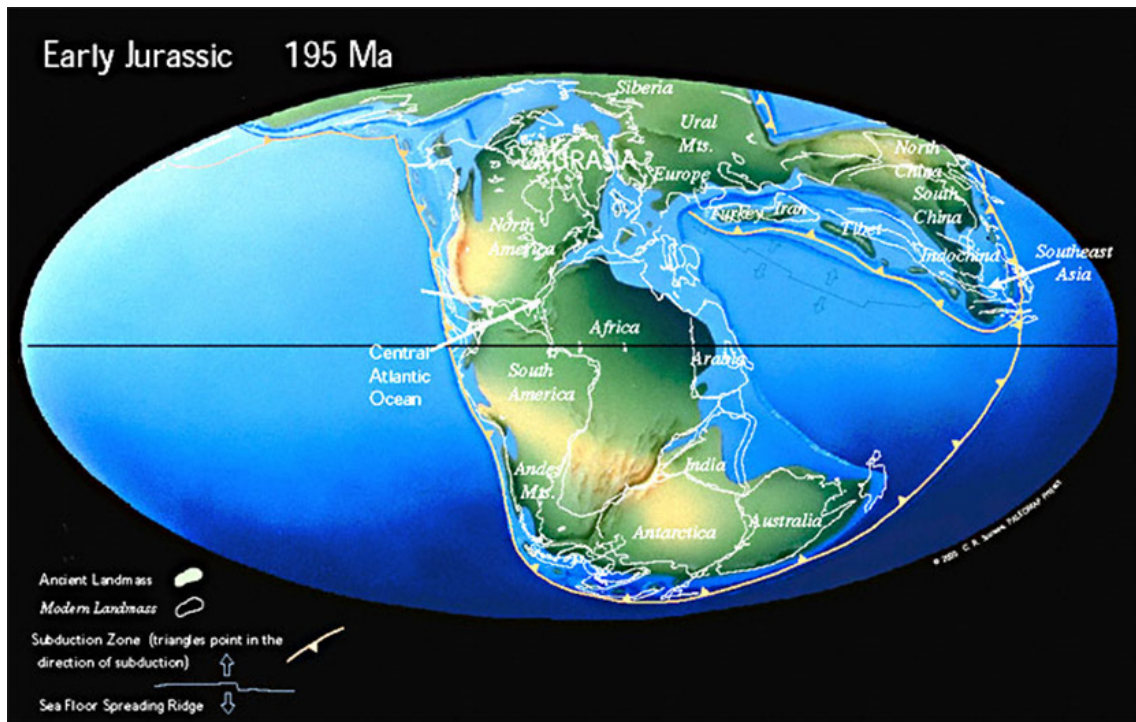


Fig. 2.10 Early Jurassic (195 Ma) plate reconstruction (after Scotese, 2001).

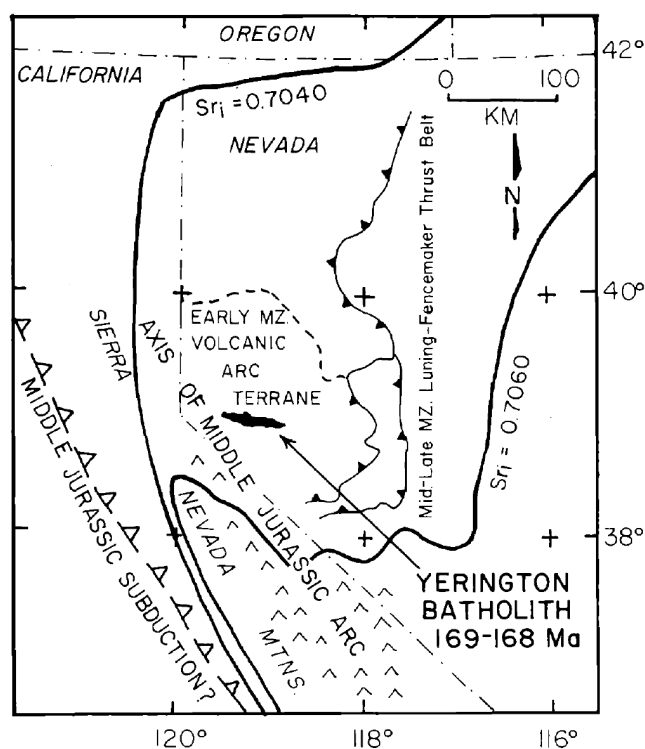


Fig. 2.11 Tectonic setting of the Yerington batholith. The batholith lies within a belt of Middle Jurassic arc rocks related to subduction to the west (Dilles and Wright, 1988). Early Mesozoic (MZ) arc terrane (Speed, 1978) and initial strontium isopleths (Sri) (Kistler and Peterman, 1973) are also shown. From Dilles (1987).

2.3.4 Early Mesozoic rocks

The oldest rocks exposed in the Yerington District comprise a sequence of late Triassic or older intermediate and felsic volcanic rocks intruded by middle to late Triassic age plutons, exposed in the Singatse and Wassuk Ranges (Dilles and Wright, 1988; Dilles et al., 2000). They include a 1400 m thick sequence (in the Singatse Range), named the 'McConnell Canyon volcanics', which is comprised of andesitic flows and breccias overlain by rhyolitic domes, flows and breccias, with minor conglomerate and volcanic sandstones (Proffett and Dilles, 1984; Dilles and Wright, 1988). A zircon U-Pb age of 232.2 ± 2.3 Ma from a quartz porphyry dyke places a minimum age on the McConnell Canyon volcanics, and is speculated to closely approximate the age of the rhyolitic part of the section. In the northern Wassuk Range, a volcanic section, which may correlate with the McConnell Canyon volcanics, is comprised of andesite and rhyolite which overlie a silicic ignimbrite. The Wassuk metadiorite (zircon U/Pb age of 232.7 ± 2.9 Ma), which intruded the silicic ignimbrite and base of the andesite-rhyolite section, places a minimum age on the silicic ignimbrite in the Wassuk Range. It is thought

that the metadiorite may be co-magmatic, and thus date, the andesite that it intrudes (Dilles and Wright, 1988), see **Fig. 2.12**.

These intrusive and volcanic rocks are unconformably overlain by a succession of marine sedimentary and volcanoclastic rocks. Moving up the succession, Dilles et al. (2000) report these as: limestone (from which Carnian ammonoid fossils have been recovered; Silberling, 1984) and black argillite; tuffaceous and limy beds; a dacitic tuff; a thick upper Triassic (Norian) limestone; tuffaceous interbedded siltstones (up to 1800 m thick; Dilles and Wright, 1988) and argillites; a thin marble; an evaporate gypsum; and an aeolian sandstone. This sequence can be broadly correlated with that in the Pine Nut Range to the West. This succession is overlain by the ~1 km thick Artesia Lake Volcanics (Proffett and Dilles, 1984).

2.3.5 The Yerington batholith

The Yerington batholith was emplaced into the base of the Artesia Lake Volcanics (**Fig. 2.9**). These are made up of intermediate to felsic flows, breccias, and shallow intrusions, as well as minor basalt flows and volcanoclastic rocks that are up to 1,500 m thick (Hudson and Oriel, 1979; Proffett and Dilles, 1984; Dilles, 1987). From their close association, overlapping ages, and similar composition to the Yerington batholith, it is believed that the Artesia Lake Volcanics represent the early, extrusive part the magmatic system that formed the batholith (Dilles, 1987; Dilles et al., 2000).

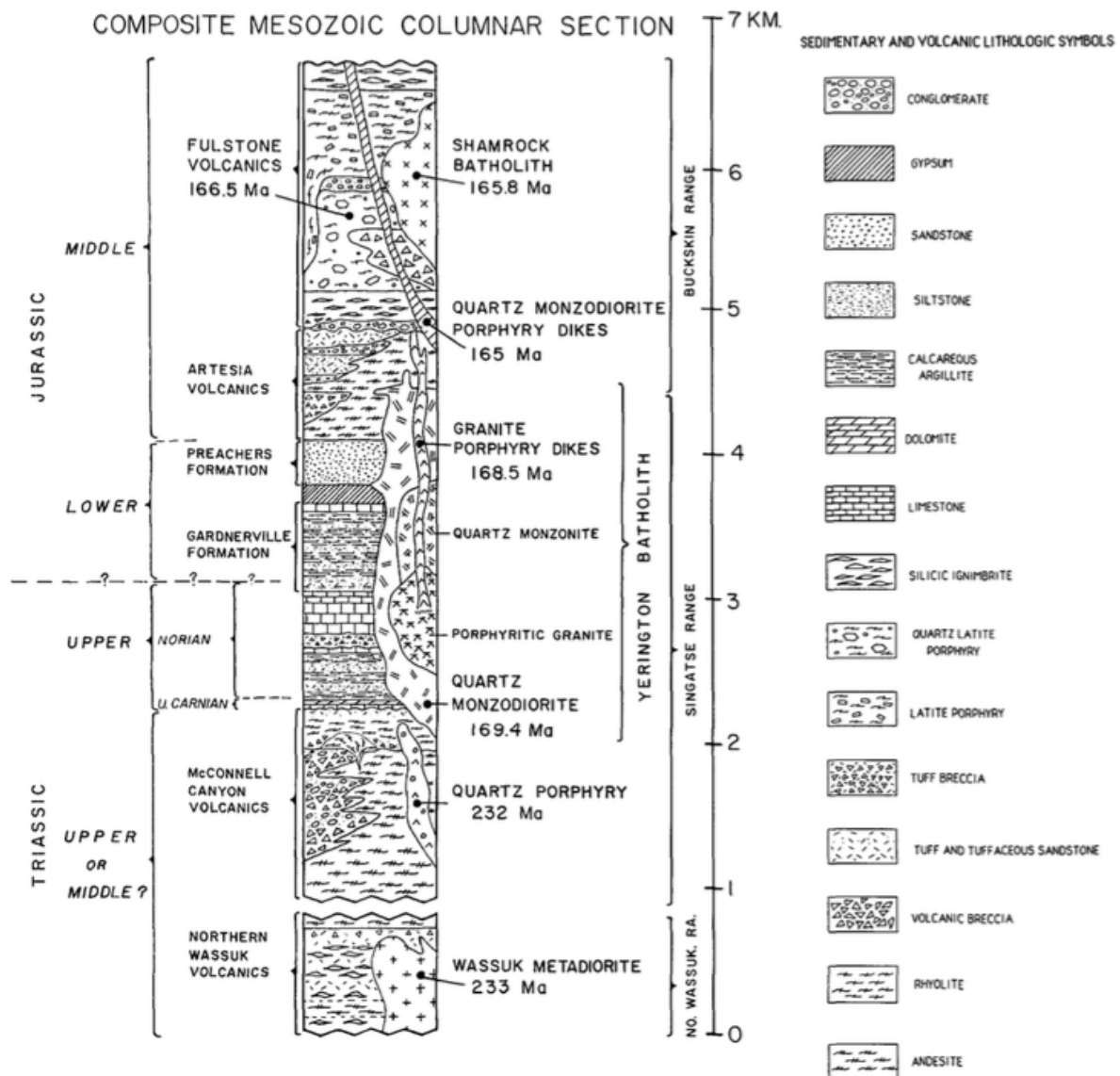


Fig. 2.12 Generalised composite column of Mesozoic volcanic, plutonic and sedimentary rocks of the Yerington District. From Dilles and Wright (1988).

The Yerington batholith is a middle Jurassic (U-Pb zircon age of 169-168 Ma; Dilles and Wright, 1988; in agreement with SHRIMP $^{206}\text{Pb}/^{238}\text{U}$ ages; Banik et al., 2017) composite batholith estimated to be more than 15 km in diameter, once the effects of late Cenozoic Basin and Range extension have been removed (Proffett, 2007). It comprises three major, sequentially emplaced plutons: McLeod Hill quartz monzodiorite, Bear quartz monzonite and Luhr Hill granite. These are cross-cut by swarms of granitic porphyry, aplite and pegmatite dykes. Each of the successively emplaced plutons were progressively smaller in volume, more deeply emplaced, coarser grained and more silicic in composition. Intrusion

volumes have been estimated to be 1000 km³ for the McLeod QMD, 256 km³ for the Bear QM and 70 km³ for the Luhr Hill granite (Dilles, 1987).

The McLeod Hill quartz monzodiorite is the earliest and most voluminous unit of the Yerington batholith, and intrudes Artesia Lake Volcanics at palaeodepths of <1 km. Early endoskarn and metasedimentary hornfels are closely associated with this intrusion. It is a high-K pyroxene-biotite and hornblende-biotite quartz monzodiorite (**Fig. 2.13**) (Proffett and Dilles, 1984; Dilles, 1987). The unit is fine to medium grained (0.5-2 mm), which increases with depth and distance from wall rock contacts. The hornblende + augite to biotite ratio is ~4:1, and accessory magnetite and titanite is abundant. It was emplaced as a series of dyke-like bodies into the overlying volcanics and adjacent hornfels (Dilles, 1987). In the unit, numerous internal contacts of steeply dipping dyke-like bodies, each 20 to 100 m in width, (Dilles, 1987; Dilles et al., 2000) indicate the McLeod Hill quartz monzodiorite was episodically emplaced (Schöpa et al., 2017).

Fine to medium grained biotite-hornblende gabbro occurs as pods and lenses, with dimensions up to 30 by 350 m, within deep (>4 km palaeodepth) exposures of the McLeod quartz monzodiorite. The gabbro is weakly layered, parallel to layering in the quartz monzodiorite, and from petrographic textures has been interpreted as a cogenetic cumulate. Mutually intrusive contact relations between the gabbro and quartz monzodiorite indicate that they formed from contemporary magmas (Proffett and Dilles, 1984; Dilles, 1987).

The Bear quartz monzonite intrusion is a hornblende (biotite) quartz monzonite with an upper border zone of granite (Proffett and Dilles, 1984; Dilles, 1987). Generally intruded into the McLeod quartz monzodiorite, it was also locally emplaced into volcanics and older hornfels. The border granite forms an irregular body as well as dykes within the quartz monzonite. It is a fine-grained (1-2 mm) biotite granite with a hypidiomorphic-granular to porphyritic texture. This border phase grades downwards, over ~100 m, into the interior quartz monzonite phase, with an increase in grain size and hornblende content and a decrease in quartz, K-feldspar and biotite. The interior phase is a medium-grained (2-5 mm), hypidiomorphic-granular, hornblende quartz monzonite (Dilles, 1987; Dilles and Wright, 1988).

The Luhr Hill granite intruded pre-existing batholith units, with a cupola well exposed within the Ann Mason area. It comprises a medium to coarse-grained feldspar megacryst-bearing hornblende-biotite-granite. The border phase (2 mm intergrown quartz and feldspar) within the exposed cupola grades downwards into normal porphyritic granite (0.2 to 1 mm quartz intergrown with 2 to 5 mm K-feldspar). In studies to date, no internal contacts have been observed in the Luhr Hill granite and it is generally said to be very uniform in character. From these observations, Proffett (2007) interpreted that the pluton once existed as a single continuous magma chamber.

Porphyry-style mineralisation in the district is associated with dyke swarms which cross-cut the Luhr Hill granite (Dilles and Proffett, 1995). These comprise of numerous generations of granite porphyry dykes as well as aplite and pegmatite dykes. Their emplacement appears to have been focused through apophyses of the Luhr Hill granite, and along prominent joint sets in the batholith. Most occur within one of the three main exposed dyke swarms, but there are also some isolated examples (Proffett and Dilles, 1984; Dilles, 1987; Proffett, 2007).

The porphyry dykes, which contain up to ~50 vol.% of phenocrysts of feldspar, biotite, hornblende and quartz in an aplitic groundmass, the latter consisting of ~0.002 mm diameter feldspar and quartz, are compositionally and mineralogically very similar to the Luhr Hill granite (Dilles et al., 2000). They can be traced for 2 km and further down into the Luhr Hill granite (Proffett and Dilles, 1984). At Yerington mine, at least five separate porphyry dyke intrusions have been mapped (QMP-N, 1, 2, 2.5, and 3; Proffett, 1979; Carten, 1986; Proffett, 2009), and at Ann Mason, at least three temporally separate intrusions (Dilles, 1987; Dilles et al., 2000). The numerous porphyry dykes cross-cut one another, indicating that they were emplaced as a result of several magma pulses. From similarities in their mineralogy and textures, they were cogenetic and emplaced within a short time interval (Dilles, 1987). Based on the compositional and mineralogical similarities between the porphyry dykes and the Luhr Hill granite, and that their groundmass coarsens downwards, Dilles (1987) and Dilles and Proffett (1995) suggested that the dykes along with mineralising fluids were sourced from upper and middle regions (~3-6 km depth) of the Luhr Hill granite.

Numerous aplite and pegmatite dykes and bodies cross-cut the cupolas as well as the lower parts of Luhr Hill granite, and are both cross-cut and are cut by porphyry dykes (Dilles, 1987; Dilles et al., 2000; Proffett, 2007). They have been suggested to have emanated from late-stage magmas deep within the Luhr Hill granite and/or are related to the porphyry dykes (Proffett et al., 2007; Runyon et al., 2017). Previous work in Yerington has suggested that aplitic and/or pegmatitic magmas likely contributed to hydrothermal alteration (Runyon et al., 2019), but they have not previously been linked to substantive hypogene mineralisation.

The Fulstone Spring Volcanics unconformably overlie the Artesia Lake Volcanics (Dilles, 1987; Dilles and Wright, 1988; Proffett, 2007). They are comprised of sub-aerial intermediate to silicic lavas, domes, ignimbrites and volcaniclastics, preserved in the Buckskin Range of the western most part of the Yerington District (Hudson and Oriel, 1979; Dilles et al., 2000). A dacite dome in the upper part of the Fulstone Spring Volcanic succession has been reported to postdate the Yerington batholith's porphyry dykes, with a zircon U-Pb age of $166.5 \text{ Ma} \pm 0.4$ (Dilles and Wright, 1988). Dilles and Wright (1988) suggest that the Fulstone Volcanics may be related to the nearby younger Shamrock batholith (a large body of hornblende-biotite granite that lies to the south of the Yerington batholith, with a zircon U-Pb age of 165.8 Ma) and to post-date porphyry mineralisation. From field relations, units of the Fulstone Spring Volcanics are however thought to have been cogenetic with granite porphyry dykes associated with the Luhr Hill granite (Proffett, 2007; Proffett, 2009). Dilles et al. (2000) also speculated that the base of the Fulstone sections may be age-equivalent to the youngest granite porphyry dykes within the Luhr Hill granite because the Fulstone Spring Volcanics contain quartz latite lava flows, breccias and ignimbrites that are petrographically similar to the porphyry dykes, containing 20 – 40 vol. % of phenocrysts of plagioclase, hornblende, biotite, quartz and local K feldspar.

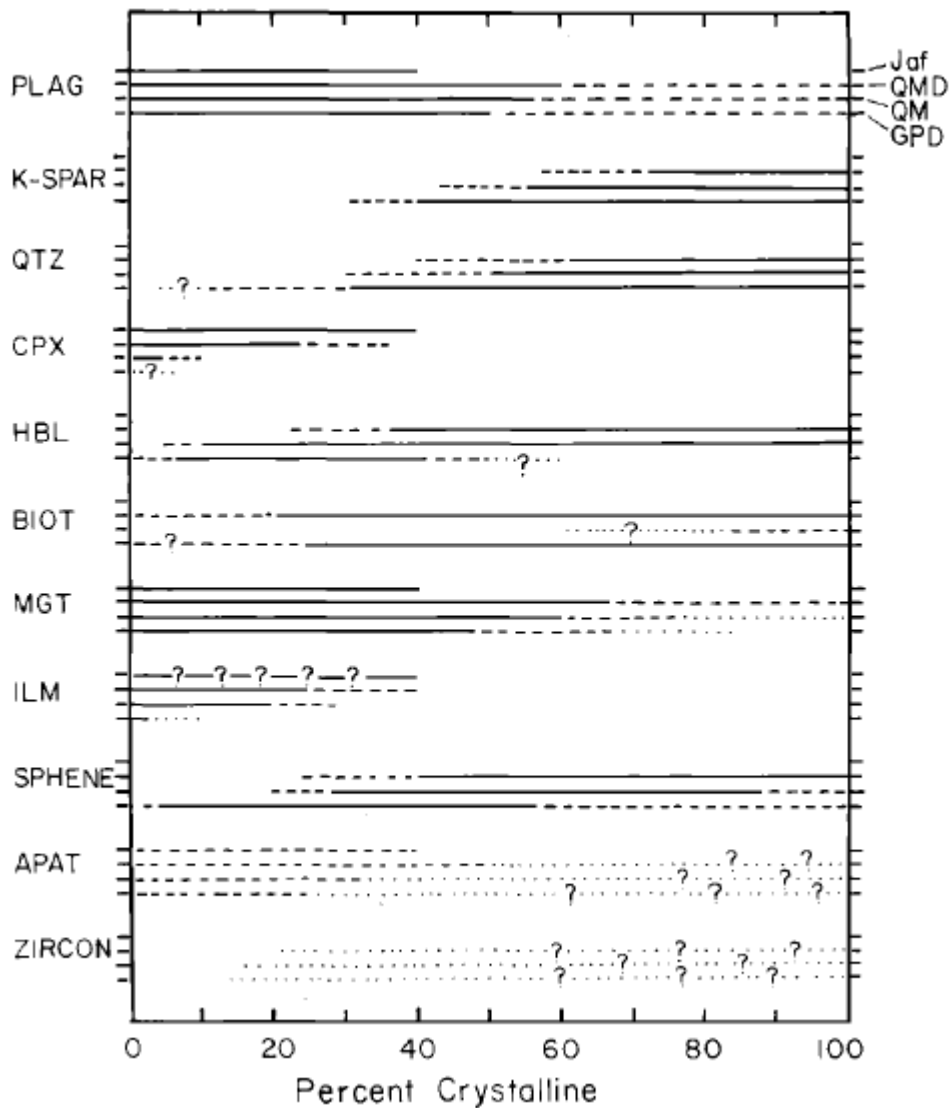


Fig. 2.13 Paragenetic diagram for the Yerington batholith, based on microtextures. For each phase, the top line is basalt of the Artesia Lake Volcanics (Jaf), second is McLeod quartz monzodiorite (QD), third line is Bear quartz monzonite (QM), lowest line is granite porphyry dyke (GPD). Plag = plagioclase, K-spar = K-feldspar, qtz = quartz, cpx = clinopyroxene, hbl = hornblende, biot = biotite, mgt = magnetite, ilm = ilmenite, apat = apatite. From Dilles (1987).

2.3.6 Younger Jurassic Igneous Rocks

A series of east-west striking, steeply dipping quartz monzodiorite porphyry dykes traverse the district; these have given a U-Pb zircon age of circa 165 Ma (Dilles and Wright, 1988). They are reported to intrude the Fulstone Spring Volcanics and were preferentially emplaced along faults that bound the Yerington batholith, and down-drop it in the region of 1 km relative to the surrounding rocks (Proffett and Dilles, 1984). Dilles et al. (2000) inferred these to be older than the nearby Shamrock batholith.

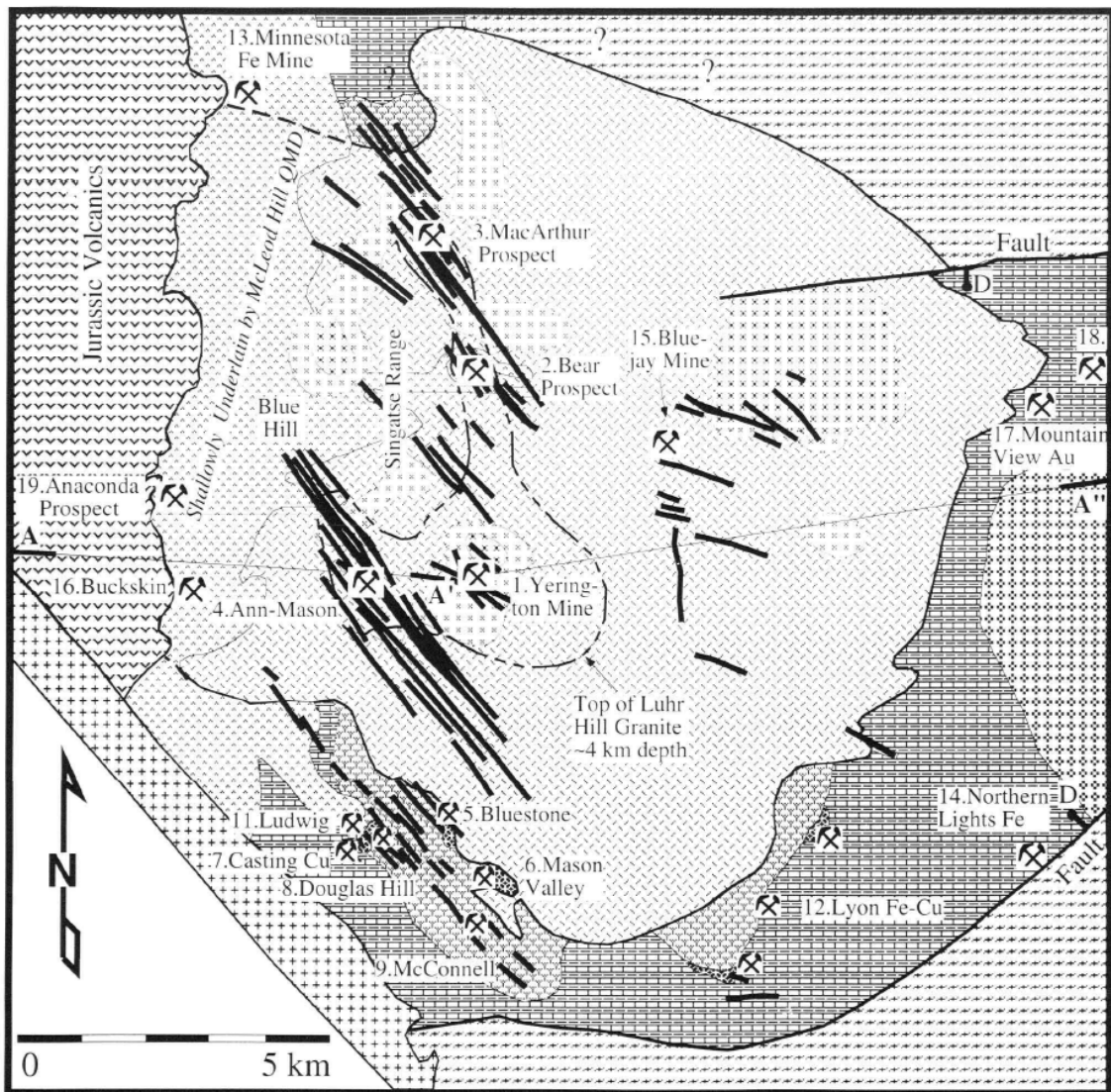
2.3.7 Cenozoic Rocks and Structural Geology

A long period of erosion or non-deposition was followed by a 0.5 – 2 km thick series of Oligocene and early Miocene ignimbrites and lava flows which blanketed the Yerington District. This series is overlain by mid-Miocene andesitic lavas (Proffett and Dilles, 1984). During this andesitic volcanism, rapid extension via closely spaced, eastward dipping extensional faults began and terminated about one million years later (Proffett, 1977). These oldest faults are offset by two sets of eastward dipping extensional faults. The younger of these includes the active fault system that bound the modern basins and ranges in the area. The down-to-the-east extensional faulting resulted in tilting of the pre-Miocene rocks, which includes the mineralised Mesozoic rocks, by roughly 60° to 90° to the west (Proffett, 1977; Dilles et al., 2000). As a consequence, present-day exposures represent cross-sections of the Jurassic palaeo-magmatic-hydrothermal system from the volcanic environment to palaeo depths of up to 8 km (Dilles et al., 2000).

2.4 The Yerington batholith, Nevada – Economic geology

2.4.1 Overview

The Yerington District contains four known Cu(-Mo) porphyries as well as Cu skarn-, Fe oxide- and Cu sulphide ores hosted in metasediments, and shallow batholith-hosted Cu-Au-Fe oxide lodes (**Fig. 2.14**). Dilles and Proffett (1995) estimated the total resource and productions of the district to be 6 Mt of Cu in sulphide ores and >100 Mt of Fe in oxide ores. Recent drilling of the four porphyry deposits has given a combined measured and indicated resource in excess of 9 Mt of contained Cu (Dilles and Proffett, 1995; Bryan, 2014; Henderson et al., 2014; Hudbay Minerals Inc., 2021; Welhener et al., 2022). Three of the four known porphyry deposits have an NI-43-101 (Ann Mason, Yerington and MacArthur) whilst the Ann Mason and MacArthur deposits have also undergone a Preliminary Economic Assessment (PEA). The Bear deposit is a large blind porphyry system which remains unconstrained by drilling. The economic geology of these four porphyry deposits is summarised in this section.



EXPLANATION			
	Cretaceous granite		McLeod Hill Gabbro
	Shamrock Batholith		Luhr Hill Granite
	Skarn		Bear Quartz Monzonite
	Skarnoid & hornfels		Bear Border Granite
	Fulstone Spring Volcanics		McLeod Hill quartz Monzodiorite
			Artesia Lake Volcanics
			Triassic sedimentary & volcanic rocks
			Triassic diorite
			Triassic volcanic rocks

Fig. 2.14 Map of the Yerington Batholith and other Mesozoic rocks as exposed beneath the lower Tertiary unconformity. The reconstruction was made by removing effects of late Cenozoic faulting and tilting. Mines and prospects are labelled. From Dilles and Proffett (1995).

2.4.2 Production history

Recorded production in the Yerington mining district dates back to 1883 (Moore, 1969) when prospectors were attracted to and investigated colorful oxidized

copper staining throughout the Singatse Range. Knopf (1918) reported that 'oxidized copper' cropped out at the historic Nevada-Empire mine located above the south center of the present-day Yerington open pit. Copper mining was first recorded at the Yerington Mine site from 1918-1920 at the Empire Mine, and later, by the Anaconda Mining Company in 1952. Between 1952 and 1979, Anaconda (purchased by Atlantic Richfield Company, 'ARCO', in 1976) extracted approximately 162 Mt of material averaging 0.54% Cu before closing due to low copper prices. Following this, the mine was owned by several different companies but was not worked. In 1989, Arimetco Inc. purchased the property and commissioned a solvent extraction / electro winning plant. It began heap leaching sub-grade waste rock stripped from the Yerington pit by Anaconda, along with acid soluble mineralised material from the MacArthur property (5 miles to the north). Arimetco produced some 95 million pounds of copper between 1989 and 1999 before declaring bankruptcy, due to low copper prices, and abandoning the property. Since 2000, remedial activity on the property has been on going by the Nevada Division of Environmental Protection (NDEP). This was mainly to manage soil and groundwater contamination, which allegedly stems from the former mining and processing operations (Bryan, 2014).

2.4.3 Yerington deposit

The Yerington deposit is a large partially mined porphyry copper deposit, as detailed above. It is reported to have a resource of 128 Mt, measured and indicated Cu, at 0.29% remaining (combining primary and secondary material) (Bryan, 2014). Mineralised porphyry dykes form an elongate body of mineralisation that extends some 6,600 feet along a strike of S62°E. In the Yerington Mine, at least five separate dyke intrusions have been mapped (Proffett, 1979; Carten, 1986; Proffett; 2007) (**Fig. 2.15**). In the porphyry dykes and quartz monzonite, as well as disseminated between veins in host rock, at a lesser grade, chalcopyrite is the dominant copper sulphide occurring with minor bornite, primarily hosted in A-type quartz veins (nomenclature after Gustafson and Hunt, 1975). The unmined mineralized material below the current pit is primarily chalcopyrite. The zone of mineralisation has an average width of 2,000 feet and has been defined by drilling to extend to an average depth of 250 feet below the Yerington Mine pit bottom (3,800-foot elevation). Due to economic constraints and low copper prices at the time, many of the 558 historic Anaconda

drill holes were stopped within mineralisation, with very few holes drilled below the 3,400-foot level where the system remains nearly unexplored (Bryan, 2014). Secondary oxide copper formed much of the upper Yerington Deposit, with chrysocolla being the dominant copper oxide mineral, occurring as fracture coatings and fills. Historic Anaconda drill logs are also reported to note lesser neotocite (black copper wad) and rare tenorite and cuprite (Bryan, 2014).

Only four historic holes have explored the deeper vertical projection of copper mineralisation in the Yerington pit, with three of these drilled along a single N-S orientated section through the centre of the pit (Bryan, 2014). According to Einaudi (1970), in a report to Anaconda, the deep drilling programme intersected a series of nested, concave upward, grade shells that project down the northward 70° dip of the dykes, with the 0.2% Cu zone extending to an overall (dip distance) depth of 2,200 feet. Although the program identified an increasing ratio of pyrite to chalcopyrite with depth, there was no indication of a 'barren core', the porphyry dykes showed a 'remarkable continuity' down dip and host a zone of molybdenite mineralization of indeterminate size and grade.

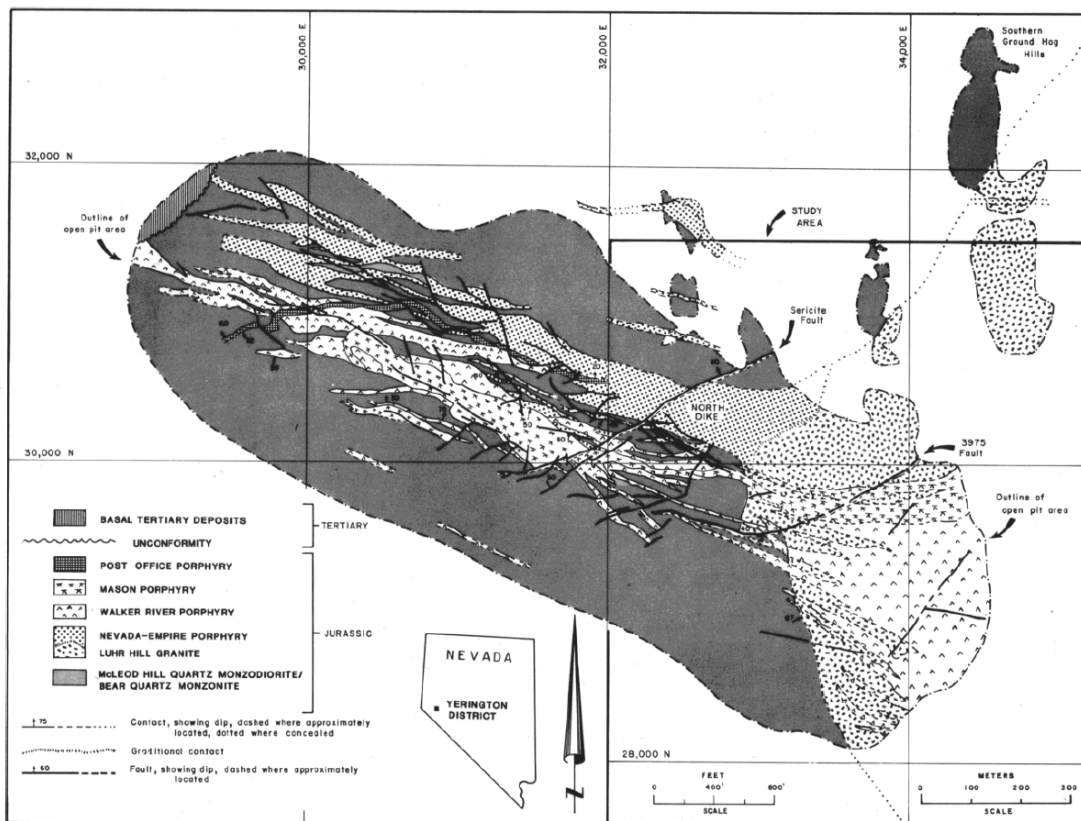


Fig. 2.15 Simplified composite-level map of the geology of the Yerington mine. From Carten (1986).

2.4.4 Bear deposit

The Bear deposit is a large, blind porphyry copper system located beneath and adjacent to the Yerington mine site; it is understood to cover an area of at least 2 square miles. It was discovered in 1961 by Anaconda through condemnation drilling and partially delineated in the 1960s and 1970s by several mining companies. These identified chalcopyrite-hosted in a porphyry system below 500 to 1,000 feet of alluvium and unmineralised bedrock (Bryan, 2014). The zone is open in several directions and has never been consolidated under a single owner. The Anaconda Mining Company drilled an approximately half square mile portion of the deposit in the 1960s and historically reported more than 500 Mt at 0.40% copper grade (Dilles and Proffett, 1995; Bryan, 2014).

2.4.5 MacArthur deposit

The MacArthur copper deposit contains 159 Mt measured and indicated secondary Cu with a 0.21% copper grade and a further 1 Mt indicated primary sulphide Cu mineralisation at 0.29% copper grade (Henderson et al., 2014). The deposit is comprised of a 50 – 150-foot-thick tabular zone of secondary copper mineralisation (oxides and/or chalcocite) covering an area of approximately two square miles. This zone of mineralisation is yet to be fully delineated and remains open to the west and north. Copper oxide mineralisation is the most abundant type and is particularly well exposed in the walls of the MacArthur pit. Chrysocolla, neotocite (black copper wad) and trace cuprite and tenorite are also present. The flat-lying zones of copper oxide are reported to mirror topography, exhibit strong fracture control and range in thickness from 50 to 100 feet. Secondary chalcocite mineralisation forms a blanket up to 50 feet thick and is mixed with and underlies the copper oxide. Primary chalcopyrite mineralisation has been intersected in several locations, below the chalcocite or within the same zone. The extent of the primary sulphide mineralisation is not known (Henderson et al., 2014).

2.4.6 Ann Mason deposit

The Ann Mason copper-molybdenum porphyry deposit is the fourth largest undeveloped copper porphyry resource in North America, with a resource of 2,219 Mt measured and indicated copper at a grade of 0.29% (Kulla et al., 2017; Hudbay, 2021). In the mineralised envelope, copper grade is dependent on vein density, sulphide species and relative age of quartz monzonite porphyry dykes –

to which mineralisation is closely related (Kulla et al., 2017). At least three generations of porphyry dykes have been mapped at Ann Mason (Dilles, 1987; Dilles et al., 2000). The top of the mineralised envelope is truncated by the Singatse Fault and much of the southwest edge is truncated by the northwest trending 1A fault (Kulla et al., 2017).

Sulphide zoning within the Ann Mason deposit is reported to be typical of porphyry deposits, consisting of an outer pyritic shell and concentric zones of increasing chalcopyrite and decreasing pyrite towards the centre, which progress into a core of chalcopyrite-bornite. Chalcopyrite occurs as individual grains in veins and as disseminations, as fillings in brecciated pyrite grains, attached to pyrite grains and as inclusions in bornite. Bornite is present as separate grains in veins, in disseminations and attached to chalcopyrite. Sparse chalcocite occurs as replacement rims on chalcopyrite and bornite. Covellite is rare. Copper oxide/carbonate mineralization, consisting of malachite, black copper-manganese oxides, and copper-bearing limonite, is only locally present within Ann Mason. Molybdenite occurs in quartz and quartz-chalcopyrite veins as centreline segregations and discontinuous selvages, and on fracture/shear surface as 'paint'. Mineralisation is observed to be closely associated with the porphyry dykes, with the earliest dykes believed to be most endowed (Proffett, 1979). Where albite alteration is associated with reduced copper grade, molybdenum mineralisation is not significantly affected beyond partial remobilization from veins into fractures and shear zones (Kulla et al., 2017; Hudbay, 2021).

3 Textural indicators of mineralisation potential in porphyry magmatic systems – a framework from the archetypal Yerington District, Nevada

This chapter is a slightly modified version of Carter, L. C. & Williamson, B. J., 2022. 'Textural indicators of mineralisation potential in porphyry magmatic systems – A framework from the archetypal Yerington District, Nevada', published in *Ore Geology Reviews* (<https://doi.org/10.1016/j.oregeorev.2022.104783>).

Supplementary figures and links to electronic supplementary data can be found at the end of the chapter.

3.1 Abstract

Porphyry-type deposits are spatially and temporally associated with the relatively shallow and texturally complex parts of magmatic systems. Whilst certain textures offer snapshots into the physical processes which result in fluid exsolution and hydrothermal mineralisation, their documentation and interpretation remains disjointed. To address this, we describe a suite of magmatic and magmatic-hydrothermal textures from the classic Yerington Cu(-Mo-Au) porphyry district, Nevada, where Cenozoic extension and tilting has exposed a unique, ~8 km palaeodepth, cross-section through the magmatic system. Within the granite cupolas that underlie the Ann Mason and Yerington porphyry deposits, these textures include pegmatitic pods and massive silica bodies. Emplaced through the cupolas, and genetically associated with ore formation, are aplite dykes that host mineralised unidirectional solidification textures (USTs), pegmatitic segregations, miarolitic cavities and early A-type quartz veins. Based on field relations, including associations with hypogene mineralisation, petrography and Ti-in-quartz crystallisation temperatures, we highlight how these textures may record the timing and location of the magmatic-hydrothermal transition and ore-formation. By doing so we provide a textural framework for exploration geologists to assess the likely 3D spatial and temporal architecture of porphyry mineralisation at the district-prospect scale before employing more invasive and expensive techniques.

3.2 Introduction

Porphyry-type deposits have a strong spatial and temporal association with dioritic to granitic intrusions (Sillitoe, 2010). Intrusive rocks that crystallise at relatively deep crustal levels usually acquire relatively homogenous/equigranular equilibrium textures that reveal little about their nature and evolution (Candela, 1997). In contrast, magmatic rocks genetically associated with magmatic-hydrothermal mineralisation tend to have more complex disequilibrium textures, typically containing porphyritic, aplitic and pegmatitic domains, miarolitic cavities, unidirectional solidification textures (USTs), massive silica bodies, quartz eyes, graphic and micrographic intergrowths and dendritic, acicular and/or skeletal crystals (e.g. Fenn, 1986; Kirkham and Sinclair, 1988; London, 1992; Candela, 1997; Kirwin, 2005; London and Morgan, 2012). These features are indicative of some of the numerous physical and chemical factors which may lead to magmatic-hydrothermal mineralisation, including: chemical evolution of magmas to more water- and ore-element-rich compositions (e.g. Rohrlach and Loucks, 2005; Richards, 2011); relatively rapid ascent into reservoirs at ~ 2–5 km depths causing undercooling; the exsolution of sufficient volumes of magmatic-hydrothermal fluids, and focussing of these fluids into relatively narrow zones of mineralisation (Candela, 1997; Richards, 2005; Sillitoe, 2010; Wilkinson, 2013). Further, the observation and interpretation of such textures offers first-order tools for field geologists to understand the ore-forming potential of different magmatic systems and their component parts.

Despite the invariable association of these textures with porphyry-style mineralisation, their documentation and interpretation remains disjointed and fragmentary. This could be because of their small size (often less than several cm in size, requiring close inspection of outcrop and/or drill core for identification), often poor preservation due to overprinting by subsequent magmatic-hydrothermal and hydrothermal processes, lack of recognition and insufficient exposure of the sub-ore root-zones of porphyry deposits in the vast majority of magmatic-hydrothermal systems (Seedorff et al., 2008). To address this, we describe a suite of magmatic-hydrothermal textures from the archetypal Yerington Cu(-Mo-Au) porphyry district, Nevada, where Cenozoic extensional faulting has exposed an exceptional ca. 8 km deep cross-section through the porphyry system, from the volcanic terrane down through a number of porphyry

centres to their plutonic root zones (Proffett and Dilles, 1984; Dilles, 1987). We discuss the genesis of these textures and their significance in exploration.

3.3 Geological setting – the Yerington porphyry system, Nevada

Late Cenozoic basin and range extensional faulting and associated fault block rotation has exposed a unique < 1 to ~ 8 km palaeodepth cross-section through the middle Jurassic composite Yerington batholith, including volcanic rocks, plutons, and several porphyry centres (Proffett, 1977; Hudson and Oriel, 1979; Proffett and Dilles, 1984; Dilles, 1987; Dilles and Wright, 1988; Dilles and Proffett, 1995). The Yerington batholith was emplaced into Triassic to Jurassic intermediate composition volcanics, volcanoclastic and argillaceous sedimentary rocks, and basal exposures of the Jurassic Artesia Lake Volcanics, which are unconformably overlain by the Jurassic latitic Fulstone Spring Volcanics (Dilles, 1987; Dilles and Wright, 1988; Proffett, 2007), see reconstructed (pre-tilt) cross-section in **Fig. 3.1** (Dilles, 1987; Schöpa et al., 2017).

The batholith comprises three main plutonic phases, which, listed in order of increasing emplacement depth, are: 1) the McLeod Hill quartz monzodiorite, 2) Bear quartz monzonite, and 3) Luhr Hill granite (Dilles, 1987). These are cross-cut by swarms of granite-composition porphyry and aplite dykes which were emplaced through cupolas at the top of the underlying Luhr Hill granite (Proffett, 1977; Dilles, 1987; Carter et al. 2021, 2022). The dyke swarms are spatially and temporally associated with the batholith's four known porphyry copper deposits: Ann Mason; Yerington; MacArthur and Bear (**Fig. 3.1**) (e.g. Proffett, 1979; Dilles, 1987; Dilles and Proffett, 1995). Combined, these host measured and indicated resources in excess of 9 Mt of contained Cu (Dilles and Proffett, 1995; Bryan, 2014; Henderson et al., 2014; Hudbay Minerals Inc., 2021).

The uniquely exposed cross section through the Yerington porphyry system provides a rare opportunity to study the root zones beneath the district's porphyry deposits and textural evidence for the magmatic-hydrothermal transition (Carter et al., 2021b), which is seldom exposed elsewhere (Seedorff et al., 2008).

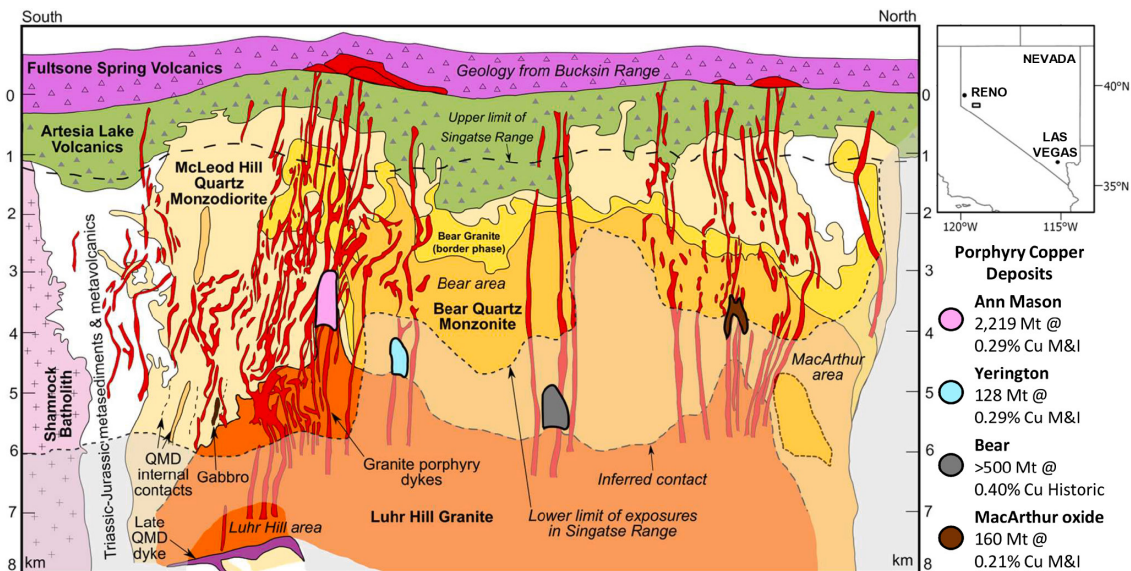


Fig. 3.1 Pre-tilt cross section through the Yerington District, Nevada, reconstructed to a palaeo-depth of 8 km, showing the intrusive units of the Jurassic Yerington batholith, including the various generations of porphyry dyke swarms which were emplaced through apophyses of the Luhr Hill granite, the district's four known porphyry copper deposits (Yerington and Bear deposits projected onto section) and overlying volcanics. Section from Dilles (1987) and Schöpa et al. (2017), with resource estimates from Bryan (2014), Dilles and Proffett (1995), Henderson et al. (2014) and Hudbay Minerals Inc. (2021). QMD = quartz monzodiorite, M&I = measured & indicated, historic = non-compliant historic estimate.

3.4 Methods

This article is based on first-order field observations of cross-cutting relationships, disequilibrium phenomena and textures indicative of fluid exsolution in outcrop from across the Yerington porphyry district, Nevada, and from several kilometres of drill core through the Ann Mason and Yerington porphyry deposits. These observations were supplemented by microscale petrographic and geochemical analyses of quartz USTs. The analytical methods used are described below and in more detail in Carter et al. (2021; Chapter 4).

3.4.1 SEM-EDX-CL

Selected samples of quartz USTs from outcrop and drill core were prepared as polished thin sections (30 μm thickness) for microscale analysis. Following optical microscopy, section surfaces were carbon coated to a thickness of around 25 nm using an Emitech K950 carbon coater. Scanning electron microscope (SEM)-based backscattered electron (BSE) and cathodoluminescence (CL) imaging and

qualitative energy dispersive X-ray (EDX) elemental mapping were carried out using an FEI Quanta 650 Field Emission Gun-SEM equipped with a Gatan monochrome CL detector and 2x Bruker SDD EDS detectors (XFlash series 6 | 30) at the University of Exeter's Environment and Sustainability Institute. The instrument was operated at an accelerating voltage of 20 kV. Elemental maps were obtained using a minimum of 4 scans and a dwell time of 32 μ s, and processed using Bruker Esprit software version 1.9a. The CL images were collected from single scans with a 30 μ s dwell time, a processing resolution of 3072 \times 2048 pixels and 256 grey levels. CL brightness and contrast were optimized to reveal inhomogeneities in quartz; other phases therefore appear either white or black. In the SEM-CL images, the different grey levels shown by quartz represent different luminescence colours that can be attributed to defects in the lattice and/ or the presence of trace elements in the crystal structure (Müller et al., 2010).

3.4.2 QEMSCAN®

The mineralogy of selected carbon-coated polished thin sections was determined using a QEMSCAN® 4300 automated mineralogical assessment system at Camborne School of Mines (Gottlieb et al., 2000; Goodall et al., 2005; Goodall and Scales, 2007). The system is based on a Zeiss Evo 50 SEM with 4 \times Bruker SDD EDS detectors (XFlash) controlled by iMeasure v. 4.2SR1 software for data acquisition and iDiscover v. 4.2SR1 and 4.3 for spectral interpretation and data processing (Rollinson et al., 2011). The QEMSCAN® was operated at an accelerating voltage of 25 kV and a beam current of 5 nA, with a working distance of around 22 mm, in high vacuum mode and with automatic beam calibration every 30 min. Fieldscan measurement mode was used to obtain a mineralogical map of nearly the whole polished section area (39 \times 20 mm) at an analytical point resolution, or pixel spacing, of 10 μ m and with 1000 X-ray counts per pixel. The data from each point of analysis was automatically compared with a Species Identification Protocol (SIP) database of mineral and non-crystalline phase spectra to identify the minerals present. The SIP used was modified from the LCU5 SIP provided with the QEMSCAN®, which includes a range of oxide, sulphate, and silicate minerals. All mineral categories were checked by manually assessing elemental abundances, element ratios, and BSE signal. A boundary phase post-processor was applied to reduce edge effects and to resolve rogue

pixels. Data collection and processing followed in house QA/QC procedures. The data were output as mineralogical maps (**Supplementary Data 3.1**) and in a mineral associations matrix (**Supplementary Data 3.1**).

3.4.3 EPMA

Concentrations of Al, Ti and Fe in quartz were determined by electron probe microanalysis (EPMA) using a JEOL JXA-8200 electron microprobe at Camborne School of Mines, University of Exeter. The thin sections used for the SEM studies were re-polished and carbon coated to a thickness of around 25 nm using an Emitech K950 carbon coater. The instrument was operated at an accelerating voltage of 20 kV, a beam current of 70 nA and a spot size of 15 μm . This relatively large spot size was used due to the sensitivity of quartz at high current and with a narrow beam (Kronz et al., 2012). SiO_2 was assumed to be 100%. Corundum (Geo MkII), rutile and hematite (Astimex) calibration standards were used for Al, Ti and Fe, respectively. For calibration at low concentrations or as 'blank'-control, some studies use a synthetic doped or pure SiO_2 -glass. This was deemed inappropriate as the behaviour of these materials during electron irradiation is very different to that of quartz (e.g. Kronz et al., 2012). Peak and background measurement count times were both 200 s. Limits of detection (LOD) were (3σ) 45 ppm for Al, 42 ppm for Ti and 42 ppm for Fe. To estimate precision, we undertook seven repeat analyses of a single homogenous, magmatic, un-zoned (from SEM-CL imaging) quartz crystal from within a polished section of Luhr Hill granite (sample YM33b in Supplementary Data 2). The mean, range and 1 s. d. of these were: Al (78; 51–101; 20 ppm); Ti (81; 70–91; 8 ppm); Fe (39; 28–52; 12 ppm). From these we used ± 2 s. d. to express our analytical uncertainties: Al ± 40 ppm; Ti ± 16 ppm; Fe ± 24 ppm. Data is provided in **Supplementary Data 3.2**. Please refer to **section 4.5.4** for more comprehensive documentation.

3.4.4 Ti-in-quartz geothermometry

Using the EPMA data (**Supplementary Data 3.2**), Ti-in-quartz geothermometry (TitaniQ, method of Wark and Watson, 2006) was used to assess the crystallisation temperatures of quartz USTs. Based on the consistent presence of titanite in the USTs' inter quartz aplite layers, the activity of TiO_2 (a_{TiO_2}) was assigned a value of 0.7, in line with other studies (e.g. Claiborne et al., 2010; McDowell et al., 2014), including specific studies on the Yerington District (Dilles

et al., 2015; Carter et al., 2021, Chapter 4). We acknowledge that the $a\text{TiO}_2$ may have changed during the evolution and crystallisation history of the system, but we assume that this was negligible given that the same Ti-bearing minerals (notably titanite and trace rutile, see **Supplementary Data 3.1**) are present in the compositionally similar granite and aplite dykes. Further, as discussed in Carter et al. (2021; Chapter 4), small changes in the $a\text{TiO}_2$ will have a minor effect on the calculated crystallisation temperature. To estimate precision, we calculated TitaniQ for seven repeat EPMA analyses of a single homogenous, magmatic, unzoned quartz phase within the Luhr Hill granite (sample YM33b in **Supplementary Data 3.2**). From this, we determined an uncertainty in our geothermometry data of around ± 26 °C. Please refer to **section 4.5.6** for more comprehensive documentation and discussion of TitaniQ.

3.5 Results and discussion

3.5.1 Massive silica bodies and pegmatitic pods

The exposed Luhr Hill granite cupola in Mason pass, which lies just below (palaeo-vertically) the Ann Mason porphyry Cu(-Mo-Au) deposit (Dilles, 1987), is relatively uniform in appearance, notwithstanding the products of pervasive subsequent hydrothermal alteration (Dilles et al., 2000; Halley et al., 2015). The Luhr Hill granite intruded, and has sharp contacts with, the McLeod Hill quartz monzodiorite, but this caused no visible signs of contact metamorphism or metasomatic alteration. In addition, there is no documented or observable textural evidence for the exsolution of mineralising fluids in the Luhr Hill granite cupola such as ore-mineral-bearing miarolitic cavities or internally sourced veins (Carter et al., 2021). Instead there are rare pegmatitic pods and orbs (**Fig. 3.2a**) which are often tens of cm in diameter, have an almost anhydrous mineralogy (quartz, K-feldspar, plagioclase, accessory titanite and Fe-oxides, and only trace biotite), have no cavities, are unmineralised, isolated (i.e. are not connected to or associated with veins), and have no adjacent alteration (Carter et al., 2021). It is likely that these formed as a result of magmatic processes, rather than involving hydrothermal fluids, because: i) they show inward-growing micro-graphic texture at their margins which is unique to the crystallisation of undercooled, non- H_2O -saturated, silicate (i.e. magmatic) liquids/melts (Fenn, 1986; London, 1992; London and Morgan, 2012); ii) they show comparable Ti-in-quartz crystallisation temperatures to their host granite (~ 730 °C; Carter et al., 2021); iii) such graphic

texture is not found in hydrothermal veins which form by the precipitation of minerals from a predominantly aqueous fluid (London and Morgan, 2012); and iv) from experimental studies, the formation of pegmatitic and graphic textures does not require water saturation (e.g. Fenn, 1986; London, 1992).

An alternative explanation for such pegmatitic pods is that they represent pockets of fluid which exsolved upon emplacement of the magma. Such fluids, however, cannot have contained enough solutes to completely mineralise the pockets themselves, and it is difficult to envisage how they could have been subsequently infilled unless they were open to through-flowing hydrothermal fluids. The latter, however, is likely to have resulted in lower Ti-in-quartz temperatures compared with those in the surrounding granites. In addition, their 'granite'-like quartz-K-feldspar-plagioclase assemblage is more indicative of crystallisation from a silicate liquid/melt.

Massive silica bodies (**Fig. 3.2b**) (nomenclature after Kirwin, 2005) also crop out in the cupola, close to the pegmatitic pods. Whilst their borders are obscured in outcrop, these rounded masses are several metres in diameter, are isolated (i.e. not associated with veins), show no hydrothermal banding, and do not host hypogene or secondary Cu mineralisation, although they do show Fe-oxide staining. As their margins are not exposed, it is possible that they have a feldspar-rich outer zone, but this cannot be confirmed. The most obvious heterogeneity within the silica bodies is rare small quartz-filled cavities (**Fig. 3.2b** inset), usually < 5 cm in diameter.

Given their textural similarities and spatial association, the massive silica bodies and pegmatitic pods likely formed due to the same magmatic phenomena, although at different scales. Their development is probably related to intense undercooling (London, 1992), defined as 'the difference between the temperature at which the melt saturates with respect to a mineral and the temperature at which the mineral actually nucleates and grows', which usually results from the rapid upward emplacement of magmas into a cooler environment (Candela, 1997). Undercooling also exerts a significant influence on crystal growth rate and morphology, and therefore the resultant textures (Swanson, 1977).

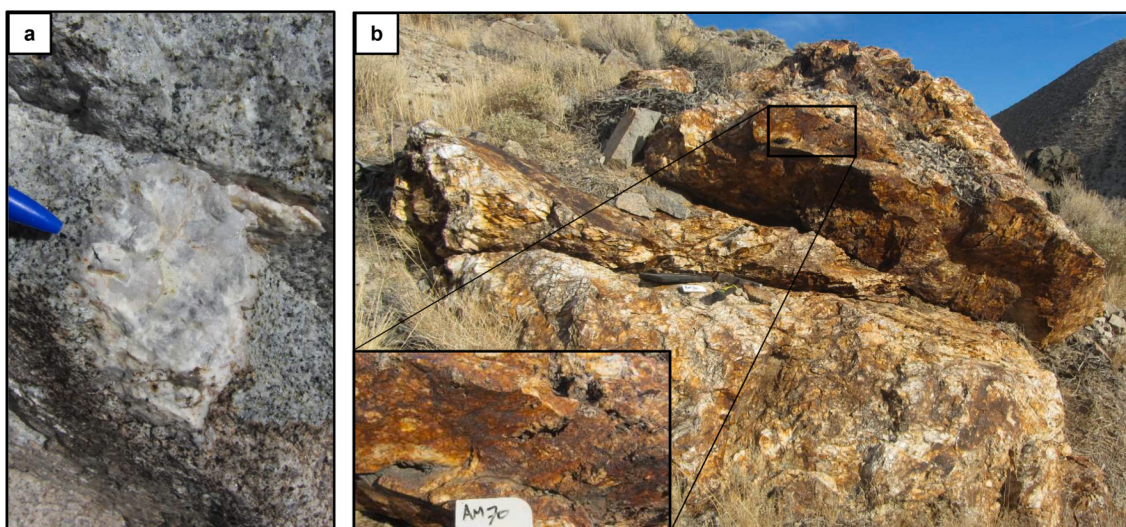


Fig. 3.2 a, Field photograph of a quartz-feldspar pegmatitic pod in the exposed cupola of the Luhr Hill granite. Pen lid for scale. **b**, Field photograph of a massive silica body (nomenclature after Kirwin, 2005) in the exposed cupola of the Luhr Hill granite, palaeo-vertically beneath the Ann Mason porphyry deposit (Dilles, 1987). The body contains no hydrothermal banding or recrystallisation textures and is not mineralised. Hammer and label for scale. Inset: Quartz lined cavities within the silica body. These contain only quartz and constitute an insignificant volume of the body.

3.5.2 Macro textures of the magmatic-hydrothermal transition

Swarms of porphyry dykes cross-cut and appear to have been focussed through apophyses of the Luhr Hill granite cupola. Whilst many are transected by A-, AB- and B-type (nomenclature after Gustafson and Hunt, 1975) and later quartz veins, in both outcrop and drill core, no direct textural evidence could be found for the exsolution of mineralising fluids (e.g. miarolitic cavities), and there is none reported in the literature. They do contain ore minerals, however, so are likely to have been mineralised by fluids from elsewhere.

Several generations of aplite dykes also appear to have been focused through the same apophyses. These vary from several cm to a few m in width and have complex cross-cutting relations between different generations. The aplite and porphyry dykes occasionally show evidence of mingling, which indicates that emplacement, of at least some generations, was contemporaneous (Carter et al., 2021). Significantly, these aplite dykes are pegmatitic, interfinger with quartz

segregations, host quartz USTs and mineralised miarolitic cavities, and are internally veined or cut by mineralised A- and B-type quartz veins. They likely have affinities with aplitic 'vein dykes' previously described elsewhere (e.g. Spurr, 1923), such as at the Henderson Mo porphyry system (White et al., 1981; Shannon et al., 1982; Kirkham and Sinclair, 1988).

The pegmatitic segregations in the aplite dykes are predominantly composed of masses of coarse K-feldspar and quartz crystals up to several cm long. They occur in aplite dykes within the porphyry deposits and in the upper (cupola) and deeper portions of the underlying Luhr Hill granite (Proffett, 2007; Runyon et al., 2017). The magmas that formed them likely underwent varying degrees of undercooling (e.g. Swanson, 1977; Fenn, 1986; London, 1992; London and Morgan, 2012).

The interfingering aplite-quartz segregations (**Fig. 3.3**) vary in thickness, appearing to pinch and swell then pinch out completely. Where present, they are always at the margins of aplite dykes but also feather into their central parts. These features appear to be similar to 'parting veins', described in other magmatic-hydrothermal systems as 'quartz veins that contain numerous septa or partings of aplite' (Kirkham and Sinclair, 1988). These textures most certainly indicate the mingling of magmatic silicate liquids and hydrothermal fluids.

The quartz USTs within the aplite dykes most commonly grew inwards from nucleation points on the wall rocks, although occasionally they also appear to have grown inwards from dyke-parallel internal granite contacts (**Fig. 3.4**). They are seen in aplite dykes that cross-cut both the granite cupola and porphyry dykes, including varieties that host embayed quartz eyes (rounded quartz phenocrysts likely to have formed due to the ease of quartz relative to feldspar nucleation and are indicative of relatively volatile-rich melts; Candela, 1997; Vasyukova et al., 2013; **Fig. 3.4e**). The USTs are localised, vary in thickness and their nucleation surfaces are often non-planar and therefore crystal growth was not always parallel.

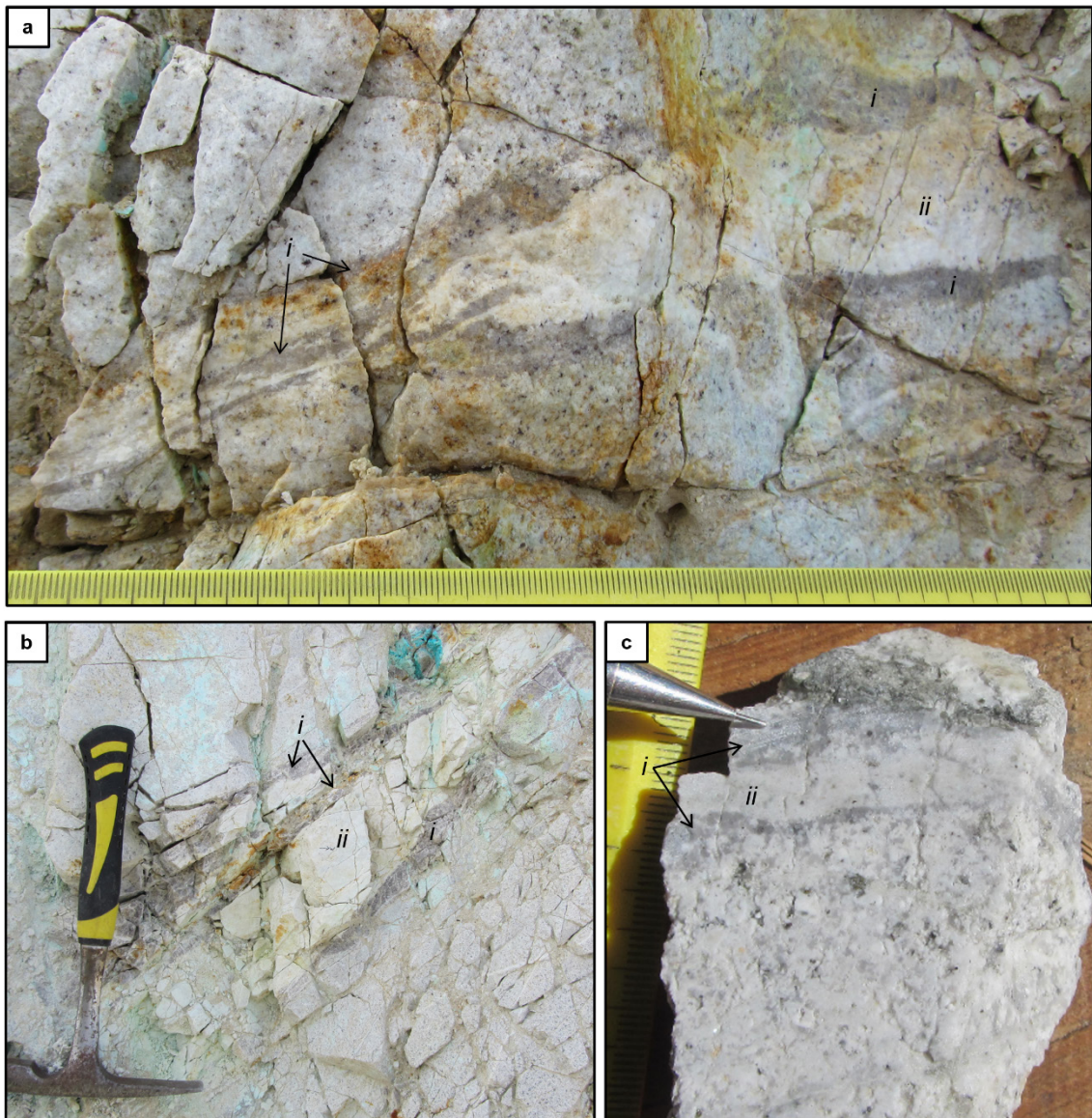


Fig. 3.3 a-c, Photographs of interfingered with quartz segregations (i) within aplite dykes (ii). The quartz segregations occur at the margins and within the aplite dykes. **a & b** are from within the Yerington Mine (Yerington porphyry deposit). **c** is drill core from the Ann Mason porphyry deposit. These textures are likely akin to previous descriptions of 'parting veins' in porphyry systems elsewhere (Kirkham and Sinclair, 1988).

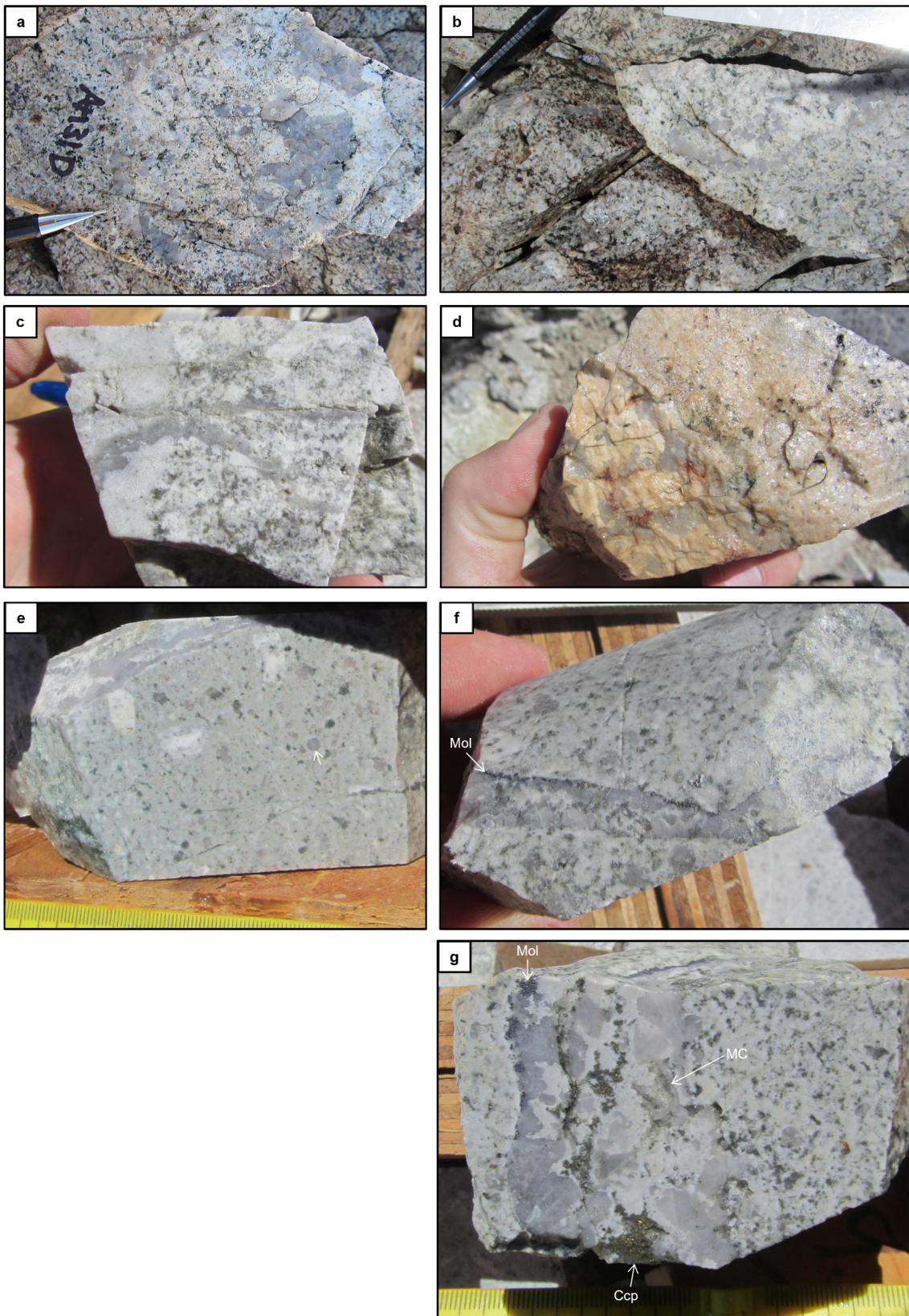


Fig. 3.4 Field photographs of quartz USTs in aplitic dykes in the exposed cupola region of the Luhr Hill granite (**a-c**) and in drill core through the Ann Mason deposit (**d-g**). The aplitic dykes are seen cutting the Luhr Hill granite and porphyry dykes. In e, embayed quartz eyes can be seen in

the porphyry dyke (e.g. white arrow). In **g**, the USTs can be seen associated with miarolitic cavities (MC) and molybdenite (Mol) and chalcopyrite (Ccp) mineralisation. These aplite dykes likely have affinities with 'vein dykes' previously described elsewhere (e.g. Spurr, 1923; White et al., 1981; Shannon et al., 1982).

In some parts of certain aplite dykes in the Yerington District, quartz USTs comprise multiple, subparallel to undulating, equally spaced bands of euhedral quartz crystals interlayered with aplite (**Fig. 3.4**). The quartz grains in the coarse bands range from a few mm to a few cm in length, are parallel to sub-parallel and appear to have nucleated on and grown perpendicular to the wall rocks, as also shown by Shannon et al. (1982) in the Henderson deposit. The aplite layers range from a few mm to several cm thick and predominantly consist of quartz and feldspar which is often micrographic (**Fig. 3.5b**). The bands can be traced for several m in outcrop and show variations in crystal morphology over this scale. In some instances, the USTs are mineralised with molybdenite and chalcopyrite (**Fig. 3.4f, g & Fig. 3.5**). Molybdenite appears to be paragenetically early, being contained as inclusions in quartz crystals nucleated on the wall rocks. Chalcopyrite appears later, being associated with subsequent quartz layers (**Fig. 3.4g & Fig. 3.5**).

From scanning electron microscope-based cathodoluminescence (SEM-CL) imaging, the quartz in the aplite dyke USTs is concentrically zoned inwards from the margins (**Fig. 3.5**). Its crystallisation temperatures, based on Ti-in-quartz thermometry (using the TitaniQ, method of Wark and Watson (2006), with Ti concentrations determined by electron microprobe), are ~ 750 to > 900 °C, which is mostly higher than for quartz in the host Luhr Hill granite cupola (~730 °C, Carter et al., 2021) (**Fig. 3.6**). This difference could be due to variations in $a\text{TiO}_2$ in the system; however, this is deemed unlikely given the comparable mineralogy (notably ubiquitous presence of titanite) of the Luhr Hill granite and aplite dykes. It could also be because the highly undercooled, disequilibrium conditions under which the quartz USTs grew caused the uptake of more Ti and other trace elements into the quartz. However, assuming that the inter-UST aplite layers crystallised at the same temperature as the quartz of the UST, it is more easily explained by certain generations of aplite dykes being intruded and crystallising from melts which were relatively higher temperature than those which formed

their Luhr Hill granite host, possibly originating from a deeper hotter source or having less time to cool during ascent to higher crustal levels.

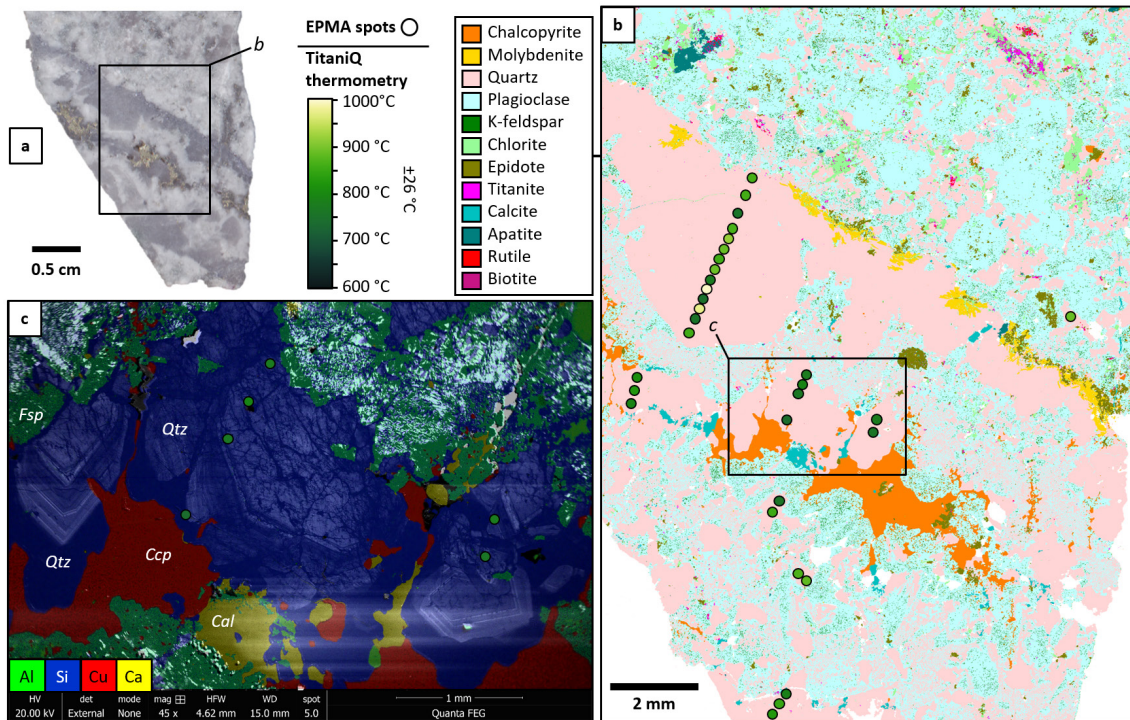


Fig. 3.5 a, Photograph of chalcopyrite-molybdenite-mineralised quartz USTs in an aplite dyke in drill core from the Ann Mason porphyry deposit. The top quartz UST layer marks the contact between the aplitic and host porphyry dyke. Location of **b** annotated; **b**, QEMSCAN® mineral map of the mineralised UST. Micro-graphitic texture can be seen in the aplite between the UST layers. Molybdenite is seen at the margin of the UST. Chalcopyrite is concentrated along an inner portion of the UST and is disseminated throughout the aplite. Overlain are the positions of EPMA spot analyses (spot size not representative) coloured according to Ti-in-quartz temperature (TitaniQ, method of Wark and Watson, 2006), see inset colour scale. Location of **c** annotated; **c**, SEM-CL image showing quartz zoning in the UST overlain by EDX elemental map and temperatures calculated from TitaniQ thermometry. Qtz = quartz, Fsp = feldspar, Ccp = chalcopyrite, Cal = calcite.

The formation of USTs is understood to be linked to undercooling (London, 2009), however this alone does not explain their rhythmic texture. The repeated nature of the UST banding is likely to indicate cyclical variations in the undercooled environment of crystallisation, probably dominated by changes in pressure across cotectic boundaries between quartz-feldspar stability fields (e.g. Kirkham and Sinclair, 1988; Kirwin, 2005). This is because the quartz stability field expands with increasing pressure (Tuttle and Bowen, 1958); quartz may therefore crystallise during periods of volatile overpressure and stop when

pressure declines. One possible mechanism to rapidly reduce pressure is hydraulic fracturing of the wall rocks (Candela, 1989). Upon healing of these fractures, e.g. due to mineral precipitation, pressure then builds up again and the process is repeated.

Miarolitic cavities offer the best evidence for volatile phase saturation and exsolution in the aplite dykes. Their formation requires bubble growth during magma ascent and decompression, and quenching of the melt during that process (Candela, 1997), before they become deformed or disappear due to flow in the magma. The miarolitic cavities, up to several cm across and often mineralised, are common within the aplite dykes which cross-cut the exposed Luhr Hill granite cupola (**Fig. 3.7**). They are characterised by euhedral quartz crystals, associated with chalcopyrite, that project into and terminate in what is likely to have been a segregation of exsolved magmatic fluids in the magma or crystal mush. The miarolitic cavities often occur in close association with USTs and pegmatitic bodies, as well as being locally connected to early-mineralised A-type veins, which are themselves cross-cut by B-type veins.

From recent micro-scale petrographic and geochemical studies of the aplite dykes from Yerington (Carter et al., 2021), the quartz within the mineralised miarolitic cavities appears to be connected to networks of multiple quartz veinlets ('wormy quartz') in the groundmass. This 'wormy quartz' was interpreted to mark the pathways (palaeo-permeability) of exsolving mineralising fluids as well as capturing a snapshot of the magmatic-hydrothermal transition within these 'crystal mush dykes'. By reducing effective stress (Terzaghi and Peck, 1948), the increased fluid pressure due to fluid exsolution and continued upward fluid flow through the palaeo-permeability would have triggered hydraulic fracturing of the host rock aplites and granites. This brittle failure would have caused a rapid decrease in pressure which, in turn, would have initiated the cyclic formation of USTs and magmatic quenching textures such as the rhythmically banded aplite-USTs. The exsolving mineralising fluids would have been able to exploit and permeate these micro-pathways and fractures before cooling and precipitating quartz and other minerals to produce what we now see as 'wormy quartz' and A- and B- type veins.

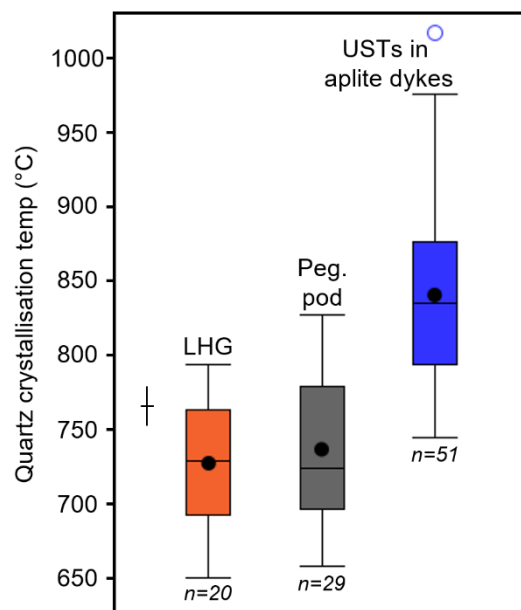


Fig. 3.6 Tukey box plot of Ti-in-quartz crystallisation temperature (TitaniQ, method of Wark and Watson, 2006) for Luhr Hill granite (LHG), a pegmatitic pod (peg. pod) within the Luhr Hill granite, and quartz USTs within aplite dykes from the Ann Mason porphyry deposit, which cross-cut the Luhr Hill granite cupola. n = number of analyses. Cross represents single data point uncertainty.

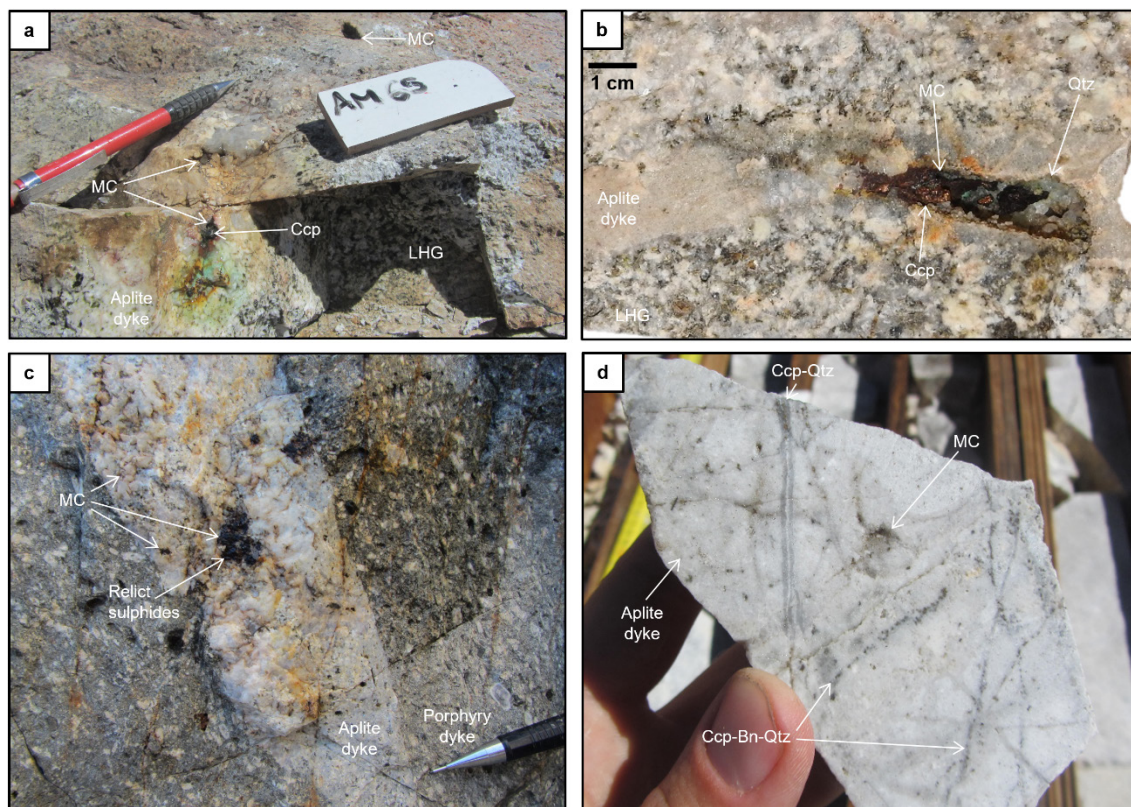


Fig. 3.7 a-d, Photographs of mineralised miarolitic cavities (MC) within aplite dykes which cross-cut the Luhr Hill granite (LHG). Miarolitic cavities are seen having close relationships with early chalcopyrite-bornite-quartz (Ccp-Bn-Qtz) A-type veins in **d**. **b** from Carter et al. (2021).

3.5.3 Magmatic-hydrothermal textures elsewhere

The textures discussed here are by no means exclusive to Yerington. USTs have also been recognised in 'Climax-type' Mo porphyry systems (e.g. White et al., 1981; Shannon et al., 1982), intrusion-related gold deposits (e.g. Kidston, Baker and Andrew, 1991; Timbarra, Mustard et al., 1988) and porphyry system-associated hydrothermal breccias (e. g. Shotgun, Rombach and Newberry, 2001), numerous Sn-W-Mo systems in Canada (e.g. Kirkham and Sinclair, 1988, who referred to them as 'comb quartz layers'), Sn mineralised granites in Tasmania (Hong et al., 2019), Cu-Au-Mo and Sn-W-Mo systems in Mongolia (Kirwin, 2005; Erdenebayar et al., 2014), and several other porphyry Au-Cu systems (e.g. North Parkes, Hithersay and Walshe, 1995; Batu Hijau, Garwin, 2002; Cadia, Wilson, 2003; Bajo de la Alumbrera, Harris et al., 2004; Ridgeway, Harris et al., 2007). We note that the documentation of USTs in Cu-rich porphyry systems in the literature appears notably rarer than for their Au- or Mo-rich counterparts. USTs within aplite dykes, or aplitic 'vein dykes' (Spurr, 1923) at Henderson (White et al., 1981; Shannon et al., 1982) have also been suggested to have a close association with hydrothermal quartz veins (Kirkham and Sinclair, 1988).

Miarolitic cavities are also documented in many other magmatic-hydrothermal ore forming systems. Examples of where they appear to be interconnected on a microscale, which may mark the pathways of exsolving magmatic-hydrothermal fluids, include the: Bajo de la Alumbrera porphyry Cu-Au deposit, NW Argentina (Harris et al., 2004); Sn- Mo-mineralised Ruby Creek granite, New South Wales, Australia; Mo-mineralised leucocratic phases of the Bemboka pluton in the Lachlan fold belt of SE Australia; and Mount Morgan and the Tuckers Range Complex in Queensland, Australia, which are associated with VMS and Cu-Au mineralisation, as outlined by Candela and Blevin (1995).

Reports of massive silica bodies elsewhere include those at: Panasqueira W-Sn-Cu deposit in Portugal (Kelly and Rye, 1979); Ravenswood porphyry Cu-Mo-Au district in Queensland, Australia, with a notably large example called the 'White Blow' (Clarke, 1969); and several Mongolian magmatic-hydrothermal ore-forming systems (e.g. Kirwin, 2005; Tungalag et al., 2019). In the latter, numerous spectacular examples are exposed at Zuun Mud (porphyry Mo-Cu), South Gobi,

where massive silica bodies within with the top levels of a granitic cupola are seen to transition, over several metres, directly into quartz UST layers (Kirwin pers. comm., 2021).

3.5.4 Exploration vectors

The textures described here from the Yerington porphyry district are most likely ubiquitous in all granitic-hydrothermal ore-forming systems. That they have been little documented is probably due to their relatively small size, poor textural preservation within the dynamic, potentially overturning, magmatic systems in which they form, limited exposure and a lack of recognition. This should not limit their use in exploration for porphyry-type mineralisation, in appropriate magmatic systems, rather we suggest that they should be sought out and considered in all field-based campaigns.

From observations of massive silica bodies and pegmatitic pods, they likely result from rapid emplacement causing intense undercooling which eventually led to fluid exsolution and periods of volatile over-pressure within relatively small granitic cupolas. In the Luhr Hill granite cupola of the Yerington District, massive silica bodies and pegmatitic pods appear isolated and not directly associated with mineralisation and we regard them as being a product of undercooling. In other localities, such as at Zuun Mud (Mongolia), they are seen to transition directly into quartz USTs, and so may serve as a marker of the initial stages in the dynamic processes that lead to magmatic-hydrothermal mineralisation. In either case, porphyry-style mineralisation would likely be adjacent to or just above the massive silica bodies (**Fig. 3.8**).

Whilst many of the USTs observed in the Yerington District are unmineralised, we have also documented mineralised examples within aplite dykes. This likely indicates that the processes and conditions that led to their formation also mark the onset of magmatic-hydrothermal mineralisation associated with the aplite dykes. This is consistent with the paragenesis observed in other Au-Cu porphyry systems, for example with gold and chalcopyrite mineralisation associated with UST formation at Oyu Tolgoi as well as in porphyry Cu-Au systems of the Lachlan Fold Belt, New South Wales, Australia (Wilson, 2003; Kirwin, 2005). In many cases, therefore, USTs in the magmatic rocks that host porphyry-type

mineralisation appear to provide vectors towards regions of plutons where magmas were more volatile-rich and are now relatively prospective for mineralisation. Further, our observations of USTs in the Yerington Cu-rich porphyry district illustrate that they are not restricted to Au- and Mo-rich systems, as it is likely that USTs are indicative of the physical processes (mainly rapid emplacement and hydraulic fracturing) and conditions (undercooling followed at some point by pressure fluctuations, rapid crystallisation and fluid exsolution) upon emplacement that may lead to ore formation.

Miarolitic cavities, where preserved, capture the nature and timing of fluid exsolution. Occasionally they are interconnected (e.g. Candela and Blevin, 1995; Harris et al., 2004) and/or lie within 'crystal mush dykes' (Carter et al., 2021) and so may also be an indicator of relatively high levels of palaeo-permeability within immediately surrounding magmas or mush, and may signal the onset of the magmatic-hydrothermal transition. Such conditions and processes may be further evidenced from the occurrence of quartz segregations within aplite dykes, e.g. in Yerington (**Fig. 3.3**), especially where they are in close association with A- and B-type veins. Along with USTs, they would be expected to be found directly below as well as within the lower levels of porphyry-type ore deposits because they offer a snapshot of the magmatic-hydrothermal transition (**Fig. 3.8**).

In summary, the discussed textures likely formed in a continuum prior to the onset of magmatic-hydrothermal mineralisation. In the Yerington porphyry-forming magmatic system, this started with the rapid emplacement of relatively oxidised, moderately water-rich (non-H₂O saturated) Luhr Hill granite magmas to shallow (<5 km deep; Dilles, 1987) levels in the crust and consequent undercooling. That the magma did not reach fluid saturation is suggested from the anhydrous mineralogy of the massive silica bodies and pegmatitic pods, which formed within or just below the upper contact with precursor intrusives. Porphyry and aplite dykes were then episodically emplaced through the cupola region, with the presence of embayed quartz eyes likely illustrating the ease of quartz precipitation over feldspar and relatively high volatile content of the melt (Candela, 1997; Vasyukova et al., 2013). Undercooling along with repeated pressure fluctuations within the aplite dykes, due to 'first-type boiling' (Candela, 1989) as a result of episodic hydraulic fracturing and fluid release, led to the

formation of USTs ('vein dyke' texture elsewhere) prior to fluid saturation, and the later exsolution of fluids to produce miarolitic cavities. Fluid exsolution caused increased fluid pressure, the triggering of further fracturing (and reactivation of previous fractures), and the formation of quartz segregations and A-type veins. Associated pressure drops resulted in rhythmic bands of USTs. Continued upward flow of fluids through palaeo-permeability in the 'crystal mush' aplite dykes (Carter et al., 2021), and further hydraulic fracturing throughout the system, caused a progressive evolution towards the production of AB- and B-type veins and disseminated mineralisation. These same processes occurred concurrently in vast numbers of dykes at different levels to give the complex cross-cutting relationships between dykes and vein generations typical of porphyry deposit-forming environments (**Fig. 3.8**).

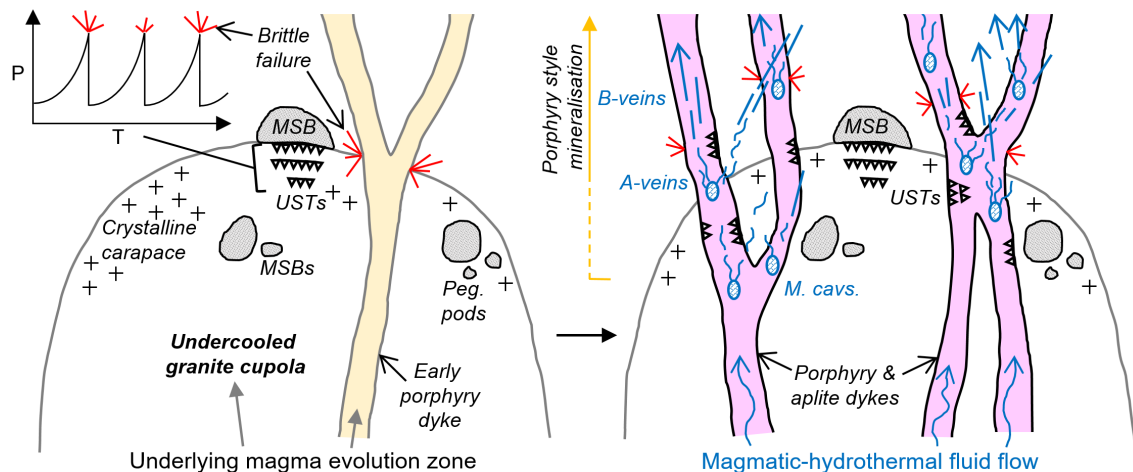


Fig. 3.8 Summary schematic section showing the spatial and temporal distribution of magmatic-hydrothermal textures within an undercooled granitic cupola associated with porphyry-style mineralisation. Inset graph is schematic showing pressure (P) versus time (T) during the formation of rhythmically banded USTs. Peg. pods = pegmatitic pods. MSBs = massive silica bodies (nomenclature after Kirwin, 2005). USTs = unidirectional solidification textures. M. cavs. = miarolitic cavities. A-veins represented by sinuous blue lines which transition to B-veins represented by straight blue lines. Vein nomenclature after Gustafson and Hunt (1975). Not to scale.

3.6 Conclusions

We hope that this compilation of magmatic-hydrothermal disequilibrium textures in the Yerington District will aid geologists in understanding and navigating the 3D architecture of granite-related magmatic-hydrothermal ore systems. Whilst

the inconsistent development or overprinting of these textures detracts from their use in some systems, in others they may provide indicators of the timing and location of the magmatic-hydrothermal transition, especially miarolitic cavities, wormy quartz segregations, USTs, massive quartz bodies and association with A- and B-type veins, and a broad indication of the location of mineralisation, usually above where they are found. Thus, they may aid in targeting in the initial stages of exploration to reduce the use of more expensive, invasive and/or environmentally impactful techniques. When combined with other geological data and observations, they can also serve as powerful tools in unravelling the intrusive history of an igneous complex.

3.7 Declaration of co-authorship

L.C.C. and B.J.W. performed the field studies. L.C.C. performed petrography, SEM-EDX-CL and EPMA analyses at Camborne School of Mines. Dr Gavyn Rollinson (Camborne School of Mines) is thanked for producing the QEMSCAN[®] mineralogical map. L.C.C. prepared the figures and drafted the manuscript. B.J.W. suggested changes to the final version of the manuscript.

3.8 Supplementary Data

Supplementary Data 3.1: QEMSCAN[®] automated mineralogical assessment data.

Supplementary Data 3.2: EPMA data

Supplementary Data files are available at <https://doi.org/10.5285/5a4bc758-ac88-4715-a665-81f69108f854>

4 Crystal mush dykes as conduits for mineralising fluids in the Yerington porphyry copper district, Nevada

This chapter is a slightly modified version of Carter, L. C., Williamson, B. J., Tapster, S. R., Costa, C., Grime, G. W. and Rollinson, G. K., 2021. 'Crystal mush dykes as conduits for mineralising fluids in the Yerington porphyry copper district, Nevada', published in *Communications Earth & Environment* (<https://doi.org/10.1038/s43247-021-00128-4>).

Supplementary figures and links to electronic supplementary data can be found at the end of the chapter.

4.1 Abstract

Porphyry-type deposits are the world's main source of copper and molybdenum and provide a large proportion of gold and other metals. However, the mechanism by which mineralising fluids are extracted from source magmas and transported upwards into the ore-forming environment is not clearly understood. Here we use field, micro-textural and geochemical techniques to investigate field relationships and samples from a circa 8 km deep cross-section through the archetypal Yerington porphyry district, Nevada. We identify an interconnected network of relatively low-temperature hydrothermal quartz that is connected to mineralised miarolitic cavities within aplite dykes. We propose that porphyry-deposit-forming fluids migrated from evolved, more water-rich internal regions of the underlying Luhr Hill granite via these aplite dykes that contained a permeable magmatic crystal mush of feldspar and quartz. The textures we describe provide petrographic evidence for the transport of fluids through crystal mush dykes, a process which may also be important in the formation of other ore deposit types.

4.2 Introduction

Porphyry deposit-forming fluids are derived from large, long-lived magmatic systems (Cline and Bodnar, 1991; Buret et al., 2016; Tapster et al., 2016) where melt or mush reservoirs are at depths of between around 5 to 15 km (Richards, 2005; Sillitoe, 2010) or in more extensive transcrustal magmatic systems (e.g. Cashman et al., 2017; Sparks and Cashman, 2017; Jackson et al., 2018). How ore-forming fluids are transported from these reservoirs and focused into narrow, relatively shallow (ca. 2-5 km deep, Sillitoe, 2010; Richards, 2018), zones of economic mineralisation (Seedorff et al., 2008; Sillitoe, 2010; Weis, 2012; Wilkinson, 2013; Richards, 2016) is an important yet 'missing link' in our understanding of porphyry deposit formation (Dilles, 1987; Sillitoe, 2010). Existing models commonly invoke: convection of bubble-rich magma in upper crustal magma chambers and upwards emplacement to form porphyritic stocks and dykes (e.g. Candela, 1991; Shinohara et al., 1995; Cloos, 2001; Richards, 2005); accumulation of volatile-saturated melts in cupolas which act as exhaust valves episodically ejecting fluids and magma by repeated dyke injections (e.g. Dilles, 1987; Proffett, 2003; Sillitoe, 2010); or through sustaining brittle fracture networks (Weis, 2012). These generic concepts are still debated as there is a paucity of observational evidence for a critical link to porphyry ore genesis. Although field observations from across magmatic systems potentially offer snapshots of the complex sequence of dynamic processes that lead to fluid extraction (Pistone et al., 2020), most are limited due to a lack of vertically extensive exposure (Seedorff et al., 2008). One of the main exceptions to this is the archetypal Yerington porphyry system, Nevada, which has been tilted to reveal a vertical section from palaeosurface to a depth of ca. 8 km (Dilles, 1987). This has therefore provided important constraints for porphyry deposit models (e.g. Richards, 2005; Seedorff et al., 2005; Corbett, 2009; Sillitoe, 2010; Wilkinson, 2013), including computational simulations of the thermal evolution of magmatic systems and ore fluid focusing (Weis, 2012; Schöpa, 2017). Despite having such examples, evidence as to how the fluids are transported upwards has been circumstantial, largely based on the spatial proximity of the ore zone to the cupola and porphyry dykes. Understanding this fluid transport step is vital for developing more reliable porphyry exploration models and may give clues as to why very few known porphyry-type magmatic systems are economically mineralised.

The section through the Yerington District has exposed surface volcanics, three major plutons, hundreds of dykes and four known porphyry deposits (**Fig. 4.1**). The plutons are the McLeod Hill quartz monzodiorite, Bear quartz monzonite and Luhr Hill granite (**Fig. 4.1**), in order of decreasing age and volume, and increasing emplacement depth and silica content (Dilles, 1987). Cross-cutting these, but focused mainly by the structure of the apophyses of the Luhr Hill granite, are granite-composition porphyry and aplite dykes. These are also concentrated in the areas of the four known porphyry copper deposits: Ann Mason, Yerington, McArthur and Bear (Bryan, 2014; Henderson et al., 2014; Kulla et al., 2017; Dilles and Proffett, 1995).

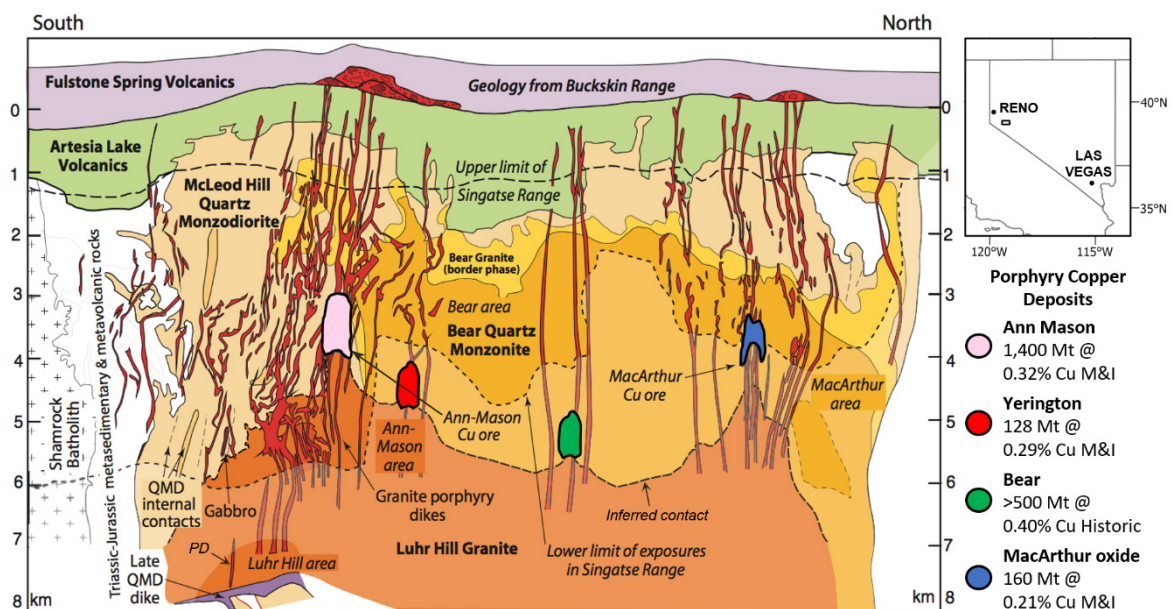


Fig. 4.1 Pre-tilt cross section through the Yerington porphyry copper district, Nevada: Reconstructed to a palaeo-depth of 8 km, showing the intrusive units of the Jurassic Yerington batholith, the various generations of porphyry dyke swarms which focus through apophyses of the Luhr Hill granite, the district's four known porphyry copper deposits and overlying volcanics. QMD = quartz monzodiorite. PD = porphyry dyke in Supplementary **Sup. fig. 4.3**. Modified after Dilles (1987) and Schöpa et al. (2017). Resource estimates (M&I = measured & indicated; historic = non-compliant historic estimate) from Bryan (2014), Dilles and Proffett (1995), Henderson et al. (2014) and Kulla et al. (2017).

4.3 Results and Discussion

From existing conceptual models for the Yerington District (e.g. Dilles, 1987; Schöpa et al., 2017), and more generalised schemes for porphyry deposits (e.g. Cloos, 2001; Richards, 2005; Seedorff et al., 2005; Corbett, 2009; Sillitoe, 2010; Wilkinson, 2013), which are mostly based on spatial relations, petrographic studies and geochemistry, the porphyry dykes and mineralising fluids are likely to have emanated from the spatially associated cupolas and upper regions (~3 to 6 km depth) of the Luhr Hill granite (Dilles, 1987). However, from our first-order field observations that span the entire cupola and upper regions of the Luhr Hill granite, where exposed, we could find no definitive textural evidence, e.g. miarolitic cavities (Candela, 1997) or directly sourced quartz or other veins, for fluid exsolution from the granite or porphyry dykes in these regions. Contacts between the granite cupola and precursor McLeod Hill quartz monzodiorite were sharp with no metasomatic effects beyond the otherwise later, pervasive, mostly sodic-calcic and propylitic porphyry-related alteration (Sillitoe, 2010).

The granite cupolas do however contain rare isolated quartz-feldspar pegmatitic orbs and massive silica bodies (nomenclature after Kirwin, 2005) (**Fig. 4.2; Sup. fig. 4.1**). These can be likened to orbicules and other spheroidal textures, found in a wide variety of magmatic rocks, whose origins are poorly understood but which are widely thought to crystallise as a result of H₂O saturation in the melt (e.g. Moore and Lockwood, 1973; Decitre et al., 2002; Grosse et al., 2010; Ballhaus et al., 2015). However, from a combination of features, the pegmatitic orbs in the Luhr Hill granite are almost certainly magmatic in origin (i.e. crystallised from a silicate melt): they have an almost entirely anhydrous mineralogy (quartz, K-feldspar, plagioclase, accessory titanite and Fe-oxides, with only trace biotite), they are unmineralised, lack concentric shells and a central nucleation point (usual in orbicules (Moore and Lockwood, 1973; Decitre et al., 2002; Grosse et al., 2010)), have no cavities (once fluid-filled, i.e. they are not miarolitic cavities), are not connected with or associated with veins (i.e. there are no fluid escape textures) or adjacent alteration, show no evidence of collapse as a result of fluid loss, grew inwards and show marginal micrographic textures (**Fig. 4.2**). Some spheroids with anhydrous mineralogies are thought to form as a result of H₂O saturation in basaltic melts, e.g. in the Troodos, however these don't show inward growth or graphic textures and are often accompanied by fluid-

escape textures and/or alteration (Ballhaus et al., 2015). The micrographic intergrowths seen in the pegmatitic orbs could be interpreted as indicating near volatile-saturated conditions in the magmas (e.g. Lentz and Fowler, 1992), a wider range of water activities (London and Morgan, 2012) or, based on experimental work, that the melts were at least water rich (~4 wt% water, Rusecka et al., 2020). Alternatively, from experimental work at significant H₂O concentrations, graphic and spherulitic quartz-feldspar intergrowths can be produced by undercooling (Baker and Freda, 2001). It has also been demonstrated that pegmatitic and graphic textures require undercooling but not water saturation for their formation (e.g. Fenn, 1986; London, 1992) and could form from highly undercooled, relatively viscous, flux poor and therefore water undersaturated magmas (Candela, 1997; London and Morgan, 2012). Further evidence to support a magmatic origin for the Luhr Hill orbs is that their mean TitaniQ crystallisation temperatures (method of Wark and Watson (2006), using Ti-in-quartz measured by EPMA) of 736°C (n=29) is comparable to a mean of 727°C (n=20) for magmatic quartz in the host Luhr Hill granite (see **Supplementary Data 4.1**). In summary, we interpret that, whilst highly undercooled, the cupola itself was unlikely to have been the direct source of mineralising fluids. Further, even if the pegmatitic orbs and massive silica bodies do represent pockets of exsolved fluids, given their isolation and rarity, we suggest that the volume of fluid escaping as a result of their crystallisation was minimal. We therefore suggest that the cupola was not the source of mineralising fluids but that these were sourced via dykes from deeper, more evolved portions of the Luhr Hill granite (Dilles, 1987).

Aplite dykes in the Yerington District occur pervasively from below to within the Ann Mason and Yerington porphyry deposits. These are numerous in number, with local occurrences of several dykes per meter (**Sup. fig. 4.2**), they cross-cut the cupolas and the apparent deepest exposures of the Luhr Hill granite (7-8 km, Dilles, 1987) (**Sup. fig. 4.3**). As such, their source is therefore likely to be deeper unexposed parts of the Luhr Hill granite. Multiple generations of aplites are seen to have complex cross-cutting relations but locally they mingle with magmas which formed the porphyritic dykes (**Sup. fig. 4.4**) and are also cross-cut by mineralised veins (**Sup. fig. 4.5**). At least some aplitite dykes were therefore contemporaneous with, yet distinct from the porphyry dykes, and were early- to

inter-mineralisation. The presence of rare unidirectional solidification textures (USTs) (**Fig. 4.3a & c**) within aplites injected into the Luhr Hill granite is likely to indicate rapid pressure fluctuations (Kirwin, 2005) and probable fluid exsolution due to depressurisation as a result of hydraulic fracturing and fluid release ('first-type boiling'; Candela, 1989). Interfingering aplite and quartz selvages (**Fig. 4.3b**) and common miarolitic cavities, where euhedral crystals grew into once fluid-filled spaces (**Fig. 4.3c & 4**), indicate the aplites' formation at the magmatic-hydrothermal transition. Previous work in Yerington and other porphyry districts suggests that aplitic and/or pegmatitic magmas likely contributed to hydrothermal alteration (e.g. Stefanova et al., 2014; Runyon et al., 2017; Chang et al., 2018), but have not previously been linked to substantive hypogene mineralisation. From our observations they are often mineralised, hosting pegmatitic segregations, sulphide-bearing miarolitic cavities, and early A- and B-type veins (nomenclature after Gustafson and Hunt, 1975) which locally terminate at the dyke margins (**Fig. 4.3 & Fig. 4.4**).

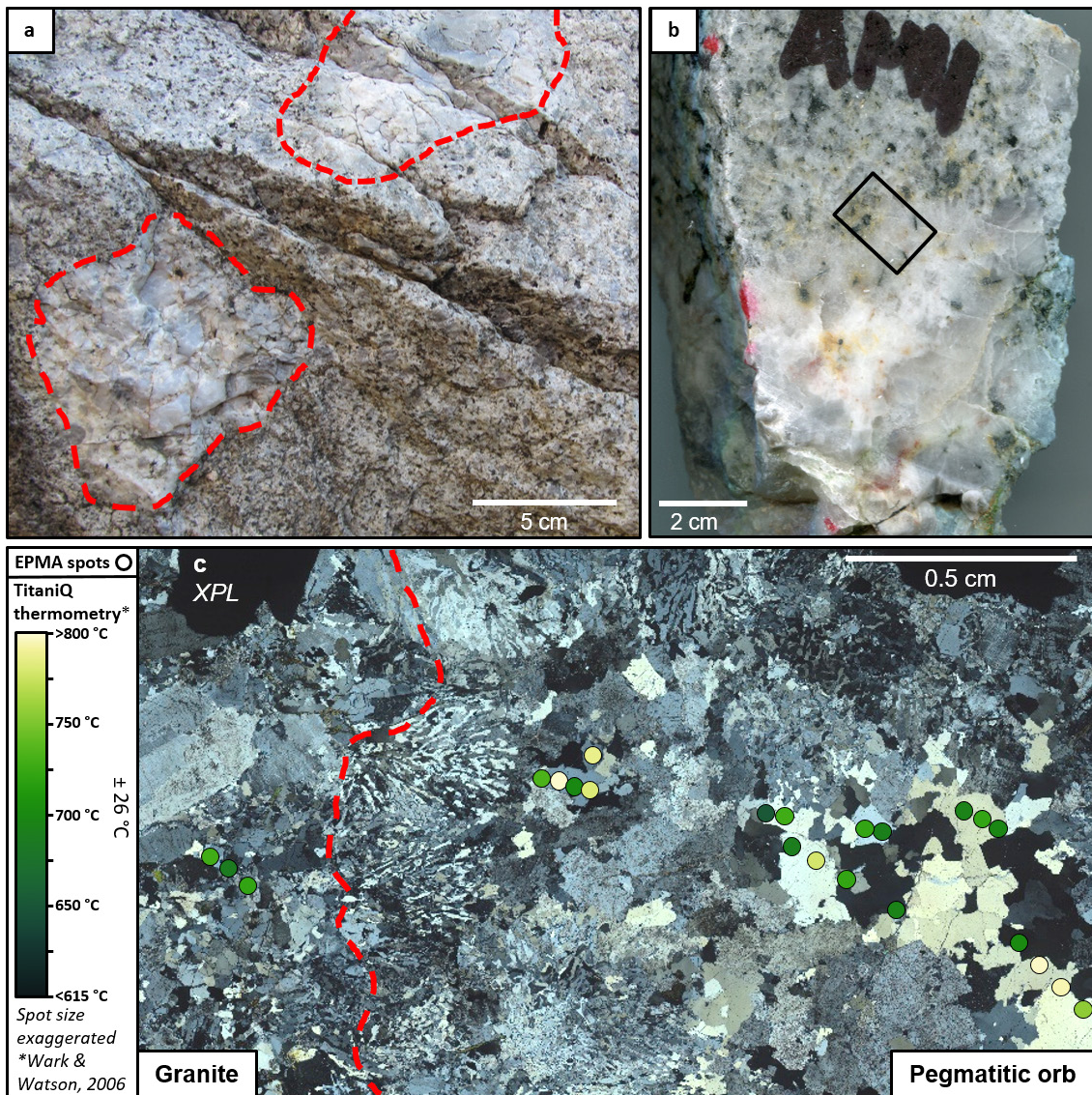


Fig. 4.2 Quartz-feldspar pegmatitic orbs in the Luhr Hill granite cupola: **a & b**, Field and sample photograph of quartz-feldspar pegmatitic orbs (outlined by red dashed lines) in the exposed cupola of the Luhr Hill granite, palaeo-vertically below the Ann Mason porphyry deposit (Dilles, 1987); **c**, Photomicrograph under cross polarised light (XPL, location in **b**), showing micrographic texture at the margins of the pegmatitic orb (red dashed line), suggesting inward crystallisation, and locations of EPMA spot analyses for TitaniQ thermometry (method of Wark and Watson, 2006) (Circles coloured as per legend).

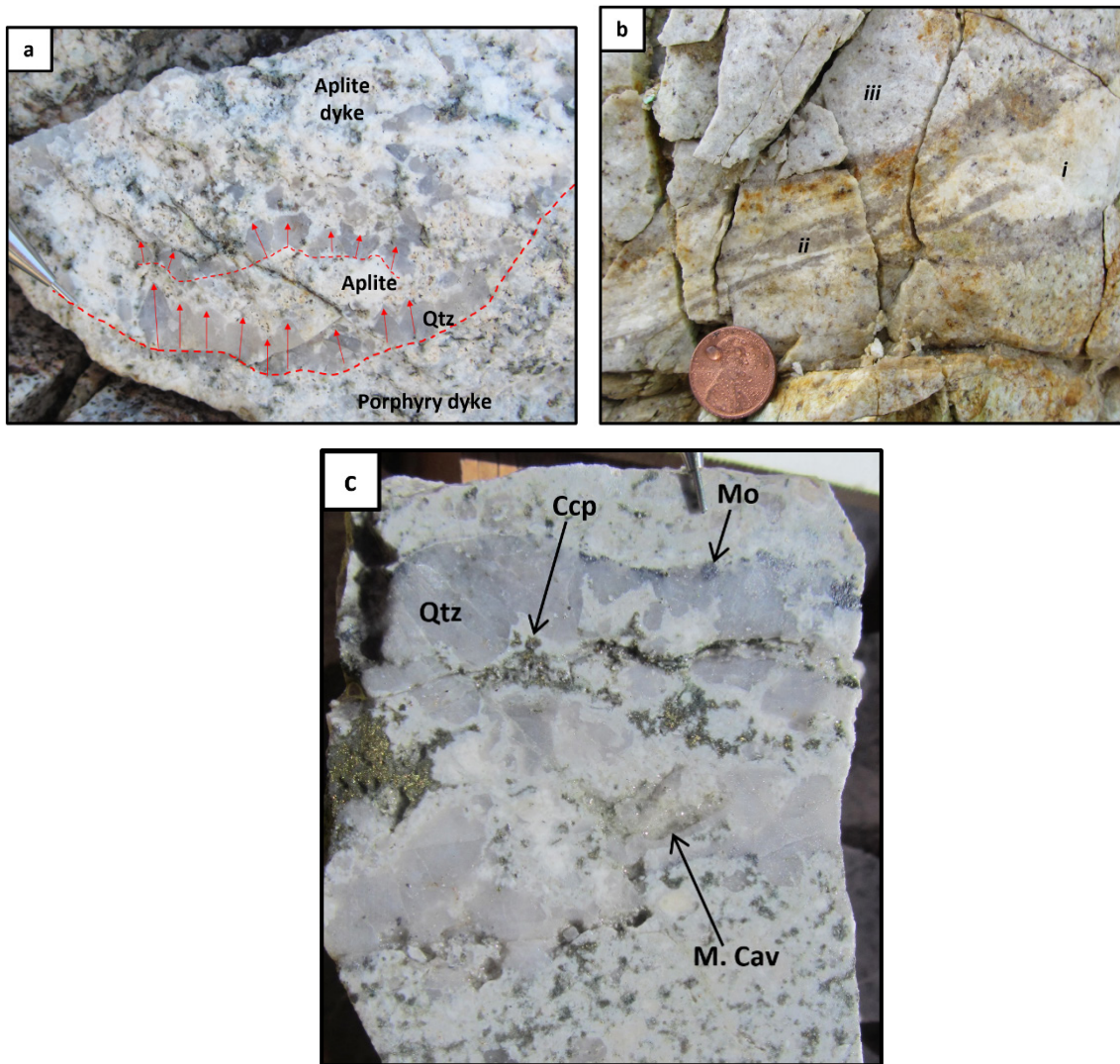


Fig. 4.3 Magmatic-hydrothermal textures in aplite dykes: **a**, Field photograph from the exposed cupola of the Luhr Hill granite showing quartz (Qtz) unidirectional solidification textures (USTs) (red arrows marking c-axes) in an aplite dyke, indicating rapid pressure fluctuations (Kirwin, 2005) or likely 'first-type boiling' during dyke emplacement (Candela, 1989). Pencil tip for scale; **b**, Field photograph from within the Yerington Mine (Yerington porphyry deposit) of interfingering aplite dyke (*i*) and quartz selvages (*ii*). The dyke is hosted within a slightly coarser-grained aplite dyke (*iii*). This is suggestive that the aplite magma was co-eval with a magmatic-hydrothermal fluid which crystallised quartz. Coin for scale; **c**, Photograph of drill core from the Ann Mason porphyry deposit showing a pegmatitic selvage in an aplite dyke which cross-cuts the Luhr Hill granite. The pegmatite shows quartz USTs growing inwards from its rim, molybdenite (Mo) along its margins, a miarolitic cavity (M. Cav) and paragenetically late hypogene chalcopyrite (Ccp) which appears to be interstitial or to have precipitated within open spaces, probably also miarolitic cavities. Pencil tip for scale.

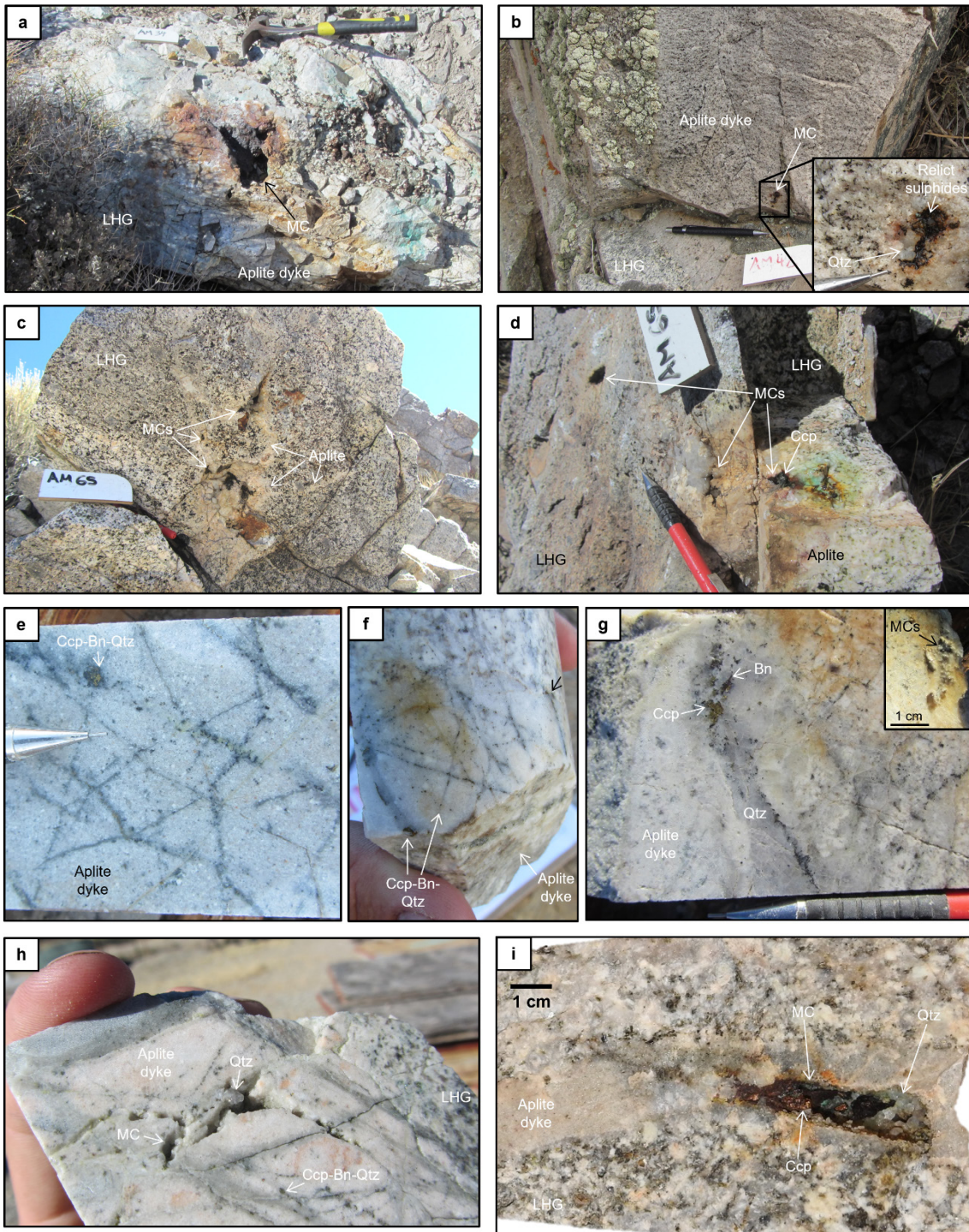
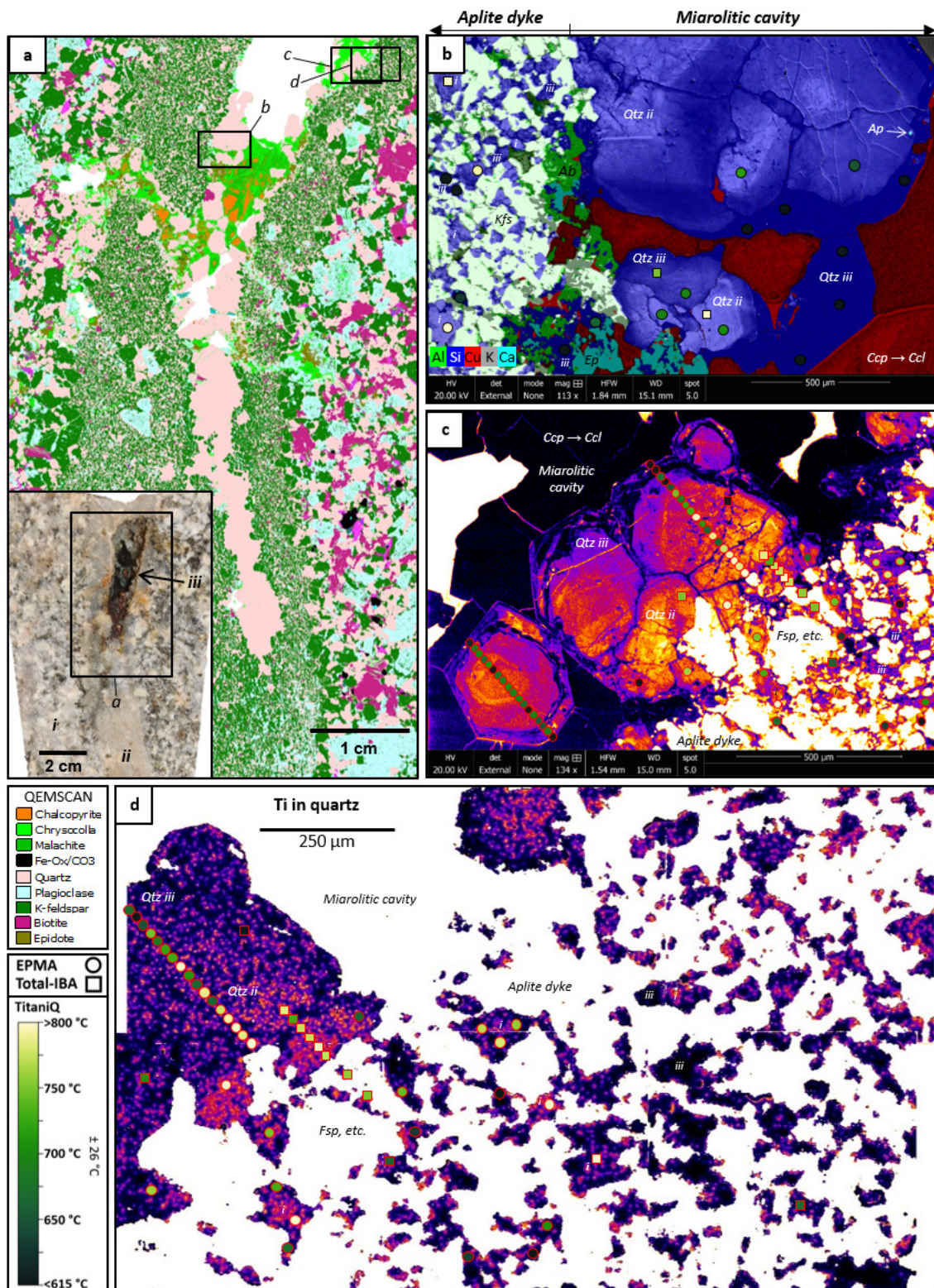


Fig. 4.4 Fluid exsolution and mineralisation in aplite dykes: **a-d**, Field photographs of miarolitic cavities (MCs) within aplite dykes, some mineralised with chalcopyrite (Ccp), which is undoubted textural evidence for mineralising fluid exsolution (Candela, 1997). The aplite dykes cross-cut the exposed cupola of the Luhr Hill granite (LHG), which, pre-tilting, would have sat beneath the Ann Mason porphyry deposit (Dilles, 1987). Qtz = quartz. Hammer and pencil for scale; **e & f**, Drill core from the Ann Mason porphyry deposit showing aplite dykes hosting early chalcopyrite-bornite(Bn)-quartz (A-type; nomenclature after Gustafson and Hunt, 1975) veins, locally terminating at dyke margins (black arrow in **f**). Pencil and thumb for scale; **g**, Drill core from the Ann Mason porphyry deposit showing a mineralised aplite dyke. Pencil for scale. **Inset**,

Miarolitic cavity on the backside of this sample; **h**, Drill core from the Ann Mason porphyry deposit showing an aplite dyke hosting mineralised miarolitic cavities closely associated with early chalcopyrite-bornite-quartz (A-type) veins. Finger for scale; **i**, Sample from the exposed cupola of the Luhr Hill granite showing the granite cut by an aplite dyke hosting a chalcopyrite mineralised miarolitic cavity. Quartz and chalcopyrite clearly crystallised into open space, with euhedral crystal shapes and terminations. This sample is the focus of **Fig. 4.5**.

On a tens of micron scale, from detailed scanning electron microscopy with energy dispersive X-ray analysis (SEM-EDX) and cathodoluminescence (CL) imaging (**Fig. 4.5**; **Sup. fig. 4.6-10**), aplite dykes contain a wormy quartz texture throughout their groundmass comprising of polycrystalline branching, highly interconnected generations of quartz (moderate to dark CL response, 'Qtz ii & iii' in **Fig. 4.5b, c & d**), in addition to discrete magmatic quartz grains (brighter CL response, 'Qtz i' in **Fig. 4.5b, c & d**). The aplites' wormy texture, which can be continuously traced in 2D across entire thin sections (e.g. **Fig. 4.5a**), indicates very high orders of connectivity in 3D, akin to descriptions of interconnected miarolitic cavities by Candela and Blevin (1995) and continuous chains of minerals which trace migration routes during melt extraction (Pistone et al., 2020). We interpret this wormy texture as marking an interconnected pathway for magmatic-hydrothermal fluids through inter-crystal spaces in a mush, the latter term referring to a continuous crystal framework (Cashman et al., 2017). It is already accepted that extensive porosity can exist within mechanically coherent frameworks of tabular silicate minerals with crystal fractions as high as ~0.75 (Holness et al., 2018). Further, it has been experimentally demonstrated that melt extraction from cooling mushes increases close to their solidus and operates efficiently at crystal fractions of 0.6-0.93 (Pistone et al., 2020).



(Ccl) in red. In the aplite, albite (green, Ab) is mostly associated with K-feldspar (light green, Kfs) as lamellae within and as individual grains. Quartz is paragenetically late in the aplite, containing few inclusions of albite and K-feldspar, being either intergranular (blocky) 'bright' CL 'Qtz i' ($T > 720^{\circ}\text{C}$), or forming branching interconnected networks comprising hydrothermal zoned 'Qtz ii' and increasingly 'darker' CL 'Qtz iii' ($T < 700^{\circ}\text{C}$). Copper-bearing minerals (Ccp and Ccl) appear mostly associated with 'Qtz iii'. Resorbed margins can be seen in all quartz generations. Ap = apatite, Ep = epidote; **c**, False colour SEM-CL image (symbols as in **b**) showing branching interconnected 'Qtz ii & iii' joining the miarolitic cavity. Non-quartz phases appear white or black. Fsp = feldspar; **d**, Total-IBA map of Ti concentrations in quartz (symbols as in **b**). All other phases appear white. Higher Ti 'Qtz i' (yellow-orange) is present as inclusions in feldspars. Lower Ti 'Qtz ii' (orange-purple) and 'iii' (purple-black) quartz occur as branching networks between all other phases.

An alternative explanation for the wormy quartz/feldspar fabric in the aplites is that it is a symplectic texture, i.e. an intergrowth of minerals that crystallised simultaneously (Allaby, 2013, p.573), formed, for example, as a result of rapid depressurization and crystallisation of the aplitic groundmass. For a number of reasons this is deemed unlikely: a) Paragenetic relations suggest albite crystallized earlier or coevally with K-feldspar precipitation, evidenced from the presence of albite inclusions in K-feldspar, but very few K-feldspar inclusions in albite; whereas quartz crystallized relatively late as there are very few quartz inclusions in the albite and K-feldspar. Rare examples of quartz inclusions within K-feldspar, which have the same CL response as discrete grains in the groundmass, are possibly due to 3-D interfingering of these phases rather than their presence as inclusions (**Fig. 4.5b; Sup. fig. 4.7-10**). From QEMSCAN[®] mineral associations data (defined as mineral/pixel adjacency, or the percentage one mineral touches another in a sample), albite is more associated in time with K-feldspar than quartz (see **Supplementary Data 4.2**); b) The aplite contains multiple generations of quartz, identifiable from CL images and from varying titanium concentrations, with lower temperature quartz ('Qtz ii & iii') forming a network around higher temperature quartz ('Qtz i'), albite and K-feldspar (**Fig. 4.5b, c & d; Sup. fig. 4.7**); c) The branching quartz generations ('Qtz ii & iii') appear to join the clearly zoned early hydrothermal quartz in the miarolitic cavity, having the same CL response, Ti concentrations and range of TitaniQ temperatures (from EPMA and Total-IBA analyses) (Quartz 'ii' and 'iii' in **Fig. 4.5b, c, d & Fig. 4.6; see Supplementary Data 4.1**), and they are therefore likely

to have crystallised contemporaneously and from the same fluid. This fluid was almost certainly aqueous rather than a silicate melt as the miarolitic cavity clearly represents a pocket of exsolved hydrothermal fluid (as per models for their formation; Candela, 1997) which crystallised a non-magmatic association of quartz and then quartz and chalcopyrite simultaneously (from the presence of chalcopyrite inclusions in late quartz overgrowths, **Fig. 4.5b**; **Sup. fig. 4.8-10**). From these mineral relations, we interpret the hypogene copper mineralisation (mostly chalcopyrite) to be associated with hydrothermal fluids that formed the relatively late branching, interconnected quartz ('Qtz *iii*' in **Fig. 4.5b, c, d** & **Fig. 4.6**). Thus, the wormy quartz texture records the pathways of mineralising hydrothermal fluids between earlier crystallised quartz and feldspars (and accessory phases). The flow of these fluids caused the partial dissolution of earlier quartz, seen as resorbed margins (**Fig. 4.5b, c** & **Fig. 4.6**), broadening the pathways and exaggerating the wormy texture. It should be noted that, because of this addition of hydrothermal quartz in the aplites, quartz proportions, relative to K-feldspar and plagioclase, will be over reported. This will affect the interpretation of petrological and geochemical data, mainly diluting the concentrations of other phases and components, not only for the aplites described herein but also in other rock types infiltrated by hydrothermal fluids.

Due to the presence of these inter-crystal (mush) pathways, mineralising hydrothermal fluids could have continuously migrated upwards through the aplite dykes from an underlying large-volume parent intrusive which had reached fluid saturation (i.e. the evolved internal regions of the Luhr Hill granite), until hydrothermal quartz sealed the inter-crystal spaces (represented by the branching 'Qtz *ii* & *iii*' generations (**Fig. 4.5** & **Fig. 4.6**). As such, the pervasive aplite dykes acted as conduits, we suggest the term "crystal mush dykes", for the upward transport and focusing of the large volumes of mineralising hydrothermal fluids necessary to create the porphyry deposits (**Fig. 4.7**).

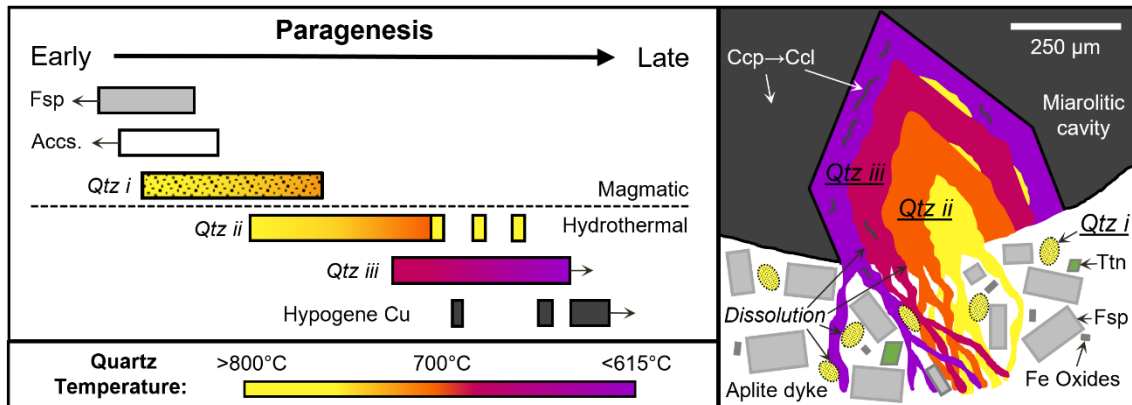


Fig. 4.6 Timing and temperature of crystallisation in aplite crystal mush dykes: Summary paragenetic diagram and sketch showing the spatial, temporal and temperature relations between magmatic phases in the crystal mush framework (comprising feldspars [Fsp], 'Qtz *i*' and accessory phases such as titanite [Ttn]), mineralised miarolitic cavities and the late wormy quartz ('Qtz *ii* & *iii*') network which marks palaeo-porosity. The hydrothermal fluids flowed through the mush's inter-crystal spaces to reach miarolitic cavities and to form veins. These fluids continued to flow after the miarolitic cavities formed, evidenced by the 'Qtz *ii* & *iii*' generations progressively filling the miarolitic cavities and partly resorbing earlier quartz generations. Repeated pulses of fluid flow are evidenced from the quartz within the miarolitic cavity, with 'Qtz *iii*' containing inclusions of slightly higher temperature 'Qtz *ii*'. Quartz generations are coloured as per their CL response and titanium concentration in **Fig. 4.5c & d**. Hypogene Cu mineralisation (chalcopyrite [Ccp], locally altered to secondary chrysocolla [Ccl]), is associated with the later quartz generations. Temperatures are approximate, based on ranges from our TitaniQ (method of Wark and Watson, 2006) thermometry.

We envisage the following sequence for the formation of the crystal mush dykes and their role in the transport and focusing of porphyry-forming fluids: 1) The incremental emplacement of the multi-pluton Yerington batholith into the shallow crust involving increasingly more evolved magmas (**Fig. 4.1**; Dilles, 1987); 2) Inward crystallization of the undercooled Luhr Hill granite and fracturing of the crystalline carapace, probably due to tectonic activity (Richards, 2018); (**Fig. 4.7**) 3) Upward emplacement of granitic magmas to form numerous generations of porphyry and aplite dykes (TitaniQ >~720°C); 4) Cessation of magma flow and crystallization within the aplite dykes during periods of rapid pressure changes and undercooling, to form UST pegmatites (Kirwin, 2005) (**Fig. 4.3**), and fluid exsolution to produce miarolitic cavities (TitaniQ ~775-700°C) (Candela 1997) (**Fig. 4.4 & Fig. 4.5**); 5) Penecontemporaneous formation of a crystal mush in the

aplite dykes, at the magmatic-hydrothermal transition, due to the last remaining vestiges of interstitial liquid consisting of aqueous fluid (**Fig. 4.6**); 6) Upward transport of pressurized fluids to the shallow porphyry environment through inter-crystal pathways in the mush dykes from extensive volumes of underlying fluid-saturated magmas (Luhr Hill granite) (**Fig. 4.6 & Fig. 4.7**); 7) Fluid pressure increase, due to upward fluid transport and accumulation, reducing effective stress (Terzaghi and Peck, 1948), to trigger brittle failure of the wall rocks and subsequent formation of A- and, in turn, B-type veins (nomenclature after Gustafson and Hunt, 1975), with an associated pressure drop. Once formed, the hydrothermal veins could have acted as the classic fluid pathways through the upper portions of the porphyry system; 8) Porphyry-style disseminated and vein-type mineralisation in a narrow zone to form porphyry deposits; 9) Sealing of porosity in the mush dyke due to cooling and/or depressurization of the system leading to progressive quartz precipitation within the inter-crystal mush network (represented by the progressive crystallisation of 'Qtz *ii*' to '*iii*', with TitaniQ down to <615°C) (**Fig. 4.5 & Fig. 4.6**). Whilst there may be other possible explanations for some aspects of this scheme, because of challenges related to determining the relative timing of different generations of dykes and veins, our textural observations can only suggest and not prove that the granite cupola or large porphyry dykes did not exsolve volatiles.

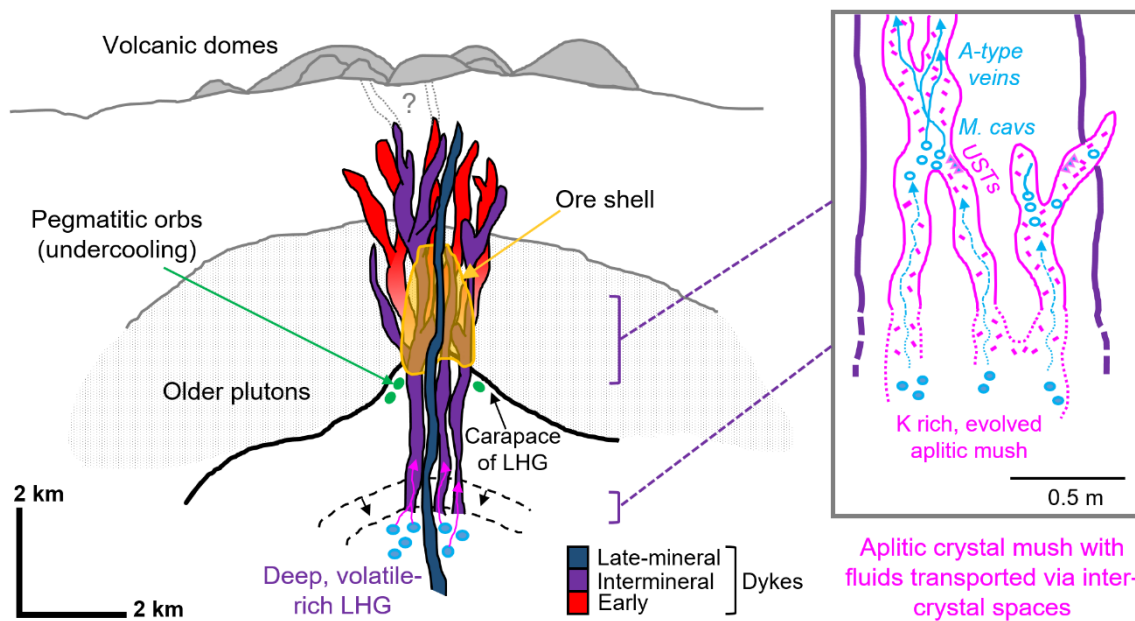


Fig. 4.7 Crystal mush dykes acting as fluid conduits: Schematic cross-section (modified after Sillitoe, 2010) through the Yerington porphyry system showing emplacement of a series of older plutons, the undercooled Luhr Hill granite (LHG), with a crystalline carapace, and multiple generations of porphyry and aplite dykes. Quartz unidirectional solidification textures (USTs) in the aplite dykes likely resulted from rapid pressure fluctuations (Kirwin, 2005) and fluid exsolution via ‘first-type boiling’ (Candela, 1989). Crystallisation of the aplitic melts led to formation of a magmatic crystal mush framework and, with fluid exsolution, miarolitic cavities (M. cavs). The aplitic crystal mush dykes continued to act as conduits for the upward flow of pressurized mineralising fluids via their inter-crystal spaces from evolved, deep portions of the Luhr Hill granite. The resultant increase in fluid pressure triggered hydro-fracturing to allow the formation of A- and, in turn, B-type veins (nomenclature after Gustafson and Hunt, 1975).

4.4 Conclusions

We conclude that, within the Yerington District, the roof zone of the Luhr Hill granite and its apophyses was a carapace rather than a mineralising cupola. It was the aplite dykes reaching water saturation and providing mush conduits for fluid flow from deeper within the magmatic system which provided the large volumes of hydrothermal fluid necessary for porphyry deposit formation, as magma and volatile transport were de-coupled. In determining this, we have presented some of the first petrographic field and microscale evidence for the occurrence of magmatic-hydrothermal mush, and highlighted the development and the potential importance of crystal mush dykes in the formation of porphyry copper deposits. Their development can explain how large volumes of magmatic-hydrothermal fluids can be extracted and focused from large regions of magmatic

systems. This is consistent with geochronological evidence from other porphyry systems that the hydrothermal systems are not linked to the lifetime of the porphyry intrusions (e.g. Li, 2017). This was difficult to reconcile when cupolas were thought the direct source of fluids (e.g. Candela, 1991; Shinohara et al., 1995; Cloos, 2001; Richards, 2005; Seedorff et al., 2005; Corbett, 2009; Sillitoe, 2010; Weis, 2012; Schöpa et al., 2017) mainly given the paucity of geophysical evidence for crystal-poor bodies of large volume in the shallow crust (e.g. Miller and Smith, 1999).

The new constraints our findings place on the temporal and spatial nature of fluid exsolution and migration will help in the further development of exploration and numerical models for porphyry style deposits. In addition to this, the recognition of hydrothermal quartz within an aplite dyke where magma and volatile transport are de-coupled, which would have been considered by most workers to be entirely magmatic in origin, may influence the interpretation of mineralogical and geochemical data for a wide variety of rocks formed at the magmatic-hydrothermal transition, e.g. Sn-W granitic systems (Lehmann, 2020). Our findings also have significance for the interpretation and forecasting of volcanic processes since dykes are important feeders of volcanic edifices. The possibility that a separate fluid phase may be transported through them, with increasing fluid pressure reducing effective stress (therefore rock strength and ductility) (Terzaghi and Peck, 1948), is likely to have major implications for degassing and in determining their stability and explosivity.

4.5 Methods

The fundamental first-order controls for this study were from field observations of cross-cutting relationships, disequilibrium phenomena and textures indicative of fluid exsolution from outcrop across the Yerington District and drill core from the Ann Mason and Yerington porphyry copper deposits. Microscale analysis was performed on select samples of interest.

4.5.1 Polished thin sections

Select samples of interest, due to specific significant textures or for petrographic purposes, were re-photographed, marked up, cut and prepared as polished slabs and polished thin sections (30 μm thickness) at Camborne School of Mines.

4.5.2 SEM-EDX-CL

Following optical microscopy, section surfaces were carbon coated to a thickness of 25 nm (determined by a peacock blue colour of a brass stub after carbon coating) using an Emitech K950 carbon coater. Scanning electron microscope (SEM) backscattered electron (BSE) and cathodoluminescence (CL) imaging alongside and qualitative energy dispersive X-ray (EDX) elemental mapping were carried out using an FEI Quanta 650F FEG-SEM equipped with a Gatan monochrome CL detector and 2x Bruker SDD EDS detectors (XFlash® series 6|30) at the University of Exeter's Environment and Sustainability Institute. The instrument was operated at an accelerating voltage of 20 kV. Elemental maps were obtained using a minimum of 4 scans and a dwell time of 32 µs, and processed using Bruker Esprit software version 1.9a. The CL images were collected from single scans with a 30 µs dwell time, a processing resolution of 3072 x 2048 pixels and 256 grey levels. CL brightness and contrast were optimized to reveal inhomogeneities in quartz, other phases therefore appear either white or black.

In the SEM-CL images, the different grey levels shown by quartz represent different luminescence colours. variability in CL colour and intensity of quartz can be attributed to defects in the lattice and/or trace elements in the crystal structure, (e.g. Wark and Watson, 2006; Müller et al., 2010; Kronz et al., 2012). Selected CL images were overlain over the area's respective EDX elemental for appreciation of different mineral phases' CL response. Some select CL images were retrospectively false-coloured using a 'fire' look-up table, using ImageJ software, to visually intensify differences in CL response from different quartz generations.

4.5.3 QEMSCAN®

The mineralogy of select carbon coated thin sections was determined using a QEMSCAN® 4300 automated mineralogical assessment system at Camborne School of Mines (Gottlieb et al., 2000, Goodall et al., 2005, Goodall and Scales 2007). The system is based on a Zeiss Evo 50 SEM with 4x Bruker SDD EDX detectors (XFlash®) controlled by iMeasure v. 4.2SR1 software for data acquisition and iDiscover v. 4.2SR1 and 4.3 for spectral interpretation and data

processing (Rollinson et al. 2011). The same 30 µm thick carbon coated polished thin sections were used as for the SEM studies. The QEMSCAN[®] was operated at an accelerating voltage of 25 kV and a beam current of 5 nA, with a working distance of around 22 mm, in high vacuum mode and with automatic beam calibration every 30 minutes. Fieldscan measurement mode was used to obtain a mineralogical map of nearly the whole polished section area (39 x 20 mm) at an analytical point resolution, or pixel spacing, of 10 microns and with 1000 X-ray counts per pixel. The data from each point of analysis was automatically compared with a Species Identification Protocol (SIP) database of mineral and non-crystalline phase spectra to identify the minerals present. The SIP used was modified from the LCU5 SIP provided with the QEMSCAN[®], which includes a range of oxide, sulphate, and silicate minerals. All mineral categories were checked by manually assessing elemental abundances, element ratios and BSE signal. A boundary phase post processor was applied to improve edge effects and to resolve rogue pixels. Data collection and processing followed in house QA/QC procedures. The data were output as mineralogical maps and in a mineral associations matrix (**Supplementary Data 4.2**).

QEMSCAN[®] 4300 analysis was performed on select carbon coated thin sections at Camborne School of Mines. Point spectra were collected with 1000 total X-ray counts at a 10 µm spacing and compared to a Species Identification Protocol (SIP) that discriminates minerals against a database (developed in house over time) on the basis of their characteristic X-ray and electron backscatter intensities. Data were validated through optical microscopy and prior manual SEM-EDX to confirm correct phase determination.

4.5.4 EPMA

Concentrations of Al, Ti and Fe in quartz in select polished thin sections were determined by Electron Probe Microanalysis (EPMA) using a JEOL JXA-8200 electron microprobe at Camborne School of Mines, University of Exeter. To mitigate any electron beam damage from prior SEM analysis, the thin sections used were re-polished and carbon coated to a thickness of 25 nm in an Emitech K950 carbon coater. The instrument was operated at an accelerating voltage of 20 kV, a beam current of 70 nA and a spot size of 15 µm. This relatively large spot size was used due to the sensitivity of quartz at high current under a narrow

beam (Kronz et al., 2012). SiO₂ was assumed to be 100%. Corundum (Geo MkII), rutile and hematite (Astimex) calibration standards were used for Al, Ti and Fe, respectively. For calibration at low concentrations or as “blank”-control, some studies use a synthetic doped or pure SiO₂-glass. This was deemed inappropriate as their behaviour during electron irradiation is very different to that of quartz (e.g. Kronz et al., 2012). Al was measured over two TAP crystals simultaneously. Due to crystal line up, Ti and Fe were only measured with one spectrometer each (on PET and LIF crystals respectively). Peak and background measurement count times were both 200 s. Limits of detection (LOD) were (3σ) 45 ppm for Al, 42 ppm for Ti and 42 ppm for Fe. To estimate precision, we undertook 7 repeat analyses of a single homogenous, magmatic, un-zoned (from SEM-CL imaging) quartz crystal from within a polished section of Luhr Hill granite (sample YM33b in **Supplementary Data 4.1**). The mean; ranging from; half of the range; 1 S.D. of these were: Al (78; 51-101; 25; 20 ppm); Ti (81; 70-91; 10; 8 ppm); Fe (39; 28-52; 12; 12 ppm). From these we used ± 2 S.D. to determine our analytical uncertainties: Al ± 40 ppm; Ti ± 16 ppm; Fe ± 24 ppm. For independent validation, locations of EPMA spot analysis were re-analysed by Total-IBA spot analysis (e.g. Fig. 4.5) – results from the two independent methods were within uncertainty.

4.5.5 Total-IBA

Total Ion Beam Analysis (Total-IBA), to determine trace elements in quartz from a selected thin section (AM13, sample details in **Supplementary Data 4.1**), was performed using the microbeam line on the 2MV Tandatron accelerator (HVEE Corporation, NL) installed at the University of Surrey Ion Beam Centre. The same thin section as for the SEM and EPMA studies was used, but prior to analysis was re-polished and carbon coated to a thickness of 25 nm using an Emitech K950 carbon coater. The experiments reported here were carried out using a 2.5 MeV proton beam, focused to a diameter of 2 μm with a beam current between 700-1000 pA, measured in a spectroscopically pure graphite Faraday cup mounted behind the samples. The X-rays were detected using a lithium drifted silicon detector with an active area of 80 mm² mounted at a central angle of 135° to the beam direction in the horizontal plane. The X-ray detector was fitted with a 130 μm beryllium foil absorber and a 30 or 75 μm (experiment dependent) Kapton foil. The beryllium foil is used routinely to avoid spectral degradation due to

backscattered particles entering the detector, and the additional Kapton foil was used to attenuate the spurious escape peak from the intense K α line of potassium in the K-feldspar regions of the sample which interferes with the Si K α line. Elastically backscattered protons (EBS) were detected using a PIPS charged particle detector with an active area of 300 mm² mounted 52 mm from the sample at a central angle of 128° to the beam direction in the vertical plane. Data were acquired using the OMDAQ-3 software package (Oxford Microbeams Ltd., UK, www.microbeams.co.uk). 6 adjacent 500 x 500 μ m areas were qualitatively mapped until 3400 nC of charge were reached, and the maps subsequently stitched together. Quantitative analyses of selected points were acquired until 100 nC of charge were reached.

Particle-induced X-ray emission (PIXE) spectra were quantified using the OMDAQ-3 interface to GUPIX (Campbell et al., 2010). GUPIX applies corrections based on the composition of the local sample matrix obtained by processing the associated EBS spectrum (Grime, 1996). This employs an algorithm implemented in OMDAQ-3 which uses non-Rutherford proton elastic scattering cross sections obtained from the IBANDL database (Abriola et al., 2011) maintained by the International Atomic Energy Agency. The only instrumental calibration routinely required is to determine variation of X-ray detector efficiency with energy. This is achieved by analysing a lead-glass standard reference material (BCR-126A, European Commission, Joint Research Centre (JRC), Geel, Belgium), and adjusting the parameters in the model of the efficiency to optimize the accuracy of determination for all detected elements (Gomez-Morilla et al., 2006). For these measurements the relative standard deviation of measured concentration from the certified values of major elements in the standard glass was 5%. The thick Kapton filter used to suppress the K K α X-ray lines introduces a significant uncertainty into the Si determination and so concentrations were normalised by scaling the PIXE concentration for Si to the concentrations determined by EBS. Results, limits of detection and analytical uncertainty are presented in **Supplementary Data 4.1**.

To generate a Ti-in-quartz map, all non-quartz phases (i.e. anything containing Al, Ca, Cu, Fe, or K as a major element) were filtered out (rendered white) using ImageJ software. The resulting Ti-in-quartz map was then false coloured using a

'fire' look-up table for direct visual comparison with similarly false coloured SEM-CL images.

For independent validation of the Total-IBA data, locations of Total-IBA spot analysis were twinned to spots analysed by EPMA spot analysis (e.g. Fig. 4.5) – results from the two independent methods were within uncertainty.

4.5.6 Ti-in-quartz geothermometry

The TitaniQ geothermometer of Wark and Watson (2006) (Equation 1) was used to assess the crystallisation temperatures of different generations of quartz. Ti concentrations were determined by EPMA and Total-IBA spot analyses (see above). TitaniQ was shown to be effective for crystallisation temperatures of between 600°C and 1,000°C, at 10 kbar (Wark and Watson, 2006). Whether and how TitaniQ can be applied at other pressures has been strongly debated (e.g. Thomas et al., 2010; Huang and Audétat, 2012; Wilson et al., 2012; Acosta et al., 2020). Wark and Watson (2006) reported that there was little temperature effect on Si-Ti interdiffusion, i.e. on temperatures derived from TitaniQ, between experiments carried out at 1 atm (Cherniak et al., 2007; and more recently Jollands et al., 2020) and those predicted at 10 kbar. In addition to this, there is general agreement that calculated temperatures vary little across the limited 1-3 kbar pressure range (e.g. Seedorff et al., 2005) typical of the porphyry environment. As such, the TitaniQ method of Wark and Watson (2006) was deemed appropriate for use in the current study without applying a pressure correction.

The activity of TiO_2 (a_{TiO_2}) was assigned a value of 0.7 based on estimates from thermodynamic modelling of felsic magmas (Ghiorso and Gualda, 2013), the presence of titanite and previous work on other felsic magmatic systems (e.g. Claiborne et al., 2010; McDowell et al., 2014) as well as specific studies on the Yerington District (Dilles et al., 2015). We acknowledge that the a_{TiO_2} may have changed during the crystallisation history and evolution of the magmatic system, but assume that this was negligible given that the same Ti-bearing minerals (notably titanite and trace rutile, see **Supplementary Data 4.2**) are present in the compositionally similar granite and aplite dykes which are the focus of the current study. At ~700 °C, an increase in a_{TiO_2} of 0.1 would decrease the calculated

temperature by only 13°C, and a decrease in $a\text{TiO}_2$ of 0.1 would increase the temperature by only 17°C. To estimate precision, we calculated TitaniQ for 7 repeat EPMA analyses of a single homogenous, magmatic, un-zoned quartz phase within the Luhr Hill granite (sample YM33b in **Supplementary Data 4.1**). These give a mean of 765°C, ranging from 748 to 779°C, with half the range being 16°C and 1 S.D. of 13°C. For Total-IBA, analytical uncertainty for individual analyses are typically less than those for EPMA (**Supplementary Data 4.1**) and therefore yield TitaniQ calculation uncertainties less than those for EPMA analyses described above. We therefore use 2 S.D. of the repeated EPMA analyses to determine our analytical uncertainty of $\pm 26^\circ\text{C}$.

$$T_{\text{Ti-qtz}} (\text{°C}) = \frac{-3765}{\log\left(\frac{X_{\text{Ti}}^{\text{qtz}}}{a\text{TiO}_2}\right) - 5.69} - 273 \quad (1)$$

Where $X_{\text{Ti}}^{\text{qtz}}$ is the Ti concentration in quartz and $a\text{TiO}_2$ is the activity of TiO_2 in the system.

To validate the geothermometry results, Luhr Hill granite quartz crystallisation temperatures calculated by TitaniQ were compared to Luhr Hill granite zircon crystallisation temperatures, calculated using the Ti-in-zircon method of Ferry and Watson (2007), using zircon LA-ICP-MS data (see **section 5.12.5**) and an $a\text{TiO}_2$ of 0.7. There is agreement in the crystallisation temperatures calculated using the two mineralogically independent geothermometers.

4.6 Declaration of co-authorship

L.C.C., B.J.W and S.T. performed proof of concept and wrote the manuscript. L.C.C. and B.J.W. performed field studies. L.C.C. carried out petrographic and textural studies, SEM-EDX, SEM-CL and EPMA analyses at Camborne School of Mines. G.K.R. performed QEMSCAN® analyses at Camborne School of Mines and contributed to the manuscript. C.C. and G.W.G. performed Total-IBA analyses at the University of Surrey's Ion Beam Centre and contributed to the manuscript. L.C.C. prepared the figures.

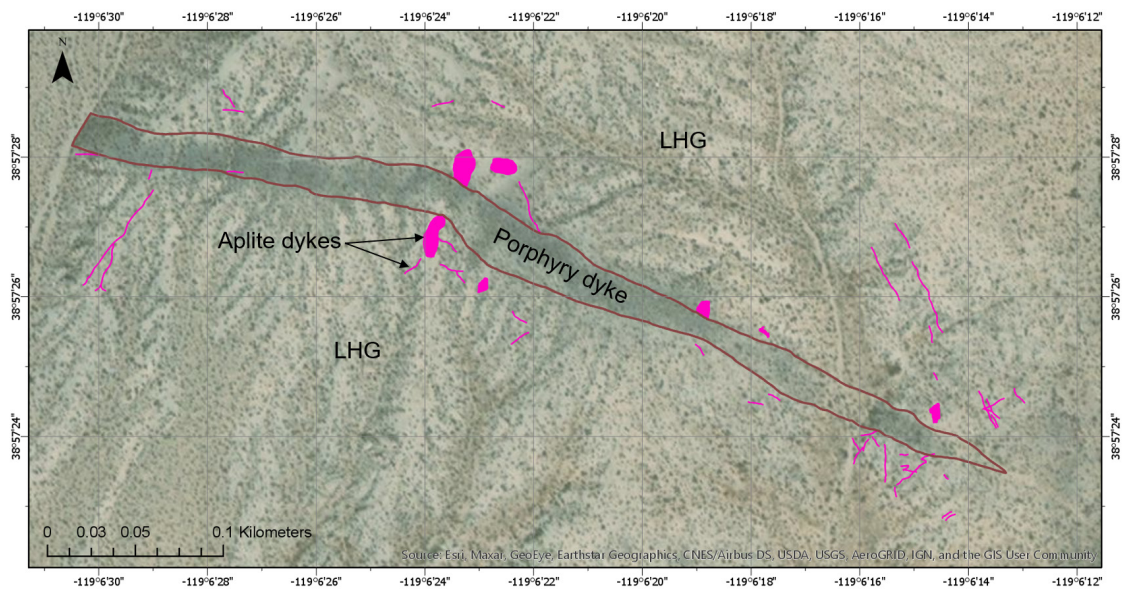
4.7 Supplementary figures



Sup. fig. 4.1 Massive silica body in the Luhr Hill granite cupola: Field photograph of a massive silica body (nomenclature after Kirwin, 2005) in the exposed cupola of the Luhr Hill granite, palaeo-vertically beneath the Ann Mason porphyry deposit (Dilles, 1987). The body contains no hydrothermal banding or recrystallisation textures and is not mineralised. Hammer, iPad and label for scale. **Inset;** Miarolitic cavities within the silica body. These contain only quartz and constitute an insignificant volume of the body. Label for scale.



Sup. fig. 4.2 Dykes in granite cupola: Field photograph from the cupola of the Luhr Hill granite, palaeo-vertically beneath the Ann Mason porphyry deposit (Dilles, 1987), showing the granite cut by a typical granitic porphyry dyke and a number of narrow aplite dykes. Some of these aplites host mineralised miarolitic cavities outside the field of view. Although numerous and pervasive, the majority of these aplite dykes are too narrow to feature on a large-scale map.



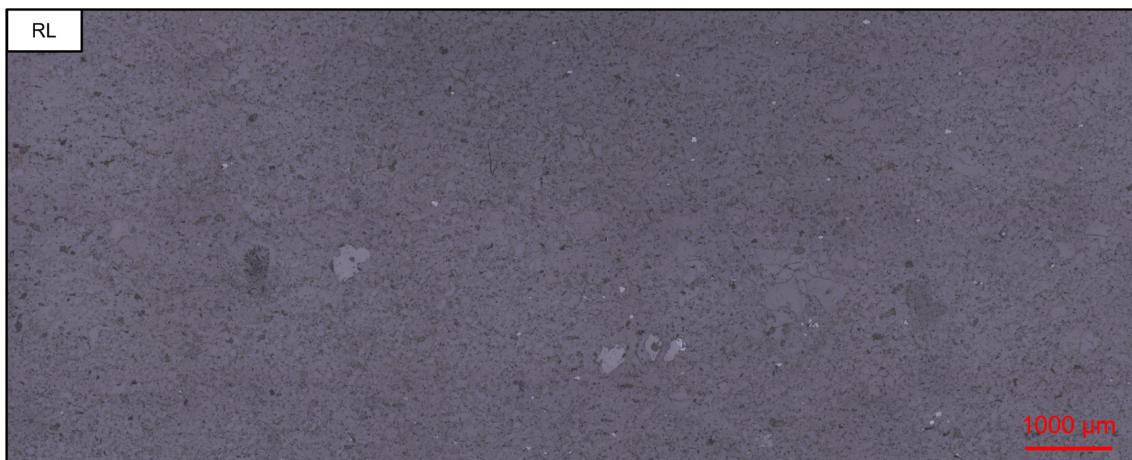
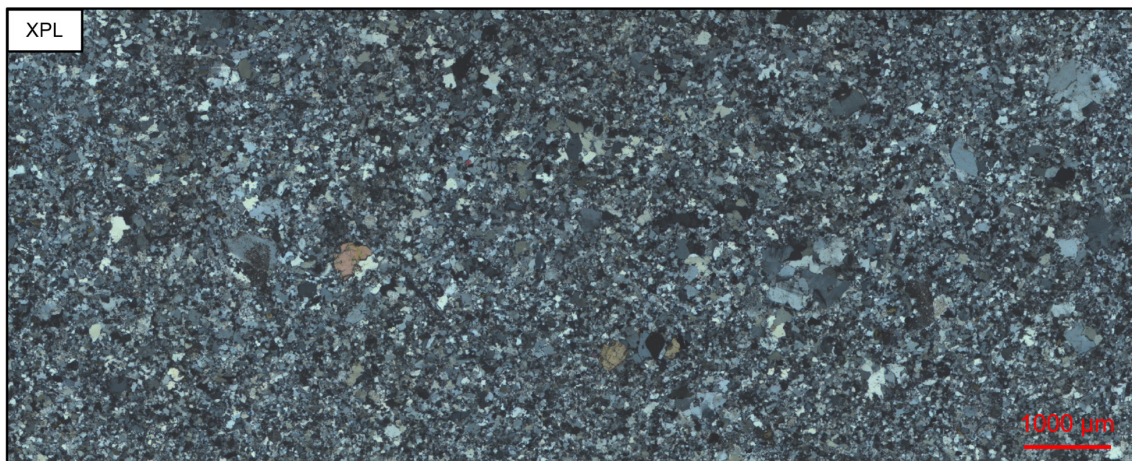
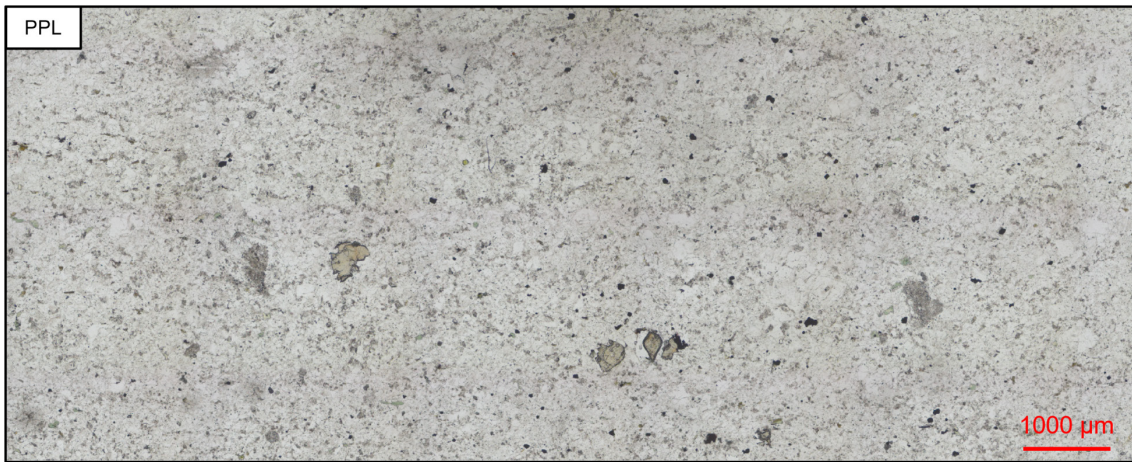
Sup. fig. 4.3 Spatial distribution of aplite dykes: Simplified small scale geological map, overlying a satellite image, from the eastern most portion of Luhr Hill (reconstructed to represent a deep portion (7-8 km palaeo-depth) of the Luhr Hill granite pluton; Dilles, 1987), showing the distribution of exposed aplite dykes (pink) around a porphyry dyke (brown) (annotated on **Fig. 4.1** as 'PD') which intrudes the Luhr Hill granite (LHG). Aplite dykes are not extrapolated between exposures. Although too narrow to appear on a larger scale map, aplite dykes are numerous, pervasive and spatially associated with the porphyry dykes. WGS84.



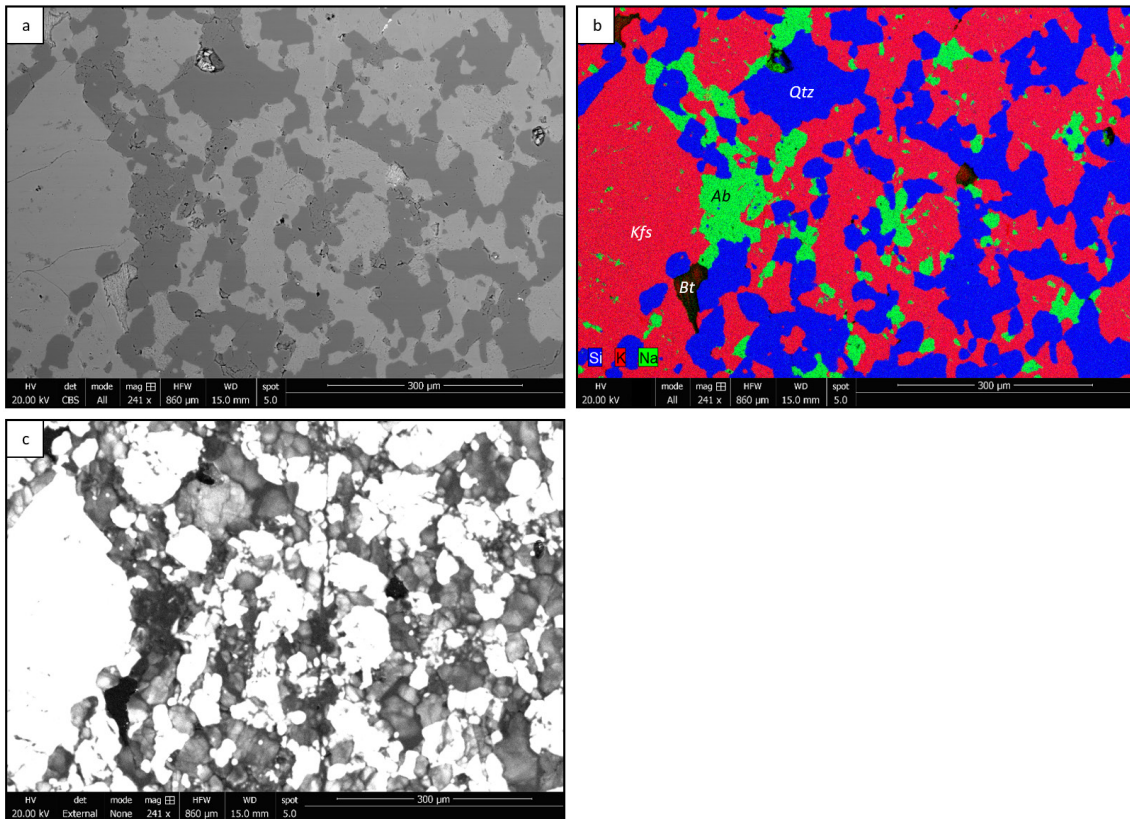
Sup. fig. 4.4 Aplite dyke temporal relations: Field photograph from the exposed cupola of the Luhr Hill granite, palaeo-vertically beneath the Ann Mason porphyry deposit (Dilles, 1987), showing lobate contacts (white dotted line) and evidence for mingling of co-eval magmas, between an aplite dyke and large porphyry dyke. Secondary copper staining prevalent. Marker pen for scale.



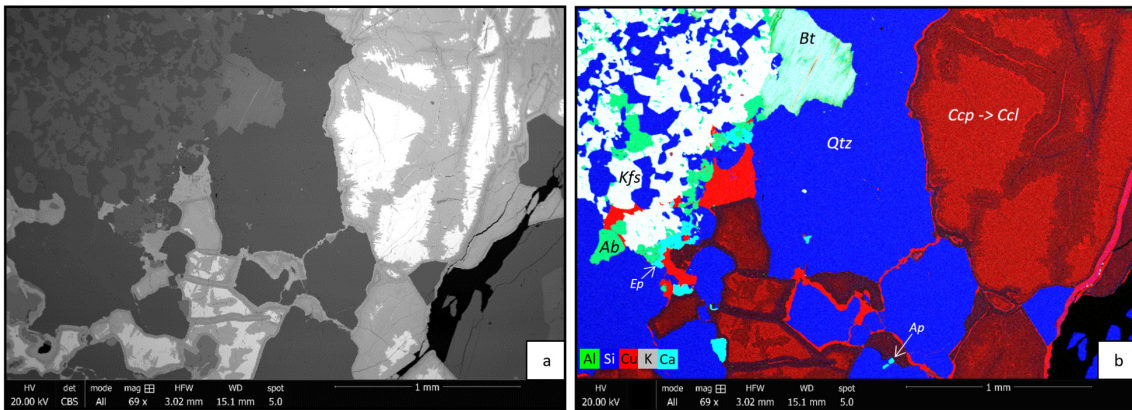
Sup. fig. 4.5 B-type veins in aplite dyke: Field photograph of a mineralised aplite dyke cutting the exposed cupola of the Luhr Hill granite (palaeo-vertically beneath the Ann Mason porphyry deposit; Dilles, 1987), bearing chalcopyrite mineralised B-type quartz veins (nomenclature after Gustafson and Hunt, 1975). Secondary copper staining prevalent.



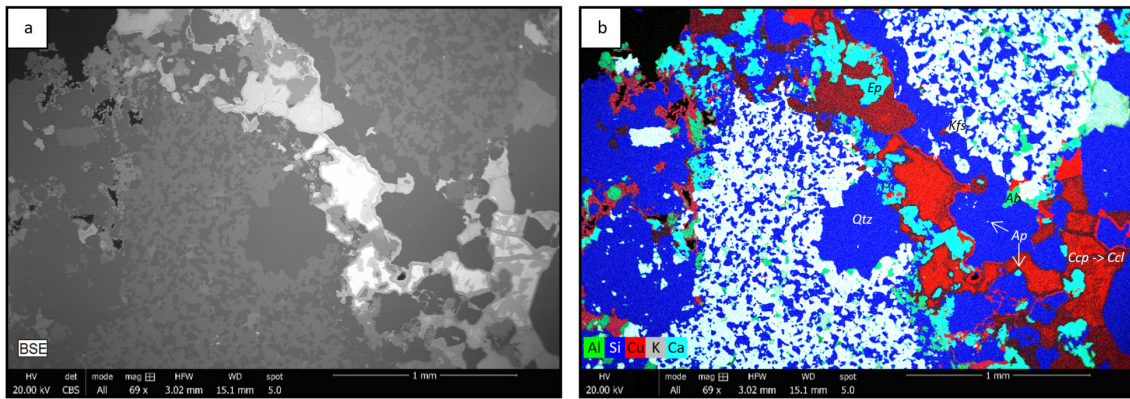
Sup. fig. 4.6 Aplite dyke groundmass. Photomicrographs, in plane polarised (PPL), cross polarised (XPL) and reflected light (RL), of an aplite dyke's groundmass (the same aplite as seen in **Fig. 4.5**). The groundmass shows typical aphanitic texture, i.e. not micro-graphic or similar. Small beige, high relief crystals in PPL are titanite.



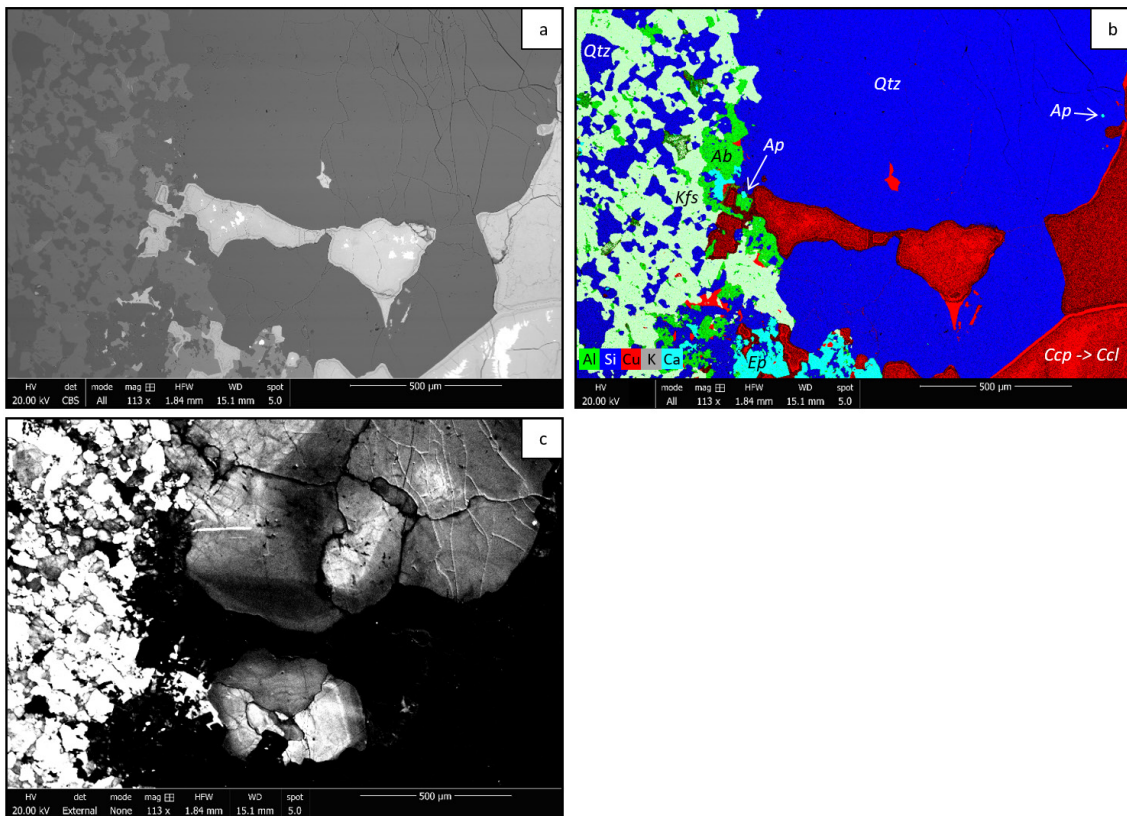
Sup. fig. 4.7 Wormy groundmass quartz in an aplite dyke: **a**, SEM-BSE image of the groundmass of the aplite dyke seen in **Fig. 4.5**; **b**, SEM-EDX elemental map of the same field of view. Albite (green, Ab) is seen to be mostly associated with K-feldspar (red, Kfs), as lamellae within K-feldspar and as individual grains. Quartz (blue, Qtz) is seen to be distinct, containing few inclusions of albite and K-feldspar, and wormy (containing several generations). There are very few quartz inclusions in the albite or K-feldspar, rare occurrences likely to be due to the effect of 2D sectioning of a 3D assemblage of interfingered quartz and feldspars, rather than being true inclusions (i.e. reflecting timing relations). These relations are interpreted as indicating crystallisation of albite, simultaneously and closely followed by K-feldspar, and then later precipitation of quartz. Bt = biotite; **c**, SEM-CL image of the same field of view. Brightness and contrast have been set to best image the quartz phase, so most other phases appear white or black. Different generations within the wormy quartz can be identified from their CL response, with discrete blocky 'bright' CL grains (early quartz) surrounded by a network of narrow veinlets of 'darker' CL (late) quartz.



Sup. fig. 4.8 Wormy groundmass quartz in an aplite dyke adjacent to a mineralised miarolitic cavity: **a**, SEM-BSE image of the aplite dyke (top left) and mineralised miarolitic cavity seen in **Fig. 4.5**; **b**, SEM-EDX elemental map of the same field of view. In the aplite, albite (green, Ab) is seen to be mostly associated with K-feldspar (white, Kfs), as lamellae within K-feldspar and as individual grains. Quartz (blue, Qtz) is seen to be wormy, and distinct from feldspars and biotite (very light green, with cleavage, Bt), with very few inclusions of either. Apatite (bright cyan, Ap) is present as inclusions. Epidote (light cyan, Ep) is late. Copper-bearing phases (mostly chalcopyrite, Ccp, and secondary chrysocolla, Ccl) is also present in the groundmass of the aplite.



Sup. fig. 4.9 Wormy groundmass quartz in an aplite dyke alongside an early quartz vein: a, SEM-BSE image of the aplite dyke (centre of field of view) and root of an early A-type quartz vein, which connects to the miarolitic cavity outside the field of view, seen in **Fig. 4.5**; **b,** SEM-EDX elemental map of the same field of view. In the aplite, albite (green, Ab) is seen to be mostly associated with K-feldspar (white to very light green, Kfs), as lamellae within K-feldspar and as individual grains. Quartz (blue, Qtz) is seen to be wormy and distinct from both feldspars, with very few inclusions of either. Apatite (bright cyan, Ap) is present as inclusions. Epidote (lighter cyan, cross-reference to BSE in **a** to distinguish from apatite, Ep) is late. Copper-bearing phases (red, mostly chalcopyrite, Ccp, and secondary chrysocolla, Ccl) are also present in the aplitic groundmass.



Sup. fig. 4.10 Multiple quartz generations in the aplite dyke and mineralised miarolitic cavity: a, SEM-BSE image of the aplite dyke (left of field of view) and mineralised miarolitic cavity. Same field of view as seen in **Fig. 4.5b**; b, SEM-EDX elemental map of the same field of view. In the aplite, albite (green, Ab) is seen to be mostly associated with K-feldspar (very light green, Kfs), as lamellae within K-feldspar and as individual grains. Quartz (blue, Qtz) is seen to be wormy and distinct from both feldspars, with very few inclusions of either. Apatite (bright cyan, Ap) is present as inclusions. Epidote (light cyan, Ep) is late. Copper-bearing phases (red, mostly chalcopyrite, Ccp, and secondary chrysocolla, Ccl) are also present in the aplitic groundmass; c, SEM-CL image of the same field of view. Multiple generations of quartz can be identified. Both bright, zoned, CL quartz and dark CL quartz can be seen in both the aplite dyke and the miarolitic cavity. Copper mineralisation appears mostly associated with the darker CL quartz generation.

4.8 Supplementary data

Supplementary Data 4.1: EPMA and Total-IBA analyses

Supplementary Data 4.2: QEMSCAN® data

Supplementary Data files are available at <https://doi.org/10.5285/5a4bc758-ac88-4715-a665-81f69108f854>

5 A rapid change in magma plumbing taps porphyry copper deposit-forming magmas

This chapter is a slightly modified version of Carter, L. C., Tapster, S. R., Williamson, B. J., Buret, Y., Selby, D., Rollinson, G. K., Millar, I. and Parvaz, D., 2022. 'A rapid change in magma plumbing taps porphyry copper deposit-forming magmas', published in *Scientific Reports* (<https://doi.org/10.1038/s41598-022-20158-y>).

Supplementary figures and links to electronic supplementary data can be found at the end of the chapter.

5.1 Abstract

Porphyry-type deposits are a vital source of green technology metals such as copper and molybdenum. They typically form in subduction-related settings from large, long-lived magmatic systems. The most widely accepted model for their formation requires that mantle-derived magmas undergo an increase in volatiles and ore-forming constituents in mid- to lower crustal reservoirs over millions of years, however, this is mostly based on observations from shallow, sporadically exposed parts of porphyry systems. To examine this paradigm, we have evaluated the timeframe and geochemical signatures of magmatism in a ~ 8 km palaeodepth cross-section through plutonic and volcanic rocks of the classic Yerington magmatic system, Nevada. We show that the magmas in the upper parts of the system (< 8 km) underwent a major and rapid change in chemistry over a period of < 200 kyrs that is coincident with the initiation of ore formation. We attribute this change to a shift from extraction of quartz monzodiorite and quartz monzonite magmas evolving in mid-crustal reservoirs, and that had relatively poor ore-forming potential, to extraction of volatile-rich granitic magmas from greater (~ 30 km) depths. As the granites crystallised, late stage melts were intruded through the carapace as aplite dykes which contain traceable expressions of the porphyry deposit-forming fluids. The rapid nature of the shift in ore-forming potential narrows the temporal-geochemical footprint of magmas associated with porphyry mineralisation and provides new constraints for exploration models.

5.2 Introduction

The transition to new and green technologies is increasing the need for metals (Jowitt et al., 2020; Herrington, 2021) such as copper for which demand is forecast to increase by 140–350% from 2010 to 2050 (Elshkaki et al., 2016; Watari et al., 2021). Porphyry-type deposits provide more than 70% of global copper, around 95% of molybdenum and important amounts of gold (20%) and other metals (Sillitoe, 2010). Most form from hydrothermal fluids associated with large and long-lived calc-alkaline to slightly alkaline, water-rich and relatively oxidising trans-crustal magmatic systems, mainly in subduction-related settings (e.g. Richards, 2005; Sillitoe, 2010; Wilkinson, 2013; Richards, 2015; Chiaradia and Caricchi, 2017). Whilst such systems are arguably rather common, porphyry-, and particularly large porphyry-type deposits are extremely rare and increasingly difficult to find (Wilkinson, 2013). Their formation may require a series of specific conditions and events during the evolution of magmatic-hydrothermal systems.

In the drive to discover new ore deposits, there have been many recent attempts to develop whole-rock and mineral geochemical indicators to assess whether certain magmatic systems may be significantly mineralised, or 'fertile' (Cooke et al., 2017). Their main advantage compared with conventional exploration techniques is that they are relatively cheap and are of low environmental impact. Most indicators reflect the hydrous nature of the magmas from which porphyry-type deposits form (e.g. Rohrlach and Loucks, 2005; Richards, 2011; Chiaradia et al., 2012; 2015; Richards et al., 2012; Wilkinson, 2013; Loucks, 2014; Lu et al., 2016; Williamson et al., 2016; Nathwani et al., 2020; Lee et al., 2021).

The current paradigm is that the hydrous magmas that form porphyry-deposits result from a long (multimillion year), arc-scale, subduction-driven 'ramp-up' in volatiles and ore-forming constituents in mid- to lower crustal magmatic reservoirs (Ballard et al., 2002; Rohrlach and Loucks, 2005; Chiaradia et al., 2009; Loucks, 2014; Rezeau et al., 2016; Chiaradia and Caricchi, 2017; Nathwani et al., 2021). Before emplacement into the upper crust, the magmatic system develops its ore-forming geochemical signatures over protracted time scales, in excess of ~ 5 Myrs, due to cyclical fractionation and re-charge of deep reservoirs by mafic magmas. The subduction-related tectonic regime has been suggested to

progressively deepen the melt evolution zone and/or slow the upwards migration of magmas through the crust (Richards, 2003; Chiaradia et al., 2009; Chiaradia and Caricchi, 2017; Lee and Tang, 2020). Alternatively, the ore-forming potential of magmas, and associated geochemical signatures, may increase during evolution within an upper crustal staging ground (e.g. Dilles, 1987; Seedorff et al., 2005; Sillitoe, 2010; Dilles et al., 2015). Distinguishing the nature of magmatic evolution in the lead up to porphyry copper ore formation is problematic because of the paucity of vertically extensive exposure over the crustal windows of porphyry ore-forming systems (Seedorff et al., 2008); this has resulted in a fragmented understanding of the magmatic timescales associated with porphyry-deposit formation.

To address this, the Yerington magmatic system, western Nevada, was studied as it has provided constraints for many of the most commonly used porphyry system models, mostly due to its unique ~ 8 km deep profile, from volcanic to plutonic environments, through at least four porphyry copper deposits (**Fig. 5.1 & Fig. 5.2**) (e.g. Dilles, 1987; Seedorff et al., 2005; Richards, 2005; Seedorff et al., 2008; Sillitoe, 2010; Weis et al., 2012; Schöpa et al., 2017; Carter et al., 2021, Chapter 4). Here we reconstruct the Yerington magmatic system across the deep plutonic to volcanic environment, encompassing deep-seated melt evolution zones, through to the development and focusing of magmatic-hydrothermal fluids to form porphyry-type deposits. We present a new 4-D model based on the timescales and drivers for the evolution of the magmatic system's ore-forming potential and associated geochemical signatures.

5.3 The construction of a porphyry-forming magmatic system

The middle Jurassic composite Yerington batholith (Proffett and Dilles, 1984; Dilles, 1987; Dilles and Wright, 1988; Banik et al., 2017) lies within a volcanic-arc terrane, in the early Mesozoic marine province (Speed, 1978), which formed due to subduction tectonics to the west (Dilles and Wright, 1988). The batholith was emplaced into Triassic to Jurassic intermediate composition volcanics, volcanoclastic and argillaceous sedimentary rocks, and basal exposures of the likely semi co-eval Jurassic Artesia Lake Volcanics, which are unconformably overlain by the Jurassic Fulstone Spring Volcanics (subaerial quartz-latic to dioritic lavas, domes, ignimbrites and volcanoclastics) (Dilles, 1987; Dilles and

Wright, 1988; Proffett, 2007) (**Fig. 5.1 & Fig. 5.2**). Late Cenozoic extensional faulting and associated fault block rotation in the Basin and Range has exposed a < 1 to ~ 8 km palaeodepth cross-section through the Yerington batholith (Proffett, 1977; Proffett and Dilles, 1984; Dilles, 1987) (**Fig. 5.1 & Fig. 5.2**).

There are three main plutonic phases, which, listed in order of increasing emplacement depth, are: (1) the McLeod Hill quartz monzodiorite (McLeod QMD); (2) Bear quartz monzonite (Bear QM); and (3) Luhr Hill granite (LHG) (Dilles, 1987). These are cross-cut by swarms of granite-composition porphyry and aplite dykes (Dilles, 1987; Carter et al., 2021, Chapter 4). Units of the Fulstone Volcanics are thought to have been cogenetic with granite porphyry dykes rooted in the LHG (Proffett, 2007; Proffett, 2009), or, alternatively, may have been cogenetic with the nearby younger Shamrock batholith and post-date porphyry mineralisation (Dilles and Wright, 1988). The dyke swarms are spatially and temporally associated with the batholith's four known porphyry copper deposits: Ann Mason; Yerington; MacArthur and Bear (**Fig. 5.1 & Fig. 5.2**) (e.g. Proffett, 1979; Dilles, 1987; Dilles and Proffett, 1995). Combined, these host a resource in excess of 9 Mt of contained Cu (Dilles and Proffett, 1995; Bryan, 2014; Hudbay Minerals Inc., 2021; Welhener et al., 2022).

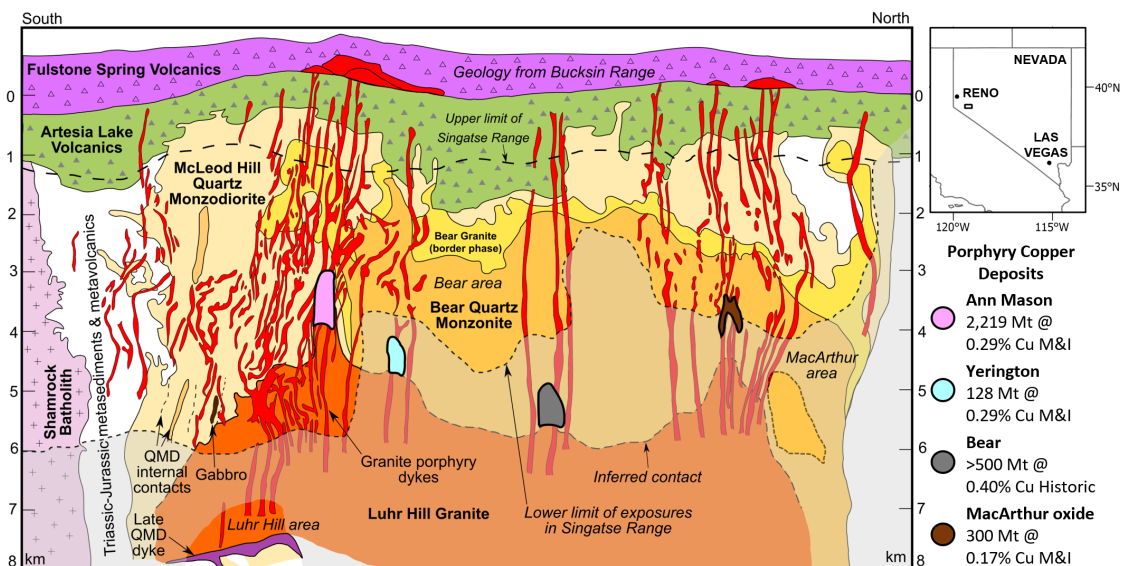


Fig. 5.1 Pre-tilt cross section through the Yerington District, Nevada: Reconstructed to a palaeo-depth of 8 km, showing the intrusive units of the Jurassic Yerington batholith, the various generations of porphyry dyke swarms which were emplaced through apophyses of the Luhr Hill granite, the district's four known porphyry copper deposits and overlying volcanics (Yerington and Bear deposits projected onto section). Section from Dilles (1984) and Schöpa et al. (2017), with

resource estimates from Bryan (2014), Dilles and Proffett (1995), Hudbay Minerals Inc. (2021) and Welhener et al. (2022). QMD = quartz monzodiorite, M&I = measured & indicated, historic = non-compliant historic estimate.

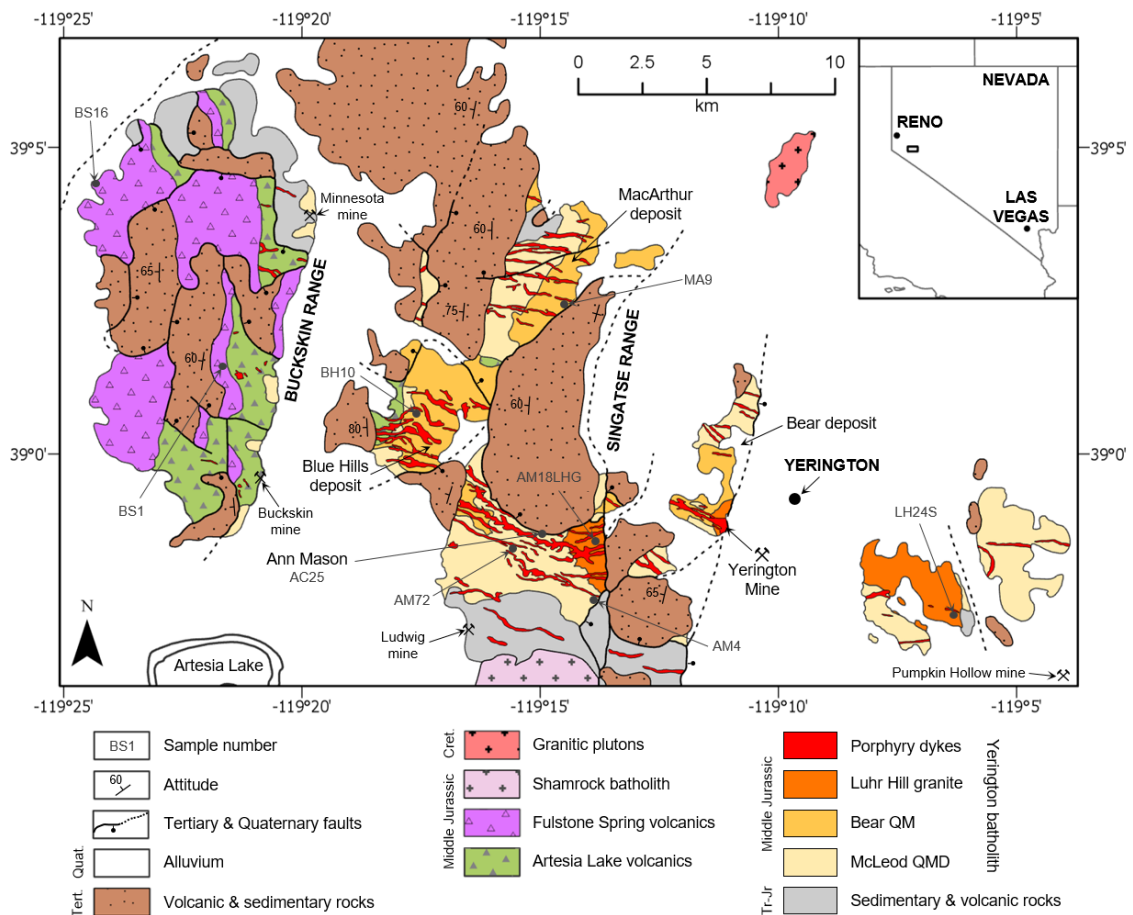


Fig. 5.2 Simplified geological map of the Yerington District, Nevada: annotated with known major mineral deposits and localities sampled for zircon U-Pb CA-ID-TIMS geochronology (Fig. 5.4). Full sample list in **Supplementary Data 5.1**. Geology from Hudson & Oriol (1979), Proffett & Dilles (1984, and references therein) and Dilles & Wright (1988). QM = quartz monzonite, QMD = quartz monzodiorite. WGS 1984.

5.4 Temporal constraints from field relationships

Field-based observations place constraints on the relative timing of magmatism, alteration and mineralisation. The LHG is the youngest of the three main plutons having been emplaced into the McLeod QMD and Bear QM (Dilles, 1987). Contacts between the LHG and previously emplaced plutons are sharp (Sup. fig. 5.1), with no chilled margins or evidence of interaction with precursor granitoids. No metasomatic effects are present at the contacts beyond the later, pervasive, mostly sodic-calcic and propylitic porphyry-related alteration (Carten, 1986; Dilles

et al., 2000). In deeper portions of the LHG (~ 7.5 km palaeo-depth, based on structural reconstructions; Dilles, 1987), banding is observed locally, defined by grain size variations (**Sup. fig. 5.2**).

The onset of porphyry mineralisation is constrained by cross-cutting relationships; it is spatially and temporally associated with multiple generations of variably mineralised granite-composition porphyry and aplite dykes that clearly cross-cut the upper (**Fig. 5.3**; **Sup. fig. 5.3**) as well as lower parts of the LHG, and appear to have been focused through apophyses of the LHG (Proffett, 1979; Dilles and Proffett, 1995; Dilles et al., 2000; Proffett, 2007; Proffett, 2009; Runyon et al., 2017; Carter et al., 2021, Chapter 4). The dykes generally have sharp contacts with the LHG, with some showing chilled margins and others lobate contacts (**Fig. 5.3a**). It was previously suggested that both the porphyry and aplite dykes emanated from cupolas and upper zones (~ 3 to 6 km depth) of the LHG (Dilles, 1987), however we could not trace either to their source and therefore suggest that they were likely to have been intruded from below the deepest levels exposed in the LHG (> ~ 7 km). Different generations of aplite dykes either cross-cut and/or mingle with the porphyry dykes (**Fig. 5.3b–d**), which indicates multiple intrusion events, with some generations emplaced penecontemporaneously with porphyry dykes and others later. In the palaeo-vertically deepest (> 6 km) exposures of the LHG (or the 'root zone' for the porphyry deposits; Seedorff et al., 2008), the majority of aplite dykes pre-date the spatially associated late-stage coarse muscovite veins and alteration (Runyon et al., 2017; 2019), as well as Na-Ca alteration. However, in deep exposures of the LHG, certain aplite dykes, which appear to post-date the muscovite and Na-Ca alteration, are thought to have been emplaced from a larger, longer-lived, deeper source (Runyon et al., 2017); as these post-date the hydrothermal alteration they are not considered further in this paper.

Despite the close temporal relationship between the porphyry and aplite dykes, they have very different textures. The porphyry dykes show no direct textural evidence for fluid exsolution (e.g. miarolitic cavities; Candela, 1997), and are only seen to be cross-cut by mineralised veins. In contrast, certain generations of aplite dykes contain miarolitic cavities, pegmatitic segregations, early 'A-type' quartz ± chalcopyrite ± bornite ± molybdenite veins (nomenclature after

Gustafson and Hunt, 1975), quartz unidirectional solidification textures (USTs) which grow inwards from their margins, and are cross-cut by mineralised veins (**Fig. 5.3c–f & Sup. fig. 5.3-6**) (Carter and Williamson, 2022). These observations are comparable with previous descriptions of aplitic ‘vein dykes’ in other porphyry systems (e.g. Spurr, 1923; Shannon et al., 1982; Kirkham and Sinclair, 1988). The presence of quartz USTs within the aplites is likely to indicate undercooling (London, 2009) and rapid pressure fluctuations due to repeated carapace fracturing (Kirkham and Sinclair, 1988; Kirwin, 2005) (which may induce fluid exsolution via ‘first-type boiling’; Candela, 1989), suggesting that these mineralising aplite dykes were emplaced rapidly to shallow depths. Given that the aplite dykes host mineralised miarolitic cavities that are closely associated with early A-type mineralised veins (**Fig. 5.3d–f & Sup. fig. 5.4**), they capture the nature and timing of magmatic-hydrothermal fluid exsolution and mineralisation. Here, we only focus on the generations of aplite dykes which cross-cut the LHG cupola and are directly associated with mineralisation.

Field relations indicate that some parts of the Fulstone volcanics were cogenetic with the emplacement of porphyry dykes associated with the LHG (Proffett, 2007; Proffett, 2009). Propylitic alteration (e.g. epidote replacing primary plagioclase, and chlorite replacing mafic minerals; **Sup. fig. 5.7**) is ubiquitous across the Fulstone Spring Volcanics, indicating that the hydrothermal system could have been active for some time after volcanism. The lack of more acid alteration (e.g. advanced argillic) may indicate that these volcanics, if related, were deposited away from the central axis of the porphyry system.

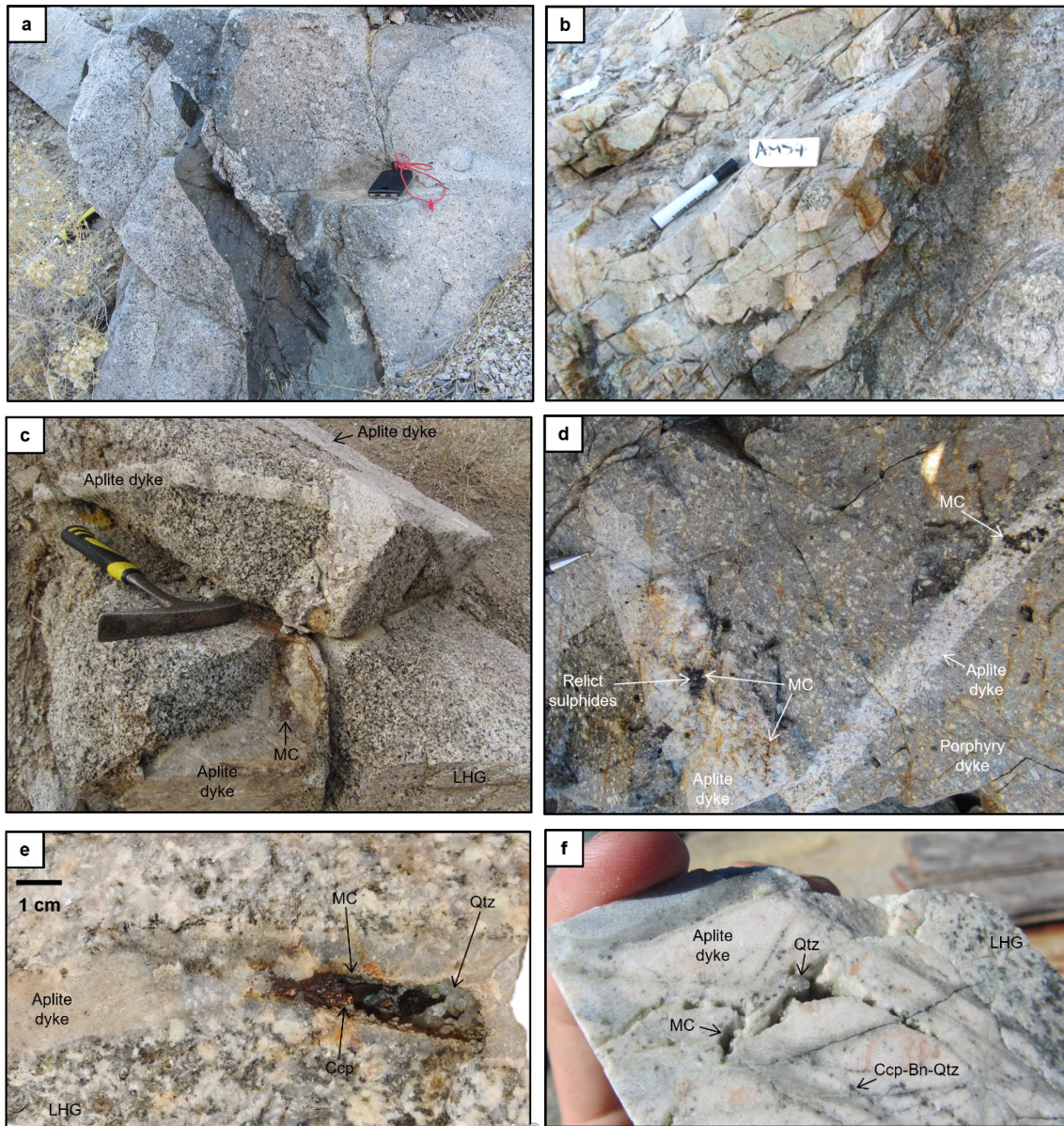


Fig. 5.3 Temporal relations in the Yerington magmatic system: Field photographs of: **a**, cross-cutting relations of multiple porphyry dyke generations which cut the LHG cupola; **b**, lobate contacts and evidence for mingling of co-eval magmas between an aplite dyke and porphyry dyke. Secondary copper staining prevalent in the aplite dyke; **c & d**, multiple generations of aplite dykes hosting pegmatitic segregations and mineralised miarolitic cavities (MC). The aplite dykes sharply cross-cut the cupola zone of the LHG and a porphyry dyke. Both the aplite and porphyry dykes lie palaeo-vertically beneath the Ann Mason porphyry deposit; **e**, cupola zone of LHG cut by an aplite dyke hosting a chalcopyrite (Ccp) mineralised miarolitic cavity. This aplite dyke is sample AM13BAP in **Fig. 5.4**. Qtz = quartz; **f**, drill core from the Ann Mason porphyry deposit showing LHG cut by an aplite dyke hosting miarolitic cavities and early chalcopyrite-bornite-quartz (Ccp-Bn-Qtz) (A-type, nomenclature after Gustafson & Hunt, 1975) veins, which locally truncate at the dyke's margin. **e & f** from Carter et al. (2021; Chapter 4).

5.5 Absolute age constraints on magmatic system evolution

The determination of crystallisation ages for igneous samples using U–Pb CA–ID–TIMS on zircons (See Methodology and **Supplementary Data 5.1**) provides a temporal framework for the construction of the Yerington batholith and eruption of overlying volcanics, over an indicated period of ~ 2.8 Myrs (~ 169.3 Ma to ~ 166.1 Ma; Zircon ages are reported in **Fig. 5.4** and **Supplementary Data 5.2**). A sensitivity analysis of the ages is presented in **Supplementary Data 5.2**). This supersedes the previous U–Pb geochronological framework which was based on multi-grain TIMS (Dilles and Wright, 1988), and ion probe analyses (Banik et al., 2017) on limited sample sets and which had relatively large uncertainties.

According to the new schema, the McLeod QMD pluton (AM72 and AM4QMD) was emplaced over a period of > ~ 0.9 Myrs (~ 168.6 Ma to ~ 167.4 Ma) and the Bear QM pluton (BH10 and MA9) > ~ 1.5 Myrs (~ 169.6 Ma to ~ 167.1 Ma). The youngest zircons for these two units are indistinguishable in crystallisation age, indicating a period of contemporaneous emplacement with crystallisation of their latest phases within ~ 100 kyrs of each other. These mineralogically and texturally distinct plutons were likely emplaced episodically to form their internal contacts (Proffett and Dilles, 1984; Dilles, 1987) and both appear to young downwards over a palaeo-vertical distance of ~ 3 km, supporting under-accretion (e.g. Menand, 2011) as the mode of emplacement (Schöpa et al., 2017).

Within the LHG, its upper region (AM18LHG; ~ 5 km palaeo-depth; Dilles, 1987) and a deeper portion (LH24S; ~ 7.5 km palaeo-depth; Dilles, 1987) show closely comparable zircon $^{206}\text{Pb}/^{238}\text{U}$ dates and weighted means of 167.365 ± 0.041 Ma and 167.275 ± 0.027 Ma, respectively (**Fig. 5.4**). These ages define the maximum emplacement time-gap between the McLeod QMD-Bear QM and LHG of 215 ± 59 kyrs. However, when the 167.440 ± 0.039 Ma age of a mineralised porphyry dyke from within the Ann Mason porphyry deposit (AC25) is considered, which cross-cuts the LHG cupola ~ 1 km higher in the system than AM18LHG, then the maximum emplacement time-gap must be shorter (140 ± 57 kyrs, or ~ 100–200 kyrs). These cross-cutting relationships imply an episodic emplacement of the exposed LHG over > ~ 150 kyrs and the new timescale that construction of the Yerington batholith was at least two times longer than the ~ 1 Myrs

previously estimated on the basis of previous geochronology (Dilles and Wright, 1988; Schöpa et al., 2017).

A stratigraphically lower unit of the Fulstone volcanics (BS1) yielded an age (168.318 ± 0.054 Ma; **Fig. 5.4**) within the emplacement duration defined by the Bear QM and McLeod QMD, whereas the stratigraphically higher unit (BS16) gave a much younger age (166.285 ± 0.059 Ma; **Fig. 5.4**), ~ 1.1 Myrs younger than the formation of the LHG cupola. This indicates the volcanic record spans over ~ 2 Myrs, rather than there having been a single post-ore volcanic event, as proposed by Dilles and Wright (1988).

From cross-cutting relations, the onset of porphyry-style Cu-Mo mineralisation in Yerington is temporally constrained by the emplacement of dyke swarms through the cupolas of the LHG (e.g. Proffett, 1979; Dilles, 1987; Dilles and Proffett, 1995). In turn, our absolute U–Pb ages for the mineralised porphyry dykes that cross-cut the cupolas of the LHG, and the youngest ages for the McLeod QMD and Bear QM, both constrain the onset of ore formation to ~ 167.4 Ma (**Fig. 5.4**). The multiple generations of aplite dykes that host mineralised miarolitic cavities and early A-type veins (AM63A and AM13BAP; **Fig. 5.3d–f** & **Sup. fig. 5.3-6**), and have been proposed to act as conduits for the transport of mineralising fluids into the ore-forming environment (Carter et al., 2021; Chapter 4), capture the timing, albeit a partial record, of magmatic-hydrothermal fluid exsolution and mineralisation. As the youngest zircon growth within these aplite dykes likely crystallised as part of the magmatic assemblage at the magmatic-hydrothermal transition (See QEMSCAN, **Sup. fig. 5.4-6**, **Supplementary Data 5.3**), the U–Pb ages of 167.282 ± 0.040 Ma and 167.045 ± 0.057 Ma (**Fig. 5.4**) constrain the timing of mineralisation to a period of at least ~ 400 kyrs.

From Re-Os molybdenite ages for chalcopyrite-bornite-molybdenite-quartz veins (A- and B-type) (samples AC11, AC12 & AC21), a chalcopyrite-molybdenite-bearing quartz UST within an aplite dyke (or vein dyke texture; e.g. Spurr, 1923; Shannon et al., 1982; Kirkham and Sinclair, 1988) (AC3) and a fine grained molybdenite vein (AC41MP) (**Fig. 5.4** & **Sup. fig. 5.8**; **Supplementary Data 5.2**) from the Ann Mason deposit, mineralisation occurred during multiple hydrothermal events over a period in excess of 1.5 Myrs, from 166.90 ± 0.1 to

165.29 ± 0.1 Ma. Comparison between the hydrothermal Re-Os molybdenite ages and magmatic zircon U–Pb ages requires that systematic uncertainties, relating to the tracer calibrations and decay constant intercalibration, must be considered, which typically equate to ± 0.8 Myrs on Re-Os dates and ~ ± 0.08 Myrs for U–Pb (Refer to **Supplementary Data 5.2**). Results therefore indicate some component of porphyry-style mineralisation within the Ann Mason deposit could potentially have occurred coincident with the eruption of the younger propylitically altered components of the Fulstone volcanics (BS16), at 166.285 ± 0.059 Ma (**Sup. fig. 5.7**). In general, the results indicate that hydrothermal mineralisation was not a single, short-lived event.

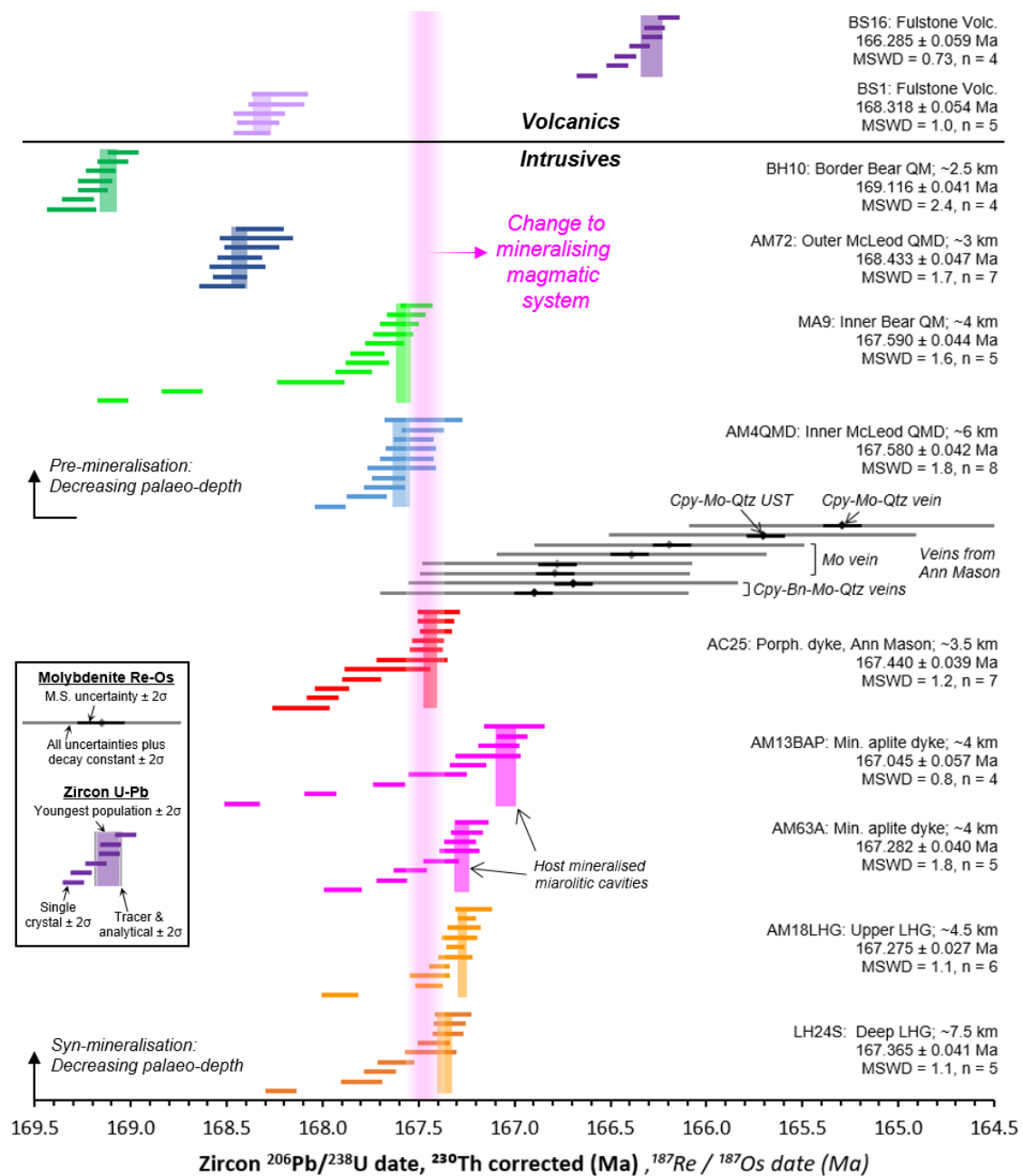


Fig. 5.4 Geochronological framework for the Yerington porphyry system: Zircon single grain U-Pb CA-ID-TIMS and molybdenite Re-Os geochronological framework for samples spanning the age range of the Yerington magmatic system. Pre- and inter-mineralisation intrusive samples are grouped and plotted in order of approximate palaeo-depth, after Dilles (1987). Sample details can be found in **Supplementary Data 5.2**. We take the weighted mean of the youngest population of zircon dates that formed a statistically acceptable Mean Square Weighted Deviation (MSWD, or chi squared) as the best approximation for the crystallisation of the host magma. Cpy = chalcopyrite, Bn = bornite, Mo = molybdenite, Qtz = quartz, UST = unidirectional solidification texture, Porph. = porphyry, Min. = mineralised, M.S. = mass spectrometry. Error bars at 2σ. For comparison of Re-Os with U-Pb data, expanded uncertainties for Re-Os (typically ± 0.8 Myrs) and decay constant and tracer uncertainty for U-Pb data (typically ± 0.08 Myrs, represented in legend) should be taken into account (Refer to **Supplementary Data 5.2**).

5.6 Geochemical change within the magmatic system

In terms of their whole-rock geochemical compositions, the McLeod QMD and Bear QM (pre-mineralisation) are similar and notably different to the LHG, porphyry and aplite dykes (syn-mineralisation) (**Fig. 5.5, Fig. 5.6, Sup. fig. 5.9 & Sup. fig. 5.10; Supplementary Data 5.4**). The McLeod QMD and Bear QM have similar ranges in SiO₂ (~ 60–68 wt%) whilst the LHG samples either overlap with these or are marginally more evolved (~ 67–69 wt.% SiO₂). The porphyry dykes show a range in SiO₂ (60–71 wt%), whilst aplite dykes are the most evolved, generally having > 73 wt.% SiO₂. Compared to the McLeod QMD and Bear QM, the LHG and porphyry dykes have higher Sr/Y ratios (Sr/Y > 130), steeper LREE/HREE and MREE/HREE patterns (e.g. La/Yb > 30; Gd/Yb > 3.7), lower ΣREEs (< 100 ppm), and positive Eu anomalies (Eu/Eu* > 1.05). Whilst the Dy/Yb values (~ 2) do not significantly change between the McLeod QMD, Bear QM and LHG, they follow a slightly negative trend with increasing SiO₂ (**Sup. fig. 5.11**).

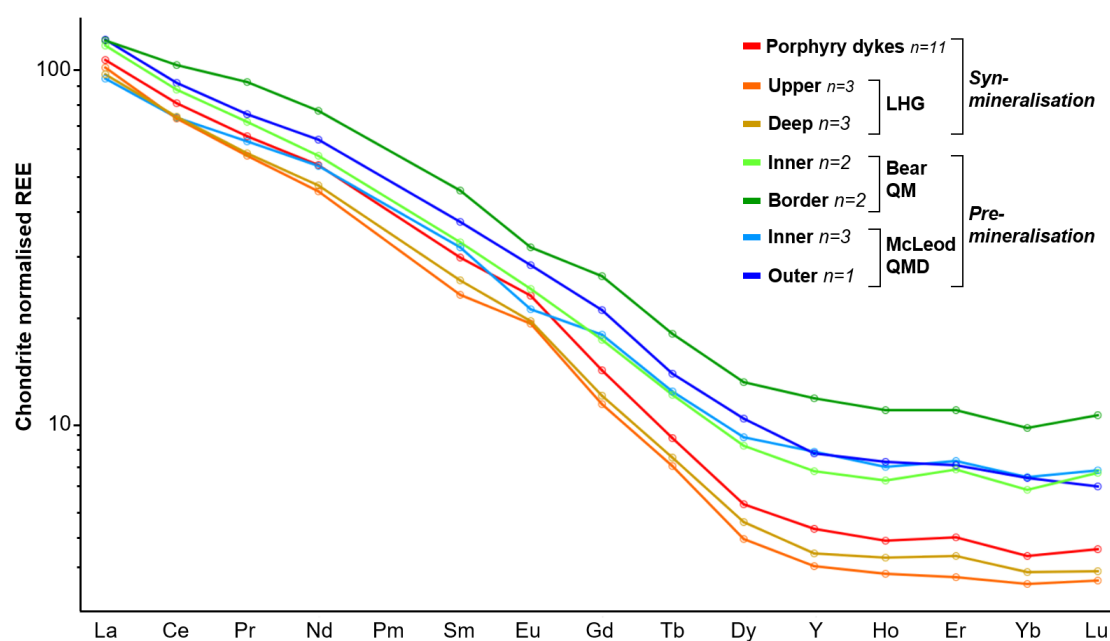


Fig. 5.5 Chondrite-normalised (McDonough and Sun, 1995) mean whole-rock REE plots. LHG and porphyry dykes are distinct from the Bear QM and McLeod QMD intrusions, having slightly positive Eu anomalies and steeper MREE/HREE curves. All data plotted in **Sup. fig. 5.9**.

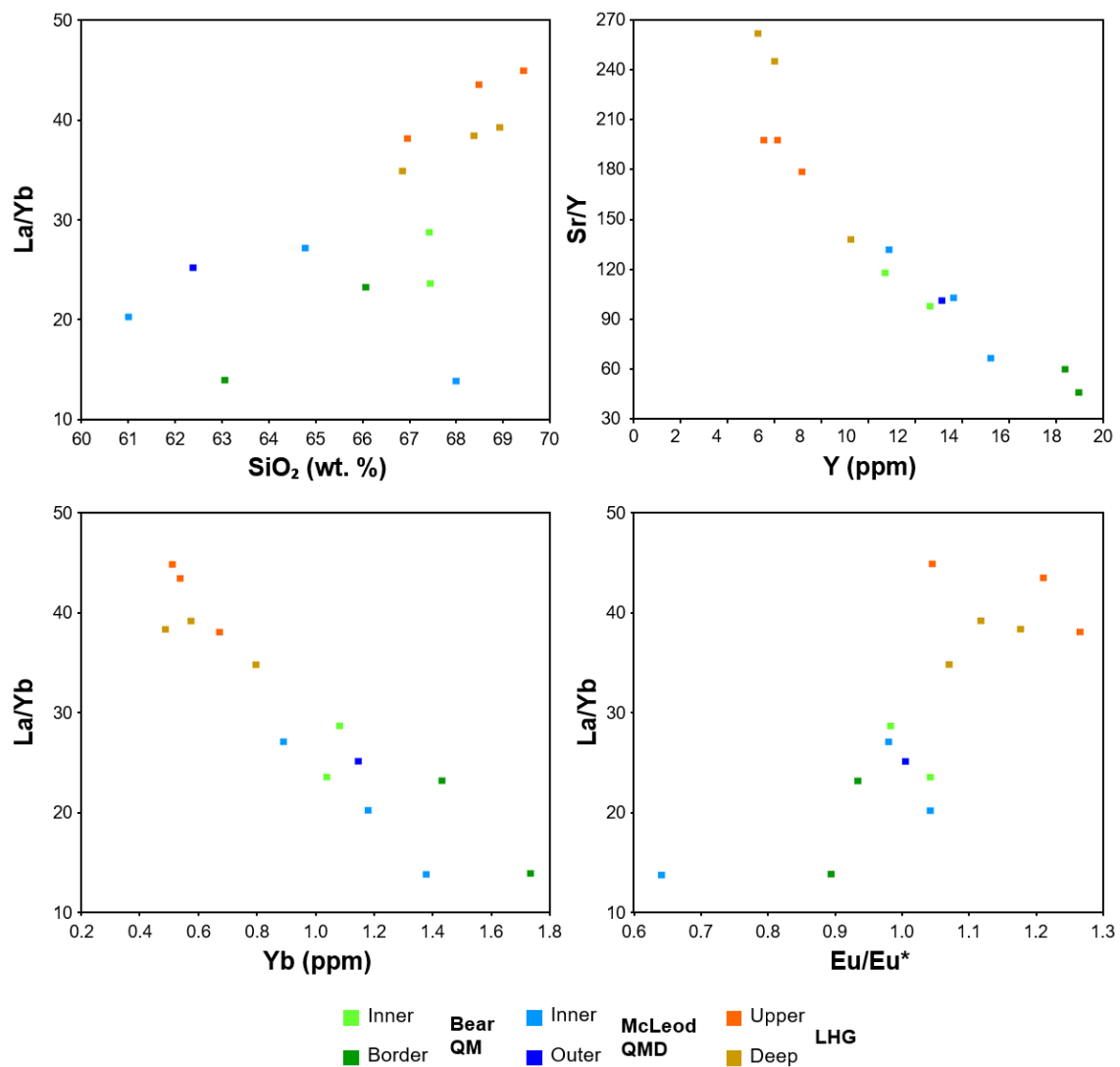


Fig. 5.6 Whole-rock geochemical compositions of plutonic units in the Yerington magmatic system. Major elements in part overlap between the mineralogically distinct (Dilles, 1987) intrusive units. Differences between pre-mineralisation (Bear QM and McLeod QMD) and inter-mineralisation (LHG) units are seen in trace element ratios. Porphyry and aplite dykes plotted in **Sup. fig. 5.10**.

From whole-rock geochemistry, the pre-mineralisation McLeod QMD and Bear QM are likely to be genetically related, despite their mineralogical and textural differences (Dilles, 1987). The more evolved composition of the syn-mineralisation LHG was probably due to a change in the bulk fractionating assemblage of the magmas. As previously shown (Dilles, 1987), this is likely to have been from clinopyroxene- (in which Y, MREEs and HREEs are compatible, although more weakly when compared to amphibole; Luhr et al., 1984; Nandedkar et al., 2016) and plagioclase-dominated fractionation (in which Sr and Eu are compatible; Aigner-Toress et al., 2007) in the pre-mineralisation units, to

deeper and wetter (e.g. Richards, 2011; Chiaradia et al., 2012) amphibole-dominated fractionation, with plagioclase crystallisation delayed until after emplacement into the upper crust, in the syn-mineralised units. The elevated melt-water contents led to higher Sr/Y and Eu/Eu* and depletion in HREEs (Lühr et al., 1984; Sisson, 1994; Nandedkar et al., 2016) (**Fig. 5.5 & Fig. 5.6**). From the work of Davidson et al. (2007), the slightly negative trend of Dy/Yb with increasing SiO₂ in the plutonic units (**Sup. fig. 5.11**) is likely to indicate that garnet did not play a role in the geochemical evolution of the system.

Zircon geochemistry is a function of pressure, temperature and melt composition (Claiborne et al., 2006; Burnham, 2020) and therefore records changes in the geochemical and physical nature of the melt from its source to level of emplacement, although only during the period of zircon saturation. Zircon from across the Yerington magmatic system (**Fig. 5.7 & Sup. fig. 5.12–15; Supplementary Data 5.5**) can be separated into two distinct geological groups: pre-mineralisation (McLeod QMD, Bear QM and older volcanic units) and syn-mineralisation (LHG, aplite dykes and younger volcanic units). Zircon Hf concentrations, typically thought to reflect melt evolution (Claiborne et al., 2006), are comparable between the pre- and syn-mineralisation units. Zircon from the pre-mineralisation McLeod QMD and Bear QM have relatively higher Ti (5–20 ppm) and lower Eu/Eu* (0.2–0.5) and Gd/Yb (MREE/HREE, 8–21) compared with the syn-mineralisation intrusives, overlapping with the pre-mineralisation Artesia volcanics and older units of the overlying Fulstone volcanics. From outer to inner portions of the McLeod QMD and Bear QM, there is an increase in zircon Gd/Yb (rising from ~ 10 to ~ 16) with decreasing Ti concentration. In contrast, zircon from the syn-mineralised LHG, aplite dykes and younger units of the Fulstone volcanics have lower Ti (2–5 ppm), higher Eu/Eu* (~ 0.4 to 0.9) and Gd/Yb (~ 10–35).

There is no major difference in zircon composition between the LHG and aplite dykes. Further, the ‘early’ and ‘late’ mineralised porphyry dykes are almost identical in their zircon compositions, from both the Ann Mason and Yerington porphyry copper deposits, in agreement with previous zircon data for dykes from the Yerington porphyry deposit (Banik et al., 2017). Regardless of age, the porphyry dykes show no clear division between the geochemical groups of pre-

and syn-mineralisation plutonic rocks, which we attribute to recycling of pre-mineralisation zircon grains from a magmatic reservoir at depth. Similarities in zircon geochemical signatures between the intrusive units and the volcanics likely indicates that are genetically linked.

As melt chemistry is largely linked to the composition and processes in the evolution zone (e.g. Annen et al., 2006), major differences in zircon chemistry, and by extrapolation melt chemistry, between the samples is likely to reflect differences prior to magma emplacement. The comparable zircon chemistry of the McLeod QMD and Bear QM indicate that these plutons had a shared source and evolution prior to emplacement, controlled by clinopyroxene- and plagioclase-dominated fractionation, despite their mineralogical and textural differences (Dilles, 1987). In contrast, the syn-mineralised units (LHG and aplite dykes) underwent amphibole-dominated fractionation, evidenced by increasing MREE/HREE, and suppressed plagioclase crystallisation in the source, caused by relatively high melt-water contents, prior to significant plagioclase crystallisation post emplacement into the upper crust, the latter indicated by relatively high Eu/Eu* values (Sisson, 1994). Elevated Eu/Eu* in zircon may also relate to increased melt fO₂ (e.g. Burnham and Berry, 2012; Dilles et al., 2015; Richards, 2015), but Δ FMQ values (calculated by the method of Loucks et al., 2020) overlap between the pre- and syn-mineralising intrusives (**Sup. fig. 5.16**), and zircon Eu/Eu* is not a robust proxy for melt redox conditions as it is also strongly controlled by the crystallisation of other phases within the melt (Loader et al., 2017). The low Ti concentration seen in the inter-mineralisation LHG and aplite dyke zircons could reflect lower temperatures defined by the Ti-in-zircon geothermometer (Watson and Harrison, 2005), induced by increased melt-water contents and reduced temperatures at which zircon dominantly crystallises within the melt (Tapster et al., 2016). However, given the paucity of good constraints on the titania activity through the evolution of the magmatic system, calculation of absolute temperatures has been avoided. Low zircon Ti concentration within later magmatic phases could also be due to decreased titania activity in the magma, due to greater incorporation of Ti into amphibole, titanite, or other Ti-bearing phases crystallising at depth. Importantly, the changes indicative of a shift from a clinopyroxene-plagioclase-dominated system to an increasingly hydrous, amphibole-dominated system at the transition from a non-mineralising to

mineralising magmatic system, both suggested in previous work (Dilles, 1987), and whole-rock data here (**Fig. 5.5 & Fig. 5.6**), are more pronounced within the zircon geochemistry than whole-rock geochemistry, both in the plutonic and volcanic record.

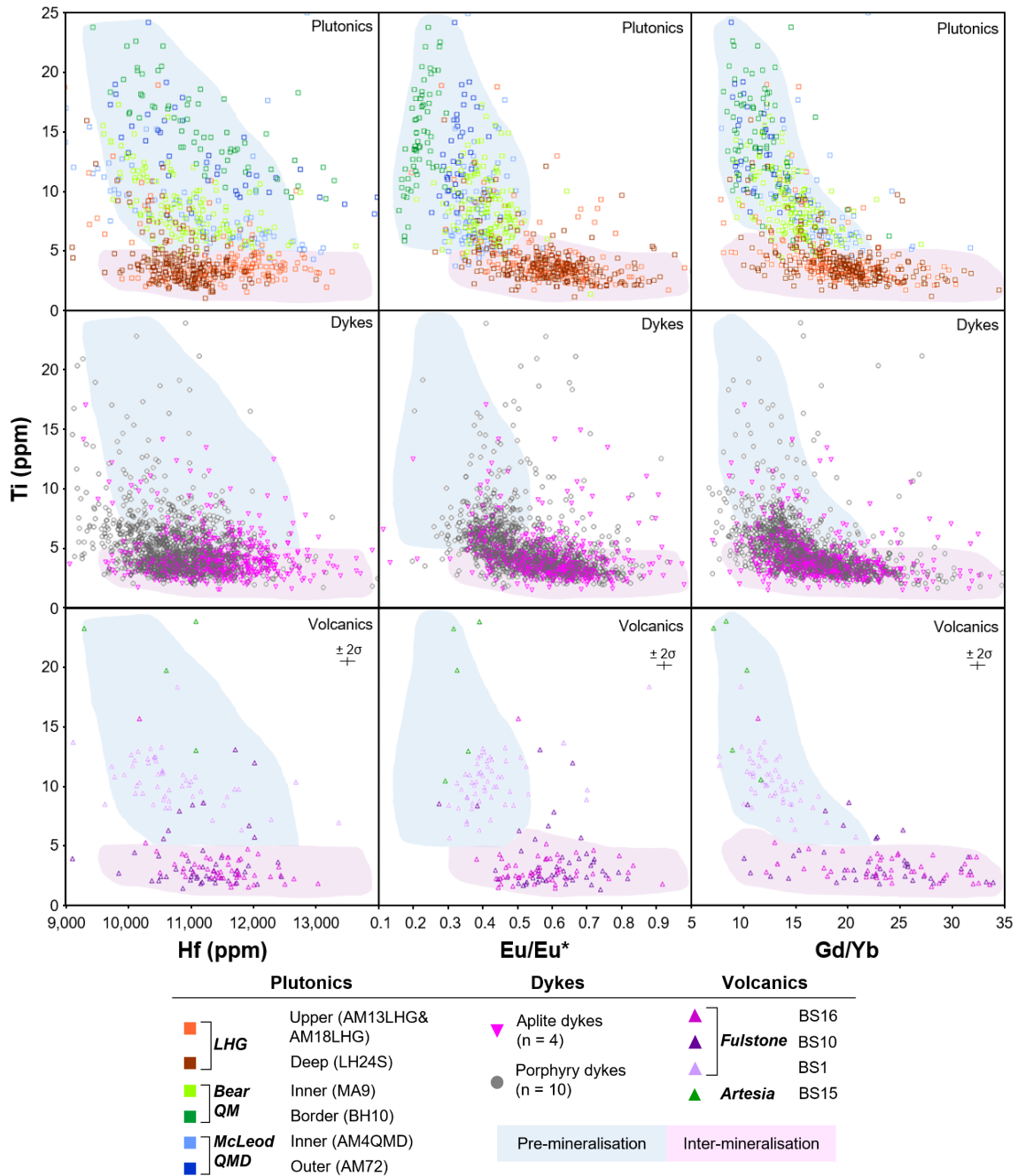


Fig. 5.7 Zircon trace element signatures through the Yerington magmatic system: Zircon LA-ICP-MS trace element data from samples spanning, temporally and spatially, the Yerington magmatic system. 'Pre-mineralisation' and 'inter-mineralisation' fields shaded to aid visualisation, based on the dominant zircon geochemical signatures of the plutonic units and projected onto the

plots for dykes and volcanics. Only zircon rim data have been plotted. See **Sup. fig. 5.13-15** for full sample breakdown along with zircon core data.

5.7 Isotopic constraints on magma pathways

From whole-rock $^{87}\text{Sr}/^{86}\text{Sr}$ data (Dilles, 1987), there appears to have been a subtle transition from more radiogenic, crustal-like values (Taylor, 1980), within the pre-mineralisation intrusions, to less radiogenic ratios within the syn-mineralisation intrusions, which suggests a decreasing amount of crustal assimilation over time. Similarly, zircon O-isotopes also show a transition from $\delta^{18}\text{O} \sim 6 \text{‰}$ (Banik et al., 2017), above values for zircon equilibrated with mantle-derived melts and indicating contamination with other crustal components, to $\sim 4.5 \text{‰}$ and is within uncertainty of the expected range for the mantle (Valley, 2003; Bindeman, 2008) (**Fig. 5.8**).

The ϵ_{Hf} compositions of the zircon crystals that yield the youngest dates by CA-ID-TIMS U-Pb are a good approximation for the late-stage melt at the emplacement level and provide further insights into the evolution of the Yerington magmatic system (**Fig. 5.8 & Sup. fig. 5.17; Supplementary Data 5.6**). Over the period of construction of the Yerington batholith, there were changes in the nature of zircon Lu-Hf isotopes. This is best illustrated by the weighted mean ϵ_{Hf} of the sample population, and differences in the corresponding over-dispersion where the MSWD is in excess of that expected for a single population at the stated level of uncertainty. With an ϵ_{Hf} uncertainty of $\sim \pm 0.5 \epsilon_{\text{Hf}} (2\sigma)$, the data show that the LHG and aplite dyke samples form reproducible single populations without over-dispersion which indicates that zircon crystallised from a melt with homogenous ϵ_{Hf} , whereas the pre-mineralisation samples ($> 167.4 \text{ Ma}$) show over dispersion that must result from variable ϵ_{Hf} between zircon grains, which suggests isotopic heterogeneity within the melt. The mean value is consistent (within $\sim 0.2 \epsilon_{\text{Hf}}$) between syn-mineralisation samples yet is $\sim 1 \epsilon_{\text{Hf}}$ lower in the oldest Bear QM sample. The increased range and lower ϵ_{Hf} indicates greater crustal assimilation, which probably occurred during ascent into the sub-volcanic environment.

Given the paucity of any major component of zircon xenocrysts older than the Triassic volcanic and sedimentary country rocks (**Fig. 5.4; Supplementary Data 5.2 & 5**), we infer that there was little continental crustal material present to impart

large variations in ϵ_{Hf}^t upon assimilation. Nevertheless, there is a systematic variation between earlier and later pre-mineralisation intrusions that is best explained by the pre-mineralising McLeod QMD and Bear QM magmas (prior to ~ 167.4 Ma) having undergone transport, storage and evolution within, and were contaminated by, the crustal column leading to the more varied and crustal isotopic signatures (Sr, O and Hf). In contrast, after ~ 167.4 Ma, these rocks no longer show this signature, indicating no discernible crustal assimilation during magma transport and storage. It suggests that the mineralising LHG-related melts reached their evolved compositions within a lower crustal environment where they were only exposed to homogenous, mantle-derived magmas. This supports different evolution zones for the pre- and syn-mineralisation melts. These could be either discretely located throughout the crust or within the same 'hot-zone' (Annen et al., 2006), reflecting melt extraction in variable proximity to the country rock, with LHG melts being entirely encapsulated by juvenile, mantle-derived rocks, with negligible assimilation of other crustal components prior to emplacement.

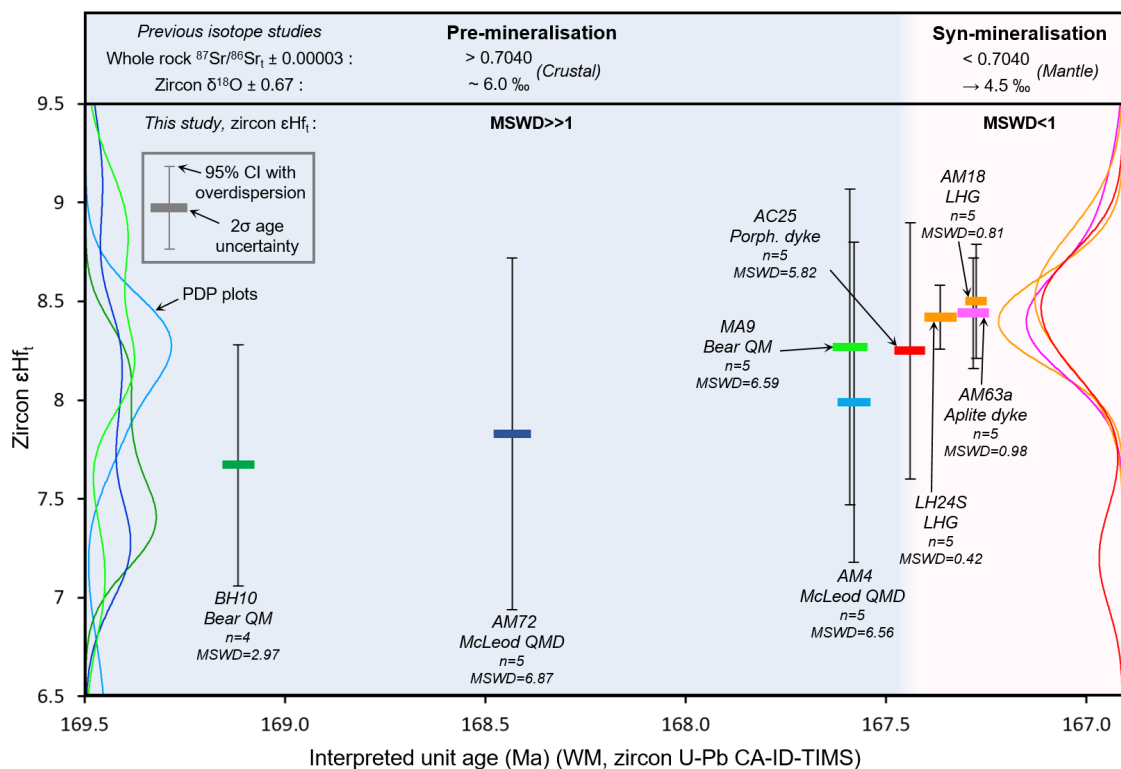


Fig. 5.8 Zircon ϵ_{Hf}^t through the Yerington magmatic system: Time corrected zircon ϵ_{Hf}^t (ϵ_{Hf}^t) versus interpreted zircon age for samples spanning the Yerington magmatic system. Age determinations for each sample are weighted mean (WM) from zircon single grain U-Pb CA-ID-TIMS analyses, with error bars at 2σ (Fig. 5.4). ϵ_{Hf}^t error bars at 95% confidence interval (CI)

with overdispersion. 'Pre-' and 'syn-mineralisation' fields shaded. Probability density plots (PDP), inset, are coloured by sample. From the MSWD data for ϵHf_t , 'pre-mineralisation' units show over dispersion (MSWD >1) and 'syn-mineralisation' units show under dispersion (MSWD <1). The data are compared (top) to previous whole rock $^{87}\text{Sr}/^{86}\text{Sr}_t$ (Dilles, 1987) and zircon $\delta^{18}\text{O}$ (Banik et al., 2017) isotope studies, which show subtle shifts from crustal to mantle isotopic signatures (Taylor, 1980; Valley, 2003; Bindeman, 2008). All data points plotted in **Sup. fig. 5.17**.

5.8 Depth of melt evolution

Since melt chemistry is partly controlled by the pressure of differentiation (e.g. Annen et al., 2006), it can offer insights into the depth at which melts evolve. For example, increased Sr/Y, as observed in the LHG, is often used to infer a greater depth of fractionation due to an increased abundance of amphibole and suppressed plagioclase crystallisation within a relatively deep fractionating assemblage (Annen et al., 2006; Richards, 2011; Chiaradia et al., 2012; Smith, 2014). The compositions and normative mineralogy of H₂O-saturated minima and eutectics for haplogranitic melts also share a relationship with pressure (e.g. Johannes and Holtz, 1996; Blundy and Cashman, 2001). This pressure equates to the approximate depth at which the melt reached the eutectic, or evolved to its bulk composition, rather than the emplacement depth.

The normative mineralogy of the LHG, porphyry and aplite dykes show a close fit to the H₂O-saturated minima and eutectics for haplogranitic melts (e.g. Johannes and Holtz, 1996; Blundy and Cashman, 2001) (**Fig. 5.9 & Sup. fig. 5.18**). LHG samples and porphyry dyke samples cluster between the ~ 450 MPa and 1000 MPa minima. Conversely, aplite dyke samples cluster between the ~ 75 MPa and 200 MPa minima. Assuming lithostatic pressure with an average overburden density of 2.5 g/cm³, determined pressures roughly equate to a melt evolution depth of ~ 20–40 km for the LHG and porphyry dykes, and ~ 3–8 km for aplite dykes.

As with the geochemical signatures (**Fig. 5.5, Fig. 5.6 & Fig. 5.7**), which are indicative of a deeper amphibole-dominated evolution (e.g. Richards, 2011; Chiaradia et al., 2012), these melt minima relationships also support a deep melt evolution (~ 20–40 km) for the LHG, and also probably for the porphyry dykes (**Sup. fig. 5.18**), rather than shallow fractionation at the emplacement level.

However, this whole rock barometry indicates that aplite dykes (including those that contain textures indicating fluid exsolution and Cu mineralisation; Carter et al., 2021, Chapter 4; Carter and Williamson, 2022, Chapter 3; **Fig. 5.3 & Sup. fig. 5.3-6**), were sourced from shallow depths (~ 3–8 km), near their level of emplacement, probably representing late-stage melts associated with the LHG.

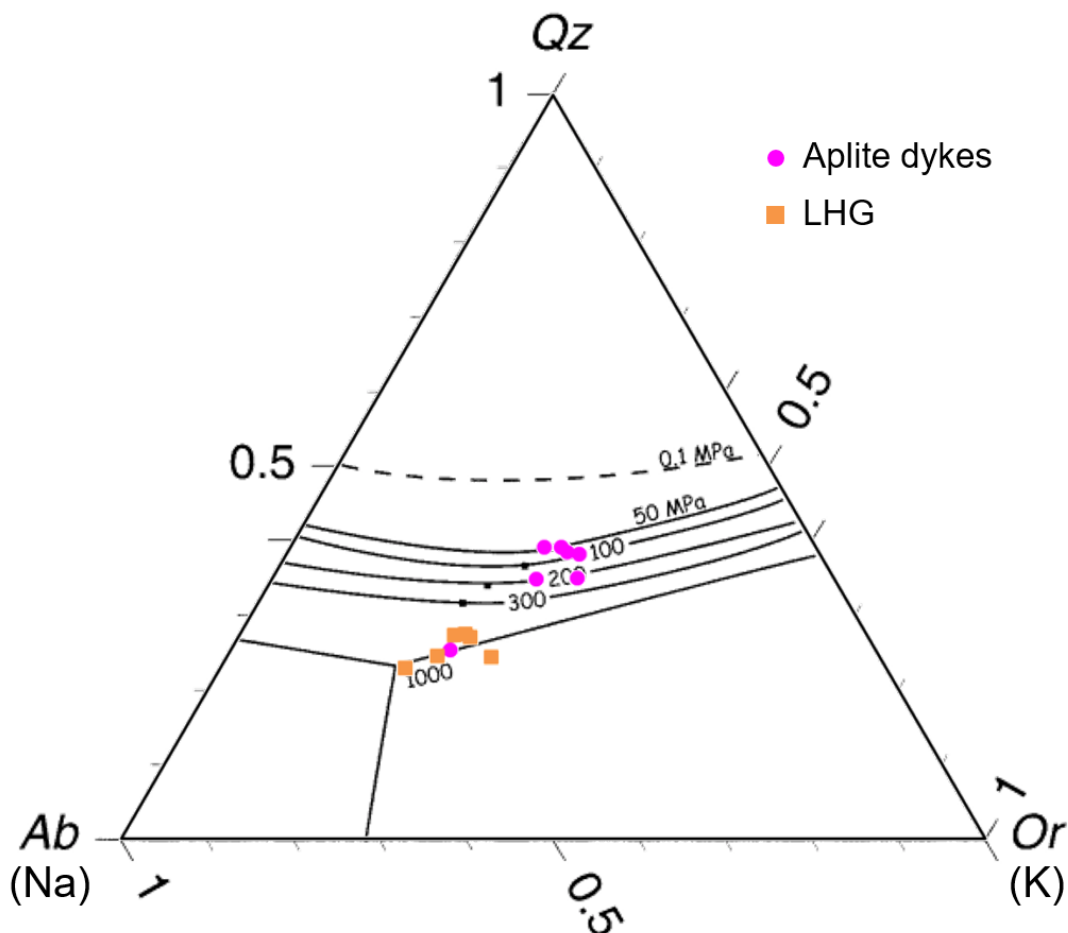


Fig. 5.9 Depth of different magma sources: CIPW normative mineralogy (method of Lowenstern, 2000) from whole-rock XRF data for aplite dykes and LHG (Luhr Hill granite) plotted on the H₂O-saturated haplogranitic melt minima plot of Blundy and Cashman (2001) (after Johannes and Holtz, 1996). Samples overprinted by intensive Na-Ca alteration are not plotted. Porphyry dykes plotted in **Sup. fig. 5.18**.

5.9 A rapid change in magmatic plumbing to tap porphyry ore-forming magmas

Previous models for the assembly of the Yerington batholith (Dilles, 1987; Dilles et al., 2000; Schöpa et al., 2017) suggest sequential emplacement of the McLeod QMD and Bear QM, yet this is at odds with the revised chronology where these two intrusive units crystallised and must have been emplaced at least in part over

the same ~ 800 kyrs time period (**Fig. 5.4 & Fig. 5.10**). Whilst these units are mineralogically and texturally distinct (Dilles, 1987), their isotopic signatures and whole-rock and zircon geochemistry are very similar (**Fig. 5.5-8**), suggesting similar sources and evolutionary pathways, likely in a mid-crustal storage zone (**Fig. 5.10**), although this must have evolved over the 1.5 Myrs of upper crustal activity. The whole-rock and zircon geochemical signatures of the pre-mineralisation McLeod QMD and Bear QM units (**Fig. 5.5-7 & Sup. fig. 5.9-15**) are consistent with clinopyroxene-plagioclase-dominated fractionation in the mid-crust (**Fig. 5.10**). This contrasts with the change to the syn-mineralisation signatures (**Fig. 5.5-7 & Sup. fig. 5.9-15**) which indicate an amphibole-dominated lower crustal evolution (~ 20–40 km depth; **Fig. 5.9 & Fig. 5.10**). The intrusions either-side of this geochemical change are both relatively evolved and have comparable indicators of fractionation, such as whole-rock SiO₂ and zircon Hf concentrations (**Fig. 5.6 & Fig. 5.7**).

The shift in the compositions of the magmas which formed the pre-mineralising intrusions and then the LHG, along with the change in the dominant fractionating assemblage, is constrained to within < 200 kyrs and is coincident with the onset of porphyry mineralisation. For the LHG and porphyry dykes, although there is little difference in their whole-rock (**Fig. 5.5 & Sup. fig. 5.10**), zircon trace element and isotopic compositions (**Fig. 5.7 & Fig. 5.8**), and where they plot on the melt minima diagram (**Sup. fig. 5.18**), there is no evidence from within the ~ 8 km depth of exposure that the porphyry dykes were derived from the upper parts of the LHG (as per previous models, e.g. Dilles, 1987). Instead, the porphyry dykes may reflect the same or similar intrusive events that formed the LHG. Once emplaced at shallow crustal levels, the LHG magmas underwent further fractionation (at ~ 3–8 km depth, based on melt minima plots; **Fig. 5.9**), potentially forming igneous banding textures (**Sup. fig. 5.2**), to form more evolved and volatile-rich melts that were episodically injected as aplite dykes over a period of at least ~ 400 kyrs (**Fig. 5.4**). Multiple, episodically emplaced generations of these aplite dykes, which provide textural evidence for undercooling and exsolution of mineralising fluids (mineralised miarolitic cavities; Carter et al., 2021, Chapter 4; Carter and Williamson, 2022, Chapter 3), are associated with early A-type veins and likely acted as crystal mush conduits for mineralising fluids (Carter et al., 2021; Chapter 4) (**Fig. 5.3c–f & Sup. fig. 5.3–6**). Zircon U–Pb and molybdenite

Re-Os ages indicate hydrothermal mineralisation occurred episodically over time-periods potentially in excess of 1.5 Myrs post-emplacement of the LHG cupola (**Fig. 5.4**), perhaps coincident with the eruption of the younger propylitically-altered components of the Fulstone Volcanics that bear the same zircon geochemical signatures as the LHG (**Fig. 5.4, Fig. 5.7, Sup. fig. 5.7, Sup. fig. 5.12-15**). The proposed time-period for porphyry ore formation, which may have exceeded 1.5 Myrs post emplacement of the LHG cupola, is not uncommon for medium to large scale, composite porphyry systems (e.g. Romero et al., 2010; Stein, 2014; Spencer et al., 2015; Chang et al., 2017; Chiaradia and Caricchi, 2017), or where multiple, episodic ore-forming magmatic-hydrothermal events are documented (e.g. Spencer et al., 2015; Tapster et al., 2016; Li et al., 2017). This all suggests that relatively evolved, internal or deep parts of the LHG remained active and continued to produce the magmas and associated magmatic-hydrothermal fluids responsible for porphyry deposit formation after emplacement and crystallisation of the cupolas and upper regions of the LHG (**Fig. 5.10**). It also implies that the LHG pluton was episodically recharged rather than being emplaced as a single intrusive event, as previously suggested by Dilles (1987) and Proffett (2007).

Given the similarities in zircon trace element geochemistry between the mineralised porphyry dykes from the Ann Mason and Yerington porphyry deposits (**Sup. fig. 5.13–15**; Banik et al., 2017), and their mineralogy (Dilles, 1987), they are probably genetically related. By extrapolation, this is also likely to be the case for porphyry dykes in the Yerington District's two other known porphyry deposits: Bear and MacArthur. Because of this, it is probably salient for future computational simulations of batholith construction and mineralisation to include fluids derived from across all porphyry centres; this will yield a considerably larger copper endowment than when individual porphyry centres are considered (> 9 Mt of contained Cu; Dilles and Proffett, 1995; Bryan, 2014; Hudbay Minerals Inc., 2021; Welhener et al., 2022).

The abrupt (~ 100–200 kyrs) change to geochemical signatures indicative of magmas from a lower crustal amphibole-stable, plagioclase-suppressed, evolution zone (from whole-rock Sr/Y and REE patterns, and zircon geochemistry, **Fig. 5.5-7**), in tandem with an increase in ore-forming potential, requires an explanation.

It is plausible that these changes could have occurred in a single magma reservoir as a result of a progressive long-term transition. Within the lower crust, the rapid change in magma chemistry could reflect a relatively discrete temporal point at which the 'amphibole-in' line was suddenly crossed. This could occur either due to a build-up of volatiles following fractionation of anhydrous phases, over a period of at least 1.5 Myrs (**Fig. 5.4**), or because of an injection of new melts into a lower crustal clinopyroxene cumulate pile or 'sponge' that reacts with new melt to become progressively replaced by amphibole (Smith, 2014). The dated porphyry dyke that sits at the temporal onset of mineralisation (AC25; **Fig. 5.4**), and has zircon geochemistry appearing to 'straddle' the pre-and syn-mineralisation signatures, could mark this threshold being crossed in a transitional phase of magmatism, although this is a feature common to all porphyry dykes, regardless of their timing (**Fig. 5.7 & Sup. fig. 5.13-15**).

Although we cannot rule out a model where the change captures a single petrological event in a transitional process, there are several features that do not support progression within a single magma evolution zone. If the change were merely due to a transition in the magma supplied to the upper crust we would perhaps not expect the sharp contacts between the mineralogically distinct McLeod QMD and LHG plutons (Dilles, 1987). A scenario where the fractionating assemblage suddenly changes in a single transitional melt extraction zone is also challenging to reconcile given the variations observed in the isotopic data (**Fig. 5.8**), i.e. from a heterogeneous distribution, indicative of variable interaction with crustal components, to a homogeneous, less contaminated, mantle-derived signature within < 200 kyrs. Instead, magmas being sourced from discrete melt evolution zones within the crust, with pre-mineralisation intrusions evolving at shallower levels, surrounded by country rocks, and the ore-related intrusions evolving within a deeper zone dominated by mantle-derived rocks would be a better fit to the data (**Fig. 5.10**). This idea is also supported by the geochemical indicators of melt evolution depth (**Fig. 5.5-7, Fig. 5.9 & Sup. fig. 5.18**). We envisage that the earlier, pre-mineralisation stage magmas were derived at the mid-crustal staging point. During protracted storage and evolution, these assimilated crustal materials. The magmatic plumbing then shifted to tap magmas from a deeper, lower crustal 'hot-zone' (~ 20–40 km; **Fig. 5.9 & Fig. 5.10**) (Annen et al., 2006), which likely evolved over extended time periods. In this scenario,

the pre-mineralisation geochemical signature of the zircon cargo of the porphyry dykes would be acquired as they intruded up through the pre-cursor magmatic system on route to their level of emplacement. It is also feasible that the mid-crustal melt evolution zones of the McLeod QMD and Bear QM could have remained active post emplacement, or during the evolution of the syn-mineralisation magmas. In addition, the geochemical differences do not exclude progressively more oxidising conditions within the magmatic system (e.g. Dilles et al., 2015), but this is unlikely to have controlled all the observed changes.

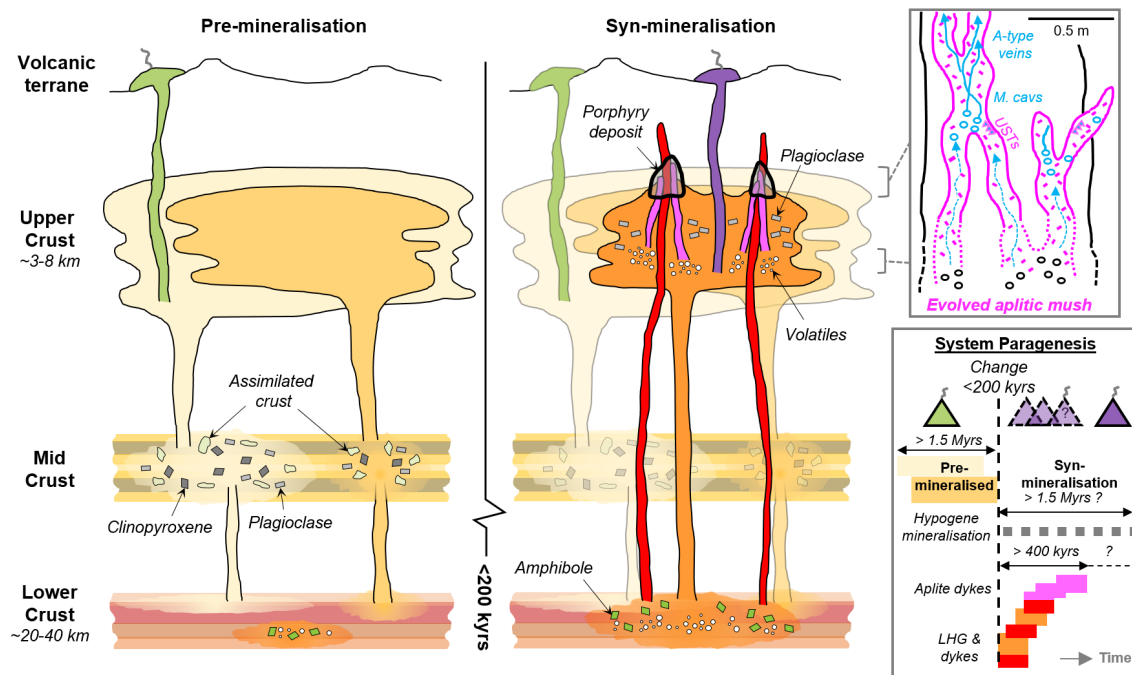


Fig. 5.10 A rapid switch in magmatic plumbing to tap porphyry-mineralising magmas: Simplified system paragenesis and conceptual cross-section through the porphyry deposit forming magmatic system. A long lived (> 1.5 Myrs) evolution and contemporaneous emplacement of precursor plutons, with volcanic activity, was followed by a rapid (< 200 kyr) change in magmatic plumbing to tap fertile porphyry deposit-forming magmas from a ~ 20 - 40 km deep lower crustal staging ground where they predominately underwent amphibole-dominated fractional crystallisation. From this zone of melt evolution, fertile magmas were emplaced into the shallow crust to form plutons and porphyry stocks. These underwent further differentiation at ~ 3 - 8 km depth, including extensive plagioclase crystallisation, with episodic upward injection of multiple generations of aplite dykes for $> \sim 400$ kyr, which likely acted as crystal mush conduits for mineralising fluids (Carter et al., 2021; Chapter 4). As mineralising fluids exploited these conduits, porphyry deposit formation continued episodically for potentially in excess of 1.5 Myrs, and may have been co-eval with volcanism. M. cavs = miarolitic cavities, USTs = unidirectional solidification textures. Vein nomenclature after Gustafson and Hunt (1975). Modified after Annen et al. (2006), Sillitoe (2010) and Carter et al. (2021; Chapter 4).

5.10 Genetic implications for porphyry deposit-forming magmatic systems

The apparent change in geochemistry (whole-rock and zircon; **Fig. 5.5-8**) as the Yerington system began to produce porphyry deposits is consistent with observations from a wide range of similar magmatic centres globally where precursor magmatism and syn-mineralisation intrusions have been examined (e.g. Chiaradia et al., 2009; Dilles et al., 2015; D'Angelo et al., 2017; Nathwani et al., 2020, 2021; Lee et al., 2021). Typically, these changes have been interpreted solely as being due to long-term, tectonically driven arc-scale, transitional processes over millions of years or 'ramp-ups' towards ore-formation (e.g. Ballard et al., 2002; Rohrlach and Loucks, 2005; Loucks, 2014; Rezeau et al., 2016). However, these explanations are relatively poorly constrained due to limited exposure in most porphyry systems (Seedorff et al., 2008). From our studies of the well exposed, ~ 8 km deep cross section through the Yerington system, the possibility exists for a much more rapid (< 200 kyrs) shift to porphyry deposit-forming magmatism. Significant changes in geochemical signatures over relatively short timescales at the transition to porphyry deposit forming magmatism have been indicated elsewhere (e.g. D'Angelo et al. 2017; Nathwani et al., 2021), but this study provides unprecedented temporal and spatial resolution due to the acquisition of our new high precision geochronological framework and the unique depth constraints at Yerington. This short timeframe does not necessarily contradict the suggestion of longer-term progressions towards ore-forming arc magmas, commonly seen in other systems. Rather it captures how rapid changes in the ore-forming potential of the magmatic system may occur. In other porphyry centres, the rapid timescales are often inconspicuous due to the limited rock record available. As such, the much longer durations between precursor and ore-related magmatism documented elsewhere, alongside their corresponding change in geochemistry, may relate to differences in the juxtaposition of upper crustal magmatic expressions over the protracted duration of the magmatic system. For example, when only the shallow levels (e.g. ~ 2 km palaeodepth) are considered at Yerington, porphyry dykes that share a comparable magmatic evolution to the LHG could yield an apparent temporal difference of ~ 1.7 Myrs with the Bear QM they cross-cut. The timescale

of the change in geochemical signatures between these units will appear drawn-out and to have developed over longer timescales, whereas at depth the system is demonstrably more concurrent.

The recognition of rapid changes within the magmatic plumbing system requires a new perspective when interpreting magmatic processes in ore-forming systems. Because the magmas responsible for ore-formation underwent different routes of evolution and likely were tapped from spatially independent, deeper melt zones, it suggests the processes and evolution histories of early-intruded plutons cannot necessarily be used to infer whether other parts of the batholith may have produced porphyry-type deposits, and we advise caution over the use of earlier parts of the magmatic system to infer the nature of what has been removed or added to the melts over longer time periods or apparent progressions of melt chemistry such as metal contents that may be removed by earlier sulphide fractionation (e.g. Park et al., 2019). With lower precision geochronology (e.g. 2% typical of microbeam U–Pb methods), these earlier intrusive phases that emanate from potentially disparate magmatic plumbing systems may even appear to be ‘coeval’ with mineralisation.

The short, < 200 kyrs timescale for the emergence of the geochemical signatures associated with mineralisation that appeared throughout the magmatic system (in plutons, dykes and volcanics) significantly narrows and better defines the temporal footprint that can be used to identify ore-forming processes within the rock record. This has significance in the development and refinement of porphyry exploration indicators by increasing the potential spatio-temporal efficacy of using these geochemical ‘fertility’ signatures to isolate areas most prospective for porphyry-style mineralisation. Whilst the large-scale long-duration, tectonically driven signatures previously identified can still be critical in defining general targets, increased resolution by which the ore forming signature can be discriminated can lead to greater confidence in identifying and discovering the next generation of porphyry deposits, which are likely to be deeper and often under cover and so will be more difficult to find (Cooke et al., 2017).

5.11 Conclusions

From this geochemical and geochronological study of the unique and archetypal Yerington magmatic system, the timing of batholith construction, magmatic evolution and magmatic-hydrothermal porphyry-style mineralisation has been constrained. These findings provide an improved framework for new conceptual models for magmatic systems and batholith construction, porphyry mineralisation and the relationships with volcanism. By doing so we have identified a rapid shift in whole-rock and zircon geochemistry at the onset of porphyry mineralisation. This is attributed to a change from extraction of magmas from mid-crustal reservoirs, to form the McLeod QMD and Bear QM, that had relatively poor ore-forming potential, to extraction of volatile-rich granitic melts from greater (~ 30 km) depths which were emplaced at shallow levels to form the LHG (~ 3–8 km). As the LHG crystallised, late stage melts were emplaced through the carapace as aplite dykes; these provided conduits for the transport of mineralising fluids into the zone of ore formation. The rapidity (< 200 kyrs) of the change in the magmatic system shows that geochemical signatures of certain plutonic and volcanic rocks can be used to interpret the specific magmatic process that eventually lead to porphyry mineralisation. Isolating short-timescale changes in magmatic plumbing, and melt chemistry, in addition to the longer, tectonically-driven multi-million-year timescales of arc-scale magmatic evolution, allows for the refinement and increased efficacy of geochemical ‘fertility indicator’ tools that extend into the volcanic environment, and aid exploration for the next generation of ore deposits.

5.12 Methods

The fundamental first-order controls for this study are from field observations of cross-cutting relationships, disequilibrium phenomena and textures indicative of fluid exsolution and mineralisation in outcrop across the Yerington magmatic system and drill core from the Ann Mason and Yerington porphyry copper deposits. Based on these observations, select samples (full list in **Supplementary Data 5.1**) were chosen for petrographic study (including QEMSCAN®, **Supplementary Data 5.3**), whole-rock XRF and ICP-MS analysis (**Supplementary Data 5.4**), zircon LA-ICP-MS (**Supplementary Data 5.5**) analysis, zircon U-Pb CA-ID-TIMS and Re-Os molybdenite geochronology

(**Supplementary Data 5.2**) and zircon Lu-Hf isotope analysis (**Supplementary Data 5.6**).

5.12.1 QEMSCAN®

Selected samples for the petrographic study were prepared as polished uncovered thin sections (30 µm thickness) at Camborne School of Mines, University of Exeter, UK. Following optical microscopy, the mineralogy of select thin sections was determined using a QEMSCAN® 4300 automated mineralogical assessment system at Camborne School Mines, using the same methods that are described in detail in Carter et al. (2021; Chapter 4). The data were output as mineralogical maps (**Sup. fig. 5.4-6**) with accompanying numerical data (**Supplementary Data 5.3**).

5.12.2 Electric Pulse Fragmentation (EPF)

Initial sample preparation for subsequent whole-rock and zircon analyses was by electric pulse fragmentation (EPF), also known as electrodynamic fragmentation (EDF), electrical disintegration (ED) and electric pulse disaggregation (EPD) (Andres et al., 1999; Bluhm et al., 2000). EPF utilises highly energetic (150–750 J/pulse) pulsed electrical discharges with a fast pulse rise time (<500 ns) to break composite materials apart along internal compositional or mechanical boundaries. Samples are submerged in a dielectric process medium such as water, which is more resistive than solids at these pulse rise times, resulting in the discharge being forced through the relatively conductive solid and along internal phase boundaries such as mineral-mineral contacts. Each discharge event is a movement of electrons from the working electrode to the ground electrode as a plasma channel (Andres et al., 1999; van der Wielen, 2013). The rapid formation of this plasma channel causes explosive expansion within the material along the discharge pathway (Andres et al., 1999; Bluhm et al., 2000). In addition to direct breakage from the plasma channel, this explosion creates a shockwave that propagates through the material. Varying elasticity moduli between minerals results in shear stresses being focussed on mineral contact surfaces, causing intra-mineral breakage and disaggregating the rock. This tensile intra-mineral breakage is less damaging to individual minerals that are liberated from the rock larger and more intact than mechanical crushing.

The treatment was conducted using the ‘Lab’, a laboratory scale EPF device for the batch processing of material, manufactured by SELFRAG AG, Switzerland. The Lab is designed to process samples of up to approximately 1 L volume, or single particles with a top passing size of 40 – 45 mm in a 4 L process vessel filled with de-mineralized water. It produces high voltage (90 – 200 kV) electric discharges of short duration between two electrodes: the ‘working’ electrode is immersed in the upper part of the process vessel, while the bottom of the vessel constitutes the ‘counter/grounding’ electrode. The operating parameters that can be changed are the discharge voltage, electrode gap, pulse repetition rate and number of electric pulses applied to the sample, with treatment conditions for this work listed in **Table 5.1**. Further information on the Lab system can be found in Bru et al. (2020).

Table 5.1 Treatment conditions for electric pulse fragmentation.

Vessel (open/closed)	Sieve Aperture	Voltage	Pulse Repetition Rate	Electrode Gap	Pulses Per Cycle
Open	2 mm	180 kV	5 Hz	40 mm	100

Samples were manually crushed to 40 – 45 mm to fit into the process vessel. From optical studies the zircons have an average grain diameter of ~200 microns, which guided selection of an appropriate aperture sieve for the SELFRAG open process vessel. Appropriate sieve aperture diameter is generally equal to 10x the target particle diameter. A series of 100 pulses were applied to the sample followed by visual inspection of the remaining sample; if >10 % of the sample remained above the sieve, another cycle of 100 pulses were administered. When >90 % of sample material had passed through the sieve, treatment was stopped, and the sample recovered from the process vessel collection cup before drying at 70°C.

5.12.3 Whole-rock XRF and ICP-MS analysis, and CIPW normative mineralogy

Fully quantitative X-ray fluorescence (XRF) for whole-rock geochemistry was performed at the University of Leicester’s Department of Geology on a PANalytical Axios Advanced XRF spectrometer. Major elements were

determined on fused glass beads (prepared from ignited powders; sample to flux ratio 1:5, 80% Li metaborate: 20% Li tetraborate flux) and trace elements were analysed on pressed powder briquettes (32 mm diameter; 7.5 g sample mixed with 15-20 drops 7% PVA solution as binding agent, pressed at 10 tons per sq. inch). Major element results were quoted as component oxide weight percent, recalculated to include loss on ignition (LOI). Information on the standards analysed and the accuracy and precision of the XRF analysis is available in **Supplementary Data 5.4**.

Inductively coupled plasma mass spectrometry (ICP-MS) for whole-rock trace element geochemistry was also performed at the University of Leicester's Department of Geology on a ThermoScientific ICAP-Qc quadrupole ICP mass spectrometer. Analysis for rare earth elements (REEs), Hf, Sr and Y was performed on solution from the same fused glass beads used for XRF analysis. Information on the standards analysed and the accuracy and precision of the ICP-MS analysis is available in **Supplementary Data 5.4**.

Whole-rock XRF geochemistry was used to calculate CIPW normative mineralogy (method of Lowenstern, 2000; after Kelsey, 1965). Normative mineralogy data was then plotted on the H₂O-saturated melt minima ternary plot of Blundy and Cashman (2001) to estimate the pressures of melt differentiation (Annen et al., 2006). Assuming lithostatic conditions, pressures from this plot were used to equate approximate depths of melt differentiation using $P = \rho gh$ and assuming an average overburden density of 2.5 g/cm³. We suggest that these depths only be used as approximations. Samples with very little apparent orthoclase either do not represent H₂O saturated melts, have complex crystal cargoes, or were subject to overprinting by Na-Ca and/or propylitic hydrothermal alteration (as previously mapped, e.g. Dilles et al., 2000; Halley et al., 2015), and were not used in our depth approximations.

5.12.4 Zircon separation

Zircons were separated from disaggregated samples at the British Geological Survey, Keyworth, using the sequentially described circuit: Sieve to <500 µm using a Fritsch automatic sieve; Pass the <500 µm fraction over a Gemini water table, twice; Separate non-magnetic minerals using a Frantz isodynamic

separator - subsequent paramagnetic charges of 0.1 A, 0.3 A, 0.7 A, 1.1 A and 1.7 A were used to reduce the bulk material in stages; Perform gravity separation utilising methylene iodide (ca. 3.32 SG) as a density medium. The final zircon (amongst other phases) separate was thermally annealed at 900°C for 12 hours. Annealed zircon grains were then picked by hand and prepared as polished blocks. Cathodoluminescence (CL) images of these were generated by SEM-CL, using an FEI Quanta 650F FEG-SEM equipped with a Gatan monochrome CL detector at the University of Exeter's Environment and Sustainability institute operating at an accelerating voltage of 20 kV, as well as using a CITL Mk5 electron source, operating at approximately 250 μ A and 10 kV. For the latter, images were captured using a Nikon DS-Ri2 camera, attached to a petrographic microscope, and operated using NiS-elements software. Images were captured in a darkened room, with an exposure time of 2 seconds.

5.12.5 Zircon LA-ICP-MS

Zircon cores and rims were analysed for their trace element geochemistry in the LODE Laboratory at the Natural History Museum, London, using an ESI (New Wave Research) NWR193 excimer laser coupled to an Agilent 7700x quadrupole ICP-MS. Individual zircon grains were located using images obtained by cold-cathode CL and SEM-CL at Camborne School of Mines. A spot size of 30 μ m was used and ablation was performed at a repetition rate of 5 Hz and fluence of 3.5 J/cm². For each spot, approximately 20 seconds of background signal followed by 40 seconds of signal acquisition during ablation. Analytical conditions, including isotopes measured and dwell times are summarised in **Supplementary Data 5.5**.

5.12.6 Zircon U-Pb CA-ID-TIMS geochronology

Chemical abrasion isotope dilution thermal ionization mass spectrometry (CA-ID-TIMS) U-Pb zircon geochronology was undertaken at the Geochronology and Tracers Facility, British Geological Survey, Keyworth. After thermal annealing at 900°C zircon were chemically abraded at 190 °C for 12 hours following Mattinson et al. (2005). The methodology for all other analytical procedures, instrumental conditions, corrections and data reduction follows that outlined in detail in Tapster et al. (2016) using the ET(2)535 tracers (Condon et al., 2015; McLean et al., 2015). Isotope ratio measurements were made using a Thermo Triton thermal

ionization mass-spectrometer (TIMS), with the U decay constants of Jaffey et al. (1971), the $^{238}\text{U}/^{235}\text{U}$ ratio of Hiess et al. (2012), and the decay constants for ^{230}Th of Cheng et al. (2000). The $^{206}\text{Pb}/^{238}\text{U}$ dates were corrected for initial ^{230}Th disequilibrium (Schärer, 1984) upon zircon crystallisation using the zircon/melt partition coefficient $f_{\text{Th/U}}$ of 0.246 (Rubatto and Hermann, 2007). Results are reported in **Supplementary Data 5.2**.

The estimates of igneous crystallisation ages after emplacement are selected from the $^{206}\text{Pb}/^{238}\text{U}$ (Th corrected) weighted mean of the youngest population of data where the date had a statistically acceptable MSWD (Mean square of weighted deviates) for the given population size and attributed 2σ uncertainties, indicating that any dispersion between the selected analyses can be attributable to the measurement of a single population. All samples, with the exception of the volcanic sample BS1, display over-dispersion between the dates of individual zircons or zircon fragment dates in excess of that expected due to analytical scatter. Dates that are older than the statistically valid weighted mean single population are attributed to antecrystic zircon growth, either being sourced from deeper within the magmatic system than the emplacement level or due to protracted crystallisation of zircon upon emplacement. To further evaluate the sensitivity of the age interpretation to the selection of dates we evaluated two further scenarios of date calculation: 1) Selecting the youngest date as being representative of youngest zircon growth; 2) selecting the weighted mean date of the youngest three dates that give a statistically acceptable MSWD. These evaluations of date selections are provided in **Supplementary Data 5.2**, and illustrate that regardless of the approach adopted the timescales we discuss are robust.

When comparing dates either internally or to other data sets that are undertaken with the Earthtime mixed U-Pb tracers (Condon et al., 2015; McLean et al., 2015) only the analytical uncertainties need to be considered. To evaluate U-Pb dates against other isotopic systems, systematic uncertainties must also be acknowledged within the interpretation. The total uncertainty including systematic components from tracer calibration and decay constants are provided with age interpretations in **Supplementary Data 5.2**. For comparison with the Re-Os dates where they include the Re-Os decay constant uncertainty we recommend that

only the tracer calibration uncertainty is considered for the U-Pb data as $\lambda^{187}\text{Re}$ is derived from inter-calibration with U-Pb data (Smoliar et al., 1996; Selby et al., 2007).

5.12.7 Zircon Lu-Hf isotopes

The Lu-Hf fractions were obtained from elements eluted under 3M HCl within the ion exchange U and Pb purification scheme during CA-ID-TIMS U-Pb analysis (e.g. Schoene et al., 2010). Results of the Lu-Hf isotope analysis (Supplementary Data 6) therefore correspond to the same volume of material as the associated zircon U-Pb date. Selecting zircon from the young weighted mean population provides temporal constraints that the volume best captures the nature of the melt upon emplacement. The Lu and Hf elution was dried at 70°C to a chloride before being dissolved in 1 ml of 2% HNO₃ + 0.1M HF, prior to analysis on a Thermo-Electron Neptune Plus mass spectrometer, using a Cetac Aridus II desolvating nebuliser. 0.006 l/min of nitrogen were introduced via the nebulizer in addition to Ar in order to minimise oxide formation. The instrument was operated in static multicollection mode, with cups set to monitor ¹⁷²Yb, ¹⁷³Yb, ¹⁷⁵Lu, ¹⁷⁶Lu+Hf+Yb, ¹⁷⁷Hf, ¹⁷⁸Hf, ¹⁷⁹Hf and ¹⁸⁰Hf. 1% dilutions of each sample were tested prior to analysis, and samples diluted to ca. 20ppb. Standard sample cones and X-skimmer cones were used, giving a typical signal of ca. 800-1000 V/ppm Hf. Correction for ¹⁷⁶Yb on the ¹⁷⁶Hf peak was made using reverse-mass-bias correction of the ¹⁷⁶Yb/¹⁷³Yb ratio empirically derived using Hf mass bias corrected Yb-doped JMC475 solutions (Nowell and Parrish, 2001). ¹⁷⁶Lu interference on the ¹⁷⁶Hf peak was corrected by using the measured ¹⁷⁵Lu and assuming ¹⁷⁶Lu/¹⁷⁵Lu = 0.02653. Data are reported relative to ¹⁷⁹Hf/¹⁷⁷Hf = 0.7325. The Hf standard solution JMC475 was analysed during each analytical session and sample ¹⁷⁶Hf/¹⁷⁷Hf ratios are reported relative to a value of 0.282160 for this standard (Nowell and Parrish, 2001). Eleven analyses of JMC475 gave a mean ¹⁷⁶Hf/¹⁷⁷Hf value of 0.282146 ± 0.000007 (1σ). Typical external precision was in the range between 13-22 ppm. Data were reduced with an in-house calculation and time corrected values include uncertainty propagated from the weighted mean U-Pb date of the sample.

5.12.8 Rhenium-Osmium molybdenite geochronology

Molybdenite Re-Os ages were determined for quartz-chalcopyrite-bornite-molybdenite-quartz veins (samples AC11, AC12 & AC21), a chalcopyrite-molybdenite bearing quartz UST (or vein-dyke texture; e.g. Spurr, 1923; Shannon et al., 1982; Kirkham and Sinclair, 1988) within an aplite dyke (sample AC3) and a fine grained molybdenite vein (sample AC41MP) sampled from drill core from the Ann Mason porphyry deposit. Sample details in **Sup. fig. 5.8** and **Supplementary Data 5.2**.

The Re-Os molybdenite analysis were carried out in the Source Rock and Sulfide Geochemistry and Geochronology, and Arthur Holmes Laboratories at University of Durham (United Kingdom) to establish the Re-Os age of molybdenite mineralisation. A total of eight analyses were conducted. One from samples AC3, AC11, AC12 & AC21 and four from sample AC41MP (For which sample AC41MP was approximately split into four equal subsamples. This offers the opportunity to check the consistency and closed behaviour of the Re-Os system within the vein). Pure molybdenite separates were obtained from the silicate matrix was achieved using the HF purification method (Lawley and Selby, 2012), and then further purified (removal of any pyrite, chalcopyrite and/or bornite and undissolved silicate phases) by hand under a binocular microscope.

An aliquant of the molybdenite separate (~20 mg) together with a known amount of tracer solution (^{185}Re + Os bearing a normal isotope composition) were placed into a carius tube and digested with 3mL HCl and 6mL HNO_3 at 220°C for 24 hrs. Osmium was isolated and purified using solvent extraction (CHCl_3) and micro-distillation methods, with the resulting Re-bearing fraction purified using NaOH-Acetone solvent extraction and anion chromatography (Selby and Creaser, 2004; Li et al., 2017). Although negligible in comparison to the Re and Os abundance in the molybdenite, the final Re-Os data are blank corrected. A full analytical protocol blank run parallel with the molybdenite analysis yields 3.9 pg Re and 0.5 pg Os, the latter possessing a $^{187}\text{Os}/^{188}\text{Os}$ composition of 0.21 ± 0.2 . Data treatment follows that outlined in Li et al. (2017). Osmium mass fractionation was monitored in real time by repeatedly determining the Os isotope composition of the tracer and correcting this to a value of 3.08761 for $^{192}\text{Os}/^{188}\text{Os}$. The isotopic composition of Re was corrected for instrumental fractionation from the difference

between the Re data obtained for the standard and the value of $^{185}\text{Re}/^{187}\text{Re} = 0.59738$ (Gramlich et al., 1973). The data are also oxide corrected, as carried out in many other studies (e.g. Markey et al., 2007; Li et al, 2017). All Re-Os data are given with 2σ absolute uncertainties (**Supplementary Data 5.2**). Molybdenite Re-Os ages are calculated using a ^{187}Re decay constant of $1.666 \times 10^{-11} \text{ y}^{-1}$ with an uncertainty of 0.31% (Smoliar et al., 1996; Selby et al., 2007). The Henderson molybdenite reference material (RM8599) analyzed during the course of this study yields a Re-Os age of 27.62 ± 0.11 (2σ ; $n = 1$), which is in good agreement with the recommended value of 27.66 ± 0.10 Ma (Markey et al., 2007; Zimmerman et al., 2014), and that reported by Li et al. (2017; 27.695 ± 0.038 Ma, $n = 9$) and previous analysis at Durham (e.g., 27.65 ± 0.12 Ma; Lawley and Selby, 2012 and references therein).

5.13 Declaration of co-authorship

L.C.C and B.J.W performed field studies. L.C.C carried out petrographic and textural studies. G.K.R. performed QEMSCAN[®] analysis at Camborne School of Mines. L.C.C., S.R.T and D.B.P. performed sample preparation. L.C.C. and Y.B. performed LA-ICP-MS analyses at the Natural History Museum, London. S.R.T. performed zircon CA-ID-TIMS analyses and I.M. performed zircon Hf-Lu isotope analyses at the British Geological Survey, Keyworth. D.S. performed molybdenite Re-Os analyses at Durham University. L.C.C. wrote the first draft of the manuscript and prepared the figures. All authors contributed to the final version of the manuscript.

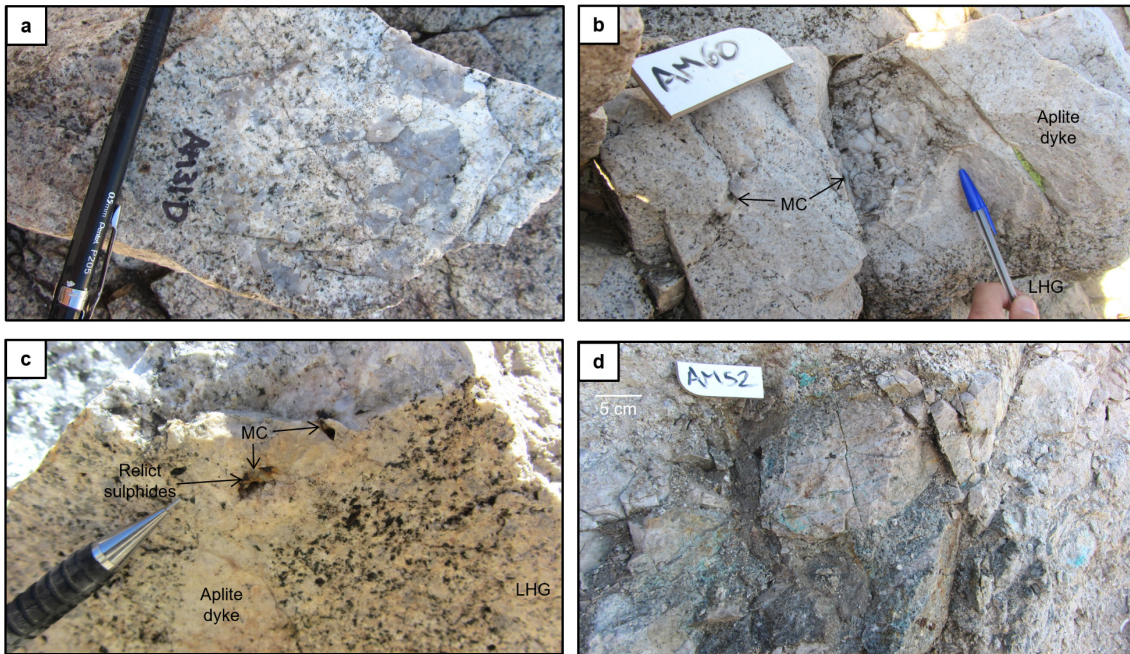
5.14 Supplementary figures



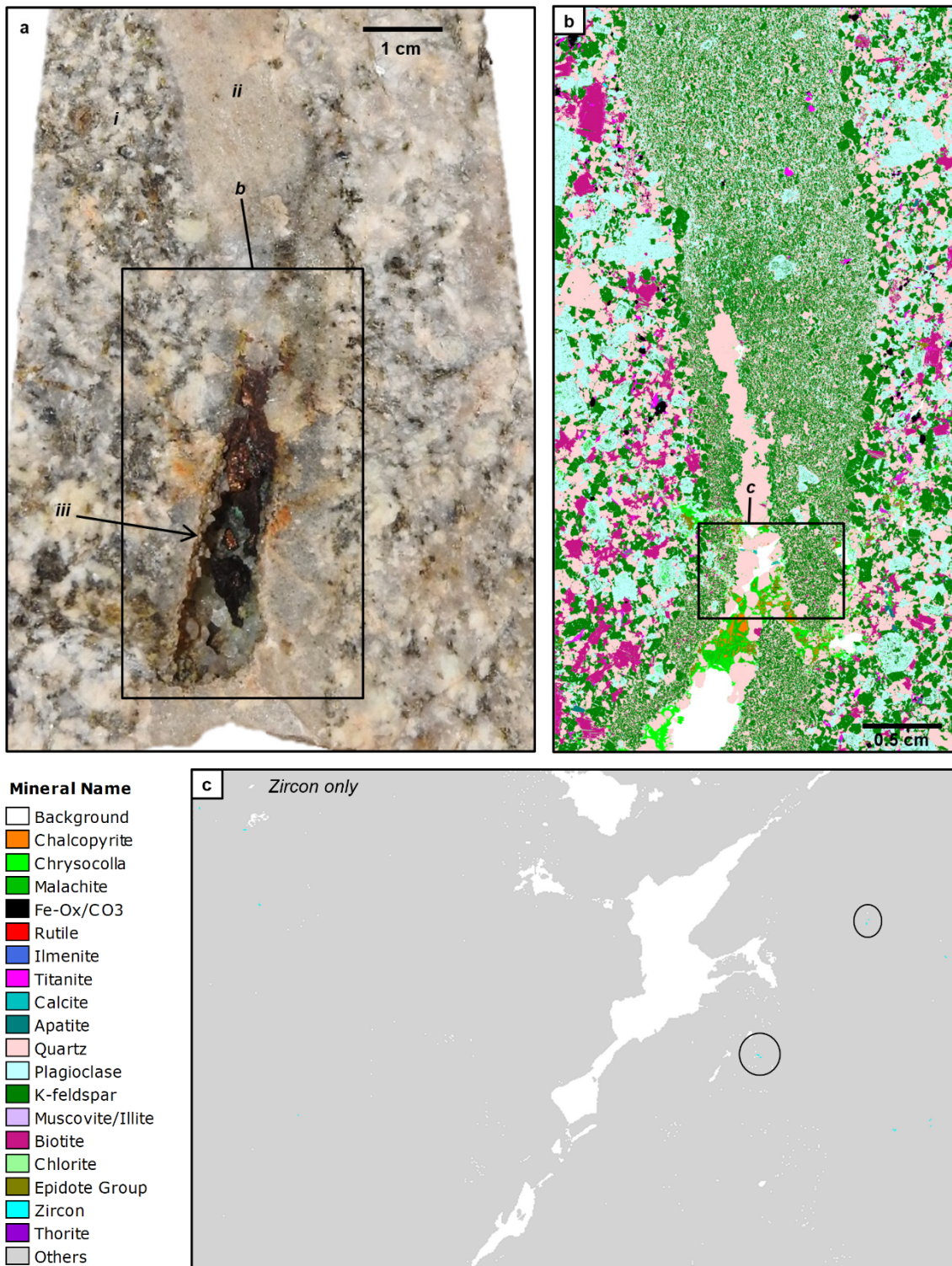
Sup. fig. 5.1 Plutonic contacts: Field photograph of the sharp contact between the McLeod QMD and LHG in the Luhr Hill area. Hammer placed at contact. No chilled margins or evidence of interaction is apparent. No metasomatic effects are present at the contacts beyond the later, pervasive, mostly Na-Ca and propylitic hydrothermal alteration.



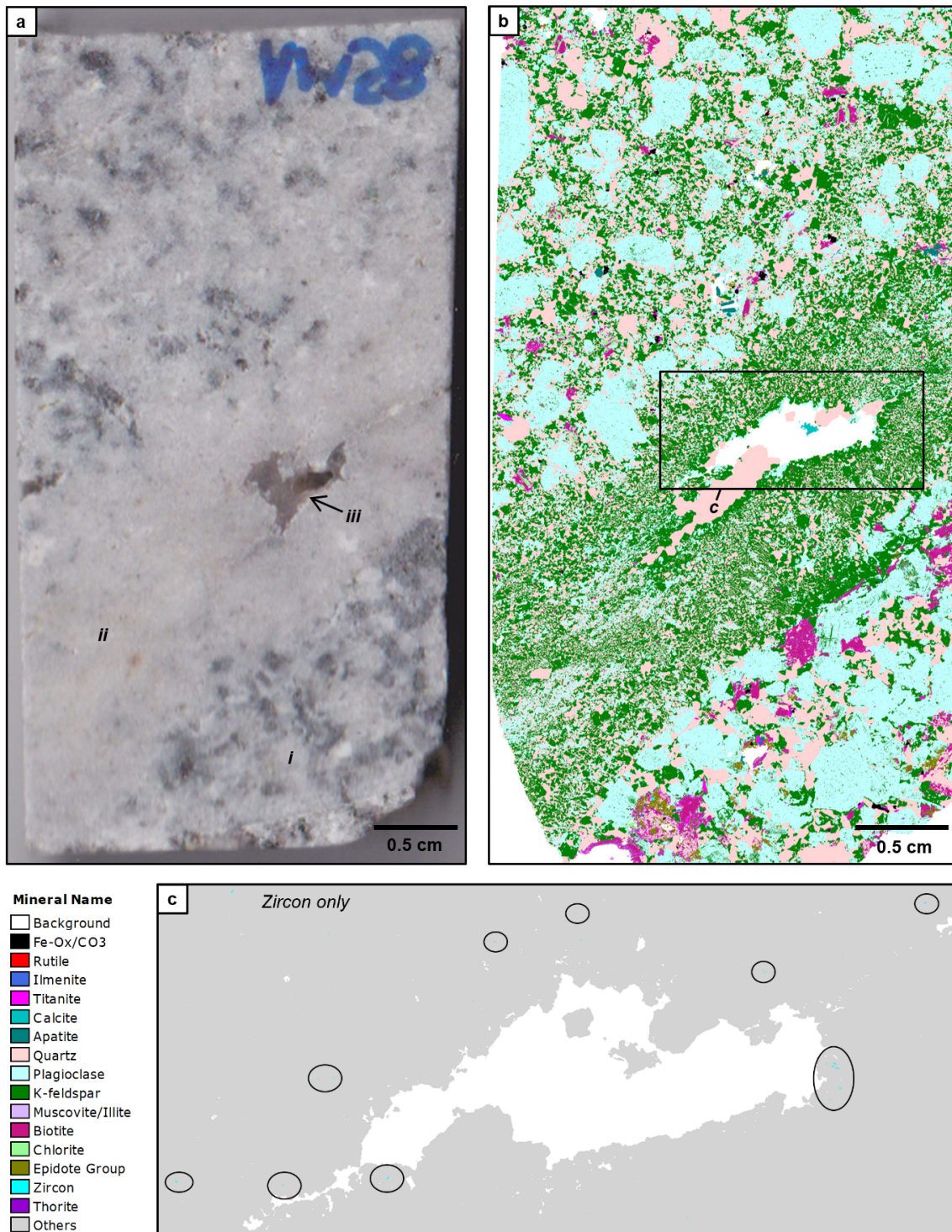
Sup. fig. 5.2 Igneous banding in Luhr Hill granite: Field photograph from a ~7.5 km palaeo-deep portion of the LHG (Luhr Hill area; Dilles, 1987) showing igneous banding, defined by grain size variations. We interpret this texture to be the product of magmatic differentiation processes post emplacement of the granitic melts into the upper crust.



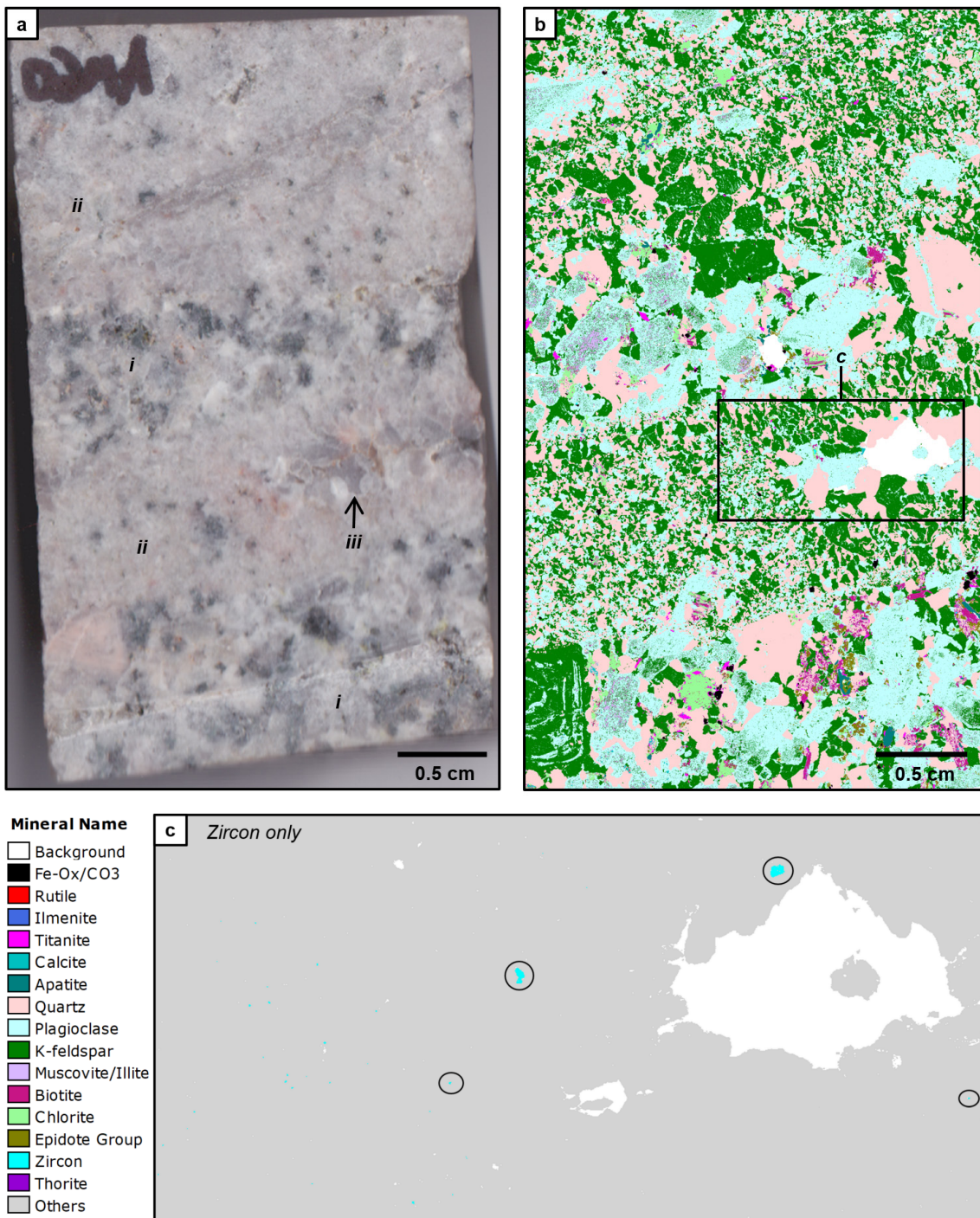
Sup. fig. 5.3 Textural evidence for undercooling, magmatic-hydrothermal fluid exsolution and mineralisation in aplite dykes: Field photographs showing; **a**, Quartz unidirectional solidification textures (USTs) in an aplite dyke which cuts the LHG cupola palaeo-vertically beneath the Ann Mason porphyry deposit; **b & c**, cupola zone of LHG cut by an aplite dyke which hosts mineralised miarolitic cavities (MC); **d**, Mineralised aplite dyke cutting the LHG cupola bearing chalcopyrite-mineralised A- and B-type quartz veins (nomenclature after Gustafson & Hunt, 1975). Secondary copper staining prevalent.



Sup. fig. 5.4 Zircons in aplite dyke which host mineralised miarolitic cavities: **a**, Photograph showing LHG from the cupola zone (*i*) cut by an aplite dyke (*ii*) which hosts hypogene Cu-mineralised miarolitic cavities (*iii*). Box shows location of **b**; **b**, QEMSCAN® mineral map of all phases. Box shows location of **c**; **c**, QEMSCAN® map of only zircon (circled), seen at the margins of the miarolitic cavity within the aplite dyke. This aplite dyke is sample AM13BAP presented in **Fig. 5.4. a & b** from Carter et al. (2021; Chapter 4).



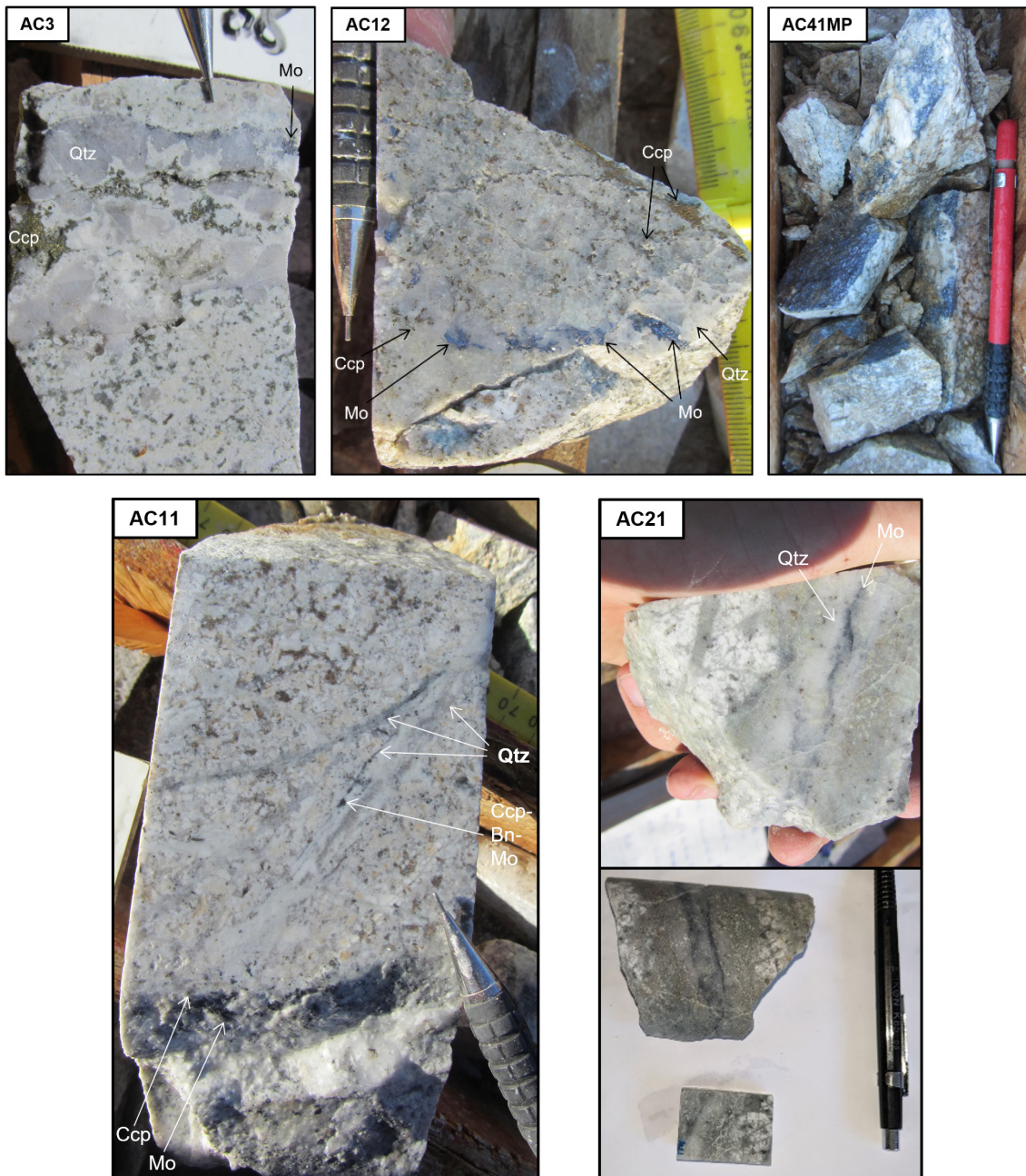
Sup. fig. 5.5 Zircons in aplite dyke which host miarolitic cavities: a, Photograph of rock chip showing LHG from the cupola zone (*i*) cut by an aplite dyke (*ii*) which hosts miarolitic cavities (*iii*); b, QEMSCAN® mineral map of all phases, same field of view as a. Box shows location of c; c, QEMSCAN® map of only zircon (circled), seen at the margins of the miarolitic cavity within the aplite dyke.



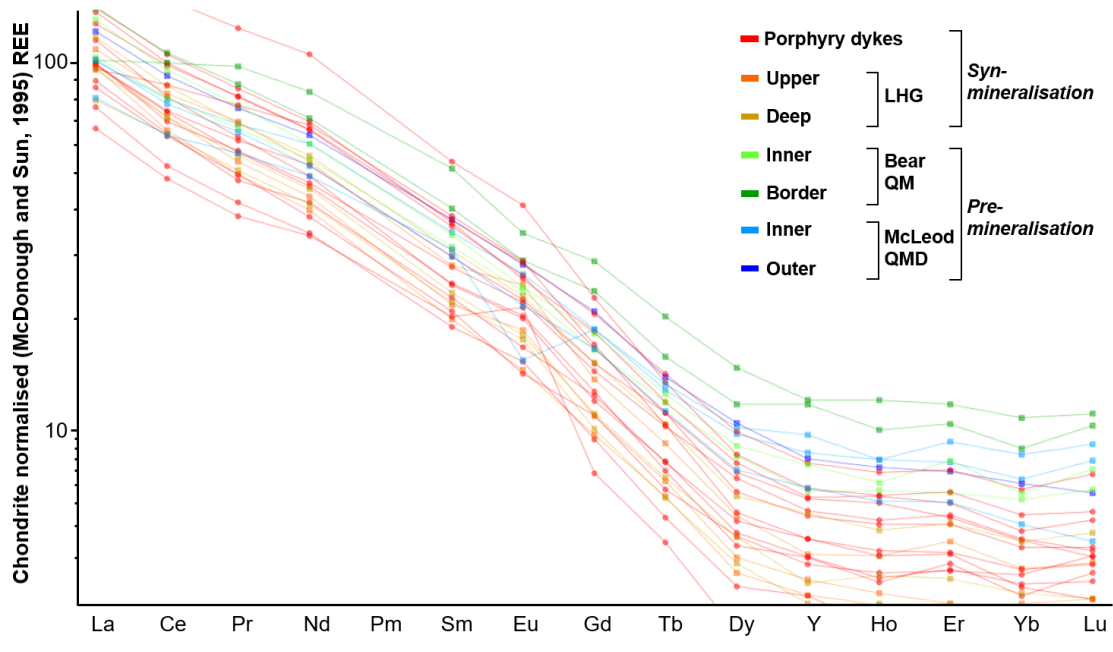
Sup. fig. 5.6 Zircons in aplite dyke which host miarolitic cavities: **a**, Photograph of rock chip showing LHG from the cupola zone (*i*) cut by two aplite dykes (*ii*) which host miarolitic cavities (*iii*); **b**, QEMSCAN® mineral map of all phases, same field of view as **a**. Box shows location of **c**; **c**, QEMSCAN® map of only zircon (circled), seen at the margins of the miarolitic cavity within the aplite dyke.



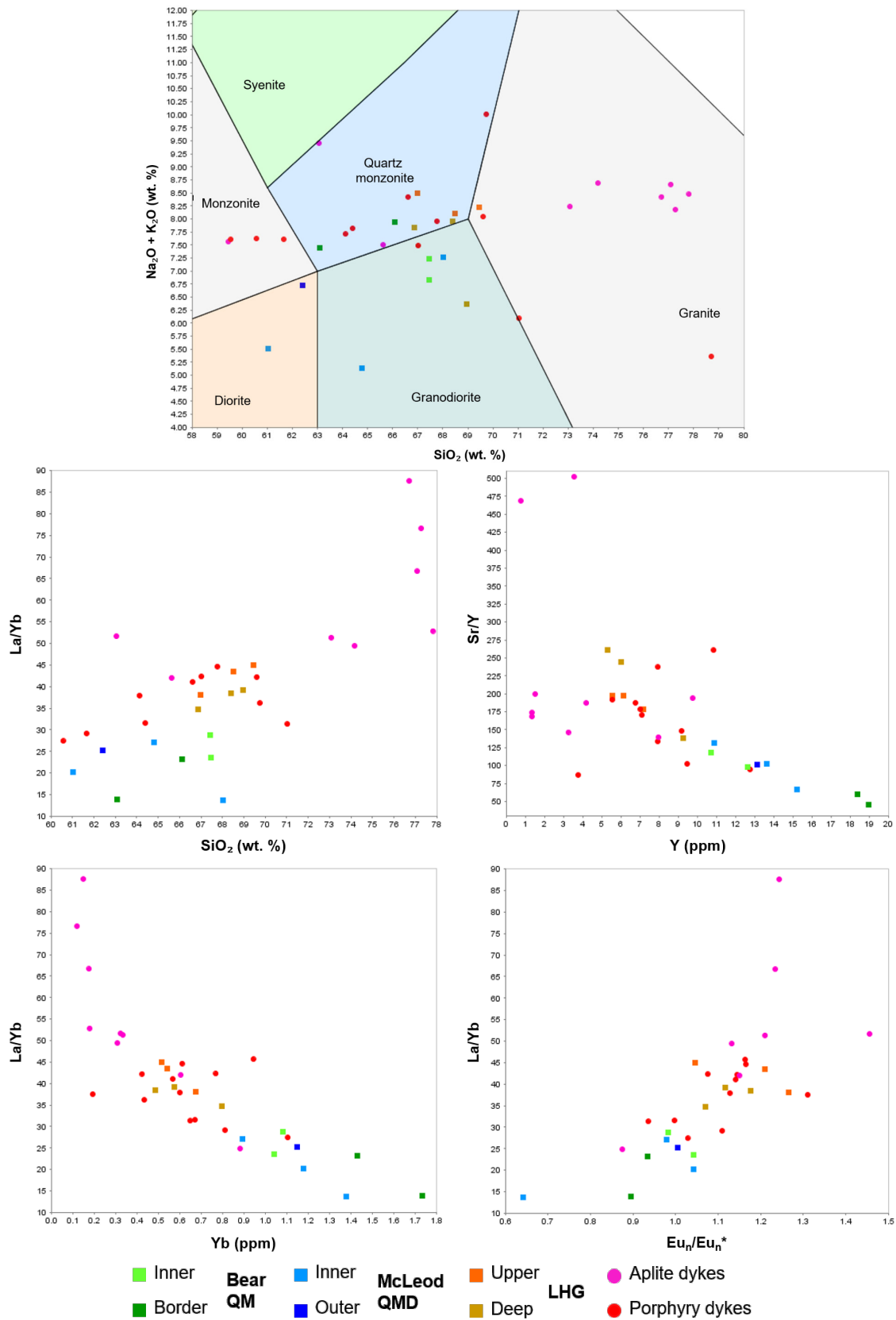
Sup. fig. 5.7 Propylitic alteration in Fulstone Spring Volcanics: which overlie the Yerington porphyry system (Dilles, 1987). Epidote (apple green; Ep) is seen replacing primary plagioclase (milky white; Pl). Pen for scale. Zircon LA-ICP-MS trace element data for this sample (BS10) is presented in **Fig. 5.7**.



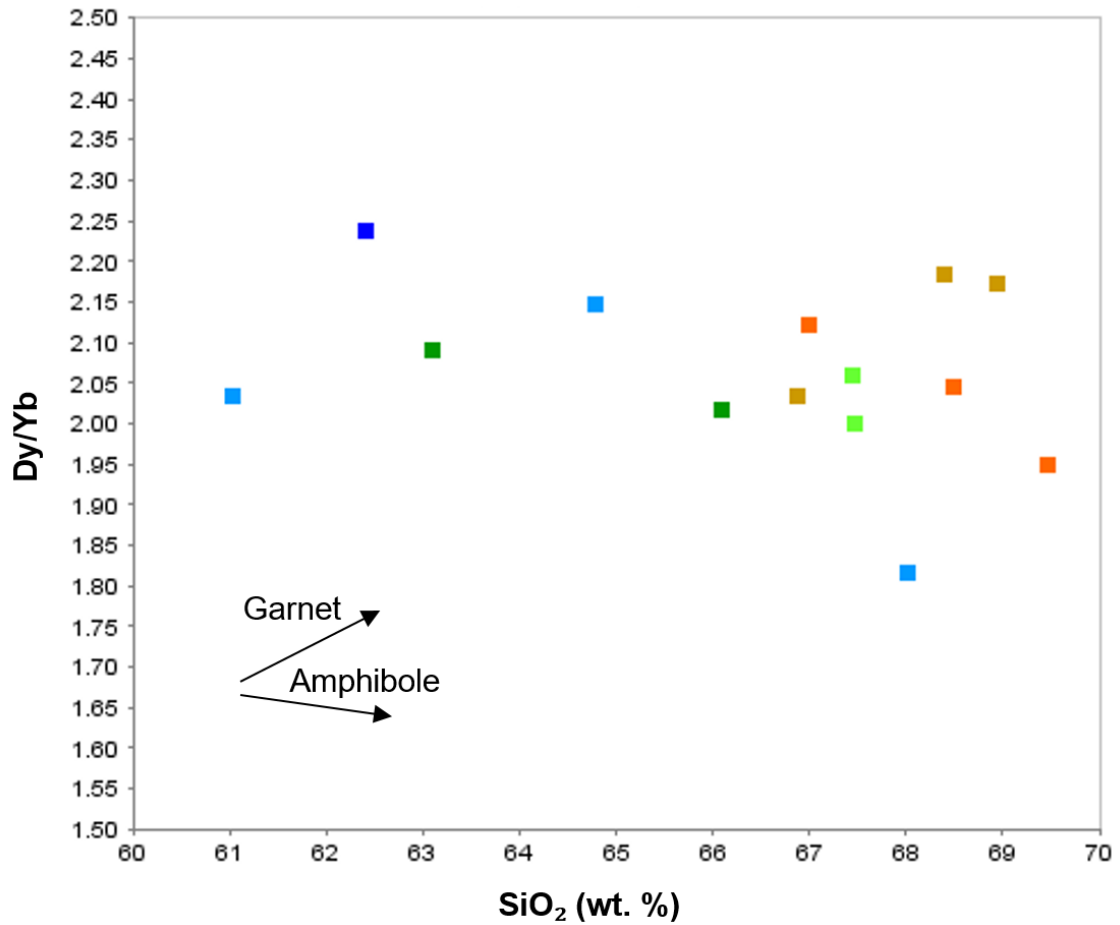
Sup. fig. 5.8 Samples for molybdenite Re-Os age determinations: Photographs of drill core samples from the Ann Mason porphyry copper deposit. Sample AC3 is a chalcopyrite-molybdenite (Ccp-Mo)-bearing quartz (Qtz) UST within an aplite dyke (or vein-dyke texture). Sample AC12 is a chalcopyrite-molybdenite-quartz vein cutting LHG. Sample AC41MP is a fine grained molybdenite vein cutting LHG which was approximately split into 4 equal subsamples. This splitting into subsamples provided the opportunity to check the consistency and closed behaviour of the Re-Os system within the vein. Sample AC11 is of sinuous (A-type) chalcopyrite-bornite(Bn)-molybdenite-quartz veins cutting an aplite dyke and LHG. Sample AC21 of is a planar (B-type) chalcopyrite-molybdenite-quartz vein with ~1 cm K-feldspar halo, with fine grained molybdenite in the central suture. See **Supplementary Data 5.1** for further details.



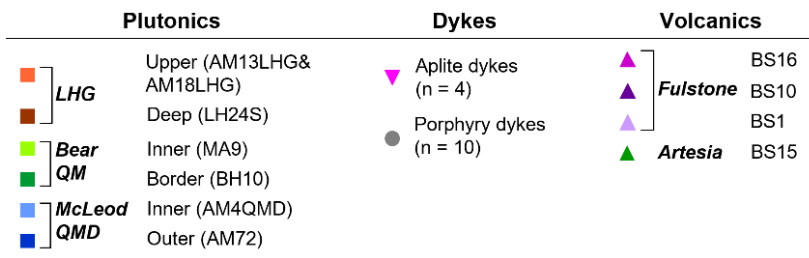
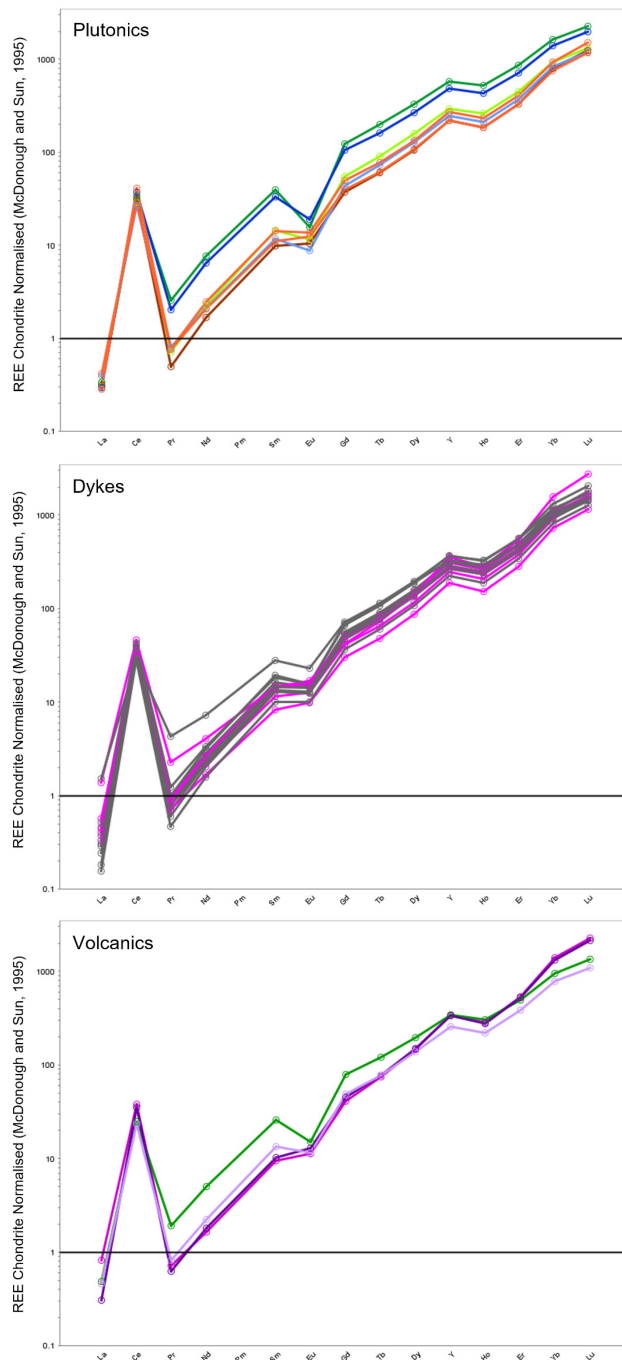
Sup. fig. 5.9 Chondrite-normalized (McDonough and Sun, 1995) mean whole-rock REE plots



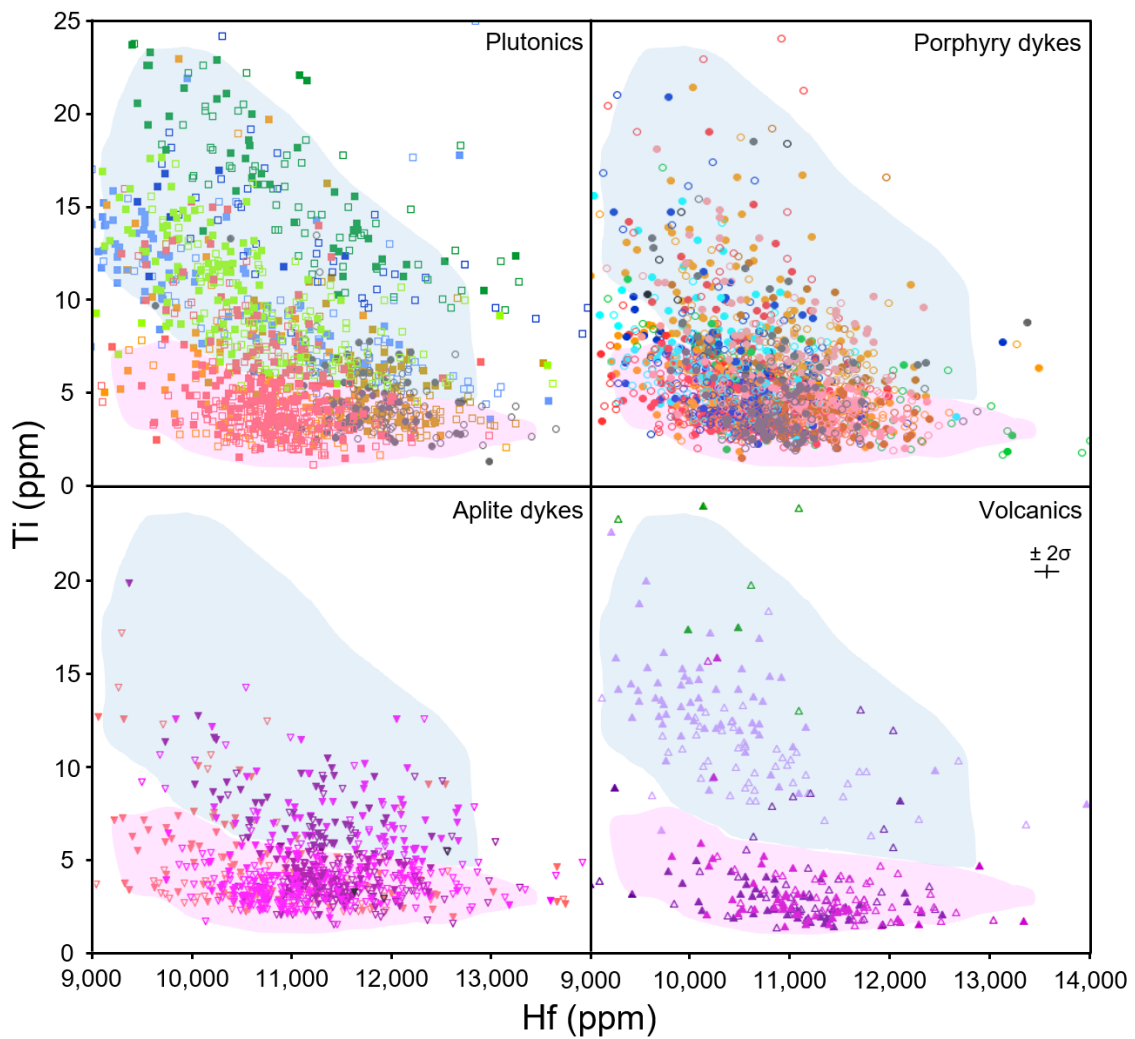
Sup. fig. 5.10 Plutonic TAS diagram (Middlemost, 1994) and whole-rock geochemistry through the Yerington magmatic system. Major elements partially overlap between the mineralogically distinct (Dilles, 1987) intrusive units. Distinct differences between pre- and inter-mineralisation units are seen in trace element ratios.



Sup. fig. 5.11 Dy/Yb versus SiO₂ for plutonic units. Whilst Dy/Yb values remain ~2, a slightly negative trend is seen with increasing SiO₂ content, following the amphibole fractionation trend and suggesting that garnet did not play a role in the geochemical evolution of the system. Vectors for garnet and amphibole fractionation from Davidson et al. (2007).

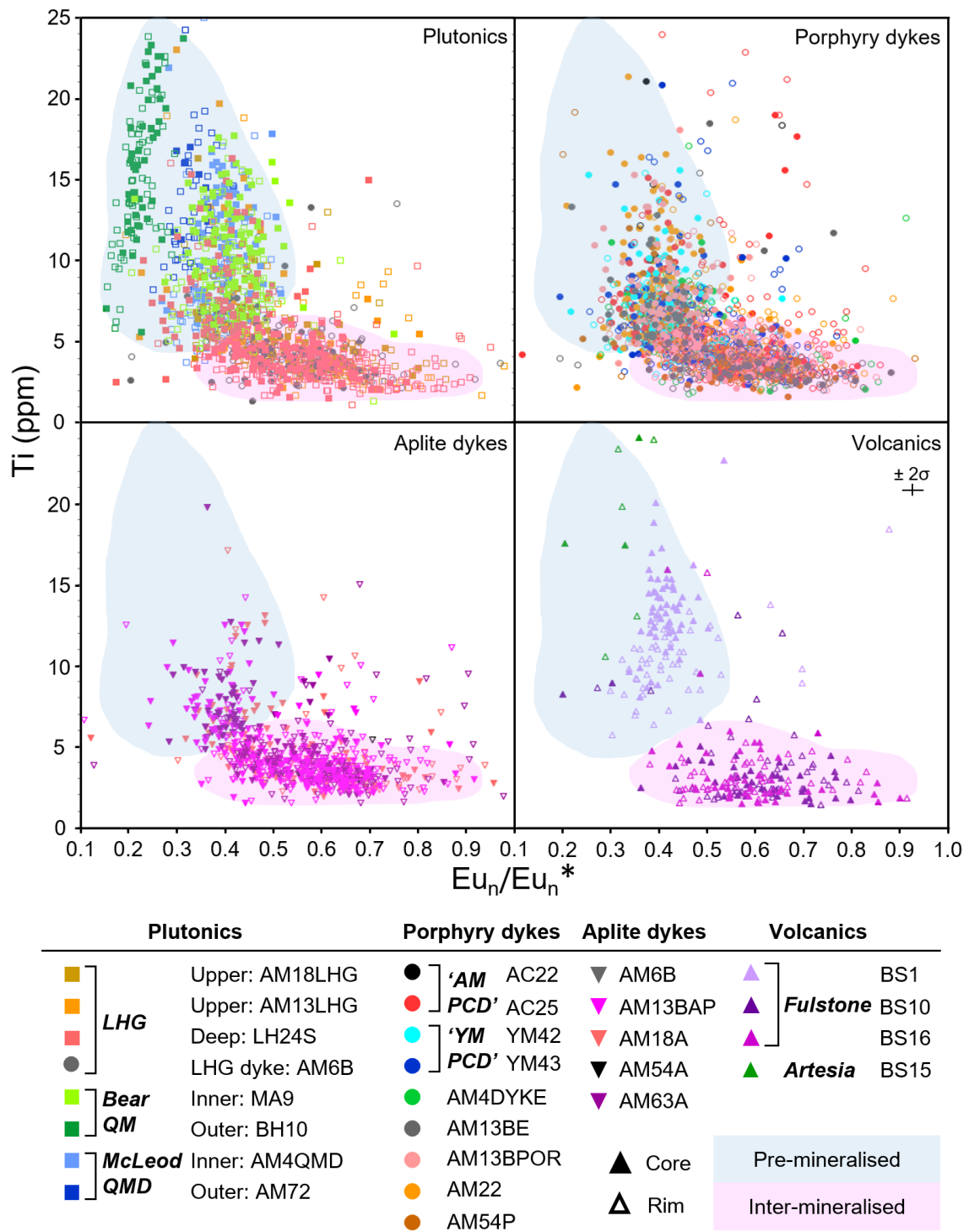


Sup. fig. 5.12 Zircon REE patterns: Zircon LA-ICP-MS REE patterns from samples temporally and spatially spanning the Yerington magmatic system.



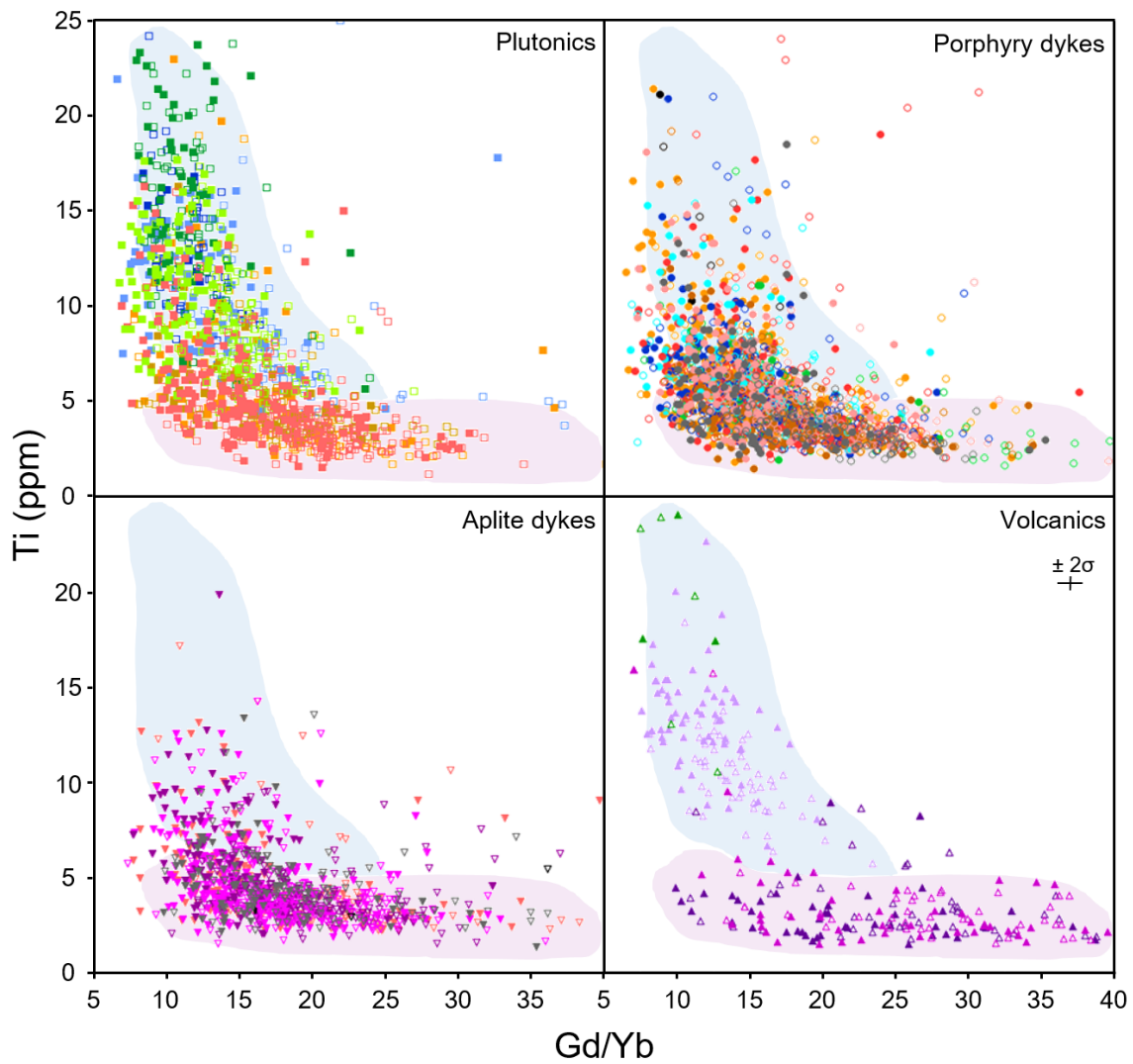
Plutonics		Porphyry dykes		Aplite dykes		Volcanics	
■	Upper: AM18LHG	●	'AM' AC22	▼	AM6B	▲	BS1
■	Upper: AM13LHG	●	'PCD' AC25	▼	AM13BAP	▲	Fulstone BS10
■	Deep: LH24S	●	'YM' YM42	▼	AM18A	▲	BS16
●	LHG dyke: AM6B	●	'PCD' YM43	▼	AM54A	▲	Artesia BS15
■	Inner: MA9	●	AM4DYKE	▼	AM63A		
■	Outer: BH10	●	AM13BE				
■	Inner: AM4QMD	●	AM13BPOR	▲	Core		Pre-mineralised
■	Outer: AM72	●	AM22	▲	Rim		Inter-mineralised
		●	AM54P				

Sup. fig. 5.13 Zircon trace element signatures through the Yerington magmatic system: Zircon LA-ICP-MS trace element data from samples spanning, temporally and spatially, the Yerington magmatic system. Both core and rim data plotted. 'Pre-mineralised' and 'inter-mineralised' fields shaded. AM = Ann Mason porphyry deposit. YM = Yerington porphyry deposit.



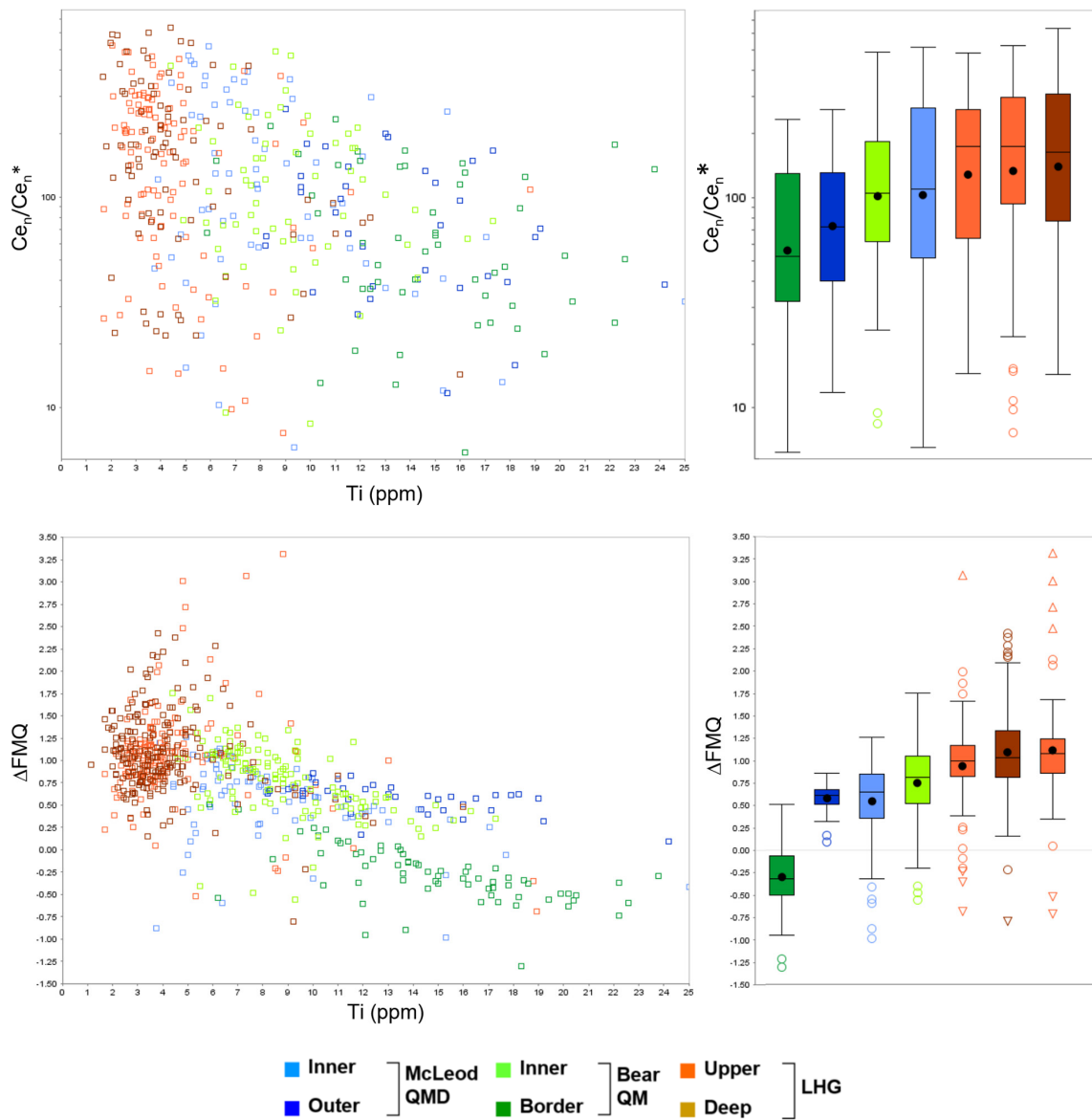
Sup. fig. 5.14 Zircon trace element signatures through the Yerington magmatic system:

Zircon LA-ICP-MS trace element data from samples spanning, temporally and spatially, the Yerington magmatic system. Both core and rim data plotted. 'Pre-mineralised' and 'inter-mineralised' fields shaded. AM = Ann Mason porphyry deposit. YM = Yerington porphyry deposit.

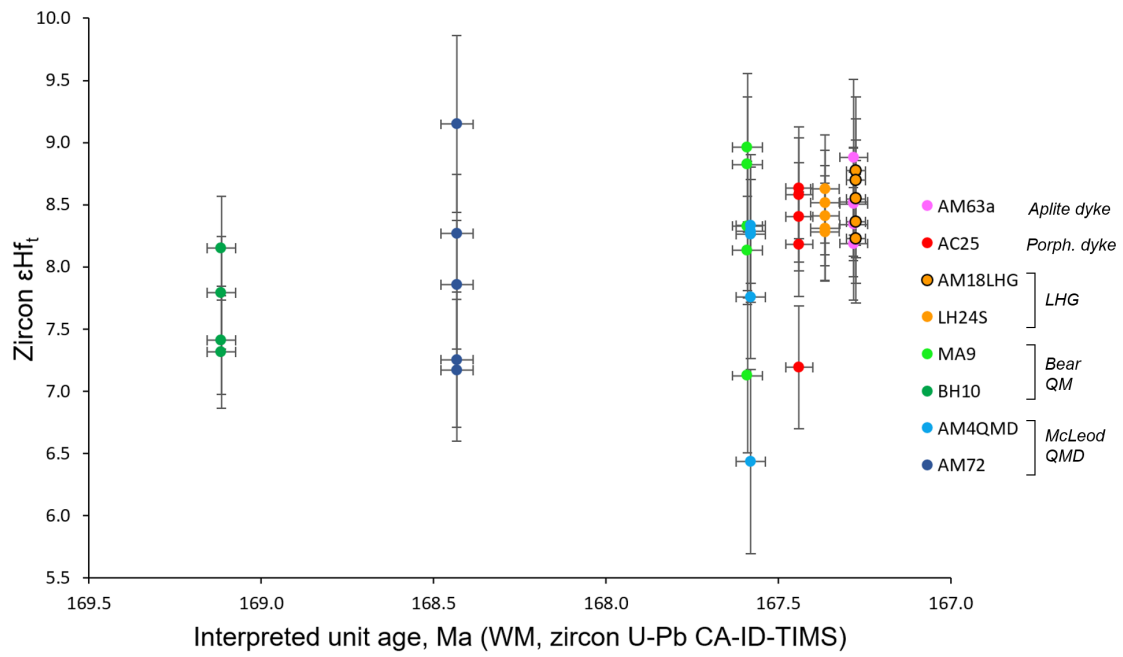


Plutonics		Porphyry dykes		Aplite dykes		Volcanics	
■	Upper: AM18LHG	●	'AM' AC22	▼	AM6B	▲	BS1
■	Upper: AM13LHG	●	'PCD' AC25	▼	AM13BAP	▲	Fulstone BS10
■	Deep: LH24S	●	'YM' YM42	▼	AM18A	▲	BS16
●	LHG dyke: AM6B	●	'PCD' YM43	▼	AM54A	▲	Artesia BS15
■	Bear Inner: MA9	●	AM4DYKE	▼	AM63A		
■	QM Outer: BH10	●	AM13BE				
■	McLeod Inner: AM4QMD	●	AM13BPOR	▲	Core		Pre-mineralised
■	QMD Outer: AM72	●	AM22	▲	Rim		Inter-mineralised
		●	AM54P				

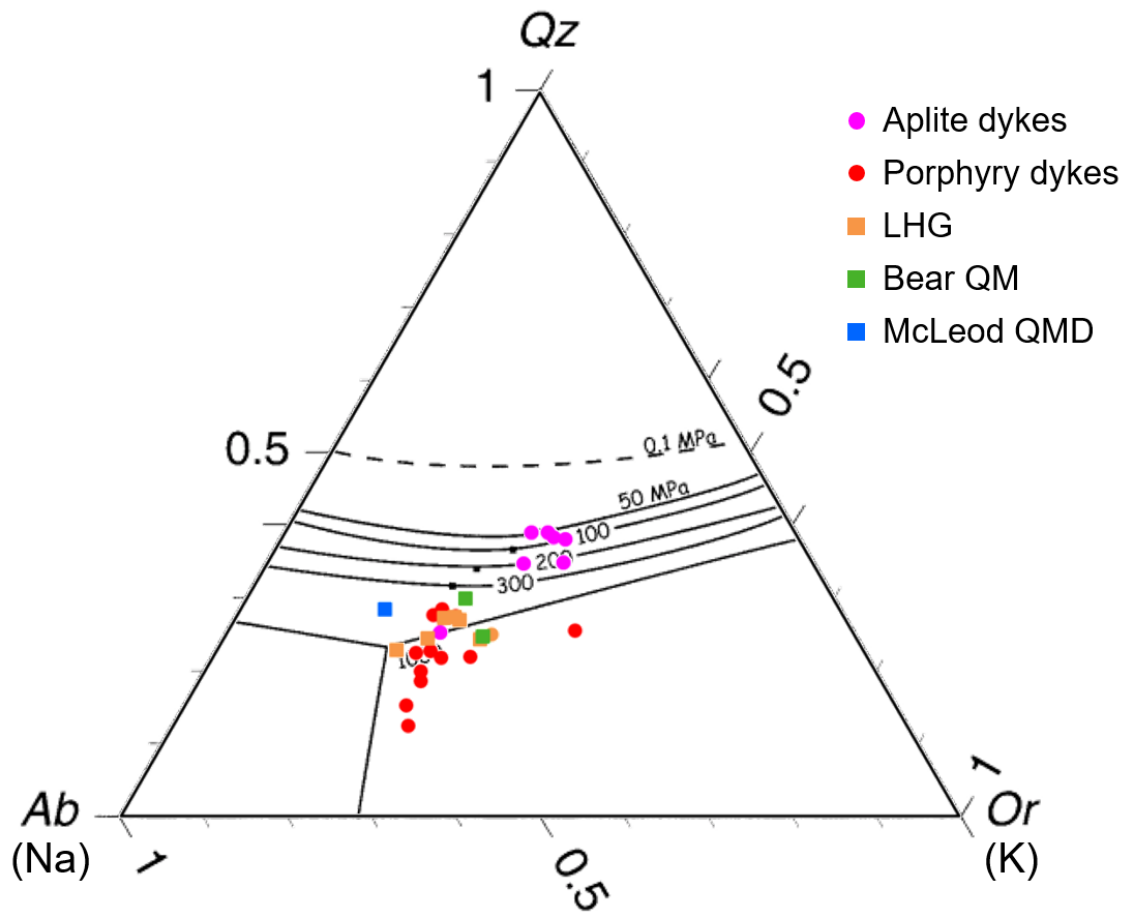
Sup. fig. 5.15 Zircon trace element signatures through the Yerington magmatic system: Zircon LA-ICP-MS trace element data from samples spanning, temporally and spatially, the Yerington magmatic system. Both core and rim data plotted. 'Pre-mineralised' and 'inter-mineralised' fields shaded. AM = Ann Mason porphyry deposit. YM = Yerington porphyry deposit.



Sup. fig. 5.16 Zircon trace element signatures for plutonic units of the Yerington porphyry system: Ce/Ce^* versus Ti; Ce/Ce^* box and whisker plot; ΔFMQ versus Ti; ΔFMQ box and whisker plot. Ce/Ce^* calculated using method of Loader et al. (2017). ΔFMQ calculated using method of Loucks et al. (2020). Only zircon rim data plotted.



Sup. fig. 5.17 Zircon ϵHf_t through the Yerington magmatic system: Time corrected zircon ϵHf (ϵHf_t) versus interpreted zircon age for samples spanning the Yerington magmatic system. Age determinations for each sample are weighted mean (WM) from zircon single grain U-Pb CA-ID-TIMS analyses, with error bars at 2σ (**Fig. 5.4**). ϵHf_t error bars 2σ .



Sup. fig. 5.18 Depth of different magma sources: CIPW normative mineralogy (method of Lowenstern, 2000) from whole-rock XRF data plotted on the H₂O-saturated haplogranitic melt minima plot of Blundy and Cashman (2001). Cotectic lines and eutectics are a function of pressure and therefore the whole-rock data can be used to provide constraints for the pressure of magma differentiation (Annen et al., 2006), from which depth can be approximated. Porphyry dyke samples are plotted here in addition to the McLeod QMD, Bear QM, LHG and aplite dyke samples plotted in **Fig. 5.9**. Porphyry dykes appear to plot along with the LHG samples around the ~450-1000 MPa minima. Samples overprinted by pervasive Na-Ca alteration are not plotted.

5.15 Supplementary data

Supplementary Data 5.1: Full sample list

Supplementary Data 5.2: Zircon U-Pb CA-ID-TIMS and molybdenite Re-Os geochronology data

Supplementary Data 5.3: QEMSCAN[®] automated mineralogical assessment data

Supplementary Data 5.4: Whole-rock XRF & ICP-MS geochemistry data

Supplementary Data 5.5: Zircon LA-ICP-MS data

Supplementary Data 5.6: Zircon Lu-Hf isotope data

Supplementary Data files are available at <https://doi.org/10.5285/5a4bc758-ac88-4715-a665-81f69108f854>

6 Synthesis and outlook

6.1 The Yerington batholith - Construction and magmatic-hydrothermal mineralisation

Construction of the Yerington batholith commenced with emplacement of the McLeod quartz monzodiorite and Bear quartz monzonite plutons over at least 1.5 Myrs (~169.1 Ma to ~167.6 Ma). These were emplaced episodically giving rise to internal boundaries and dyke-like bodies (Dilles, 1997). Previous models for the assembly of the Yerington batholith (Dilles, 1987; Dilles et al., 2000; Schöpa et al., 2017) suggested sequential emplacement of the McLeod quartz monzodiorite and Bear quartz monzonite, yet the revised chronology (Carter et al., 2021; Chapter 5) show that these two intrusive units crystallised and must have been emplaced, at least in part, over the same ~800 kyrs time period (~168.4 Ma – ~167.6 Ma), indicating that their magmatic source zones must have been active contemporaneously.

Whilst being texturally and mineralogically distinct (Dilles, 1987), the McLeod quartz monzodiorite and Bear quartz monzonite have very similar isotopic signatures and whole-rock and zircon geochemical compositions suggesting that the magmas they formed from were derived from the same source. From trends in their major and trace element concentrations and zircon geochemistry, the McLeod and Bear magmas underwent clinopyroxene-plagioclase-dominated fractionation, and, from their ϵHf_t isotopic signatures, contamination with crustal components. Along with their position on the H_2O -saturated haplogranitic melt minima plot of Blundy and Cashman (2001) (using normative compositions, although this is based on a limited number of data points), this is likely to have been in the mid- to lower continental crust (likely ~15-20 km depth) (Carter et al., 2022; Chapter 5). Similar zircon geochemical characteristics are shown by the overlying Artesia Lake Volcanics and early units of the Fulstone Spring Volcanics. This, along with overlapping zircon U-Pb ages, suggests that the formation of the McLeod and Bear plutons was associated with volcanism.

The intrusion of the Luhr Hill granite into the McLeod and Bear plutons at ~167.4 Ma was marked by a rapid (<200 kyrs) and abrupt change in magma chemistry which is attributed to a switch in its source and associated plumbing system. This

switch coincided with the onset of mineralisation in the Yerington District. From its whole-rock and zircon geochemical characteristics, the Luhr Hill granite had a deeper, lower crustal (~20-40 km deep), source than the McLeod and Bear plutons (~15-20 km depth) and the magmas underwent amphibole- rather than clinopyroxene-plagioclase-dominated fractionation. In addition to this, the Luhr Hill granite shows no discernible contribution from crustal components, which suggests that they acquired their relatively evolved compositions solely as a result of fractionation of mantle-derived magmas (Carter et al., 2022; Chapter 5).

From cross-cutting relationships, the emplacement of porphyry dykes through the cupolas of the Luhr Hill granite, at around ~167.4 Ma, is known to have marked the onset of porphyry-style mineralisation (e.g. Proffett, 1979; Dilles, 1987; Dilles and Proffett, 1995). This age was determined from U-Pb dating of zircons from mineralised porphyry dykes and the Luhr Hill granite cupola, and further constrained from the youngest ages for the McLeod quartz monzodiorite and Bear quartz monzonite (Carter et al., 2022; Chapter 5). As the porphyry dykes have indistinguishable ϵ_{Hf} isotopic signatures to the Luhr Hill granite, and, based on their position on the H₂O-saturated haplogranite melt minima plot, were derived from comparable depths, they are likely to have had the same deep source (i.e. at around 20-40 km depth; Carter et al., 2022; Chapter 5), rather than being derived from a magma storage zone in the upper parts of the Luhr Hill granite, as previously proposed by Dilles (1987).

Intense undercooling of the Luhr Hill granite magmas as they were emplaced at shallow, ~3-8 km, depths caused the formation of pegmatitic pods and massive silica bodies (Carter and Williamson, 2022; Chapter 3). Cupolas, in apical parts of the Luhr Hill granite, crystallised to become carapaces whilst the magmas continued to evolve in deeper parts of the pluton to form more volatile-rich melts. These were episodically emplaced as multiple generations of aplite dykes over a period of at least ~400 kyrs (Carter et al., 2022; Chapter 5), probably via new or reactivated existing faults (Richards, 2018). Repeated pressure fluctuations within the aplite dykes, due to cyclical hydraulic fracturing and 'first-type boiling' (Candela, 1989), led to the formation of USTs prior to fluid saturation; USTs in aplite dykes are referred to as 'vein dykes' elsewhere (Shannon et al., 1982; Kirkham and Sinclair, 1988). Fluid exsolution led to the production of miarolitic

cavities and caused an increase in fluid pressure, triggering further fracturing (and reactivation of previous fractures), and the formation of quartz selvages and A-type veins. Associated pressure drops resulted in more USTs (Carter et al., 2021; Carter and Williamson, 2022; Chapter 3 & 4). Continued upward flow of fluids from deep within the Luhr Hill granite pluton, through still permeable 'crystal mush' aplite dykes (Carter et al., 2021; Chapter 4), and further hydraulic fracturing throughout the system, caused progressive evolution towards the production of AB- and B-type veins and disseminated mineralisation. These same processes occurred concurrently in vast numbers of dykes at different levels to give the complex cross-cutting relationships between dykes and vein generations typical of porphyry-type deposits.

From zircon U-Pb and molybdenite Re-Os age determinations, hydrothermal mineralisation is likely to have occurred episodically over >1.5 Myrs, post-emplacement of the Luhr Hill granite. Mineralisation was roughly coincident with the eruption of the younger propylitically-altered components of the Fulstone Spring Volcanics, which contain the same zircon geochemical signatures as the Luhr Hill granite (Carter et al., 2022; Chapter 5).

6.2 Plumbing of porphyry deposit-forming magmatic systems

Magmatic systems that produce porphyry-type deposits are known to have distinctive 'fertile' whole-rock and mineral (e.g. zircon) geochemical signatures (e.g. Loucks, 2014; Lu et al., 2016), which are being increasingly used in exploration (e.g. Cooke et al., 2017). Their compositions are mostly used to assess melt fO_2 and water contents as 'fertile' magmas are usually at least moderately oxidising and water-rich (e.g. Rohrlach and Loucks, 2005; Richards, 2011; Chiaradia et al., 2012; 2015; Richards et al., 2012; Wilkinson, 2013; Loucks, 2014; Lu et al., 2016; Williamson et al., 2016; Nathwani et al., 2020; Lee et al., 2021). Changes in geochemical signatures between pre- and inter-mineralisation intrusives have been observed across a range of porphyry deposit-forming magmatic systems (e.g. Chiaradia et al., 2009; Dilles et al., 2015; Nathwani et al., 2021; Lee et al., 2021), and interpreted to be due to millions of year-, tectonically-driven, arc-scale 'ramp-ups' towards ore-formation (e.g. Ballard et al., 2002; Rohrlach and Loucks, 2005; Loucks, 2014; Rezeau et al., 2016). However, these models, which are based on observations from a range of

localities, are poorly constrained as almost all porphyry systems are only partly exposed (Seedorff et al., 2008).

The rapid (<200 kyrs) switch in source and fractionating assemblage between the formation of the pre-mineralisation McLeod and Bear plutons and inter-mineralisation Luhr Hill granite was at least an order of magnitude faster than previously envisaged. The rapid nature of the switch may not be evident in other systems due to poor exposure or the lower precision of previous geochronological studies (e.g. 2% typical of microbeam U-Pb methods). It also highlights the need to reassess published numerical models on the rates of assembly of the Yerington batholith such as that provided by Schöpa et al. (2017) which was based on the outdated geochronological framework of Dilles and Wright (1988).

The <200 kyrs period of the switch is considerably less than the multi-million year arc-scale magmatic 'ramp-up' previously thought necessary to produce a fertile system (Ballard et al., 2002; Richards, 2003; Rohrlach and Loucks, 2005; Chiaradia et al., 2009; Loucks, 2014; Rezeau et al., 2016; Chiaradia and Caricchi, 2017; Lee and Tang, 2020; Nathwani et al., 2021). Rather than being driven by a protracted magmatic evolution or macro-tectonic deepening, it is therefore likely that fertility was enhanced by short duration magmatic processes during partial melting and/or melt evolution. A likely causative process, rapid enough for the switch, was the injection of mantle-derived magmas into a lower-crustal 'hot-zone'. This could have triggered a change in the magma plumbing system to extract melts from a more fertile melt evolution zone (**Fig. 6.1**).

An additional implication of the switch, important in exploration, is that the nature of pre-mineralisation plutons cannot necessarily be used to infer whether later intrusives produced porphyry-type deposits. In the Yerington batholith, the pre-mineralisation McLeod and Bear plutons were emplaced at higher levels than the Luhr Hill granite and therefore, if the upper crust had not been tilted tectonically, mineralisation associated with the latter may have been blind or too deep to be discovered.

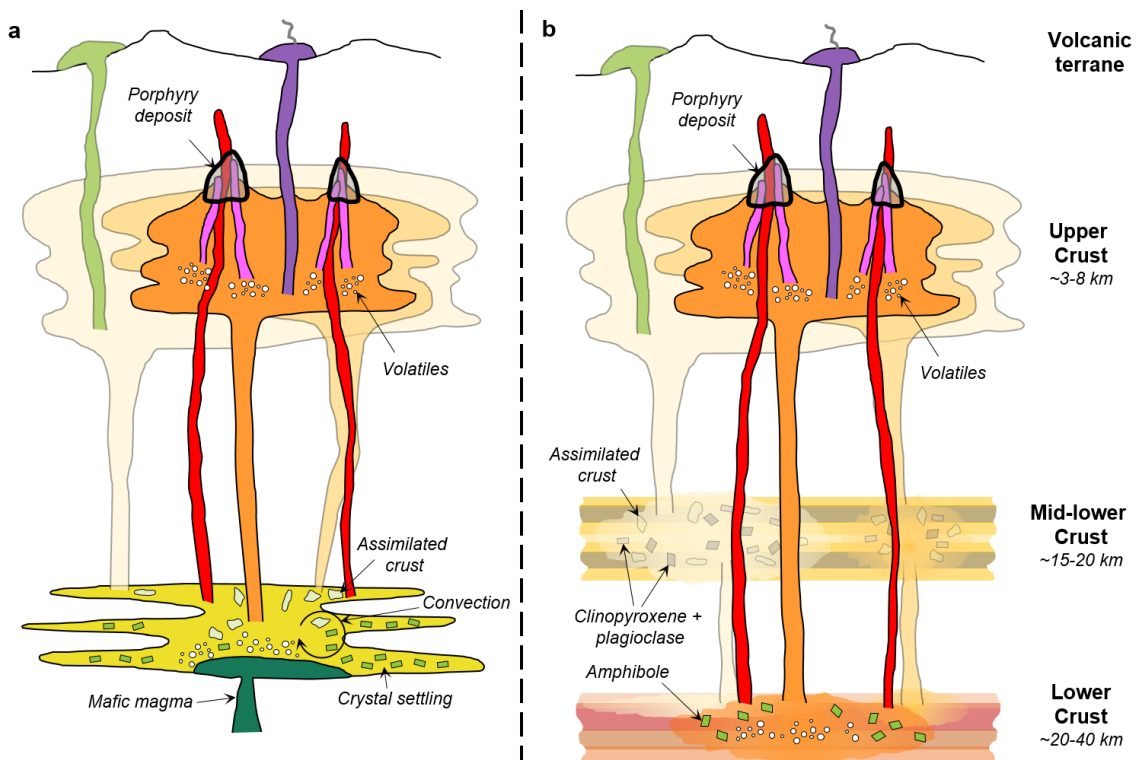


Fig. 6.1 Schematic models for the plumbing of porphyry deposit-forming magmatic systems: **a**, Protracted (multi-million year) evolutionary arc-scale 'ramp-up' towards ore-forming magmatism. Modified after Wilkinson (2013). **b**, An abrupt switch in magmatic plumbing to tap ore-forming magmas from a lower-crustal 'hot-zone'. Modified Carter et al. (2022; Chapter 5).

6.3 Crystal mush fluid conduits in porphyry systems

It is well understood that porphyry-type deposits are spatially and temporally associated with plutonic activity in subduction-related magmatic arcs (e.g. Richards, 2005; Seedorff et al., 2005; Sillitoe, 2010), but the mechanisms by which mineralising fluids are extracted and focused into narrow, shallow (ca. 2-5 km) zones of economic mineralisation in these systems has remained uncertain. Traditional models, which invoke the direct release of mineralising fluids from porphyry stocks or cupolas following convection of bubble-rich magmas (e.g. Dilles, 1987; Cloos, 2001; Richards, 2005; Corbett, 2009; Sillitoe, 2010; Schöpa et al., 2017), lack observational evidence, such as large numbers of mineralised veins emanating from miarolitic cavity-rich portions of plutons, i.e. where there is extensive evidence of fluid exsolution. It is also difficult to envisage how the vast volumes of fluids required to form porphyry deposits and their associated alteration (Seedorff et al., 2005; Sillitoe, 2010) could be supplied from volumetrically small porphyry stocks and/or cupolas or the upper regions of plutons. Further, within Yerington's uniquely exposed cupolas, where the Luhr

Hill granite is spatially associated with porphyry-type mineralisation, there is no textural evidence for the magmas having reached fluid saturation. Indeed, from the presence of pegmatitic pods and massive silica bodies, and an absence of miarolitic cavities and very few veins, the magmas were likely fluid undersaturated (Carter et al., 2021; Carter and Williamson, 2022; Chapter 3 & 4). Hence, it is likely that the roof zone and apophyses of the Luhr Hill granite acted as a crystalline carapace through which dykes were focused, rather than a mineralising cupola.

In Yerington, multiple, episodically emplaced aplite dykes (Carter et al., 2022; Chapter 5) show direct evidence for the exsolution of mineralising fluids (mineralised miarolitic cavities) beneath and within the district's porphyry deposits (Carter et al., 2021; Carter and Williamson, 2022; Chapter 3 & 4). Undercooling as well as depressurisation and associated volatile exsolution ('first-type boiling'; Candela, 1989) upon their emplacement gave rise to USTs (Carter et al., 2021; Carter and Williamson, 2022; Chapter 3 & 4). From micro-textural and geochemical investigations, the aplite dykes contain an interconnected, wormy quartz texture throughout their groundmass, which links mineralised miarolitic cavities to early A-type veins (nomenclature after Gustafson and Hunt, 1975). These textures are interpreted to record the pathways of mineralising fluids between earlier formed crystals of quartz, feldspar and accessory phases; i.e. palaeo-permeability which allowed ore-forming fluids to ascend from large volumes of underlying magmas (Carter et al., 2021; Chapter 4).

The ability of fluids to flow through crystal mush is rapidly gaining acceptance (e.g. Cashman et al., 2017; Holness, 2018) however, so far, there has been very little textural evidence to confirm it. This has now been provided from observations at Yerington in the form of petrographic field and microscale textures which record fluid transport through 'crystal mush dykes' (Carter et al., 2021; Chapter 4). There is no reason for this phenomenon to be restricted to Yerington, however, as interconnected miarolitic cavities have been recognised at Baja de la Alumbrera, Argentina, and other granitic systems (e.g. Candela and Blevin, 1995; Harris et al, 2004). That mush textures were not recognised is probably because the necessary micro-scale imaging and analysis techniques were not applied.

The main implication of the observations at Yerington is that fluids can be decoupled from silicate melts and crystals and travel upwards until they precipitate ore and gangue minerals. This would allow a much larger volume of fluids to be involved in mineralisation, sourced from much more extensive portions of the underlying magmatic/crystal mush system, and over much longer time periods, than previously assumed; in most previous models, fluids were derived from the stock or other shallow parts of the magmatic system (**Fig. 6.2**).

Prolonged fluid flow through episodically emplaced crystal-mush dykes aligns with the geochronology presented in Carter et al. (2022; Chapter 5), and other recent studies that show porphyry-style magmatic-hydrothermal mineralisation to be much longer lived than the emplacement of associated magmatic parts of the system (e.g. Romero et al., 2010; Stein, 2014; Spencer et al., 2015; Chang et al., 2017; Chiaradia and Caricchi, 2017; Li et al., 2017). These studies indicate that hydrothermal mineralisation can episodically occur for timescales in excess of 1.5 Myrs after emplacement of a system's shallow magmatic components, and this research shows that in Yerington this may overlap with dome-forming volcanic eruptions. This longevity can be explained by ongoing crystal mush dyke fluid flow processes focussing fluids from deeper, longer-lived portions of a magmatic system. These findings contradict previous models where fluid release is constrained to the upper parts of closed systems in the upper crust (e.g. Dilles, 1987; Cloos, 2001; Richards, 2005; Corbett, 2009; Sillitoe, 2010; Weis et al., 2012; Schöpa et al., 2017), and should be incorporated into future porphyry formation and exploration models. They also bring into question the temporal association of mineralisation with dome-forming volcanism, and also highlight the need to readdress the temporal-thermal frameworks that form the basis of numerical simulations of porphyry systems.

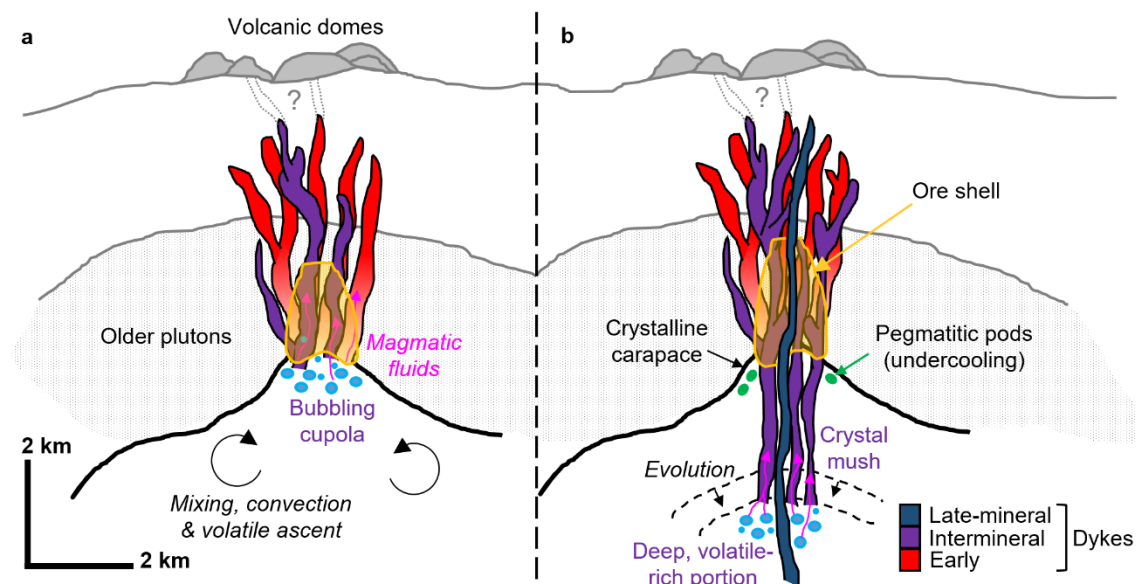


Fig. 6.2 Schematic models for the source of magmatic aqueous fluids in porphyry systems: **a**, Classical model showing fluids accumulating within and being directly released, along with dykes, from the cupola region of a granitic pluton. Modified after Seedorff et al. (2005). **b**, revised model, based on the first-order observations of this research, whereby an intensely undercooled cupola formed a crystalline carapace through which numerous dykes were intruded. Magmatic aqueous fluids used inter-crystal ‘crystal mush’ porosity within these dykes as conduits, to flow from evolved, volatile-rich, deep portions of the underlying pluton up into the porphyry-deposit-forming environment.

6.4 Exploration tools

6.4.1 Geochemical signatures

In recent years there has been a focus on developing our understanding of the whole-rock and mineral geochemical signatures associated with potentially mineralised, or ‘fertile’, magmatic systems, which can be used as exploration tools to identify potentially fertile magmatic suites (e.g. see reviews in Cooke et al., 2017; Cooke et al., 2020; Wilkinson et al., 2020). From studies carried out on the chemistry of zircon, herein (Chapter 5; Carter et al., 2022), the Fulstone Spring Volcanics overlying the Yerington batholith have ‘fertile’ zircon geochemical signatures (**Fig. 5.7**). This has significance in the development and refinement of porphyry exploration indicators (e.g. Sr/Y whole-rock and zircon REE geochemistry; Loucks, 2014; Lu et al., 2014; Cooke et al., 2017) by increasing the potential spatial-temporal efficacy of using these geochemical ‘fertility’ signatures in systematic studies at the district scale to isolate areas mostly prospective for porphyry-style mineralisation, including the assessment of

overlying volcanics. This may aid in the discovery of new deposits, which are likely to be deeper and often under cover (Cooke et al., 2017).

6.4.2 Textural vectors


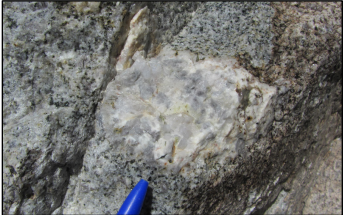




Disequilibrium textures preserved within granitic magmatic systems can offer snapshots of the physical processes that may result in ore-formation. Despite being ubiquitous in granitic-hydrothermal ore-forming systems, they have been little documented, most likely because of their relatively small size, poor textural preservation, insufficient exposure and lack of recognition (e.g. Kirkham and Sinclair, 1988). The self-consistent textural framework from Yerington provided by this research (Chapter 3; Carter and Williamson, 2022) now illustrates a guide for their recognition and interpretation. For example, isolated pegmatitic pods within the granite cupolas indicate intense undercooling, whilst USTs within aplite dykes may result from depressurisation and associated volatile exsolution ('first-type boiling'; Candela, 1989) upon dyke emplacement, and in some instances the onset of magmatic-hydrothermal mineralisation. Certain textures, such as miarolitic cavities, may act as indicators that the magmatic-hydrothermal transition was reached, which is a significant marker in the spatial and temporal evolution of magmatic systems towards ore-formation. Despite their inconsistent development, it is suggested that such textures should be sought out and considered in all field-based campaigns and drill core logging. Their recognition and interpretation, in concert with the use of whole-rock and mineral geochemical indicators (which can only indicate potentially fertile magmatic suites) (e.g. Cooke et al., 2007), will aid in vectoring towards mineralisation in the initial stages of exploration at the district-prospect scale before more invasive and expensive techniques are employed (**Fig. 6.3**).

Regional to district scale: Geochemical indicators

Whole-rock geochemical indicators e.g. Sr/Y (Richards, 2011); Al_2O_3/TiO_2 , V/Sc (Loucks, 2014)

Mineral geochemical indicators e.g. excess Al in plagioclase (Williamson et al., 2016); zircon Eu/Eu^* , Dy/Yb , Ti (Lu et al., 2016; Carter et al., 2022); apatite Sr/Y, Eu/Eu^* (Nathwani et al., 2020)

District to prospect scale: Magmatic-hydrothermal textural vectors (Carter and Williamson, 2022)

Textural feature	Example	Significance
<p>Massive silica bodes 'Ring' with hammer blow. Can form 'cap' at top of cupola.</p>		<p>Probably form by accumulation of exsolved fluids or by replacement of top part of granite cupola due to ingress of silica brought in by fluids exsolving from underlying magmas.</p>
<p>Pegmatitic pods Patches and pods mostly at the tops of 'granite' sheets and within dykes.</p>		<p>Indicates intense undercooling (rapid, shallow emplacement). May represent pockets of trapped exsolved fluids. Likely within cupola zone, may occur beneath a potential zone of hypogene mineralisation.</p>
<p>USTs Parallel to sub-parallel bands of (most commonly) quartz with orientated c-axes</p>		<p>Indicates undercooling (rapid, shallow emplacement) and repeated rapid pressure fluctuations (likely due to repeated hydrofracturing and healing of carapace). Indicates onset of magmatic-hydrothermal transition. Likely just below or within lower levels of mineralisation.</p>
<p>Miarolitic cavities Crystals projecting into and terminating in a void, or subsequently filled void.</p>		<p>Direct evidence for fluid exsolution and magmatic-hydrothermal transition. Likely just below or within zone of hypogene mineralisation. Often spatially and genetically associated with A-type veins.</p>
<p>Parting veins Quartz veins that contain numerous septa or partings of aplite.</p>		<p>Magmas coeval with hydrothermal fluids at the magmatic-hydrothermal transition. Often spatially associated with A- and B-type veins. Usually occur just below or within lower levels of hypogene mineralisation.</p>
<p>A-veins Sinuous veinlets containing sugary quartz ± sulphides.</p>		<p>Early, sinuous, high temperature, randomly orientated, primarily quartz ± bornite ± chalcopyrite veinlets with no symmetry. Often associated with potassic alteration. Confirms magmatic-hydrothermal transition reached and onset of vein-style mineralisation, in semi-ductile environment. Either within or just beneath hypogene ore-zone.</p>
<p>B-veins Planar, coarse grained, symmetrical quartz ± sulphide veins, with central suture.</p>		<p>Planar, regular, parallel to sub-parallel to each other, coarse grained, symmetrical quartz ± chalcopyrite ± pyrite ± molybdenite veins. Confirms magmatic-hydrothermal transition reached, with marked flow of mineralising fluids through secondary-porosity. Directly within possible zone of hypogene mineralisation.</p>

Integrate with geological mapping, targeted soil geochemistry & geophysics

Synthesise into geological model & test by **diamond drilling**

Fig. 6.3 Summary integration of magmatic-hydrothermal textural exploration vectors.

6.5 Scope for future research

As our understanding of magmatic plumbing evolves away from closed systems in the upper crust, new self-consistent temporal-thermal models for trans-crustal magma/mush-hydrothermal systems are needed to help develop our understanding of the nature of fluid extraction and transport. These frameworks must be multi-faceted and span the lifetime of the system, from early magma emplacement through to the last stages of hydrothermal activity, and should test whether mineralising fluids can be extracted and flow from much deeper and larger portions of magmatic systems than previously thought. These models will also allow for the development and testing of new mineralogical toolkits, which are currently in their infancy, to further aid in exploration and the discovery of the next-generation of metal resources.

Strands of potential future research are summarised in the following sub-sections. These will rely on an integration of multiple scales of observation, from field mapping and large-scale sampling to detailed petrography, mineral chemistry, fluid inclusion and geochronological studies.

6.5.1 Study areas for future research

The research presented in this thesis has further demonstrated the utility of the Yerington District as an exemplar of a porphyry-forming system, specifically in respect to evidence of the magmatic-hydrothermal transition, the ability of aplite dykes to act as fluid conduits (Carter et al., 2021; Chapter 4) and the timing of batholith construction through to mineralisation (Carter et al., 2022; Chapter 5).

Additional constraints on the nature of magmatic-hydrothermal fluid flow in the formation of porphyry deposits could be sought from other magmatic-hydrothermal systems, mainly to see if this varies. Potential options include the Ruby Creek monzogranite of the New England orogen, Eastern Australia, where previous work has identified textural evidence for volatile-phase connectivity (Candela and Blevin, 1995) as well as Laramide porphyry copper systems in Arizona, where porphyry root zones are extensively exposed (Seedorff et al., 2008).

6.5.2 Develop a self-consistent thermal and temporal framework for the magmatic components of the porphyry deposit-forming system.

Porphyry deposits are mainly hosted in large, polyphase intrusive complexes in the shallow crust, with magmas having been sourced from deeper zones of melt generation and evolution (e.g. Wilkinson, 2013). Previous geochronological studies have improved our understanding of the development timescales of these systems (e.g. summary in Chiaradia and Caricchi, 2017), but they have been limited by insufficient exposure of the deeper portions of the systems, or focus only on zircon-based investigations; these limitations leave fundamental gaps in the temporal/spatial record.

Tied to first-order field observations, future research could provide such a framework by building upon the recently acquired high precision zircon U-Pb geochronological dataset from Yerington, presented in Chapter 5 and Carter et al. (2022), and thermal constraints from Ti-in-zircon (method of Ferry and Watson, 2007), Ti-in-titanite (method of Hayden et al., 2008) and Ti-in-quartz thermometry (method of Wark and Watson, 2006). Further temporal constraints could be provided by titanite U-Pb geochronology. Since zircon, titanite and quartz have different closure temperatures, they could provide constraints on the thermal regime through different phases of cooling and crystallisation of the magmatic system. However, a sound understanding of the paragenesis of zircon and titanite phases (primarily from SEM and QEMSCAN[®] analysis) would be required for interpreting the mineralogical data, mainly through a specific assessment of the activity of TiO₂ (a_{TiO_2} ; based on Ti-bearing phases) for the thermometry. Geochemistry and dates acquired by LA-ICP-MS spot analyses and maps could be used to target specific crystals, and portions of crystals, to analyse by more precise CA-ID-TIMS. As demonstrated in Carter et al. (2022; Chapter 5), the high precision from CA-ID-TIMS is required in order to resolve the discrete intrusive events that occurred in a short timeframe around the onset of mineralisation in Yerington.

6.5.3 Develop a self-consistent thermal and temporal framework for the hydrothermal components of porphyry systems.

The paragenesis of mineralisation and alteration in porphyry-forming systems is well-documented, mainly from vein classification (from A- through to D-type

veins), which is largely based on mineralogy and cross-cutting relationships. Veins either formed early, from high temperature magmatic-hydrothermal fluids (i.e. the magmatic-hydrothermal transition), or late, from lower temperature fluids, which may contain component derived externally (e.g. Gustafson and Hunt, 1975; Sillitoe, 2010). Whilst this relative thermal evolution is widely recognised, no study to date has provided a consistent framework coupled to absolute age determinations. Without this, we cannot access the longevity of mineralising hydrothermal systems, and so by no means grasp the true relationship with the underlying magmatic components which drive it. This could be addressed by carrying out multi-faceted thermal-temporal analyses, based on field-observations, petrographic and CL studies, absolute thermal constraints from high temperature components ($>\sim 600^{\circ}\text{C}$), using Ti-in-quartz thermometry (method of Wark and Watson, 2006) and fluid inclusion thermometry for lower temperature phases, as well as absolute age determinations for mineralised veins from molybdenite Re-Os geochronology. Constraints for late-stage, post-mineralisation hydrothermal activity could be derived from absolute age determinations for epidote using U-Pb CA-ID-TIMS. Epidote forms a major component of late stage, Na-Ca alteration overprints deep within many porphyry systems (e.g. Seedorff et al., 2005; Sillitoe, 2010), and Yerington is one of the few examples worldwide where deep Na-Ca alteration is exposed (Carten, 1986; Seedorff et al., 2008).

The use of Ti-in-quartz from EPMA data has already been shown by Carter et al. (2021; Chapter 4) to be effective in assessing and differentiating crystallisation temperatures for magmatic quartz and early quartz veins. This method cannot however be used for lower temperature ($<\sim 600^{\circ}\text{C}$) quartz generations as the Ti concentration is below the detection limit of EPMA (~ 42 ppm, 3σ), and because the thermometer is not calibrated for lower temperature hydrothermal quartz (Wark and Watson, 2006). Thermal constraints for lower temperature generations of quartz could be derived from conventional fluid inclusion microthermometry.

Re-Os geochronological data (Carter et al., 2022; Chapter 5) for five samples collected from the Ann Mason deposit has demonstrated the ability of Re-Os dating to resolve different generations of molybdenite mineralisation between and within distinct vein-types. More such analyses would help to further constrain the

timing of mineralisation and its association with the emplacement of the magmatic parts of the Yerington system.

6.5.4 Define ‘crystal mush’ fluid flow parameters

Detailed micro-textural studies have illustrated the preservation of fluid flow pathways in igneous rocks (Candela and Blevin, 1995; Harris et al., 2004; Carter et al. 2021, Chapter 4). Beyond this, Carter et al. (2021) have directly demonstrated how this can occur within crystal mush, and evidence for the timing and nature of the magmatic-hydrothermal transition and hypogene mineralisation. Whilst these studies provide textural evidence for fluid flow through inter-crystal spaces (i.e. mush; Cashman et al, 2017), they do not provide constraints on palaeo-porosity and palaeo-permeability which are essential for robust numerical simulations. This could be addressed by expanding the methods developed and described in Carter et al. (2021) to incorporate other analytical techniques, and to apply these across a broader sample suite. In particular, micro-textural and mineral-scale analyses of quartz generations by cold-cathode CL, SEM-EDX-CL and EPMA, along with electron backscatter diffraction (EBSD) could be used to provide inter-crystal fluid flow parameters (recorded in wormy quartz) and to determine major and trace metals to link metal release to specific fluid generations. X-ray micro-computed tomography (Micro-CT) may also be useful in this regard. However, initial attempts using this technique (when trialling as a method to use for the work presented in Carter et al., 2021; Chapter 4), specifically to image the 3D connectivity of quartz generations within a small block of ‘crystal-mush’ aplite dyke, were unsuccessful due to a lack of density contrast between quartz and feldspar.

6.5.5 Develop new integrated numerical simulations for the crustal-scale extraction and transport of mineralising fluids within porphyry systems.

The Yerington batholith has provided important constraints for a number of recent numerical simulations to assess rates of batholith construction (Chelle-Michou et al., 2017; Schöpa et al., 2017), physical hydrology (Weis et al., 2012) and their controls on ore formation. These studies show that porphyry copper deposit formation is largely controlled by magma flux and needs sustained extraction of mineralising fluids from the source pluton. These existing models however are

based on the incomplete geochronological framework of Dilles and Wright (1988) and assume that mineralising fluids are concentrated and released directly from the granite cupolas. Hence, these models do not align with recent fundamental first-order observations of fluid extraction mechanisms (Carter et al., 2021; Chapter 4) and geochronology that rather indicates longer lived, deeper fluid flow regimes (Carter et al., 2022; Chapter 5). The frameworks and parameters defined from the approaches described above (Sections 6.5.2, 6.5.3 & 6.5.4), along with consideration of models of volatile solubility (e.g. Wieser et al., 2022, and references therein), will create the opportunity for new integrated modelling to readdress our understanding of the timing of batholith construction and nature and scale of flow and extraction of mineralising fluids from trans-crustal magmatic-hydrothermal systems.

6.5.6 Develop new mineralogical toolkits for exploring magmatic-hydrothermal systems.

Our rapidly expanding technological and analytical capabilities is making it possible to study an increasing array of mineral phases, each providing new, and sometimes unique insights into geological processes. Porphyry systems host ubiquitous suites of such magmatic and hydrothermal minerals, but the majority of studies focus only on zircon. The self-consistent frameworks provided by the approaches described above (Sections 6.5.2 & 6.5.3) will provide the context for detailed geochemical, thermo and geochronological studies. This will allow for potential development and testing of new mineralogical toolkits that may further unveil different aspects of porphyry-forming systems and further aid in targeting new resources. Such an approach could also be taken for other deposit types such as epithermal, skarn and Sn-W-dominated magmatic-hydrothermal systems.

6.6 Key conclusions

Key findings from this research on the Yerington District are:

- (i) The pre-mineralisation McLeod quartz monzodiorite and Bear quartz monzonite plutons had similar sources and evolutionary pathway and were in-part contemporaneous. From their whole-rock and zircon geochemistry, the magmas which formed them underwent clinopyroxene-plagioclase-dominated

fractionation in the mid- to lower crust (likely ~15-20 km) over a protracted, >1.5 Myrs evolutionary period.

(ii) Magmas being emplaced within the Yerington system underwent a major and abrupt change in chemistry over a period of <200 kyrs that was coincident with the initiation of ore formation. This change is documented across the plutonic to volcanic record and attributed to a switch in the source, to a depth of 20-40 km, the nature of the fractionating assemblage (becoming amphibole-dominated) and the magmatic plumbing system where deep-seated volatile-rich granitic melts were emplaced to shallow levels (~3-8 km) as porphyry and then aplite dykes.

(iii) Within the Yerington District, the roof zone of the Luhr Hill granite and its apophyses was a carapace rather than a mineralising cupola. Isolated pegmatitic pods and massive silica bodies in the cupolas indicate intense undercooling due to rapid emplacement.

(iv) Multiple generations of undercooled aplite dykes beneath and within the Yerington District's porphyry deposits host mineralised unidirectional solidification textures (USTs), pegmatitic segregations, miarolitic cavities and early A-type quartz veins, which record the timing and location of the magmatic-hydrothermal transition and ore formation. Magmas within these aplite dykes reached fluid saturation to form a permeable crystal mush of feldspar and quartz, with intra-crystal fluid, which provided a pathway for fluid flow from deeper and much larger volumes of underlying magmas.

(v) Porphyry-style mineralisation continued for potentially in excess of 1.5 Myrs post emplacement of the Luhr Hill granite's cupolas, temporally overlapping with the eruption of the overlying Fulstone Spring Volcanics.

(vi) The same 'fertile' geochemical signature shown by the inter-mineralisation aplite dykes is seen throughout the magmatic system, including in zircons from overlying volcanics. The rapidity of the change from 'pre-' to 'inter-mineralisation' or 'fertile' geochemical signatures narrows the temporal-geochemical range of magmas associated with ore formation and allows for the refinement and increases the efficacy of these geochemical tools in exploration.

7 References

- Abriola, D., Barradas, N. P., Bogdanović-Radović, I. *et al.*, 2011. Development of a reference database for Ion Beam Analysis and future perspectives. *Nucl. Inst. Meth. Phys. Res. Sect. B-Beam Inter. Mater. Atoms* **269**, 2972–2978.
- Acosta, M. D., *et al.*, 2020. Ti-in-quartz: Evaluating the role of kinetics in high temperature crystal grown experiments. *Geochimica et Cosmochimica Acta* **281**, 149-167. <https://doi.org/10.1016/j.gca.2020.04.030>
- Ahmed, A., Crawford, A. J., Leslie, C. *et al.*, 2020. Assessing copper fertility of intrusive rocks using field portable X-ray fluorescence (pXRF) data. *Geochemistry: Exploration, Environment, Analysis* **20**, 81-9. <https://doi.org/10.1144/geochem2018-077>
- Allaby, M. A., 2013. Dictionary of Geology and Earth Sciences 4th Edn., p. 573. Oxford University Press, Oxford.
- Anderson, A. T., 1976. Magma mixing - petrological process and volcanological tool. *J. Volcanol. Geotherm. Res.* **1**, 3–33. [https://doi.org/10.1016/0377-0273\(76\)90016-0](https://doi.org/10.1016/0377-0273(76)90016-0)
- Andres, U., Jirestig, J. & Timoshkin, I., 1999. Liberation of minerals by high-voltage electrical pulses, *Powder Technology* **104**, 37–49. [https://doi.org/10.1016/S0032-5910\(99\)00024-8](https://doi.org/10.1016/S0032-5910(99)00024-8)
- Annen, C., Blundy, J. D. & Sparks, R. S. J., 2006. The Genesis of Intermediate and Silicic Magmas in Deep Crustal Hot Zones. *Jour. Petrol.* **47(3)**, 505-539. <https://doi.org/10.1093/petrology/egi084>
- Aigner-Torres, M., Blundy, J., Ulmer, P. & Pettke, T., 2007. Laser Ablation ICPMS study of trace element partitioning between plagioclase and basaltic melts: An experimental approach. *Contrib. Mineral. Petrol.* **153**, 647–667. <https://doi.org/10.1007/s00410-006-0168-2>
- Audetat, A. & Simon, A. C., 2012. Magmatic Controls on Porphyry Copper Genesis. *Society of Economic Geologists, Special Publication* **16**, 553–572.
- Baker, E. M. & Andrew, A. S., 1991. Geologic, fluid inclusion, and stable isotope studies of the gold-bearing breccia pipe at Kidston, Queensland, Australia. *Econ. Geol.* **86 (4)**, 810–830.
- Baker, D. R. & Freda, C., 2001. Eutectic crystallization in the undercooled Orthoclase-Quartz-H₂O system: experiments and simulations. *Eur. J. Mineral.* **13**, 453–466.
- Ballard, J. R., Palin, J. M. & Campbell, I. H., 2002. Relative oxidation states of magmas inferred from Ce(IV)/Ce(III) in zircon: application to porphyry copper deposits of northern Chile. *Contrib. Mineral. Petrol.* **144**, 347-364. <https://doi.org/10.1007/s00410-002-0402-5>
- Ballhaus, C., Raúl, O. C., Fonseca, C. M., Kirchenbaur, M. & Zirner, A., 2015.

- Spheroidal textures in igneous rocks – Textural consequences of H₂O saturation in basaltic melts. *Geochimica et Cosmochimica Acta* **167**, 241–252.
- Banik, T. J., Coble, M. A. & Miller, C. F., 2017. Porphyry Cu formation in the middle Jurassic Yerington batholith, Nevada, USA: Constraints from laser Raman, trace element, U-Pb age, and oxygen isotope analyses of zircon. *Geosphere* **13** (4), 1113-1132. <https://doi:10.1130/GES01351.1>
- Bindeman, I., 2008. Oxygen isotopes in mantle and crustal magmas as revealed by single crystal analysis. *Rev. Mineral. Geochem.* **69**, 445-478. <https://doi.org/10.2138/rmg.2008.69.12>
- Bluhm, H., Frey, W., Giese, H. *et al.*, 2000. Application of pulses HV discharges to material fragmentation and recycling, *IEEE Trans. Dielectr. Electr. Insul.* **7**, 625-636.
- Blundy, J. & Cashman, K., 2001. Ascent-driven crystallisation of dacite magmas at Mount St Helens, 1980-1986. *Contrib. Mineral. Petrol.* **140**, 631-650. <https://doi.org/10.1007/s004100000219>
- Breiter, K., Müller, A., Leichmann, J. & Gabašová, A., 2005. Textural and chemical evolution of a fractionated granitic system: the Podlesí stock, Czech Republic. *Lithos* **80** (1-4), 323-345. <https://doi.org/10.1016/j.lithos.2003.11.004>
- Bru, K., Beaulieu, M., Sousa, R., *et al.* 2020. Comparative laboratory study of conventional and Electric Pulse Fragmentation (EPF) technologies on the performances of the comminution and concentration steps for the beneficiation of a scheelite skarn ore. *Minerals Engineering* **150**, 106302. <https://doi.org/10.1016/j.mineng.2020.106302>
- Bryan, R. C., 2014. NI 43-101 Technical Report Mineral Resource Update Yerington Copper Project Lyon County, Nevada. *TetraTech*. Available: <https://guaterra.com/projects/guaterras-yerington-copper-projects/yerington-deposit/>. Accessed 21/07/2020.
- Buret, Y., von Quadt, A., Heinrich, C. *et al.*, 2016. From a long-lived upper-crustal magma chamber to rapid porphyry copper emplacement: reading the geochemistry of zircon crystals at Bajo de la Alumbrera (NW Argentina). *Earth Planet. Sci. Lett.* **450**, 120–131.
- Burnham, C. W., 1979. Magmas and hydrothermal fluids, *In*: Barnes, H. L. (Ed.), *Geochemistry of hydrothermal ore deposits*. New York, Wiley Intersci., 71-163.
- Burnham, A. D. & Berry A. J., 2012. An experimental study of trace element partitioning between zircon and melt as a function of oxygen fugacity. *Geochimica et Cosmochimica Acta.* **95**, 196-212. <https://doi.org/10.1016/j.gca.2012.07.034>
- Burnham, A. D., 2020. Key concepts in interpreting the concentrations of the rare earth elements in zircon. *Chem. Geol.* **551**, 119765. <https://doi.org/10.1016/j.chemgeo.2020.119765>

- Carten, R. B., 1986. Sodium-Calcium Metasomatism: Chemical, Temporal and Spatial Relationships at the Yerington, Nevada, Porphyry Copper Deposit. *Econ. Geol.* **81**, 1495-1519.
- Carter, L. C., Williamson, B. J., Tapster, S. R., Costa, C., Grime, G. W. & Rollinson, G. K., 2021. Crystal mush dykes as conduits for mineralising fluids in the Yerington porphyry copper district, Nevada. *Commun. Earth Environ.* **2**, 59. <https://doi.org/10.1038/s43247-021-00128-4>
- Carter, L. C., Tapster, S. R., Williamson, B. J. Buret, Y., Selby, D., Rollinson, G. K., Millar, I. & Parvaz, D., 2022. A rapid change in magma plumbing taps porphyry copper deposit-forming magmas. *Sci. Rep.* **12**, 17272. <https://doi.org/10.1038/s41598-022-20158-y>
- Carter, L. C. & Williamson, B. J., 2022. Textural indicators of mineralisation potential in porphyry magmatic systems – A framework from the archetypal Yerington District, Nevada. *Ore Geol. Rev.* **143**, 104783. <https://doi.org/10.1016/j.oregeorev.2022.104783>
- Campbell, J. L., Boyd, N. I., Grassi, N., Bonnicksen, P. & Maxwell, J. A., 2010. The Guelph PIXE software package IV. *Nucl. Inst. Meth. Phys. Res. Sec. B* **268**, 356–3363.
- Candela, P. A., 1989. Felsic magmas, volatiles, and metallogenesis. *In*: Whitney, J. A. & Naldrett, A. J. (Eds.), *Ore Deposition Associated with Magmas. Reviews in Economic Geology*, 223-233.
- Candela, P. A., 1991. Physics of aqueous phase evolution in plutonic environments. *American Mineralogist* **76**, 1081–1091.
- Candela, P. A. & Blevin, P. L., 1995. Do some miarolitic granites preserve evidence of magmatic volatile phase permeability? *Econ. Geol.* **90** (8), 2310–2316.
- Candela, P. A., 1997. A review of shallow, ore-related granites: Textures, volatiles, and ore metals. *J. Petrol.* **38** (12), 1619-1633.
- Cashman, K. V., Stephen, R. J. & Blundy, J. D., 2017. Vertically extensive and unstable magma systems: A unified view of igneous processes. *Science* **355**, 6331. <https://doi.org/10.1126/science.aag3055>
- Chang, J., Li, J.-W. & Audétat, A., 2018. Formation and evolution of multistage magmatic-hydrothermal fluids at the Yulong porphyry Cu-Mo deposit, eastern Tibet: Insights from LA-ICP-MS analysis of fluid inclusions. *Geochem. Cosmochim. Acta* **232**, 181–205.
- Chang, J., Li, J.-W., Selby, D., Liu, J.-C. & Deng, X.-D., 2017. Geological and chronological constraints on the long-lived Eocene Yulong porphyry Cu-Mo deposit, eastern Tibet, China: implications for lifespan of magmatic-hydrothermal processes forming giant and supergiant porphyry Cu deposits. *Econ. Geol.* **112** (7), 1719-1746. <https://doi.org/10.5382/econgeo.2017.4527>

- Chelle-Michou, C., Rottier, B., Caricchi, L. *et al.*, 2017. Tempo of magma degassing and the genesis of porphyry copper deposits. *Sci. Rep.* **7**, 40566. <https://doi.org/10.1038/srep40566>
- Chelle-Michou, C. & Schaltegger, U., 2018. 'U-Pb dating of mineral deposits: From age constraints to ore-forming processes'. *In*: Huston, D. *et al.* (eds.) *Isotopes in economic geology, metallogenesis and exploration*. SGA special volume. <https://doi.org/10.31223/osf.io/b7pw9>
- Cheng, H. Edwards, R. L. Hoff, J. *et al.*, 2000. The half-lives of uranium-234 and thorium-230. *Chem. Geol.* **169** (1-2), 17-33. [https://doi.org/10.1016/S0009-2541\(99\)00157-6](https://doi.org/10.1016/S0009-2541(99)00157-6)
- Cherniak, D. J., Hanchar, J. & Watson, E., 1997. Rare-Earth diffusion in zircon. *Chem. Geol.* **134**, 289–301.
- Cherniak, D. J., Watson, E. B. & Wark, D. A., 2007. Ti diffusion in quartz. *Chem. Geo.* **236**, 65–74.
- Chiaradia, M., Meino, D. & Spikings, R., 2009. Rapid transition to long-lived deep crustal magmatic maturation and the formation of giant porphyry-related mineralization (Yanacocha, Peru). *Earth. Planet. Sci. Lett.* **288**, 505-515.
- Chiaradia, M., Ulianov, A., Kouzmanov, K. *et al.*, 2012. Why large porphyry Cu deposits like high Sr/Y magmas? *Sci. Rep.* **2**, 685. <https://doi.org/10.1038/srep00685>
- Chiaradia, M., 2015. Crustal thickness control on Sr/Y signatures of recent arc magmas: an Earth scale perspective. *Sci. Rep.* **5**, 8115. <https://doi.org/10.1038/srep08115>
- Chiaradia, M., Caricchi, L., 2017. Stochastic modelling of deep magmatic controls on porphyry copper deposit endowment. *Sci. Rep.* **7**, 44523. <https://doi.org/10.1038/srep44523>
- Claiborne, L. L., Miller, C. F., Walker, B. A. *et al.*, 2006. Tracking magmatic processes through Zr/Hf ratios in rocks and Hf and Ti zoning in zircons: An example from the Spirit Mountain batholith, Nevada. *Mineral. Mag.* **70**:517–543.
- Claiborne, L. L., Miller, C. F. & Wooden, J. L., 2010. Trace element composition of igneous zircon: a thermal and compositional record of the accumulation and evolution of a large silicic batholith, Spirit Mountain, Nevada. *Contrib. Miner. Petrol.* **160** (4), 511–531. <https://doi.org/10.1007/s00410-010-0491-5>
- Clark, A. H., 1993. Are outsize porphyry copper deposits either anatomically or environmentally distinctive? *Society of Economic Geologists Special Publication* **2**, 213–283.
- Clarke, D. E., 1969. Geology of the Ravenswood 1-mile sheet area, Queensland. Bureau of Mineral Resources, Geology and Geophysics. Record No.

1969/117.

- Cline, J. S. & Bodnar, R. J., 1991. Can economic porphyry copper mineralization be generated by a typical calc-alkaline melt? *J. Geophys. R.* **96**, 8113–8126.
- Cloos, M., 2001. Bubbling magma chambers, cupolas, and porphyry copper deposits. *International Geology Review* **43**, 285–311.
- Condon, D. J., Schoene, B., McLean, N. M., Bowring, S. A. & Parrish, R. R. 2015. Metrology and Traceability of U-Pb Isotope Dilution Geochronology (EARTHTIME Tracer Calibration Part I). *Geochim. Cosmochim. Acta.* **164**, 464-480. <https://doi.org/10.1016/j.gca.2015.05.026>
- Cooke, D. R., Agnew, P., Hollings, P. *et al.*, 2017. Porphyry indicator minerals (PIMS) and porphyry vectoring and fertility tools (PVFTS) – Indicators of mineralisation styles and recorders of hypogene geochemical dispersion halos. *In: Tschirhart, V. & Thomas, M. D. (eds.) Proceedings of Exploration 17: Sixth Decennial International Conference on Mineral Exploration*, 457-470.
- Cooke, D. R., Agnew, P., Hollings, P. *et al.*, 2020. Recent advances in the application of mineral chemistry to exploration for porphyry copper–gold–molybdenum deposits: detecting the geochemical fingerprints and footprints of hypogene mineralization and alteration. *Geochemistry: Exploration, Environment, Analysis*, **20**, 176-188.
- Corbett, G., 2009. Anatomy of porphyry-related Au-Cu-Ag-Mo mineralised systems: Some exploration implications. *AIG Bull.* **49**, 33–46.
- Costa, A., Caricchi, L. & Bagdassarov, N., 2009. A model for the rheology of particle-bearing suspensions and partially molten rocks. *Geochem. Geophys. Geosyst.* **10**, Q03010. <https://doi.org/10.1029/2008GC002138>
- Daly, R. A., 1911. The nature of volcanic action. *Proc. Am. Acad. Arts Sci.* **47**, 48–119.
- Decitre, S., Gasquet, D. & Marignac, C., 2002. Genesis of orbicular granitic rocks from the Ploumanac'h Plutonic Complex (Brittany, France): petrographical, mineralogical and geochemical constraints. *Eur. J. Mineral.* **14**, 715–731.
- DePaolo, D. J., 1981. Trace-element and isotopic effects of combined wallrock assimilation and fractional crystallization. *Earth Planet. Sci. Lett.* **53**, 189–202. [https://doi.org/10.1016/0012-821X\(81\)90153-9](https://doi.org/10.1016/0012-821X(81)90153-9)
- Dilles, J. H., 1987. Petrology of the Yerington Batholith, Nevada: Evidence for evolution of porphyry copper ore fluids. *Econ. Geol.* **82**, 1750-1789.
- Dilles, J. H. & Wright, J. E., 1988. The chronology of early Mesozoic arc magmatism in the Yerington District of western Nevada and its regional implications. *GSA Bull.* **100** (5), 644-652.
- Dilles, J. H. & Einaudi, M. T., 1992. Wall-rock alteration and hydrothermal flow paths about the Ann-Mason porphyry copper deposit, Nevada – A 6-km vertical

- reconstruction. *Econ. Geol.* **87**, 1963-2001.
- Dilles, J. H. & Proffett, J. M., 1995. Metallogensis of the Yerington batholith, Nevada. *In: Pierce, F. W., & Bolm, J. G. (Eds.), Porphyry copper deposits of the American cordillera: Arizona Geological Society Digest*, **20**, 306–315.
- Dilles, J. H., Einaudi, M. T., Proffett, J. & Barton, M. D., 2000. Overview of the Yerington Porphyry Copper District: Magmatic to Nonmagmatic Sources of Hydrothermal Fluids, Their Flow Paths, Alteration Affects on Rocks, and Cu-Mo-Fe-Au Ores. *Society of Economic Geologists Guidebook Series* **32**, 55-66. <https://doi.org/10.5382/GB.32>
- Dilles, J. H., Kent, A. J. R., Wooden, J. L. *et al.*, 2015. Zircon compositional evidence for sulfur-degassing from ore-forming arc magmas. *Econ. Geol.* **110**, 241–251. <https://doi.org/10.2113/econgeo.110.1.241>
- Einaudi M. T., 1970, Final Report Deep Drilling Project Yerington Mine: unpublished private report for The Anaconda Company, p. 9.
- Elshkaki, A., Graedel T. E., Ciacci, L. & Reck, B. K., 2016. Copper demand, supply, and associated energy use to 2050. *Global Environmental Change* **39**, 305-315. <https://doi.org/10.1016/j.gloenvcha.2016.06.006>
- Erdenebayar, J., Ogata, T., Imai, A. & Sereenen, J., 2014. Textural and chemical evolution of unidirectional solidification textures in highly differentiated granitic rocks at Kharaatyagaan, Central Mongolia. *Resource Geol.* **64** (4), 283–300.
- Fenn, P. M., 1986. On the origin of graphic granite. *Am. Mineral.* **71** (4), 325–330.
- Ferry, J. M & Watson, E. B., 2007. New thermodynamic models and revised calibrations for the Ti-in-zircon and Zr-in-rutile thermometers. *Contrib. Mineral. Petrol.* **154**, 429-437. <https://doi.org/10.1007/s00410-007-0201-0>
- Garwin, S., 2002. The geology of intrusion-related hydrothermal systems near the Batu Hijau porphyry copper-gold deposit, Sumbawa, Indonesia. *In: Goldfarb, R. & Nielsen, R. (Eds.), Integrated Methods for Discovery. Reviews in Economic Geology, Special Publication 9*, pp. 333-366.
- Gelman, S. E., Gutierrez, F. J. & Bachmann, O., 2013. On the longevity of large upper crustal silicic magma reservoirs. *Geology* **41**, 759–762. <https://doi.org/10.1130/G34241.1>
- Ghiorso, M. S. & Gualda, A. R., 2013. A method for estimating the activity of titania in magmatic liquids from the compositions of coexisting rhombohedral and cubic iron–titanium oxides. *Contrib. Mineral. Petrol.* **165**, 73–81.
- Glazner, A. F., 2021. Thermal Constraints on the Longevity, Depth, and Vertical Extent of Magmatic Systems. *Geochemistry, Geophysics, Geosystems* **22**(4), e2020GC009459. <https://doi.org/10.1029/2020GC009459>
- Gomez-Morilla, I., Simon, A., Simon, R. *et al.*, 2006. An evaluation of the accuracy and precision of Xray microanalysis techniques using BCR-126A glass

- reference material. *Nucl. Instr. Meth. Phys. Res. Sect. B: Beam Inter. Mater. Atoms* **249**, 897–902 (2006).
- Goodall, W. R., Scales, P. J. & Butcher, A. R., 2005. The use of QEMSCAN and diagnostic leaching in the characterisation of visible gold in complex ores. *Miner. Eng.* **18** (8), 877–886. <https://doi.org/10.1016/j.mineng.2005.01.018>.
- Goodall, W. R. & Scales, P. J., 2007. An overview of the advantages and disadvantages of the determination of gold mineralogy by automated mineralogy. *Miner. Eng.* **20** (5), 506–517. <https://doi.org/10.1016/j.mineng.2007.01.010>.
- Gottlieb, P., Wilkie, G., Sutherland, D., Ho-Tun, E., Suthers, S., Perera, K., Jenkins, B., Spencer, S., Butcher, A. & Rayner, J., 2000. Using quantitative electron microscopy for process mineralogy applications. *JOM* **52** (4), 24–25. <https://doi.org/10.1007/s11837-000-0126-9>
- Gramlich, J. W., Murphy, T. J., Garner, E. L. & Shields, W. R., 1973. Absolute isotopic abundance ratio and atomic weight of a reference sample of rhenium. *J. Res. Nat. Bur. Stand.* **77**, pp. 691-698.
- Grosse, P., Toselli, A. J. & Rossi, J. N., 2010. Petrology and geochemistry of the orbicular granitoid of Sierra de Velasco (NW Argentina) and implications for the origin of orbicular rocks. *Geol. Mag.* **147**, 451–468.
- Gustafson, L. B. & Hunt, J. P., 1975. The porphyry copper deposit at El Salvador, Chile. *Econ. Geol.* **70**, 857-912.
- Gustafson, L. B. & Quiroga, G. J., 1995. Patterns of mineralization and alteration below the porphyry copper orebody at El Salvador, Chile. *Econ. Geol.* **90**, 2-16.
- Halley, S., Dilles, J. H. & Tosdal, J. H., 2015. Footprints: Hydrothermal Alteration and Geochemical Dispersion Around Porphyry Copper Deposits. *SEG Newsletter* **100**, 12-17.
- Harris, A. C., Cuisson, A. L. G., Chang, Z., Cooke, D. R., Bonnici, N., Faure, K. & Cross, C., 2007. Fe-rich magmatic volatiles in the Ridgeway Au-Cu porphyries: evidence from magnetite-quartz comb-layered textures. *In: C. J. Andrew (Ed.)*, Digging Deeper, Proceedings of the 9th Biennial SGA Meeting, Dublin. pp. 415–418.
- Harris, A. C., Kremenetsky, V.S., White, N.C. & Steele, D.A., 2004. Volatile phase separation in silic magmas at Bajo de la Alumbrera porphyry Au-Cu deposit NW Argentina. *Resour. Geol.* **54**, 341–356.
- Hayden, L. A., Watson, E. B., & Wark, D. A., 2008. A thermobarometer for sphene (titanite). *Contrib. Mineral. Petrol.* **155**, 529-540. <https://doi.org/10.1007/s00410-007-0256-y>
- Henderson, M. R., Byan, R. C., Welhener, H. E., Jolk, R. W. & Willow, M. A., 2014. MacArthur Copper Project; Amended NI 43-101 Technical Report Preliminary

- Economic Assessment. *M3 Engineering*. <https://quatterra.com/download/ni43-101-technical-report-mineral-resource-update-january-3-2014-yerington-copper-project-lyon-county-nevada/> Accessed 04/10/2021.
- Herrington, R., 2021. Mining our green future. *Nat. Rev. Mater.* **6**, 456-458. <https://doi.org/10.1038/s41578-021-00325-9>
- Hiess, J., Condon, D. J., McLean, N., & Noble, S. R., 2012. U-238/U-235 Systematics in Terrestrial Uranium-Bearing Minerals. *Science* **335 (6076)**, 1610-1614. <https://doi.org/10.1126/science.1215507>
- Hildreth, W. & Moorbath, S., 1988. Crustal contributions to arc magmatism in the Andes of Central Chile. *Contrib. Mineral. Petrol.* **98**, 455–489.
- Hithersay, P. S. & Walshe, J. L., 1995. Endeavour 26 North: a porphyry copper-gold deposit in the Late Ordovician shoshonite Goonumbla volcanic complex, New South Wales, Australia. *Econ. Geol.* **90**, 1506–1532.
- Holness, M. B., 2018. Melt segregation from silicic crystal mushes: a critical appraisal of possible mechanism and their microstructural record. *Contrib. Mineral. Petr.* **173**, 48.
- Hong, W., Cooke, D. R., Zhang, L., Fox, N. & Thompson, J., 2019. Cathodoluminescence features, trace elements, and oxygen isotopes of quartz in unidirectional solidification textures from the Sn-mineralized Heemskirk Granite, western Tasmania. *Am. Mineral.* **104**, 100–117.
- Huang, R. & Audétat, A., 2012. The titanium-in-quartz (TitaniQ) thermobarometer: a critical examination and re-calibration. *Geochem. Cosmochim. Acta* **84**, 75–89.
- Hudbay Minerals Inc., 2021. Mason Preliminary Economic Assessment Summary. <https://hudbayminerals.com/investors/press-releases/press-release-details/2021/Hudbay-Announces-Positive-Preliminary-Economic-Assessment-for-its-Mason-Copper-project/default.aspx> Accessed 04/10/2021.
- Hudson, D. M. & Oriel, W. M., 1979. Geologic map of the Buckskin Range, Nevada. Nevada Bureau of Mines and Geology, map 64.
- Ishihara, S., 1981. The granitoid series and mineralization. *Econ. Geol.* **75th Anniversary Volume**, 458-484.
- Jackson, M. D., Blundy, J. & Sparks, R. S. J., 2018. Chemical differentiation, cold storage and remobilization of magma in the Earth's crust. *Nature* **564**, 405–409.
- Jaffey, A. H., Flynn, K. F., Glendenin, L. E. *et al.*, 1971. Precision Measurement of Half-Lives and Specific Activities of U-235 and U-238. *Phys. Rev.* **4 (5)**, 1889-1906.

- Jagoutz, O. & Schmidt, M. W., 2012. The formation and bulk composition of modern juvenile continental crust: The Kohistan arc. *Chem. Geol.* **298**, 79–96. <https://doi.org/10.1016/j.chemgeo.2011.10.022>
- Johannes, W. & Holtz, F., 1996. The Haplogranite System Qz-Ab-Or. *In: Petrogenesis and Experimental Petrology of Granitic Rocks. Minerals and Rocks*, vol 22. Springer, Berlin, Heidelberg. https://doi.org/10.1007/978-3-642-61049-3_2
- Jollands, M. C., Bloch, E. & Müntener, O., 2020. New Ti-in-quartz diffusivities reconcile natural Ti zoning with time scales and temperatures of upper crustal magma reservoirs. *Geology* **48(7)**, 654-647. <https://doi.org/10.1130/G47238.1>
- Jowitt, S. M., Mudd, G. M. & Thompson, J. F. H., 2020. Future availability of non-renewable metal resources and the influence of environmental, social, and governance conflicts on metal production. *Commun Earth Environ* **1**, 13. <https://doi.org/10.1038/s43247-020-0011-0>
- Kelly, W. C. & Rye, R. O., 1979. Geologic, fluid inclusion, and stable isotope studies of the tin–tungsten deposits of Panasqueira, Portugal. *Econ. Geol.* **74(8)**, 1721–1822.
- Kelsey, C. H., 1965. Calculation of the C.I.P.W. norm. *Mineral. Mag.* **34**, 276-282.
- Kirkham, R. V. & Sinclair, W. D., 1988. Comb quartz layers in felsic intrusions and their relationship to porphyry deposits. *In: Taylor, R. P. & Strong, D. F. (Eds.), Recent advances in the geology of granite-related mineral deposits. Canadian Institute of Mining, Special Volume 39*, 50-71.
- Kirwin, D. J., 2005. Unidirectional solidification textures associated with intrusion-related Mongolian mineral deposits. *In: Seltmann, R., Gerel, O., & Kirwin, D. J. (Eds.), Geodynamics and metallogeny of Mongolia with special emphasis on copper and gold deposits: Society of Economic Geologists-International Association for the Genesis of Ore Deposits Field Trip, 2005: IAGOD Guidebook Series 11: London, Centre for Russian and Central EurAsian Mineral Studies, Natural History Museum*, 63–84.
- Kistler, R. W. & Peterman, Z. E., 1973. Variations in Sr, Rb, K, Na and initial ⁸⁷Sr/⁸⁶Sr in Mesozoic granitic rocks in central California. *Geol. Soc. America Bull.* **84**, 3489-3512.
- Knopf, A., 1918. Geology and ore deposits of the Yerington district, Nevada. *UGS Professional Paper 114*, 68.
- Kronz, A., Van den Kerkhof, A. M. & Müller, A., 2012. Analysis of Low Element Concentrations in Quartz by Electron Microprobe. *In: Götze, J. & Möckel, R. (Eds.), Quartz: Deposits, Mineralogy and Analytics. Springer Geology*. Springer, Berlin, Heidelberg. https://doi.org/10.1007/978-3-642-22161-3_9
- Kulla, G., Oshust, P., Desautels, J., Melnyk, J., Zurowki, G., Jones, L. & Colantonio, M., 2017. Updated Preliminary Economic Assessment on the Ann Mason Project Nevada, U.S.A. AGP Mining Consultants Inc. and Amec Foster

Wheeler Americas Limited. Available:
https://www.sec.gov/Archives/edgar/data/1271554/000110262417000140/exh99_1.htm Accessed: 30/03/2022

- Lawley, C. J. M. & Selby, D., 2012. Re-Os Geochronology of Quartz Enclosed Ultra-fine Molybdenite: Implications for Ore Geochronology. *Econ. Geol.* **107** (7), 1499-1506. <https://doi.org/10.2113/econgeo.107.7.1499>
- Lee, C. T. A. & Tang, M., 2020. How to make porphyry copper deposits. *Earth Planet. Sci. Lett.* **529**, 115869. <https://doi.org/10.1016/j.epsl.2019.115868>
- Lee, R. G., Byrne, K., D'Angela, M. *et al.*, 2021. Using zircon trace element composition to assess porphyry copper potential of the Guichon Creek batholith and Highland Valley Copper deposit, south-central British Columbia. *Miner. Deposita* **56**, 215-238.
- Lehmann, B., 2020. Formation of tin ore deposits: A reassessment. *Lithos*, **402-403**, 105756 <https://doi.org/10.1016/j.lithos.2020.105756>
- Lentz, D. R. & Fowler, A. D., 1992. A dynamic model for graphic quartz-feldspar intergrowths in granitic pegmatites in the Southwestern Grenville Province. *Canadian Mineralogist* **30**, 571–585.
- Li, Y., Selby, D., Condon, D. & Tapster, S., 2017. Cyclic magmatic-hydrothermal evolution in porphyry systems: High-precision U-Pb and Re-Os geochronology constraints from the Tibetan Qulong porphyry Cu-Mo deposit. *Econ. Geol.* **112** (6), 1419-1440. <https://doi.org/10.5382/econgeo.2017.4515>
- Liu, L., Richards, J., Creaser, R. & DuFrane, S. A., 2016. Geology and age of the Morrison porphyry Cu-Au-Mo deposit, Babine Lake area, British Columbia. *Canadian Journal of Earth Sciences* **53** (9), 950-975.
- London, D., 1992. The application of experimental petrology to the genesis and crystallisation of granitic pegmatites. *Can. Mineral.* **30**, 499–540.
- London, D., 2009. The origin of primary textures in granitic pegmatites. *Can. Mineral.* **47** (4), 697–724.
- London, D., & Morgan, G. B., 2012. The pegmatite puzzle. *Elements* **8** (4), 263–268.
- Loader, M. A., Wilkinson, J. J. & Armstrong, R. N., 2017. The effect of titanite crystallisation on Eu and Ce anomalies in zircon and its implications for the assessment of porphyry Cu deposit fertility. *Earth Planet. Sci. Lett.* **472**, 107-119. <https://doi.org/10.1016/j.epsl.2017.05.010>
- Loucks, R. R., 2014. Distinctive composition of copper-ore-forming arc magmas. *Aust. J. Earth Sci.* **61**, 5–16. <https://doi.org/10.1080/08120099.2013.865676>
- Loucks, R. R., Fiorentini, M. L. & Henríquez, G. J., 2020. New Magmatic Oxybarometer Using Trace Elements in Zircon. *Jour. Petrol.* **61** (3), egaa034. <https://doi.org/10.1093/petrology/egaa034>

- Lowenstern, J. B., 2000. C.I.P.W. norm. Calculator. USGS. https://volcanoes.usgs.gov/observatories/yvo/jlowenstern/other/software_jbl.html Accessed 04/10/2021.
- Lowell, J. D. & Guilbert, J. M., 1970. Lateral and vertical alteration-mineralization zoning in porphyry copper deposits. *Econ. Geol.* **65**, 363-408.
- Lu, Y., Loucks, R. R., Fiorentini, M. *et al.*, 2016. Zircon Compositions as a Pathfinder for Porphyry Cu ± Mo ± Au Deposits. *Society of Economic Geologists. Special Publications Series 19*, 329-347. <https://doi.org/10.5382/SP.19.13>
- Luhr, J. F., Carmicheal, I. S. E. & Varekamp, J. C., 1984. The 1982 eruptions of El Chichón Volcano, Chiapas, Mexico: Mineralogy and petrology of the anhydrite bearing pumices. *J. Volcanol. Geotherm.* **23 (1-2)**, 69-108. [https://doi.org/10.1016/0377-0273\(84\)90057-X](https://doi.org/10.1016/0377-0273(84)90057-X)
- Markey, R., Stein, H. J., Hannah, J. L., Zimmerman, A., Selby, D., & Creaser, R. A., 2007. Standardizing Re-Os geochronology: A new molybdenite reference material (Henderson, USA) and the stoichiometry of Os salts. *Chem. Geol.* **244**, 74–87.
- Mattinson, J. M., 2005. Zircon U-Pb chemical abrasion (“CA-TIMS”) method: Combining annealing and multi-step partial dissolution analysis for improved precision and accuracy of zircon ages. *Chem. Geol.* **220 (1-2)**, 47-66. <https://doi.org/10.1016/j.chemgeo.2005.03.011>
- McDonough, W. F. & Sun, S. S., 1995. The composition of the Earth. *Chem. Geol.* **120**, 223-253.
- McDowell, S. M., Miller, C. F., Mundil, R., Ferguson, C. A. & Wooden, J. L., 2014. Zircon evidence for a ~200 k.y. supereruption-related thermal flare-up in the Miocene southern Black Mountains, western Arizona, USA. *Contrib. Miner. Petrol.* **168**, 1031. <https://doi.org/10.1007/s00410-014-1031-5>
- McLean, N. M., Condon, D. J. Schoene, B. & Bowring, S. A., 2015. Evaluating uncertainties in the calibration of isotopic reference materials and multi-element isotopic tracers (EARTHTIME Tracer Calibration Part II). *Geochim. Cosmochim. Acta.* **164**, 481-501. <https://doi.org/10.1016/j.gca.2015.02.040>
- Menand, T., 2011. Physical controls and depth of emplacement of igneous bodies: A review. *Tectonophysics* **500 (1-4)**, 11-19. <https://doi.org/10.1016/j.tecto.2009.10.016>
- Miller, D. S. & Smith, R. B. P., 1999. S velocity structure of the Yellowstone volcanic field from local earthquake and controlled source tomography. *J. Geophys. Res.* **104**, 15105–15121.
- Misra, K., 2000. Understanding Mineral Deposits. Springer, pp. 353-370.
- Moore, J. G., 1969. Geology and Mineral Deposits of Lyon, Douglas, and Ormsby

- Counties, Nevada. *Nevada Bureau of Mines and Geology Bulletin* **75**, 45.
- Moore, J. G. & Lockwood, J. P., 1973. Origin of comb layering and orbicular structure, Sierra Nevada Batholith, California. *GSA Bulletin* **84**, 1–20.
- Müller, A., Herrington, R., Armstrong, R., Seltmann, R., Kirwin, D. J., Stenina, N. G. & Kronz, A., 2010. Trace elements and cathodoluminescence of quartz in stockwork veins of Mongolian porphyry-style deposits. *Miner. Deposita* **45** (7), 707–727.
- Mustard, R., Neilsen, R., Ruxton, P. A., 1988. Timbarra gold deposits. In: Berkman, D.A., Mackenzie, D.H. (Eds.), *Geology of Australia and Papua New Guinea Mineral deposits*. Australian Institute of Mining and Metallurgy, Melbourne, 551–560.
- Nandedkar, R. H., Hürlimann, N., Ulmer, P. & Müntener, O., 2016. Amphibole–melt trace element partitioning of fractionating calc-alkaline magmas in the lower crust: an experimental study. *Contrib. Mineral. Petrol.* **171**, 71. <https://doi.org/10.1007/s00410-016-1278-0>
- Nathwani, C. L., Loader, M. A, Wilkinson, J. J. *et al.*, 2020. Multi-stage arc magma evolution recorded by apatite in volcanic rocks. *Geology* **48** (4), 323-327. <https://doi.org/10.1130/G46998.1>
- Nathwani, C. L., Simmons A. T., Large, S. J. E. *et al.*, 2021. From long-lived batholith construction to giant porphyry copper deposit formation: petrological and zircon chemical evolution of the Quellaveco District, Southern Peru. *Contrib. Mineral. Petrol.* **176**, 12. <https://doi.org/10.1007/s00410-020-01766-1>
- Nowell, G. M. & Parrish, R. R., 2001. Simultaneous acquisition of isotope compositions and parent/daughter ratios by non-isotope dilution-mode plasma ionisation multi-collector mass spectrometry (PIMMS). In: Holland, G. & Tannser, S. D. (Eds.) *Plasma Source Mass Spectrometry: The New Millennium. Royal Soc. Chem., Spec. Publ.* **267**, 298-310.
- Pacey, A. *et al.*, 2020. Magmatic fluids Implicated in the Formation of Propylitic Alteration: Oxygen, Hydrogen, and Strontium Isotope Constraints from the Northparkes Porphyry Cu-Au District, New South Wales, Australia. *Econ. Geol.* **115** (4), 729-748.
- Park, J. W., Campbell, I. H., Malaviarachchi, S. P. K. *et al.*, 2019. Chalcophile element fertility and the formation of porphyry Cu ± Au deposits. *Miner. Deposita* **54**, 657–670. <https://doi.org/10.1007/s00126-018-0834-0>
- Pistone, M., Baumgartner, L. P., Bégué, F. *et al.*, 2020. Felsic melt and gas mobilization during magma solidification: An experimental study at 1.1 kbar. *Front. Earth Sci.* **8**, 175.
- Proffett, J. M., 1977. Cenozoic geology of the Yerington District, Nevada, and implications for the nature and origin of Basin and Range faulting. *GSA Bull.* **88** (2), 247-266.

- Proffett, J. M., 1979. Ore deposits of the western United States: A summary. *In*: Ridge, J. D. (Ed.), Papers on Mineral Deposits of Western North America: Nevada Bureau of Mines and Geology Report 33, 13–32.
- Proffett, J. M., 2003. Geology of the Bajo de la Alumbrera porphyry copper-gold deposit, Argentina. *Econ. Geol.* **98**, 1535–1574.
- Proffett, J. M., 2007. Report on the geology and genesis of the Yerington porphyry copper district, Nevada, a four dimensional study. *Final report for: USGS mineral resource external research program grant 06HQGR0171*.
- Proffett, J. M., 2009. High Cu grades in porphyry Cu deposits and their relationship to emplacement depth of magmatic sources. *Geology* **37** (8), 675-378. <https://doi.org/10.1130/G30072A.1>
- Proffett, J. M. & Dilles, J. H., 1984. Geological map of the Yerington District, Nevada: Nevada Bureau of Mines and Geology, map 77.
- Redmond, P. B. & Einaudi, M. T., 2010. The Bingham Canyon porphyry Cu-Mo-Au deposit. I. Sequence of intrusions, vein formation, and sulfide deposition, *Econ. Geol.* **105**, 43–68.
- Reed, M. H., 1997. Hydrothermal Alteration and its Relationship to Ore Fluid Composition. *In*: Barnes, H. L. (Ed.) *Geochemistry of Hydrothermal Ore Deposits, Volume 1, Third Edition*. Wiley, 303-317.
- Rezeau, H., Moritz, R., Wotzlav, J. *et al.*, 2016. Temporal and genetic link between incremental pluton assembly and pulsed porphyry Cu-Mo formation in accretionary orogens. *Geology* **44** (8), 627–630. <https://doi.org/10.1130/G38088.1>
- Richards, J. P. & Tosdal, R. M., 2001. Structural controls on ore genesis. 1st ed. Littleton, Colorado. *Society of Economic Geologists*.
- Richards, J. P., 2003. Tectono-Magmatic Precursors for Porphyry Cu-(Mo-Au) Deposit Formation. *Econ. Geol.* **98**, 1515-1533. <https://doi.org/10.2113/gsecongeo.98.8.1515>
- Richards, J. P., 2005. Cumulative factors in the generation of giant calc-alkaline porphyry Cu deposits. *In*: Porter, T.M. (Ed.), Super porphyry copper and gold deposits: A global perspective, v. 1: Adelaide, PGC Publishing, 7–25.
- Richards, J. P., 2009. Postsubduction porphyry Cu-Au and epithermal Au deposits: Products of remelting of subduction-modified lithosphere. *Geology* **37**(3), 247-250. <https://doi.org/10.1130/G25451A.1>
- Richards, J. P., 2011. High Sr/Y arc magmas and porphyry Cu±Mo±Au deposits: Just add water. *Econ. Geol.* **106** (7), 2075-1081. <https://doi.org/10.2113/econgeo.106.7.1075>
- Richards, J. P., 2012. High Sr/Y Magmas Reflect Arc Maturity, High Magmatic Water Content, and Porphyry Cu ± Mo ± Au Potential: Examples from the

- Tethyan Arcs of Central and Eastern Iran and Western Pakistan. *Econ. Geol.* **107(2)**, 295-332. <https://doi.org/10.2113/econgeo.107.2.295>
- Richards, J. P., 2015. Tectonic, magmatic, and metallogenic evolution of the Tethyan orogen: From subduction to collision. *Ore Geol. Rev.* **70**, 323-345. <https://doi.org/10.1016/j.oregeorev.2014.11.009>
- Richards, J. P., 2016. Clues to hidden copper deposits. *Nature Geoscience* **9**, 195–196.
- Richards, J. P., 2018. A shake-up in the porphyry world? *Econ. Geol.* **113**, 1125–1233.
- Rohrlach, B. & Loucks, R., 2005. Multi-million-year cyclic ramp-up of volatiles in a lower crustal magma reservoir trapped below the Tampakan copper-gold deposit by Mio-Pliocene crustal compression in the southern Philippines. Adelaide, PGC Publ. 2:369–407.
- Rollinson, G. K., Andersen, J. C. Ø., Stickland, R. J., Boni, M. & Fairhurst, R., 2011. Characterisation of non-sulphide zinc deposits using QEMSCAN®. *Miner. Eng.* **24 (8)**, 778–787. <https://doi.org/10.1016/j.mineng.2011.02.004>
- Rombach, C. S. & Newberry, R. J., 2001. Shotgun deposit: granite porphyry-hosted gold-arsenic mineralisation in southwestern Alaska, USA. *Miner. Deposita* **36**, 607–621.
- Romero, B. Kojima, S, Wong, C. *et al.*, 2010. Molybdenite mineralization and Re-Os geochronology of the Escondida and Escondida Norte porphyry deposits, Northern Chile. *Resour. Geol.* **61 (1)**, 91-100. <https://doi.org/10.1111/j.1751-3928.2010.00150.x>
- Rosenberg, C. L. & Handy, M. R., 2005. Experimental deformation of partially melted granite revisited: Implications for the continental crust. *J. Metamorph. Geol.* **23**, 19–28. <https://doi.org/10.1111/j.1525-1314.2005.00555.x>
- Rubatto, D. & Hermann, J., 2007. Experimental zircon/melt and zircon/garnet trace element partitioning and implications for the geochronology of crustal rocks. *Chem. Geol.* **241**, 38–61. <https://doi.org/10.1016/j.chemgeo.2007.01.027>
- Runyon, S. E., Steel-MacInnis, M., Seedorff, E. *et al.*, 2017. Coarse muscovite veins and alteration deep in the Yerington batholith, Nevada: insights into fluid exsolution in the roots of porphyry copper systems. *Miner. Deposita* **52**, 463-470. <https://doi.org/10.1007/s00126-017-0720-1>
- Runyon, S. E., Seedorff, E., Barton, M. D. *et al.*, 2019. Coarse muscovite veins and alteration in porphyry systems. *Ore Geol. Rev.* **113**, 103045 (2019). <https://doi.org/10.1016/j.oregeorev.2019.103045>
- Rusiecka, M. K., Bilodeau, M. & Baker, D. R., 2020. Quantification of nucleation delay in magmatic systems: experimental and theoretical approach. *Contrib. Mineral. Petrol.* **175**, 47.

- Schärer, U., 1984. The effect of initial ^{230}Th disequilibrium on young U-Pb ages: the Makalu case, Himalaya. *Earth. Planet. Sci. Lett.* **67**, 191-204.
- Schoene, B., Latkoczy, C., Schaltegger, U. & Günther, D., 2010. A new method integrating high-precision U-Pb geochronology with zircon trace element analysis (U-Pb TIMS-TEA). *Geochim. Cosmochim. Acta.* **74 (24)**, 7144-7159. <https://doi.org/10.1016/j.gca.2010.09.016>
- Schoene, B., 2014. 'U-Th-Pb Geochronology'. In: Holland, H. D. and Turekian, K. K. (eds.) *Treatise on Geochemistry*, 2nd edition. Elsevier. 341-378. <https://doi.org/10.1016/B978-0-08-095975-7.00310-7>
- Schöpa, A., Annen, C., Dilles, J. H., Sparks, R. S. J. & Blundy, J. D., 2017. Magma emplacement rates and porphyry copper deposits: Thermal modeling of the Yerington Batholith, Nevada. *Econ. Geol.* **112**, 1653-1672.
- Scotese, S. R., 2001. Atlas of earth history, PALEOMAP Project, Arlington, Texas, 52.
- Seedorff, E., Dilles, J. H., Proffett, J. M. *et al.*, 2005. Porphyry deposits: Characteristics and origin of hypogene features. *Econ. Geol.* **100**, 251-298.
- Seedorff, E. & Einaudi, M. T., 2004. Henderson porphyry molybdenum system, Colorado: I. Sequence and abundance of hydrothermal mineral assemblages, flow paths of evolving fluids, and evolutionary style. *Econ. Geol.* **99**, 3–37.
- Seedorff, E., Barton, M. D., Stavast, W. J. A & Maher, D. J., 2008. Root Zones of Porphyry Systems: Extending the Porphyry Model to Depth. *Econ. Geol.* **103**, 939-956.
- Selby, D. & Creaser, R. A., 2004. Macroscale NTIMS and microscale LA-MC-ICP-MS Re-Os isotopic analysis of molybdenite: Testing spatial restrictions for reliable Re-Os age determinations, and implications for the decoupling of Re and Os within molybdenite. *Geochim. Cosmochim. Acta.* **68**, 3897-3908. <https://doi.org/10.1016/j.gca.2004.03.022>
- Selby, D., Creaser, R. A., Stein, H. J., Markey, R. J. & Hannah, J. L., 2007. Assessment of the ^{187}Re decay constant by cross calibration of Re-Os molybdenite and U-Pb zircon chronometers in magmatic ore systems. *Geochim. Cosmochim. Acta.* **71 (8)**, 1999-2013. <https://doi.org/10.1016/j.gca.2007.01.008>
- Shannon, J. R., Walker, B. M., Carten, R. B. & Geraghty, E. P., 1982. Unidirectional solidification textures and their significance in determining relative ages of intrusions at the Henderson Mine, Colorado. *Geology* **10**, 293-297.
- Shinohara, H., Kazahaya, K. & Lowenstern, J. B., 1995. Volatile transport in a convecting magma column: Implications for porphyry Mo mineralization. *Geology* **23**, 1091–1094.

- Silberling, N. J., 1984. Map showing localities and correlation of age-diagnostic lower Mesozoic megafossils, Walker Lake 1° x 2° quadrangle, Nevada and California: U.S. Geological Survey Miscellaneous Field Studies Map MF-1382-0, scale 1:250,000.
- Sillitoe, R. H., 1973. The tops and bottoms of porphyry copper deposits. *Econ. Geol.* **68**, 799-815.
- Sillitoe, R. H., 1998. Major regional factors favouring large size, high hypogene grade, elevated gold content and supergene oxidation and enrichment of porphyry copper deposits, *In: Porter, T.M. (Ed.), Porphyry and hydrothermal copper and gold deposits: A global perspective: Adelaide, Australian Mineral Foundation*, pp. 21–34.
- Sillitoe, R. H., 2000. Gold-rich porphyry deposits: Descriptive and genetic models and their role in exploration and discovery. *Reviews in Economic Geology* **13**, 315–345.
- Sillitoe, R. H., 2005. Supergene oxidised and enriched porphyry copper deposits related to alkaline rocks and consequences for exploration. *Mineralium Deposita* **37**, 4-13.
- Sillitoe, R. H., 2010. Porphyry Copper Systems. *Econ. Geol.* **105**, 3-41.
- Sisson, T. W., 1994. Hornblende-melt trace-element partitioning measured by ion microprobe. *Chemical Geology* **117 (1-4)**, 331-344.
- Smith, D., 2014. Clinopyroxene precursors to amphibole sponge in arc crust. *Nat. Commun.* **5**, 4329. <https://doi.org/10.1038/ncomms5329>
- Smoliar, M. I., Walker, R. J., & Morgan, J. W., 1996. Re-Os ages of group IIA, IIIA, IVA, and IVB iron meteorites. *Science* **271**, 1099–1102.
- Sparks, R. S. J. & Cashman, K. V., 2017. Dynamic magma systems: implications for forecasting volcanic activity. *Elements* **13**, 35–40.
- Speed, R. C., 1978. Paleogeographic and plate tectonic evolution of the early Mesozoic marine province of the western Great Basin. *In: Howell D. G., and McDougall, K. A. (eds.), Mesozoic paleogeography of the western United States, Pacific Coast Paleogeography Symposium 2: Soc. Econ. Paleontologist Mineralogists, Pacific Sec., 1978, Sacramento, California*, 253-270.
- Speed, R. C., 1979. Collided Paleozoic microplate in the western United States. *Jour. Geology* **87**, 279-292.
- Spencer, E. T., Wilkinson, J. J., Creaser, R. A. & Seguel, J., 2015. The distribution and timing of molybdenite mineralization at the El Teniente Cu-Mo porphyry deposit, Chile. *Econ. Geol.* **110 (2)**, 387-421.
- Spurr, J. E., 1923. The ore magmas. McGraw-Hill, New York, 915.

- Stefanova, E., Driesner, T., Zajacz, Z. *et al.*, 2014. Melt and fluid inclusions in hydrothermal veins: the magmatic to hydrothermal evolution of the elatsite porphyry Cu-Au deposit, Bulgaria. *Econ. Geol.* **109**, 1359–1381.
- Stein H. J., 2014. Dating and Tracing the History of Ore Formation. *In*: Holland H. D. and Turekian K. K. (eds.) *Treatise on Geochemistry*, Second Edition, **13**, 87-118. Oxford: Elsevier.
- Stewart, J. H., 1972. Initial deposits of the Cordilleran geosyncline: Evidence of a late Precambrian (<850 m.y.) continental separation. *Geol. Soc. America Bull.* **83**, 1345-1360.
- Swanson, S. E., 1977. Relation of nucleation and crystal-growth rate to the development of granitic textures. *Am. Mineral.* **62**, 966–978
- Tapster, S., Condon, D. J., Naden, J. *et al.*, 2016. Rapid thermal rejuvenation of high-crystallinity magma linked to porphyry copper deposit formation; evidence from the Koloula Porphyry Prospect, Solomon Islands. *Earth. Planet. Sci. Lett.* **442**, 206-217. <https://doi.org/10.1016/j.epsl.2016.02.046>
- Taylor, H. P., 1980. The effects of assimilation of country rocks by magmas on ¹⁸O/¹⁶O and ⁸⁷Sr/⁸⁶Sr systematics of igneous rocks. *Earth. Planet. Sci. Lett.* **47**, 243-254.
- Terzaghi, K. & Peck, R.B., 1948. *Soil Mechanics in Engineering Practice*. John Wiley & Sons, New York.
- Thomas, J. B., Watson, E. B., Spear, F. S. *et al.*, 2010. Titanite under pressure: the effect of pressure and temperature on the solubility of Ti in quartz. *Contrib. Mineral. Petrol.* **160**, 743–759.
- Thompson, A. J. B. & Thompson, J. F. H., 1996. *Atlas of Alteration: A Field and Petrographic Guide to Hydrothermal Alteration Minerals*. *Geol. Assn. of Canada*.
- Tungalag, N., Jargalan, S., Khashgerel, B.-E., Mijiddorj, C., Kavalieris, I., 2018. Characteristics of the Late Devonian Tsagaan Suvarga Cu-Mo deposit, Southern Mongolia. *Miner. Deposita* **54 (3)**, 369–380.
- Tuttle, O. F. & Bowen, N. L., 1958. Origin of granite in the light of experimental studies in the system NaAlSi₃O₈-KAlSi₃O₈-SiO₂-H₂O. *Geol. Soc. Am. Memoir* **74**, 153.
- Valley, J. W., 2003. Oxygen isotopes in zircon. *Rev. Mineral. Geochem.* **53 (1)**, 343-385. <https://doi.org/10.2113/0530343>
- van der Wielen, K. P., 2013. Application of high voltage breakage to a range of rock types of varying physical properties. Ph.D. thesis, Camborne School of Mines, University of Exeter, UK.
- Vasyukova, O. V., Goemann, K., Kamenetsky, V. S., MacRae, C. M. & Wilson, N. C., 2013. Cathodoluminescence properties of quartz eyes from porphyry-type

- deposits: Implications for the origin of quartz. *Am. Mineral.* **98** (1), 98–109. <https://doi.org/10.2138/am.2013.4018>
- Vry, H. V., 2010. Geological and Hydrothermal Fluid Evolution at El Teniente, Chile. PhD thesis, Imperial College London.
- Wark, D. A., Watson, E. B., 2006. TitaniQ: a titanium-in-quartz geothermometer. *Contrib. Miner. Petrol.* **152** (6), 743–754.
- Watari, T., Nansai, K. & Nakajima, K., 2021. Major metals demand, supply, and environmental impacts to 2100: A critical review. *Resources, Conservation and Recycling* **164**, 105107. <https://doi.org/10.1016/j.resconrec.2020.105107>
- Watson, E. B. & Harrison, T. M., 2005. Zircon thermometer reveals minimum melting conditions on earliest earth. *Science* **308**, 841-844. <https://doi.org/10.1126/science.1110873>
- Weis, P., Driesner, T. & Heinrich, C. A., 2012. Porphyry-copper ore shells form at stable pressure-temperature fronts within dynamic fluid plumes. *Science* **338**, 1613-1616.
- White, W. H., Bookstrom, A. A., Kamilli, R. J., Ganster, M. W., Smith, R. P., Ranta, D. E. & Steininger, R. C., 1981. Character and origin of Climax-type molybdenum deposits. *Econ. Geol.*, **75th Anniversary Volume**, 270–316.
- Wieser, P. A. *et al.*, 2022. VESlcal: 2. A Critical Approach to Volatile Solubility Modeling Using an Open-Source Python3 Engine. *Earth and Space Science*, 9, e2021EA001932. <https://doi.org/10.1029/2021EA001932>
- Wilkinson, J. J., 2013. Triggers for the formation of porphyry deposits in magmatic arcs. *Nature Geoscience* **6**, 917-925.
- Wilkinson, J. J., Baker, M. J., Cooke, D. R. & Wilkinson, C. C., 2020. Exploration Targeting in Porphyry Cu Systems Using Propylitic Mineral Chemistry: A Case Study of the El Teniente Deposit, Chile. *Econ. Geol.* **115**, 771-791. <https://doi.org/10.5382/econgeo.4738>
- Williamson, B. J., Herrington, R. & Morris, A., 2016. Porphyry copper enrichment linked to excess aluminium in plagioclase. *Nature Geoscience* **9**, 237–241. <https://doi.org/10.1038/ngeo2651>
- Wilson, A. J., 2003. The geology, genesis and exploration context of the Cadia gold-copper porphyry deposits. University of Tasmania, New South Wales, Australia. PhD thesis.
- Wilson, C. J. N., Seward, T. M., Allan, A. S. R., Charlier, B. L. A. & Bello, L., 2012. A comment on: ‘TitaniQ under pressure: the effect of pressure and temperature on the solubility of Ti in quartz’, by Jay B. Thomas, E. Bruce Watson, Frank S. Spear, Philip T. Shemella, Saroj K. Nayak and Antonio Lanzirotti. *Contrib. Mineral. Petrol.* **164**, 359–368.
- Zimmerman, A., Stein, H. J., Morgan, J. W., Markey, R. J., & Watanabe, Y., 2014.

Re-Os geochronology of the El Salvador porphyry Cu-Mo deposit, Chile: Tracking analytical improvements in accuracy and precision over the past decade. *Geochim. Cosmochim. Acta.* **131**, 13–32.